A STUDY OF HEXAVALENT AND TRIVALENT CHROMIUM CONVERSION COATINGS ON ZINC SURFACES

by

ROSHAN CHAPANERI

A Doctoral Thesis submitted in partial fulfilment of the requirements for the award of Doctor of Philosophy of Loughborough University

2010

Supervisors:

Dr. G.W. Critchlow

Dr. G.D. Wilcox

Department of Materials, Loughborough University

Industrial Superivisors:

Dr. T. Pearson

Dr. A. Rowan

MacDermid plc.

Certificate of Originality

This is to certify that I am responsible for the work submitted in this thesis, that the original work is my own except as specified in acknowledgements or footnotes, and that neither the thesis nor the original work contained herein has been submitted to this or any other institution for a higher degree.

…… (Roshan Chapaneri)
…… (03/10/2010)

Abstract

Physical, chemical and corrosion properties of a hexavalent chromium conversion coating (CCC) and that of a commercial third generation trivalent chromium system; Tripass LT1500, on zinc electrodeposited steel has been studied. Moreover, the role of additives has been studied to elucidate film formation and corrosion resistance mechanisms. Micro-cracking and self-repair corrosion protection behaviour commonly associated with hexavalent CCCs has also been investigated.

Scanning Electron Microscopy (SEM) studies showed that for both hexavalent and trivalent CCCs were in general, flat with a spherical-like structure and in the case of the former micro-cracked beyond 122 nm conversion coating thickness. In general, the micro-crack pattern observed e.g. a dense crack network, depended upon the underlying zinc substrate morphology. The study has also demonstrated the effect of SEM imaging and prior specimen preparation conditions on hexavalent CCC micro-cracking and blistering.

X-ray Photoelectron Spectroscopy (XPS), Auger Electron Spectroscopy (AES) and Infrared (IR) data has indicated that the hexavalent CCC film formation appears to be a electrochemical / sol-gel mechanism given the lack of zinc content at surface and subsurface regions within the conversion coating, presence of H_2O and in particular the contribution of $Cr(OH)_3$ as opposed to Cr_2O_3. An alternative film formation mechanism may exist for trivalent CCC given a higher proportion of zinc at surface and sub-surface regions, IR data analysis indicating that chromium is possibly deposited from a chromium (III) complex ion such as $[CrC_2O_4(H_2O)_4]^+$, moreover as $Cr(OH)_3$ and Cr_2O_3 compounds as indicated by XPS data analysis. The role of cobalt nitrate during film formation is unclear given that cobalt was not detected within the trivalent CCC from XPS and AES data.

Electrochemical LPR measurements, polarisation curves and XPS data has shown in general, self-repair corrosion protection properties for hexavalent CCC to be lacking. Instead, it is proposed that the corrosion protection behaviour for hexavalent and trivalent CCC to be barrier. Polarisation curves and LPR data showed that the corrosion resistance performance for trivalent CCC was higher than hexavalent CCC, in general. LPR data showed that the omission of cobalt nitrate and increased addition of sodium molybdate content within the

Tripass LT1500 treatment solution formulation was found to overall decrease corrosion resistance within the trivalent CCC.

In addition, silica based topcoat and black trivalent CCCs was also investigated and characterised using AES, SEM and LPR. Zinc whiskers was also observed from zinc electrodeposits following exposure to thermal treatment (150°C for 1 h). Elemental analysis and grain pattern investigations failed to help determine the cause of zinc whisker initiation. Zinc whiskers was seen to protrude out of hexavalent and trivalent CCCs, with the latter requiring a longer thermal exposure time.

Keywords:
Chromium conversion coatings (CCC), surface analysis, hexavalent chromium, trivalent chromium, electroplated zinc, zinc whiskers.

Acknowledgements

It is extremely difficult to conduct a project such as this without failing to acknowledge the considerable contribution of many people.

Firstly, I would like to thank my academic supervisors Dr G. W. Critchlow and Dr. G. D. Wilcox for their support and guidance throughout the project. Secondly, I would like to acknowledge the sponsorship that MacDermid plc. and the Engineering and Physical Sciences Research Council (EPSRC) have provided in support of this project. Many thanks to Dr. T. Pearson, Dr. A. Rowan, Dr. A. Chojnicki, Mrs S. Damji and all other technical staff of MacDermid plc. who have helped with this project. A thank you also goes to Dr. G. Beamson of the National Centre for Electron Spectroscopy and Surface Analysis (NCESS) and Dr. I. Sutherland and Dr. P. Cropper of the Materials Department, Loughborough University for their valuable technical input and discussions of XPS data associated with this project.

I would also like to thank all colleagues and technical staff at the Materials Department, Loughborough University.

Finally, last, but certainly not least, I would like to give thanks for the support that my family and Sri Sathya Sai Baba have played throughout my lifetime.

Abbreviations

AES	Auger electron spectroscopy
AFM	Atomic force microscopy
ATR	Attenuation total reflectance
ASTM	American Standards for Testing Materials
BE	Binding energy
CCC	Chromium conversion coating
CHA	Concentric hemispherical analyser
CMA	Cylindrical mirror analyser
DRIFT	Diffuse reflectance infrared fourier transform spectroscopy
DSIMS	Dynamic secondary ion mass spectrometry
EDX	Energy dispersive X-ray spectroscopy
EIS	Electrochemical impedance spectroscopy
ELV	End of life vehicles directive
EPA	Environmental protection agency
ESCA	Electron spectroscopy for chemical analysis
FEGSEM	Field emission gun scanning electron microscopy
FIBSEM	Focused ion beam scanning electron microscopy
FTIR	Fourier transform infrared
FWHM	Full width at half maximum
GDOES	Glow discharge optical emission spectroscopy
IR	Infrared
ISO	International standards organisation
IMP	Intermetallic particles
KE	Kinetic energy
LPR	Linear polarisation resistance
MIR	Multiple internal reflection spectroscopy
NCESS	National Centre for Electron Spectroscopy and Surface Analysis
NSS	Neutral salt spray
OCP	Open circuit potential
RAIRS	Reflection absorption infrared spectroscopy
RoHS	Restriction of hazardous substances

RSF	Relative sensitivity factor
SCE	Saturated calomel electrode
SEM	Scanning electron microscopy
SHE	Standard hydrogen electrode
SIMS	Static ion mass spectroscopy
TEM	Transmission electron microscopy
TGA	Thermo-gravimetric analysis
TOA	Take off angle
VP	Variable pressure
WEEE	Waste electrical & electronic equipment directive
XANES	X-ray absorption near edge spectroscopy
XPS	X-ray photoelectron spectroscopy
XRD	X-ray diffraction

Contents

1 Introduction

Surface coatings are required to provide a wide range of properties to the substrates onto which they are deposited. The requirement can be dictated by many factors such as the use of a particular substrate or base material as well as important in-service conditions. In particular, carbon steel is often chosen as a base material for many applications such as automotive body panels [1-4] due to its advantages of low cost, availability, formability, weldability, recyclability and the attainment of desired mechanical and thermal properties. However, it's corrosion resistance is poor and thus a major drawback. Surface coatings such as hot-dip galvanising, electroplating or spraying with molten zinc can provide the necessary corrosion resistance. The zinc applied provides not only a barrier to a surrounding environment, but also undergoes galvanic coupling with the steel in cases where the surface becomes damaged and becomes anodic with respect to the steel. In recent years the trend has been for the metal finishing industry to use zinc alloys for increased corrosion performance. However, this industry has recently moved back towards pure zinc in order to outweigh the cost of using zinc alloys.

Zinc and zinc alloy coatings have often been supplemented with conversion coatings for prolonging the onset of zinc corrosion. These coatings can be found on a number of automotive components, primarily fastener type applications such as nuts, bolts and washers. From an industrial context these coatings are potentially exposed to corrosive media such as chlorides and water for exterior automotive components. In addition, fasteners may also be subjected to thermal exposure. This may include components used in close proximity to the engine block of a vehicle i.e. 'under the bonnet' or during the curing of an adhesive between two mating conversion coated components. Conversion coatings may also require abrasion resistance during exposure to road grit and processing such as barrel treatment. Industry also requires that conversion coatings are consistent in colour and that they can be easily identified and matched accordingly. For applications such as automotive body panels, an additional primer and organic topcoat paint finish are applied, with the conversion coating acting as a pretreatment. Therefore conversion coatings must also provide sufficient adhesion between the underlying substrate and organic topcoats.

Conversion coatings are effective in prolonging the time period prior to the formation of white and red rust i.e. zinc and iron corrosion products, on zinc coated steel in mildly

corrosive conditions. In addition, they have the advantages of providing an aesthetically pleasing appearance, improved paintability and optimised surfaces for subsequent adhesive bonding. Unfortunately, the most widely used conversion coating is based on chromium in the hexavalent oxidation state (Cr(VI)). Hexavalent chromium conversion coatings (CCCs) have the prime advantage of superior corrosion resistance, however, due to the toxicity of hexavalent chromium, there are major health and safety and environmental problems during the processing, service and disposal stages. It is therefore, not surprising to find, that hexavalent CCCs are currently in the stage of being phased out by industry in order to meet legislation such as 'The End of Life Vehicle' (ELV), and 'The Waste Electrical and Electronic Equipments' (WEEE) directives [5]. Other derivatives of chromium used for conversion coatings are trivalent (Cr(III)) systems these, at present, meet current legislation and are regarded as the 'next best available technology' [6-8]. It is important to note that some legislators may still regard trivalent chromium processes with suspicion as they are still based on 'chromium'. A more recent controversial study has even indicated that certain current commercial trivalent systems actually fail legislative requirements due to a hexavalent chromium content [9].

The search for a direct replacement for hexavalent CCCs has been of interest, as early as the late 1970s [5]. A common consensus is that the first trivalent chromium systems developed at the time lacked the oxidising power of Cr(VI) species during film formation and thus resulted in relatively thin conversion coatings which could only provide limited corrosion resistance. In the years that followed, the addition of specific additives such as oxidising agents, organic acids and metal ions to trivalent chromium formulations has played a significant role in improving the film formation process and has enabled corrosion performance to be similar, if not better, than hexavalent CCCs. A more recently developed trivalent chromium commercial system; Tripass LT1500, can be operated at reduced processing temperatures thus enabling it to be more economically viable in relation to hexavalent chromium systems. Despite the fact that commercial trivalent chromium products are currently available for industrial use, an understanding of their film formation and corrosion protection mechanisms is somewhat lacking, as is the true hexavalent chromium content, if any. Such information is required for further formulation improvements to be made.

Although much research has been conducted into hexavalent CCCs, their unique ability to self-repair under corrosive conditions and the mechanism by which this is achieved is still

open to debate. Self-repair is a mechanism in which Cr(VI) species within the coating are thought to reduce to Cr(III) corrosion products under certain conditions and thus regenerate and prolong corrosion resistance before the advent of zinc corrosion products. Also open to debate is the mechanism by which micro-cracks, observed using surface analytical equipment such as Scanning Electron Microscopy (SEM), are initiated within hexavalent CCCs, particularly when this coating is known for its corrosion protection. A better understanding of hexavalent CCCs will only further knowledge in the subject area encompassing conversion coatings.

1.1 Research objectives

The aim of this thesis was to investigate a standard hexavalent CCC against a commercial third generation trivalent chromium system (Tripass LT1500) on acid zinc electrodeposited steel using a range of analytical techniques to study the resultant surface morphology and carry out both chemical and corrosion characterisation. Moreover the role of additives used in their treatment solution formulation on subsequent film formation, physical / chemical structure and corrosion performance were major subject areas of interest. In addition to these studies, black trivalent CCCs on acid and alkaline zinc electrodeposited steel and organic topcoats were also investigated. Parameters of particular interest include the following:

Surface morphology

Surface morphology of hexavalent and trivalent CCCs has been characterised using Field Emission Gun Scanning Electron Microscopy (FEGSEM), Atomic Force Microscopy (AFM) and Cyro-stage Scanning Electron Microscopy (Cryo-stage SEM). To evaluate the effect of processing immersion time, the conversion coatings were studied using FEGSEM and AFM. FEGSEM was also applied to study the effects of thermal treatment and exposure to corroding environments. As part of the investigations into corrosion protection mechanisms, such as self-repair, surface topography was evaluated following manual scratching of coatings in accordance with the ASTM D1654 standard [10] and exposure to a corrosive environment (18 h 5% NaCl solution). Quantitative elemental analysis using Energy Dispersive X-ray (EDX) spectroscopy was used to determine the elemental composition of specific areas of interest. Cryo fracture specimen preparation was used in conjunction with FEGSEM imaging to elucidate coating thickness and to analyse cross-sections to complement studies into the effect of processing immersion time and exposure to corrosive environments.

In this study the effect of thermal and vacuum exposure from SEM imaging as a possible source for the initiation of cracking within hexavalent CCCs was also investigated using Cryo-stage SEM, AFM and the various imaging modes of FEGSEM. The influences of zinc substrate type and hexavalent CCC treatment solution formulation on micro-cracking pattern were also investigated.

Chemical characterisation

Chemical characterisation of hexavalent and trivalent CCCs has been carried out using X-ray Photoelectron Spectroscopy (XPS), Auger Electron Spectroscopy (AES) and Infra-red (IR) spectroscopy. To elucidate the hexavalent and trivalent chromium content within the surface of the conversion coatings, XPS high resolution scans were obtained using a monochromatic Al X-ray source following evaluation with curve fitting software. AES depth profiling, XPS survey scans and depth profiling via high resolution scans taken at different incident beam take off angles, and IR data were also used. The information gained from these techniques also helped to propose film formation mechanisms and the role of additives. It is important to note that a systematic approach was developed and applied to curve fitting of XPS high resolution data. Also important to note was the problem of overlapping Zn Auger peaks in similar binding energy positions to that of Cr 2p photoelectron peaks thus making high resolution and survey scans difficult to interpret.

To study corrosion protection behaviour of hexavalent and trivalent CCCs following exposure to a corrosive environment (18 h 5% NaCl solution), XPS and AES depth profiling analysis were conducted.

Corrosion characterisation

Relative corrosion performance of hexavalent and trivalent CCCs was determined using electrochemical testing. To evaluate the self-repair theory of hexavalent CCCs, Linear Polarisation Resistance (LPR) measurements were taken to observe corrosion protection behaviour over a prolonged period of exposure. In addition polarisation curves were undertaken in oxygen containing and deficient conditions following nitrogen gas purging. Electrochemical polarisation corrosion tests were carried out in accordance with ASTM G59 [11].

The following section provides details of the relevant literature to this study.

2 Literature review

2.1 What is corrosion?

Corrosion is fundamentally an electrochemical reaction. In an electrochemical reaction simultaneous anodic and cathodic reactions occur in equal measure; see Equations 2.1, 2.2, 2.3 and 2.4, with an electrical circuit provided by the conducting material and exposure to an electrolyte such as water. Corrosion basically, results in metal loss, however, a visual indication of the corrosion process is the formation of an insoluble corrosion product originating from an anodic region of the metal. The corrosion and its rate will be dependent upon the metal in question e.g. steel or aluminium, the surrounding environment e.g. acidic, neutral and alkaline; see Equations 2.1, 2.2, 2.3 and 2.4, and the constituting cathodic agents e.g. hydrogen ions, water and oxygen under aerated conditions [12]. Corrosion products of metals such as steel and zinc are red and white in colouration respectively, chemically they comprise iron and zinc oxides or hydrated oxides following reaction of the metal salt (Me^{+}) with oxygen, water and other species (e.g. NO_2, SO_2) in the surrounding environment. Environmental factors that increase the corrosion rate include high temperatures, agitation/flow of electrolyte to the corrosion site, supply of cathodic agents (e.g. oxygen / hydrogen ions) for promoting cathode reactions and corresponding anodic reactions, and an acidic in the case of steel and neutral/alkaline electrolyte in the case of pure aluminium [12].

(Anodic reaction) $Me \rightarrow Me^{+} + e^{-}$ **Equation 2.1**
(metal) (metal salt) (electron)

(Cathodic reaction) $2H^{+} + 2e^{-} \rightarrow H_2$ **Equation 2.2**
(Acidic environment - hydrogen ions plentiful)

(Cathodic reaction) $O_2 + 2H_2O + 4e^{-} \rightarrow 4OH^{-}$ **Equation 2.3**
(Neutral environment – oxygen available i.e. non-deaerated)

(Cathodic reaction) $2H_2O + 2e^{-} \rightarrow H_2 + 2OH^{-}$ **Equation 2.4**
(Alkali environment – hydrogen ions rare initially, water reduction)

An electrochemical corrosion reaction can take place either at independent sites of the same metal surface or at two different metal sites in direct electrical contact, with one site acting as the anode and the other as the cathode. The former, related to potential difference, could exist

due to scratches, stress, temperature differences, surface chemical composition, or changes in surrounding metal surface environment such as electrolyte oxygen concentration, in which local anodic and cathodic sites exist due to oxygen being depleted or enriched [13]. In the latter case, this will be dependent upon which of the metals has a greater tendency to be oxidised into its metal ions; see Equation 2.1, thus resulting in a more electronegative state. A galvanic series has been compiled; see Table 2.1, to take this into account, with the potential measurements taken with reference to the standard hydrogen electrode (SHE) given as 0 V. Consequently, pairing of certain metals in direct contact with one another, such as steel and aluminium or zinc, should be avoided, unless specifically designed for sacrificial (cathodic) protection. Such mechanisms have found applications in deep sea protection of steel piping.

Table 2.1 A typical galvanic series for some commonly used metals [14].

2.2 Selection of a metallic material

In an ideal scenario in which a metallic material is selected for an application requiring high corrosion resistance, noble metals such as gold and platinium would be chosen; see Table 2.1. These metals not only meet corrosion requirements but can also have the relevant thermal and

mechanical properties too. Unfortunately, their abundance, raw material and processing costs limit their usage. Therefore in general a compromise is made, particularly on cost where metals such as steel and aluminium are in wide use even though their corrosion performance is often inferior.

The composition of all steels is based primarily on iron 'alloyed' with carbon. The demand for steel had been steadily increasing following post war reconstruction and economic growth of industrialised nations. In recent years the demand for steel production has rapidly increased with the advent of emerging economies. The content of carbon within the steel can range from 0 to 2 wt-% (low, medium and high carbon steel) [15], with an increase in carbon level improving properties such as hardness and tensile strength at the expense of ductility. Above 2 wt-% carbon incorporation, the steel is commonly termed as cast iron. A limitation of steel is it's high rate of corrosion under corroding environments, consequently surface coating systems are commonly used for corrosion inhibition [12]. Alternatively, alloying carbon steel with additional elements in combination such as manganese, silicon, nickel, chromium, molybdenum and vanadium at specified levels can also improve the corrosion resistance [12]. Stainless steels which typically have a high incorporation of chromium, nickel and sometimes molybdenum do not require surface coatings, in general, in order to meet corrosion resistance performance [16]. Stainless steels are protected by a thin layer of chromium-rich oxide, however, under a reducing environment this can be lost and the underlying metal can corrode [12].

The use of aluminium as a base substrate may also require the use of a surface coating in certain applications. Like steel, aluminium as a base material is in wide demand. Unlike steel, however, it's general corrosion resistance is better, due to its natural tendency to form an oxide film following exposure to air. The oxide film with a thickness between 4-10 nm is composed of two distinct oxide layers. The inner layer being a compact and amorphous barrier coating, with the outer layer being less compact and porous [17]. It is also important to note that aluminium is also amphoteric.

To further improve corrosion, thermal and mechanical performance, aluminium may also be alloyed with lithium, iron, silicon, copper, manganese, magnesium and chromium. However, in some cases corrosion performance may actually reduce, since the potential difference between the additional phases within the core solid solution matrix of aluminium results in

galvanic corrosion. For example aluminium-copper alloys can form precipitates of $CuAl_2$ particles at grain boundaries and leave adjacent solid solution aluminium anodic and prone to corrosion [16].

2.3 Surface coatings for steel

Surface coatings may be composed either of organic or inorganic materials, with the latter being favoured in most applications. There are a number of metals that can be used as inorganic surface coatings for steel applications. For example tin on mild steel has been used for the interior surfaces of food cans and containers [18], tin provides sacrificial corrosion protection and importantly a relatively inert and non-toxic food container. For decorative applications (e.g. sanitary, automotive exterior and interior trims) in which high reflectivity, tarnish, corrosion and wear resistance is required, chromium (typically 0.1 to 0.3 μm) in the hexavalent or in the trivalent state is electrodeposited onto steel with a nickel and/or copper under-coat [19-21]. The underlying nickel coating, in either single or duplex layers preferentially corrodes instead of the chromium, in regions of pores and cracks (local galvanic cells) [22]. In applications where hardness and wear resistance is desired e.g. cylinders, engine valves and piston rings [23], chromium primarily, in the hexavalent state, is directly electrodeposited onto steel with a coating thickness up to 100 μm [24]. In automotive applications such as fasteners e.g. nuts, bolts, washers, strip and non-strip, cadmium had been used as a surface coating of steel as a replacement for earlier zinc coating systems. Cadmium provides sacrificial corrosion protection and is generally more corrosion resistant than its less noble zinc counterpart, particularly under a marine environment [18,25]. However, environmental and health and safety issues associated with cadmium's toxicity has resulted in the automotive industry moving back to zinc coatings, with zinc alloys used in more demanding applications e.g. chassis hardware, fuel and brake systems, heating and air conditioning components [26]. For a number of important safety critical applications (e.g. fasteners) such as in the aerospace and military sectors, in which no suitable alternatives have yet been identified for corrosion resistance and lubricity, cadmium use is expected to continue [27].

In this investigation zinc coated steel specimens were used and therefore this will be discussed in more detail.

2.3.1 Zinc coatings

Zinc coatings are thought to provide corrosion protection for steel via three mechanisms. Firstly, as an insoluble barrier. Secondly, as it's fresh surface develops a thin film of corrosion product, mainly zinc oxide forms following exposure to atmospheric oxygen under dry air which reduces the rate of further corrosion [28]. Thirdly, via sacrificial cathodic protection of steel at regions of damage. Zinc coatings can be applied to steel via a range of methods. These include electrodeposition, hot-dip immersion, thermal spraying, mechanical, electroplating and painting via brush or roller. The selection method will be dependent upon the coating application, examples of such are listed in Table 2.2. In the present investigation zinc coatings are produced by electrodeposition and therefore this technique will be discussed in more detail.

Table 2.2 Zinc coating methods, processes, specifications and applications [28]**.**

2.3.2 Zinc electroplating

The basic requirements for zinc electroplating include an anode, cathode, electrolyte and a electrical power supply to drive the process.

The type of anode typically used industrially for aqueous zinc electrodeposition is soluble and based on zinc, which undergoes dissolution during electroplating to maintain the zinc metal ion concentration within the electrolyte. The use of insoluble anodes for aqueous zinc electrodeposition is limited mainly due to cost. This type of anode is based on an inert material such as platinised titanium or stainless steel. Its prime advantage includes a superior current efficiency i.e. efficient oxygen evolution (loss of electrons) to maintain the cathodic part of the electrolysis process.

The steel cathode is placed into the electrolyte as an entity or within a metallic cage moulded with a organic coating as in rack or barrel electroplating, the surface is degreased and acid pickled to remove unwanted oils, grease, rust and other potential scales and soils which could have a negative effect on the electroplating process. It is important to note that in an aqueous electrolyte the presence of hydrogen ions may result in hydrogen evolution at the cathodically charged steel which is undergoing electrodeposition. Consequently, this reduces the cathode current efficiency for the electrodeposition of metal ions and increases the possibility of hydrogen embrittlement of many substrates. In a move to improve cathode current efficiency ionic liquids which are based on a non-aqueous electrolyte are being researched as potential replacements for aqueous electrolytes in niche applications [29]. At the present moment in time there does not appear to be a move to replace aqueous zinc electrolytes with these systems.

The electrolytes used for zinc electroplating have commonly been based upon aqueous acid or alkaline formulations. Simple acid zinc electrolyte formulations are usually based upon zinc chloride or zinc sulphate, with the former known to provide a brighter surface appearance [26]. Modern alkaline zinc electrolytes include many organic additives and are chiefly based on zinc oxide and hydroxide.

Cyanide has been used as a complexing agent within alkaline zinc electrolyte formulations. The use of a complexing agent is to increase the ionic stability of the metal ion, to ease deposition initiation and increase the deposition rate [30]. The complexing agent is also

thought to modify the cathode polarisation potential [30], effectively enabling a wider metal alloy co-deposition window. In a step to avoid the toxicity and hazards associated with cyanide, industry has moved to more environmentally friendly aqueous acid and alkaline systems with the aid of additives based on organic material such as brighteners, levellers, surfactants, anode depolarisers (or depassivators) and carriers. Experimentation with organic additives in zinc electroplating can be traced back to the turn of the 20th century when formaldehyde was reported to reduce the grain size of acid zinc electrodeposits [31]. Since then many additives have been investigated in an attempt to improve deposit and electrolyte properties such as grain size, brightness, current efficiency, and electrolyte throwing power. A review by Boto in 1975, provides details of some of the early additives used and their potential mechanisms [31]. Since then many additional studies have been conducted to investigate the role of additives within the zinc deposit and electrolyte [32-35].

2.3.3 Zinc alloy electrodeposition

An extension of zinc electrodeposition is to alloy zinc with another metal. Alloying can improve properties, such as hardness, by distortion of the lattice matrix via straining, or corrosion resistance by the introduction of a more noble alloying metal thus changing the overall potential of the electrodeposit. However, not all metal ions can be easily co-deposited with zinc. In general zinc can only really be co-deposited with a metal ion of similar electrode potential, within +/-0.30 V. If this is not the case the more noble metal ion would preferentially deposit first onto the cathode before the other metal ion deposits. Mechanisms used to bring the potential of metal ions closer together involve the use of a complexing agent, which decrease the potential of the more noble metal ion. Metal ions that are known to co-deposit with zinc are the anomalous ‘iron block’ alloying metals which include Fe, Ni, Mn, Co, Sn and Cr [36]. The classification of anomalous ‘iron block’ alloying metals co-deposition with zinc is given as the less noble Zn deposits preferentially in most plating conditions, however, the mechanism for this is still yet to be fully elucidated [37].

2.3.4 Passivation

Another method in which the corrosion performance of zinc and its alloys can be improved is to convert their surface into a relatively stable oxide structure i.e. the passive state. The ability to achieve a passive state is dependent upon the ability of the metal in chemisorbing suitable corrosion inhibiting species which can reduce the rate of corrosion in the corroding

environment: these inhibiting substances may include oxygen, metal oxides, corrosion products and organic absorbants [18]. In the case where metal compounds are adsorbed and form a surface film from a chemical solution, this is commonly referred to as conversion coating. In cases when a non-artificial passive state is achieved via the formation of a corrosion product in an oxidising environment, protection may only be achieved if the product is insoluble and stable. The environment in which a metal such as zinc is passive, corrosive or immune can be determined from Pourbaix diagrams, Potential-pH plots. In general, passivity is maintained by conditions of high oxygen concentration but is destroyed by the presence of certain ions such as chlorides [38].

2.3.5 Conversion coatings

A conversion coating consists of a mixed metal oxide composition following an electrochemical reaction of the metal surface with a suitable anion containing medium. The mechanism behind this process is that the metal surface undergoes anodic dissolution, this along with the incorporation of metal ions, oxides and other constituents from the treatment solution forms a gel layer which consolidates into a coating. Conversion coatings are not homogeneous in chemical composition or structure and vary from their metal substrate interface to the surface.

A conversion coating can either be applied by simple immersion or spraying of solution, or an electrolytic cathodic or anodic process via an impressed electrical current. The origin of conversion coatings when referring to those formed from chromate based systems can be traced back to 1924 when hexavalent chromium based conversion coatings were applied to magnesium [39]. This was then followed by application onto zinc, cadmium, copper, aluminium, silver, tin, nickel, zirconium, beryllium, and alloys of these metals [39].

The main elements known to form conversion coatings in which metal oxides are produced and which are relatively insoluble in water, acids or alkalis include Cr, Mo, W, Ru, Os and Rh [40]. Other chemical species have also been investigated for conversion coating formation such as permanganates, and vanadates [41]. A phosphate conversion coating can also be formed using phosphoric acid and various phosphates [25]. Phosphate conversion coatings were originally invented before chromate based conversion coatings. The processes available today are developments on the Coslettising process, which was devised in 1907. In this process iron or steel articles were treated by immersion (typically 30 min) in a hot solution of

ferrous phosphate (5-10 g/l) [14]. Other formulations developed thereafter include those based on zinc phosphates, for the treatment of zinc substrates. In general, phosphate based conversion coatings are used in applications for example on automotive body panels [1,42], in which an improvement in adhesion is required e.g. prior to a paint or primer finish. In applications in which corrosion resistance is of upmost importance chromium based conversion coatings are favoured, as phosphate conversion coatings, generally have inferior performance. Lightweight phosphate coatings can provide temporary corrosion protection during storage and between production stages, with medium to heavyweight coatings for longer term protection often also supplemented with oil, grease or wax [14].

2.3.5.1 Properties of conversion coatings

Advantages of conversion coatings, such as those based on hexavalent chromium chemistry, include; improved adhesion for subsequent primer or paint finishes, aesthetic appearance, and primarily the prolonging of the corrosion protection of the underlying substrate. The main method by which corrosion resistance is improved, in general, is based upon the coating acting as a barrier. This is achieved chemically due to the passive oxide composition, which reduces electrical conductivity and the presence of anodic and cathodic regions important for electrochemical corrosion to occur. The physical properties important for barrier performance include film thickness, adhesion to substrate, surface finish, the non-porous, compact nature of the film, insolubility and non-permeability to corrosive ions. Another method thought to improve corrosion resistance is via self-repair, however, this property is only associated with hexavalent CCCs and on metal substrates such as zinc and aluminium. Self-repair is a mechanism in which soluble Cr(VI) species within the coating are thought to reduce to insoluble Cr(III) corrosion products under certain conditions and thus regenerate the conversion coating and prolong corrosion resistance before the advent of underlying substrate corrosion [7,43-51].

Upon initial formation, a conversion coating is naturally soft and lacks adequate mechanical properties, however, over time its structure hardens as it dries. In order to accelerate this process conversion coatings are often dried within an oven. It is important to note that for hexavalent CCCs, loss of soluble Cr(VI) species, shrinkage and cracking has been reported if they are dried above 66°C [49]. However, conversion coatings can be used in applications such as the ‘under the bonnet’, areas of an automobile where temperatures close to 150°C are expected [6].

Conversion coatings are not particularly known for their mechanical properties hence they are often supplemented with an organic sealer and/or topcoat. Types of sealers include silicates, phosphates and silanes [52]. Types of topcoats include organic lacquers, polymers, lubricants, waxes, oils, and oil emulsions with suspended particles and colouring dyes [52]. In general, the use of a sealer and/or topcoat has consequently enabled conversion coatings to be used in a wider range of applications such as mating components requiring a low coefficient of friction (torque/tension) or lubrication, applications requiring abrasion resistance and improving their resistance to elevated heat treatment e.g. in the baking during curing of an organic paint finish or of adhesive joints.

The average thickness of a conversion coating, used industrially, is less than 1 µm. Process variables which influence thickness include concentration of solution, pH, immersion time and temperature of treatment solution. Chemical additives also influence thickness these include the type of acid used for controlling pH and specific chemical additives e.g. cobalt and malonic acid.

2.3.5.2 Industrial factors (processing, cost, legislation)

A systematic processing line for conversion coating a zinc coated steel component is likely to include a water rinse, an activation step via immersion (typically dilute nitric acid), conversion coating (typically via immersion), a water rinse, and finally drying via an oven. In addition it is common for an organic sealer and/or topcoat to be applied depending upon the service requirements. It is important to note that water rinse stations are used to reduce potential drag out contamination of conversion coating treatment solutions.

A favoured route industrially for conversion coating of components is immersion within a processing solution as it is a cheap and effective method. Depending upon the geometry of the components they are either barrel or rack treated. In the case of barrel treatment, small components such as bolts, nuts and washers are placed within a rotating barrel filled with processing solution. Rack treated components are placed onto a jig and immersed in the processing solution, with the solution agitated mechanically or via pressurised air. Common processing problems associated with these methods include uniform thickness distribution, surface finish, stability of the processing solution (i.e. zinc, Cr^{6+} or Cr^{3+} content control), solution maintenance (i.e. additives) and damage of coatings particularly of barrel treated

components. It is also important to note that the underlying substrate may also have an influence on the end product.

A variety of conversion coating colourations can be produced e.g. black, yellow, blue, green and with some exhibiting iridescent colourations. These are, however, dependent upon process parameters and additives. Industrially, it is important for the production of consistent and uniform colourations for identification and colour matching of components. In order to apply or improve existing colourations, conversion coatings are also capable of absorbing dyes [49].

The cost of conversion coatings is a function of processing conditions i.e. immersion time, temperature, number of additives required and cost of raw material. These factors in the past have aided hexavalent chromium in being a favoured choice for conversion coatings amongst industry up until the advent of the End of Life Vehicle (ELV) and Waste Electrical and Electronic Equipment (WEEE) directives [5,53,54] which have restricted their use. Details of this will be discussed in Section 2.5.5.3.

2.4 Surface analysis techniques for studying conversion coatings

Before discussing the surface morphology, chemical composition and corrosion properties of conversion coatings in detail it is important to introduce the techniques commonly used in their characterisation. Outlined in the following sections are background information and details of the advantages and potential limitations of these types of analysis techniques.

2.4.1 Surface morphology characterisation

2.4.1.1 Scanning Electron Microscopy (SEM)

The basis of an electron microscope is to generate and focus a stream of electrons onto a specimen using a series of electromagnetic condensing and objective lenses. The beam can then be rastered across the surface of the specimen using electromagnetic scan coils. At the point of contact between the electron beam and the specimen a number of interactions may occur and may result in the emission of secondary electrons, backscattered electrons or X-rays; see Figure 2.1. In SEM mode a detector counts the electrons and sends specific interaction signals to an amplifier which is then sent to a cathode ray tube screen for a magnified image.

A secondary electron imaging mode, typically using an Everhard-Thornley detector, is used to construct topographical images. A typical primary electron beam accelerated by a voltage of 5-40 kV is used to excite low energy secondary electrons (1-200 eV) from the outermost surface region. At higher accelerating voltage and vacuum conditions an image with improved resolution of up to ~ 1-10 nm can be achieved. This, however, induces charge build-up on the surface leading to possible specimen damage. A conversion coating, which is thought to be semi-conductive due to its mixed metal oxide chemistry, is likely to undergo charge build up. However, it has been found in certain instances to be conductive as well as non-conductive [55].

Figure 2.1 Schematic of sources for electron and X-ray scattering in a sample following impingement of the primary electron beam [56]**.**

At higher accelerating voltages, high energy electrons are produced which penetrate more deeply into the sample and spread more widely than low energy electrons, see Figure 2.1. This excites backscattered electrons and X-ray emissions at greater depth. Backscattered electron images can enable determination of intense elemental regions within the general matrix of the specimen. This imaging mode could be an excellent method for the detection of secondary phases within a conversion coating, such as accumulation of silica nano-particles.

A cold or thermal Field Emission Gun (FEG) is an improvement to the conventional thermionic electron gun emitter in electron microscopes. Both of which have been used in the present study. Advantages include a small electron spot size for resolution and brightness and a longer service life; see Table 2.3. The emission of electrons is provided via high electrical potential gradients instead of a high electrical current build up. A direct result of this is a more focused filament source without compromising probe current. Consequently, improved spatial resolution (~1-5 nm) and electrical field for reducing electrostatic distortions is achieved. In contrast to conventional SEMs an additional improvement which Field Emission Gun Scanning Electron Microscopy (FEGSEM) systems provide, particularly for the study of conversion coatings, is the ability to image at low and high specimen chamber pressures. Low pressure secondary electron imaging can be carried out in the variable pressure (VP) mode (~ 0.02 to 2 Torr). The variable pressure methodology employs a gaseous environment around the sample to help diminish the charge build-up that occurs under irradiation with the electron beam [57]. This reduction in charging of non-conductive specimens, could potentially enhance the imaging of semi-conductive conversion coatings and prohibit in many cases the need for specimen preparation such as gold sputter coating.

In this investigation the In-Lens mode was also used which is a unique combination of the thermal FEG and electromagnetic condenser lens in maximising electron count transfer from the electron gun to sample. Consequently many of the advantages such as reduced spot size and brightness are achieved. However, this mode does require a higher operating vacuum and does expose the sample to a higher electron current.

Table 2.3 Differences in SEM electron gun operating parameters and requirements after Hafner [58]**.**

A SEM can also be used in conjunction with cryo fracture sample preparation as used in the present study in which specimens are placed in liquid nitrogen before fracturing for analysis

of cross-sectional information and approximation of sample coating thickness. Note that coating thickness measurements are dependant upon the angle of beam and specimen.

An SEM with a built-in cryo-stage, as used in the present study, can be used to image specimens in a frozen hydrated state. The specimens are held at sub-zero temperature and thus avoid potential electron beam and vacuum exposure. Such a method can provide a valuable insight into dehydration and consequent micro-cracking in conversion coatings

An addition to SEM is its use in conjunction with an Energy Dispersive X-ray (EDX) detector (lithium drifted silicon detector). An EDX detects and collects X-rays emitted from a specimen following bombardment by the incident electron beam, typically 20 kV. An electron is ejected from an inner electron shell following bombardment from the primary electron beam. This leads to an electron replacing this electron from an outer shell; see Figure 2.2. It is the difference in energy between the vacant shell and the shell contributing the electron, which gives rise to a unique X-ray emission for detection. These X-ray emissions of specific energy (and wavelength) can be compared with known emission energies of elements to assess chemical composition (weight or atomic %) at the site of bombardment.

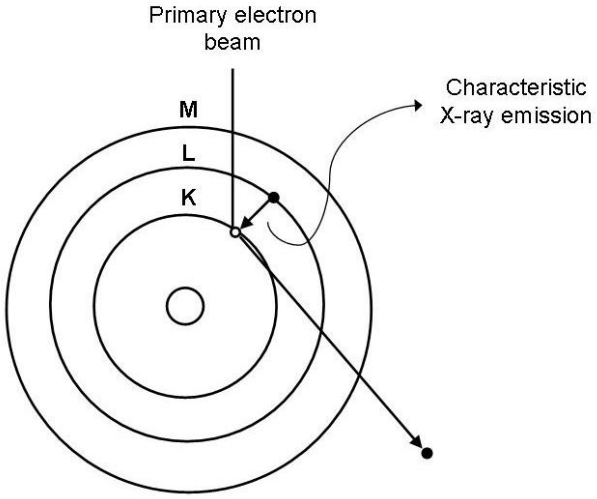

Figure 2.2 Schematic of X-ray emission following impingement of primary electron beam.

The sampling depth of this technique is ~1-10 µm, and therefore as many conversion coatings are thinner than 1 µm, the underlying substrate material will be detected, for example, zinc and possibly iron from the substrate in this present investigation.

A limitation of this technique is that the lowest element that can be detected using the EDX detector is sodium which has an atomic number of 11 [59]. A beryllium window fitted to the detector for protection (e.g. contamination) produces this limitation. Without the beryllium window it is possible to detect characteristic X-rays of elements with atomic number as low as 4 [60].

2.4.1.2 Atomic Force Microscopy (AFM)

An alternative imaging method to SEM is Atomic Force Microscopy (AFM). The basic function of this technique involves scanning near atomically sharp probe across the specimen surface utilising the forces and energy dissipated between the probe tip and sample surface in order to construct images or measurements. The probe tip, which has a radius of ~10 nm, is attached onto a silicon cantilever, ~100-500 µm in length, and is driven and monitored using a piezo-electric scanner and optical laser. A piezo-electric scanner rasters the probe or sample in the X-Y plane and moves the cantilever up and down depending upon the surface topography. This is achieved using an optical laser and four-quadant photodetector which monitors the cantilever deflection thus acting as a force-feedback loop; see Figure 2.3.

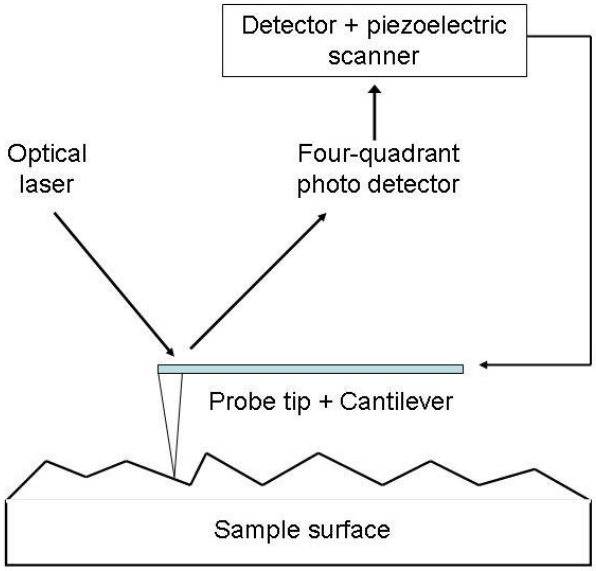

Figure 2.3 Schematic of AFM analytical process and key parts of equipment.

AFM is often compared to SEM for imaging and topographical studies. In particular, for the latter AFM has advantages in that it can be operated in liquids, air and without a vacuum. It can also be used in the actual operating environment (e.g. at room temperature and pressure)

and can analyse a wide range of materials (e.g. conducting and non-conducting). AFM resolution in the X-Y plane of 10 nm is approximately proportional to the probe tip radius and would be viable in resolving micro-cracks within conversion coatings which are of the order of ~100 nm width. The resolution of AFM can also be affected by the scanner used, scan speed and the number of lines in the scan, however, probe tip radius is the most significant variable. AFM has disadvantages in that it has long acquisition times compared to SEM and that images can sometimes be difficult to interpret.

The main AFM operating modes include contact, non-contact and intermittent. In the intermittent mode the cantilever would be expected to vibrate across the surface at ~100-500 kHz and at a 100 nm amplitude with a tip force of the order of 10^{-12} N. Other operating modes include pulse force, chemical force and point/force. Using such modes it is possible to derive topographical images (2 and 3D maps), electrical properties, electrochemical (e.g. potential mapping) and mechanical properties e.g. friction, hardness and roughness.

2.4.1.3 Focused Ion Beam Scanning Electron Microscopy (FIBSEM)

Focused Ion Beam Scanning Electron Microscopy (FIBSEM) is a relatively new technique used for analysing surface and sub-surface morphology and grain structure of materials. Originally FIBSEM was used by analysts in the semi-conductor industry for micro-machining or depositing over unwanted electrical connections with non-conducting material such as silicon oxide, however, more recently it has become an tool for material science investigations. FIBSEM is now considered a very effective method for preparing TEM sample cross-sections to observe features such as grains, interfaces and other specific areas of interest. FIBSEM has, for example, been utilised in the investigation of zinc whiskers [61] and similarly been used in the present study.

The basic operation of FIBSEM is via the use of a focused gallium ion beam that is rastered across a sample surface. A low beam current is typically used for imaging of secondary ions (+ve, -ve, neutral) or secondary electrons emitted from the sample surface. A higher beam current is typically used to sputter or mill the sample.

2.4.2 Chemical characterisation

2.4.2.1 X-Ray Photoelectron Spectrometry (XPS)

XPS, also known as Electron Spectrometry for Chemical Analysis (ESCA), is a surface analytical technique for the analysis of chemical compositions. The technique involves focussing a beam of X-rays onto a specimen from which low energy electrons are emitted following the release of a photoelectron from its inner electron shell; see Figure 2.4. The photoelectron can be emitted from a range of energy levels (electron shells) of an atom e.g. 1s, 2s, 2p, 3s etc... The typical depth of analysis is ~ 3-10 nm based on a low energy Al Kα X-ray source at an incident beam angle of 90°. This is determined by the attenuation length of the emitted photoelectrons.

In more detail the production of X-rays (Kα) from an anode material such as aluminium is achieved following the bombardment by electrons from a thermal source such as an electrically heated tungsten filament emitter. The resultant X-rays with a specific photon energy (e.g. 1486.6 eV) and a flux which is proportional to the electron current striking the anode, is then focused onto the sample. To improve efficiency the anode is water-cooled to dissipate heat [62].

Figure 2.4 The process for the emission of a $2p_{3/2}$ X-ray photoelectron following interaction with a X-ray beam [60]**.**

The induced electrons with sufficient kinetic energy (E_k) to pass through the surface are detected by an electron analyser (concentric hemispherical analyser, CHA), and are related to

the binding energy (E_b) of the electron within its electron shell. This relationship is given in Equation 2.5. The symbol ø refers to the 'Work function' which is constant for a given spectrometer. The symbol h_v; see Equation 2.6, refers to the energy of the incident photon beam e.g. 1486.6 eV in the case of Al Kα.

$$E_k = h_v - E_b - ø \qquad \textbf{Equation 2.5}$$

$$h_v = (h \text{ x } c) / \lambda \qquad \textbf{Equation 2.6}$$

(Plancks constant x velocity of light) / wavelength of the light being used

X-ray source anode materials are typically based on magnesium or aluminium. In some XPS equipment a twin anode assembly, for inter-changeability, could be included. A number of characteristic X-ray photon energies and line widths are listed in Table 2.4, along with some other potential anode materials. Ideally an X-ray line width less than 1.0 eV is desirable for spectrum resolution, hence why aluminium and magnesium are commonly selected [63]. In addition, the anode may also be fitted with a monochromatic quartz crystal for the diffraction of X-rays. This has several advantages in improving the spectral resolution via a reduced X-ray line width (e.g. 0.25 in comparison to 0.9 eV for an Al Kα source), improved signal-to-noise ratio, reduction in the influence of spectral background features such as Bremsstrahlung radiation (photon radiation emitted as a result of a change in velocity of an incident electron within that material following interaction with its nucleus) and X-ray satellites (minor photoelectron peaks produced as a result of additional X-ray lines of the main X-ray beam) and reduction in the thermal damage of specimens and the analytical sample spot size [62].

Table 2.4 Possible X-ray source anode materials and their photon energies and peak widths [62].

XPS is carried out under ultra high vacuum conditions (~ 10^{-9} Torr). This prevents potential surface contamination and reduces low energy electron scattering and interactions with residual gas molecules before detection [62].

The two major modes of operation for XPS is the creation of a survey scan and a high resolution scan. A survey scan spectrum is the detection of photoelectrons from a wide energy range (typically 0 to ~1350 eV) with an energy step of ~0.4 eV, thus enabling elements ranging from Li to U, which have at least one XPS peak that can be examined, to be detected. An electron spectrum of electron count vs. binding or kinetic energy can thus be produced. The characteristic peaks on the spectrum are due to elastic electron interactions whilst that of the spectrum background is due to inelastic electron scattering. Energy positions of characteristic peaks (E_k or E_b) can then be cross-referenced to standards for identification and/or quantitative analysis. Quantitative elemental compositional analysis, often cited in atomic percentage (atom %) terms can be equated by dividing the number of electrons detected within a characteristic peak area by a relative sensitive factor (RSF) and normalised over all of the elements detected. Detection limits for most elements are ~0.1 to 1 %.

A high resolution scan is the detection of photoelectrons from a narrow energy range (e.g. 570 to 600 eV for Cr 2p) under conditions designed to give maximum energy resolution using a lower analyser pass energy often in combination with an increased number of sweeps and consequently increased acquisition time. From a high resolution spectrum it may be possible to attribute structure due to different types of chemical bonding via differences or shifts in the binding energy position. The term ‘chemical shift’ is commonly used to describe changes in the position of photoelectrons due to local electron-electron interactions and which may be observed in the case of an element with more than one oxidation state. To derive relative amounts of the different elemental oxidation states, curve fitting of the data is often carried out. In addition, peak deconvolution is also used in the interpretation of peak structure.

2.4.2.1.1 Limitations of XPS

A limitation associated with XPS is that this technique cannot detect hydrogen and helium. In addition, acquisition times are long and overall set up and operating cost are high. More technical issues, however, are associated with possible sample damage from the XPS X-ray beam such as charging of the sample surface leading to a chemical shift, as well as sensitivity issues where the detection of certain elements is easier compared to others. Known sensitivity

factors are, however, incorporated to alleviate problems associated with the latter. In the case of the former, studies have been carried out to examine the direct influence of X-ray beam radiation damage on hexavalent CCCs and hexavalent chromium state compounds [48,64,65] in particular investigating the reduction and/or decomposition of hexavalent chromium state species under operating conditions such as under cooling, hydrocarbon-free pumping procedures, mechanical rotary rough pumping, water vapour free environment and repeated beam exposure.

A problem associated with high resolution scans and in particular those derived from insulating samples is a shift in binding / kinetic energy as a result of a positive charge build up during the photoelectron emission process. However, a high resolution scan binding / kinetic energy data can be charge corrected with reference to carbon-carbon or-hydrogen bonds typically taken as 285 eV. Alternatively, an electron flood gun can also be used for charge compensation. In this case the electron gun operates at a lower energy (0-12 eV) thus lowering the charge build up due to photoelectron emission.

2.4.2.1.2 Depth analysis using XPS

As photoelectrons originate from the upper surface regions of materials, surface sensitivity (or information gained) can be increased by varying the take-off angle (TOA) for electrons from the typical 90°. A reduced incident beam angle enables a smaller sampling depth and thus greater surface sensitivity and hence more information can be established from the first few atomic layers.

Information regarding the bulk composition of a coating can be collected in conjunction with an argon sputtering gun in depth profiling. However, atoms may undergo collisions and mixing, thus possibly changing the elemental composition and oxidation state of the reorganised surface. An alternative method of equating sub-surface information (~10-20 nm) is calculation of the Auger Parameter (α); see Equation 2.7, via the use of a high energy X-ray source such as Ti, Cr or Cu which have photon energies h_v of 4510.9, 5417.0, and 8047.8 eV respectively. The primary basis of this method focuses on the ability of, for example, the Cu Kα X-ray incident beam energy of 8047.8 eV to have sufficient energy to provide the necessary attenuation length for the probing of photoelectrons from deep 1s core shells as well as associated Auger electrons emitted from e.g. KLL or LMM Auger transitions. These would be unreachable using Al Kα X-rays (h_v = 1486.6 eV). Using such data the final state

Auger parameter (α) can be calculated and used to equate chemical shifts to standard chromium compounds (for chromium containing conversion coatings) without the influence of electrostatic charging associated with the initial state Auger parameter or the analysis of outer photoelectron spectra e.g. Cr 2p.

α = Photoelectron binding energy (Cr 1s) + Auger kinetic energy (Cr KLL) **Equation 2.7**

An advantage of analysing photoelectrons derived from the 1s shell is that their spectra are not influenced by charging, induced outer core levels, spin-orbital splitting or multiplet splitting e.g. 2p spectra of Cr_2O_3 [66,67]. A limitation of the Cu X-ray source is its natural X-ray line width of ~2.3 eV [68,69]. In comparison Al and Mg, which have a full-width half maximum of 0.85 and 0.7 eV respectively, see Table 2.4, are significantly narrower and thus allow for the analysis of narrower spectral peaks such as those from photoelectrons derived from outer core shells. However, for the analysis of 1s photoelectrons, which have wider spectral peaks, the Cu X-ray line width is thought to be acceptable [69].

2.4.2.2 Auger Electron Spectroscopy (AES)

Auger Electron Spectroscopy (AES) is another surface analytical technique, similar to XPS, for the analysis of surface and the near surface chemical compositions. AES principally differs from XPS in that an electron beam is used, compared to an X-ray beam for the latter. The possible types of electron beam emitters include thermionic tungsten wire, lanthanum hexaboride (LaB_6) crystal, cold field emitter and hot field emitter (Schottky); see Table 2.5.

In AES, a electron beam is focused onto a specimen surface leading to the release of a secondary electron from an inner electron shell, for example the K energy level, of an atom thus leaving a core hole; see Figure 2.5. The incident electron beam typically has an energy of between 1 to 10 keV [70]. An electron then falls from a higher electron shell e.g. energy level L_1 in Figure 2.5 to fill the core hole as start of the relaxation process. As a result, a further electron (Auger electron) is emitted from a higher energy shell (energy level $L_{2,3}$) in order to balance the excess kinetic energy from the preceding electron drop from a high to low energy shell [71]. The Auger electron emitted is detected with a specific kinetic energy ($E_{KL_1,L_{2,3}}$) in correspondence to the energy of the core hole (K) and two outer electrons (E_{L_1}-$E_{L_{2,3}}$); see Equation 2.8.

Table 2.5 Comparison of electron emitter operating parameters and requirements used in AES [62]**.**

Figure 2.5 The process for the emission of a $KL_1L_{2,3}$ Auger electron following interaction with a primary electron beam [60]**.**

$$E_{KL_1,L_{2,3}} = E_K - E_{L_1} - E_{L_{2,3}} \qquad \textbf{Equation 2.8}$$

The emitted Auger electrons will pass through a Cylindrical Mirror Analyser (CMA) to an electron detector, to determine their associated kinetic energy. Only electrons travelling at a specific pass energy follow the geometry of the analyser and arrive at the output slit for subsequent detection.

The resulting AES spectrum is often plotted as the first derivative of electron count versus kinetic energy. As it can be difficult to interpret a small Auger peak superimposed on an

background spectrum. Differentiation can be achieved electronically by application of a modulating voltage in the energy analyser so that there is a greater accentuation of small Auger peaks.

It is important to note that other than the main Auger peak for an element, additional minor Auger peaks of the same element could also be detected and plotted. Secondary and backscattered electrons can also be emitted and detected too. These enable surface morphology images of the specimen to be formed; see Figure 2.6.

Figure 2.6 Schematic presentation of Auger electron scattering following impringement of primary electron beam during AES analysis [63]**.**

The surface sensitivity of AES limits sampling depth, as with XPS the attenuation length is only a few atomic layers i.e. Auger electrons travel only a certain distance before undergoing either elastic or inelastic collisions thus losing energy to form the background within a spectrum rather than forming part of the specific Auger peak [70].

The Auger spectrum produced can be used as a ‘fingerprint’ for identifying elements present within the surface by observing the major peak and kinetic energies in conjunction with reference data. Elemental analysis of these peaks is limited to elements above He in the periodic table, as these have sufficient electrons for the Auger process to occur as described above. Therefore, alternative techniques have to be applied, such as Dynamic Static Secondary Ion Mass Spectroscopy (DSIMS), which can take into account hydrogen and

helium. However, DSIMS does not quantify elements present in non-model systems as is the case for AES and XPS. In order to quantify the atomic percentage of elements in AES the peak height amplitudes are recorded and compositions are determined in accordance with their Relative Sensitivity Factors (RSF), determined from known reference materials. Oxidation states of an element can also be identified, as in the case of XPS, via peak/kinetic energy shifts e.g. Si 92 eV to SiO_2 76 eV [72].

Chemical depth profiling of a coating can be carried out following etching of the surface using an inert argon ion beam. Etching rates are typically ~10 nm/min^{-1}. This method relies upon a constant sputter yield as well as alignment of the detector with the resulting crater. An x-y beam deflection unit can be used for the adjustment. Limitations associated with this method may include the uniformity of the specimen surface and the potential change of elemental composition and structure. The method is also not suitable for the analysis of non-conductive materials [30].

A distinct advantage of AES over XPS is that the incident electron beam used enables a higher lateral resolution (e.g. ~ >0.1 µm vs. >1 mm). This allows mapping of the entire surface including specific defects (e.g. micro-cracks of a hexavalent CCC). AES like XPS has a similar detection limit of 0.1 to 1 atom%. AES, like XPS, can reduce its sampling depth in order to achieve more surface specific information by lowering the incident beam TOA, but interpretation of data is thought to be more difficult. The method of analysis for oxidation states is also more complicated in comparison to XPS [71]. XPS benefits from a larger reference database for the determination of elemental oxidation states.

2.4.2.3 Infra-red (IR) spectroscopy

Infra-red (IR) spectroscopy provides an alternative means of characterising chemical composition to that of XPS, AES and EDX. Electromagnetic radiation, with wavelengths between $7.8x10^{-5}$ and $3x10^{-2}$ cm^{-1} is categorised as infrared; see Figure 2.7. In the case of most IR spectroscopy interpretation, this value is often converted into, recipocal wavenumbers (cm^{-1}). A beam of IR electromagnetic radiation beam is produced from a nichrome wire or cooled rod of silicon carbide following electrical heating. When the resultant electromagnetic radiation matches the energy of a specific molecular vibration, absorption occurs. This molecular vibration energy is a change of dipole moment in the form of bending or stretching. Stretching either asymmetric or symmetric, involves changes in the

inter-atomic length of a bond, whilst that of bending either rocking, scissoring, wagging or twisting involves a change in the angle between two bonds. Molecular vibrations are also affected by the nearby chemical environment e.g. functional groups, double bonds, stretch or bend bonds. It is important to note that not all molecular vibrations are detected or stimulated due to a lack of energy of the primary beam.

Figure 2.7 Electromagnetic radiation spectrum.

In a standard IR spectrum, the reciprocal wavenumber (cm^{-1}) is plotted typically against transmission (%). Transmission displays the percentage of the infra-red beam collected with or without absorption of molecular vibrations e.g. 100% for the latter. Some plots may also be presented as wavenumber against absorbance, which is calculated from transmission values; see Equation 2.9. The signal-to-noise ratio of the spectrum is influenced by the number of scans taken (i.e. square root of the number of scans). In general, the resolution can be taken as less than 4 cm^{-1}. Infra-red equipment is also commonly fitted with a Fourier Transform programme for measuring the energy absorbed over a number of wavelengths, thus reducing the time taken for analysis of each scan.

$$\text{Absorbance} = \text{Log}_{10}(1/\text{Transmission}) \qquad \textbf{Equation 2.9}$$

Analysis of IR absorption peaks can be correlated directly to bonds within the compound in question from reference data. For instance, stretch absorption peaks are typically of higher energy molecular vibrations than those from bend absorptions, typically above 1500 cm^{-1}. Absorption peaks found below 1500 cm^{-1} are known as the 'fingerprint region'. Individual peaks in this region are difficult to assign and therefore taken as a collective peak pattern in most cases, hence the 'fingerprint' terminology.

A distinct limitation of IR spectroscopy, particularly for this current investigation, is the limited number of investigations into inorganic materials which primarily have absorption peaks within the fingerprint region. Other limitations include a small absorption range between ~400-4000 cm^{-1}, potential overlapping of absorption peaks, a pre-determined knowledge of potential molecular vibrations, and resolution of weak absorption peaks.

A number of operating modes can be used to produce an infrared spectrum of a sample. The choice of mode is very much dependent upon the state of the sample e.g. liquid or solid.

The simplest IR operating mode basically involves passing the electromagnetic beam through a disc containing a small amount of the sample. Solid state samples are prepared by grinding ~1-2 mg of the sample with ~200 mg of KBr using a pestle and mortar and shaping into a disc under pressure within a die. KBr does not produce an absorption peak between 650 and 4000 cm^{-1}. Liquid state samples are prepared by placing a small volume of the neat solution (e.g. 1 ml) between two NaCl discs.

An Attenuation Total Reflectance (ATR) infra-red attachment enables the use of solid samples that have thin, flat geometry. The operation is dependent upon a high reflective index crystal held in close contact with the sample. Therefore, when an infra-red beam is passed through the optical crystal as an evanescent wave in contact with the sample surface, an intrusion of up to 0.5-5.0 µm will be made within the sample. As a result the infra-red wave will undergo attenuation (energy loss interactions) from vibrations with the sample, which can then be characterised on an infra-red spectrum. A limitation of this method, which would hinder evaluation of conversion coatings, would be the positioning of the sample panel parallel and permanently in contact against the crystal. Surface roughness would also be a factor. It is unlikely that the refractive index of the sample would be higher than the optical crystal for reading errors to occur.

The other IR mode is a reflection absorption (also known as variable angle specular reflectance). This method involves reflecting the infrared beam off the sample surface via a set of mirrors. The infrared radiation can either undergo specular or diffuse reflection. For the former this is the energy not absorbed by the sample, and thus the method could be classified as 'external'. A high refractive index, such as that of a conversion coating, is required as well as a smooth surface. The analysis depth of this technique is a few monolayers. In the case of diffuse reflectance the infrared beam is absorbed by the sample before being detected, and thus the method could be classified as 'internal' similar to that of ATR. This technique is more commonly used for rough surfaces and for obtaining bulk information.

2.4.3 Corrosion characterisation

Corrosion is fundamentally an electrochemical process which can often be monitored via measurement of potential and/or current. The corrosion properties of a material are primarily based at the metal/solution interface.

2.4.3.1 Neutral Salt Spray (NSS) corrosion testing

There are many test methods for the determination of corrosion and corrosion rates, however, none are really thought to be a direct substitute for 'real-life' outdoor corrosion environments. Such environments range from rural, urban, industrial to marine. For instance, a harsh environment such as marine could be represented by neutral salt spray corrosion tests. A standard corrosion test commonly used is ASTM B117-90 [73]. The basis of this accelerated test is to produce relative corrosion resistance information for specimens in sodium chloride based fogs. Even though salt spray testing has not been conducted in this investigation, the inclusion of this method in the literature review is important as conversion coatings are tested in accordance to ASTM B117 from a commercial and research and development stand point. Many patents and journal papers include such data, see Section 2.7.5.2. To complement this technique, particularly to reduce analysis time and identify small changes in corrosion resistance variation within samples, electrochemically based trails are often used. In this investigation such testing has been carried out.

2.4.3.2 Electrochemical corrosion characterisation

Electrochemical corrosion studies are a time efficient and recognised method for the study of general corrosion resistance. They importantly allow, for the ranking of protective coatings or metals in order of a specific electrochemical characteristic e.g. polarisation resistance or rest

(open-circuit) potential, and keep the specimen surface fully immersed within the corrosive environment (e.g. 5% NaCl solution) unlike salt spray conditions in which the solution is continously sprayed onto the specimen surface and forms a thin film. However, caution must be taken when extrapolating laboratory results to that of in-service conditions e.g. when there are variations in factors such as oxygen concentration, humidity, temperature and pH. Also some electrochemical data assumes that the corrosion rate is a function of general corrosion and does not take into consideration that a specimen might actually be corroding as a result of pitting or other forms of localised corrosion.

In an electrolytic cell a designated electrode can function either as an anode or cathode. However, in an electrochemical corrosion cell both cathodic and anodic behaviour can be examined using a potentiostat on the same electrode i.e. the working electrode. An electrochemical corrosion study includes an electrolyte, working, auxiliary and reference electrodes. The reference electrode e.g. Saturated Calomel Electrode (SCE) provides a datum to which the potential of the working electrode is measured. The auxiliary electrode completes the electrical circuit. The electrolyte is typically 3 or 5 wt-% NaCl which importantly provides both a conductive and corrosive environment. The solution may also be purged with nitrogen gas to reduce the oxygen concentration for characterisation of samples under a less oxidising corrosion environment.

Typical electrochemical corrosion data includes potential plotted against current, E verses log I. Interpretation of the data can then be carried out to determine corrosion behaviour. For example the corrosion potential (E_{corr}) or rest potential is the potential at which there is no external current and no applied potential and indicates when the specimen is at open circuit.

Electrochemical polarisation curves illustrate full anodic and cathodic branches from which corrosion behaviour can be interpreted. The anodic and cathodic branches are a plot of current when potentials typically between +/- 1500 mV around the rest potential (depending on the system) at a sweep rate of 10 mV/min are applied to the sample. From these plots the corrosion current (i_{corr}) can also be estimated; see Figure 2.8, as well as calculating polarisation resistance (R_p) from the Stern-Geary equation if the Tafel regions have a linear relationship; see Equation 2.10 and 2.11 [74]. This value determines the corrosion resistance of the sample when undergoing polarisation (e.g. anodic reactions greater than cathodic reactions or vice versa).

$$R_P = \frac{B}{i_{corr}} = \frac{(\Delta E)}{(\Delta i)}$$ **Equation 2.10**

R_p Polarisation resistance

i_{corr} Corrosion current

B Proportionality constant (calculated from anodic and cathodic Tafel slopes b_a and b_c)

$$B = \frac{b_a \bullet b_c}{2.3(b_a + b_c)}$$ **Equation 2.11**

Note that the Tafel regions are taken as the gradient of the cathodic and anodic curves on the E/log I plot (straight lines should be at least one decade of log current).

Figure 2.8 A typical galvanostatic polarisation curve for mild steel in 1.0 M HCl which illustrates the evaluation of corrosion kinetic parameters such as ba, bc, E_{corr} and i_{corr} [75]**.**

Another method of calculating polarisation resistance is the technique of Linear Polarisation Resistance (LPR). This technique differs in that the corrosion resistance is measured over a smaller potential window (+/- 20 mV around the rest potential, E_{corr}). This measurement is the gradient of the data slope intersecting at E_{corr}. This range indicates when the specimen is undergoing natural corrosion as if it had no applied potential.

2.5 Hexavalent CCCs

Hexavalent chromium based treatment solutions have been widely used to conversion coat a range of substrates such as zinc, zinc alloys, aluminium and cadmium for a number of years. The original Cronak process, which was US patented in the 1930's [76] and commercialised in the 1950's [77] utilised sodium dichromate as it's hexavalent chromium source in treatment solutions of zinc and cadmium substrates.

Mined chromite ($FeCr_2O_4$) ore is the chief commercial source from which primary industrial hexavalent CCC raw material compounds such as sodium chromate, sodium dichromate and chromic acid are produced. These compounds are also used to form secondary hexavelent chromium (potassium chromate / dichromate and ammonium dichromate) and trivalent chromium compounds (chromium nitrate, chromium sulphate, chromium chloride and chromium oxide) [78].

For steel that has been electrodeposited with zinc, the favoured type of CCC has been based on hexavalent chromium (Cr VI). It is inexpensive, easy to apply [8] in comparison to its competitors and therefore relates well to industrial manufacture. Most importantly, hexavalent CCC's demonstrate all of the advantages of conversion coatings discussed earlier, in particular corrosion performance, and adhesion properties for subsequent application of organic primer or paint finish.

2.5.1 Film formation

2.5.1.1 Hexavalent CCC on zinc coated steel

The mechanism of film formation for hexavalent CCC on zinc coated steel has been proposed by many authors [79,80]. A typical hexavalent chromium treatment solution is likely to contain sodium (or potassium) dichromate ($Na_2Cr_2O_7$ or Na_2CrO_4), chromic acid (H_2CrO_4), an additional acid such as hydrochloric (HCl) or sulphuric acid (H_2SO_4) and deionised (DI) water. Listed below is a step by step chemical reaction path for the theoretical film formation based on a hexavalent CCC solution:

1) As the pH of the treatment solution is low (~2), the solution is therefore acidic and thus the acid is likely to dissociate within water into its constituent ions.

$H_2SO_4 \leftrightarrow 2H^+ + SO_4^{2-}$ **Equation 2.12**

2) The potassium dichromate in acidic solution will favour the formation of a yellow chromate colouration.

   $Cr_2O_7^{2-} + H_2O \leftrightarrow 2CrO_4^{2-} + 2H^+$ **Equation 2.13**

   (Orange Dichromate) (Yellow chromate)

3) The acidic pH of the passivating solution as well as the presence of cations such as H^+ is thought to initiate anodic dissolution of zinc at contact surfaces of a galvanised or electrodeposited zinc steel coupon when immersed into a treatment solution.

   $Zn + 2H^+ \leftrightarrow Zn^{2+} + H_2$ **Equation 2.14**

4) Along with zinc dissolution and hydrogen reduction, hexavalent chromium ions are also thought to be reduced to a trivalent state.

   $2Cr^{6+} + 3Zn \rightarrow 2Cr^{3+} + 3Zn^{2+}$ **Equation 2.15**

   Note that hexavalent chromium is a highly oxidising compound and therefore whilst being reduced could contribute towards further oxidation of zinc.

5) The Cr (III) intermediate formed is thought to either form a complex hexa-aqua structure and move back into the solution; Equation 2.16, or precipitate as an insoluble chromium hydroxide; Equation 2.17, [81] as a result of an increased pH following hydrogen evolution.

   $Cr(H_2O)_6^{2+}$ (Turquoise colour) or $Cr(H_2O)_6^{3+}$ (Blue-violet) **Equation 2.16**

   $Cr^{3+} + 3OH^- \rightarrow Cr(OH)_3$ **Equation 2.17**

6) During precipitation of the chromium oxide/hydroxide, zinc cations and other anions, water, as well as some hexavalent chromium is thought to be incorporated into the conversion coating.

   $Cr(OH)_3 + Zn^{2+} + Cr^{6+} \rightarrow Cr^{3+}, Cr^{6+}, Zn^{2+}, 3OH^-$ **Equation 2.18**

7) The conversion coating will continue to grow electrochemically until no further zinc dissolution is possible, following passage of ions such as H^+, SO_4^{2-} and Cl^- through pores and cracks of the growing conversion coating. Therefore overall film formation and growth of hexavalent CCC on zinc coated steel is a dissolution-precipitation mechanism [82]. It is also important to note that any soluble zinc ions entering into the treatment solution and not precipitating as part of the conversion coating could affect the growth, thickness and composition of the coating.

2.5.1.2 Black hexavalent CCC on zinc and zinc alloy coated steel

The automotive industry often favours the use of black conversion coatings for some of their components. The lustrous black visual appearance is thought to be due to a small content of metal oxides such as Cu, Ag, Co or Fe within the composition of the hexavalent CCC. It has been proposed that a thin layer containing these types of compounds are found adjacent to the zinc or zinc alloy interface with a thicker traditional hexavalent CCC chemistry based on chromium and oxygen found on top [79,83]. Therefore the film formation and growth of black hexavalent CCC varies to that proposed earlier for a traditional hexavalent CCC on zinc coated steel.

2.5.1.3 Hexavalent CCCs on aluminium

A short review detailing the film formation mechanism of hexavalent CCC on aluminium based substrates has been included as similar and alternative mechanisms have been proposed in comparison to that on zinc based substrates. As in the case of a zinc substrate, dissolution is also a fundamental initial step albeit that the natural surface aluminium oxide is partially dissolved and thinned following strong attack by fluoride ions (F^-), present as part of the hexavalent CCC formulation, as well as the treatment solution pH [84,85]. Consequently, the electron tunnelling required for the oxidation of aluminium and reduction of chromate / dichromate, oxygen, Cr(III) and hydrogen evolution can occur; see Equations 2.19-2.22 and 2.2.

$$Al \leftrightarrow Al^{3+} + 3e^- \quad \textbf{Equation 2.19}$$

$$Cr_2O_7^{2-} + 14H^+ + 6e^- \leftrightarrow 2Cr^{3+} + 7H_2O \quad \textbf{Equation 2.20}$$

$$HCrO_4^- + 7H^+ + 3e^- \leftrightarrow Cr^{3+} + 4H_2O \quad \textbf{Equation 2.21}$$

$$O_2 + 4H^+ + 4e^- \leftrightarrow 2H_2O \quad \textbf{Equation 2.22}$$

Following reduction of Cr(VI) to Cr(III) species as outlined above, the precipitation of $Cr(OH)_3$ is possible [86]. This model relies upon a constant supply of aluminium dissolution for chromate reduction / precipitation. Thus the coating thickness initially increases exponentially with immersion time until the pathways allowing access of the chromate based solution to the aluminium substrate are closed e.g. pores. At which point the increase in coating thickness ceases with increasing immersion time [87].

Another model is based on sol-gel theory commonly associated with organic/ceramic based coatings [88]. In this proposed model the Cr(III) ions are thought to hydrolyse into metal hydroxide complexes. As the hydrolysis process continues the number of metal complexes increases and eventually lead to the formation of polymeric-type chains and nuclei for 3D colloidal particles. On reaching a critical size, the colloidal particles, which have low density and high porosity, coagulate and form a gel in close proximity to the aluminium surface [89]. High resolution SEM and AFM studies on hexavalent CCC on aluminium by Treverton et al. [90], and Campestrini et al. [89] also help to support this theory; see Section 2.5.2.2. Layered spherical shaped particles of ~10-60 nm size were deposited and observed. The growth of the model coating is sustained via its open structure and high water retention i.e. it has permeability and ionic conductivity for the required redox reactions. The second part of this model results in loss of water from the gel during drying, consequently leading to an overall coating shrinkage via capillary forces. A micro porous coating composed of small spherical particles is thus commonly observed [89-92].

Another model is based on a chemical deposition following initial electrochemical chromate reduction and aluminium oxidation [93]. Excess reduced Cr(III) is not used instantaneously as in the case of the first model proposed but retained for further growth of the already thinly conversion coated surface.

2.5.1.4 Hexavalent CCCs on zinc alloy substrate

It is thought to be more difficult to form conversion coatings on zinc-alloy deposits, as opposed to pure zinc. For example an alloy content above 1 wt-% Fe was found to be more difficult to hexavalent chromium conversion coat than those below 1 wt-% Fe [44]. Work by R. Ramanauskas et al. [94] showed that conversion coating thickness was found to be less on zinc alloys than pure zinc deposits with Zn-conversion coating 240-300 nm, ZnFe(0.4%)-conversion coating 110-140 nm, and ZnCo(0.6%)-conversion coating 72-100 nm for a particular process. The composition for a hexavalent CCC on a zinc alloy also differed from that on zinc. A higher concentration of Cr(VI) was found to be present at the surface of the conversion coating for the zinc alloy than that on a pure zinc substrate following deconvolution of the XPS Cr $2p_{3/2}$ envelope; see Figure 2.9a-c, (Cr(VI): 32% for Zn, 45% for ZnFe and 60% for ZnCo). Note that the remaining percentage content for each spectrum was thought to be composed of Cr(III).

Studies by Gigandet et al.. [79] showed that traces of transition elements, such as iron or cobalt, influence conversion coating kinetics by increasing their formation and the dissolution of zinc.

Figure 2.9 XPS Cr $2p_{3/2}$ high resolution spectra, curve fitted with Cr(VI) and Cr(III) standards for hexavalent CCC on Zn (a) and Zn alloy (b and c) surfaces [94]**.**

2.5.1.5 Hexavalent CCC on aluminium alloy substrates

Film formation studies for hexavalent CCCs have also been carried out on aluminium alloys [51,84,95-97]. Formation on an aluminium alloy allows researchers to observe film formation, surface morphology and electrochemical behaviour on different phases of the substrate due to inter-metallic compounds (IMC) within the general aluminium matrix e.g. Al-Cu-Mn-Fe, Al-Cu-Mg in AA2024. The heterogeneous physical and chemical structure of IMC's provide local regions for either anodic or cathodic behaviour, with the latter commonly observed given more noble elements than aluminium.

Campestrini et al. [95] have investigated the initiation and growth of a hexavalent CCC on an aluminium 2024 using SEM, EDX and Scanning Kelvin Probe Force Microscopy (SKPFM). It was found that reduction of chromate species and corresponding Cr(III) precipitation occurs initially above IMCs due to their more noble cathodic potential. This was also observed by Kulinich et al. [97]. The thin/dense conversion coating formed over the IMC reduces its electron transfer and ion migration and consequently the hexavalent CCC begins to deposit

over the aluminium matrix. A porous/nodule-like conversion coating is formed and favours continued growth over a longer treatment time as electrochemical interaction pathways are still available. It is also important to note that Campestrini et al. [95] also observed discontinuities and potential defects at the periphery between the conversion coated IMC and aluminium matrix due to the different rate and time of coating formation.

However, it must be noted that certain IMCs, via their constituent elements, are thought to inhibit conversion coating formation, thickness, adherence and may also undergo de-alloying (e.g. Mg) or enrichment (e.g. Cu). For example copper and/or copper oxide along with cyanide species from the chromate formulation render a passive surface [95].

2.5.2 Surface morphology

2.5.2.1 Micro-cracking

Hexavalent CCCs have been found to exhibit a micro-cracked surface morphology both on zinc and aluminium substrates [45,48,88,90,98,99]. Crack patterns range from simple crack networks to that of a 'dried cracked river bed morphology'; see Figure 2.10. In this investigation the term 'micro-cracking' will be defined as a crack exhibiting a width less than 2 µm.

Figure 2.10 SEM images for zinc treated in a chromate bath with different immersion times (A) 5 s (B) 10 s (C) 30 s (D) 60 s [48]**.**

Micro-cracking can either be viewed as positive or negative, however, the overriding consensus is that it is the latter. Micro-cracking could increase the surface area for improved

mechanical adhesion of subsequent primer or paint finishes. The increased surface area could alternatively be viewed to reduce corrosion resistance by increasing exposure to corrosive ions and reducing the barrier thickness.

Theories as to why micro-cracks appear are discussed below:

- Studies have shown that as the coating thickness increases the appearance of micro-cracks are observed, see Figure 2.10, and this has been associated with increasing tensile stress [99]. An increase in thickness has also been related to the pH of the treatment solution in which a lower pH increases thickness and residual stress for cracks and defects to form [85]. An increase in thickness could provide sufficient tensile stress for crack propagation of surface defects to form micro-cracks i.e. the tip radius of a surface crack effectively acts as a region of high stress concentration. Surface defects could include an incomplete conversion coating region during film formation and growth. The application of a tensile stress in this region would further increase the penetration and size of crack through the coating. The number of stress fields in close proximity will determine whether a dense crack network can be generated
- Studies have also shown that thermal exposure has a direct influence on the widening of these cracks [6,45]. It is possible that water taken up by the conversion coating following treatment/rinse stage [48,100] may be lost by dehydration under harsh thermal conditions. Therefore loss of water could initiate contraction via internal compressive forces, and that if the contraction forces within the coating coupled with adhesive forces to the substrate increase the stress beyond the local tensile strength, the coating will fracture to relieve the stress. The crack tip will propagate until the stress is reduced to less than the local strength of the material [101]. Thermal drying gradients such as isotropic and directional have been shown to influence crack patterns for alumina/water slurry dies [102].
- It is important to note that the high vacuum and electron beam exposure used during SEM analysis could also contribute to dehydration followed by cracking. This could be verified, to a certain degree, by monitoring the surface structure on increasing acquisition times, variable pressure as opposed to high vacuum mode for FEGSEM, and analysis using a non-vacuum imaging method such as AFM. The specimen could also be observed on a cryo-stage thus reducing influence of the SEM vacuum and electron beam. Chemically, water within the conversion coating could be monitored via XPS high resolution O 1s spectra, IR spectra or thermo gravimetric plots.

- It is possible that micro-cracks may be intrinsic to defects left by the rolling preparation of the mild-steel substrate, however, if this was the case defects would also be found on the zinc substrate surface. Therefore lattice structure, grain boundaries, physical defects and chemical imperfections within the zinc could also result in cracking. Work by Deflorian et al. [103] found that the surface morphology of a hexavalent CCC is different when formed on a zinc electrodeposit as opposed to a hot-dip galvanised layer; see Figure 2.11. For a zinc electrodeposit the surface morphology is a typical dried riverbed morphology, however, for a zinc hot dipped galvanised layer the conversion coating appears only locally and is non-continuous. This was verified using EDX in which a low overall Cr content was detected. A possible prognosis suggested was that the surface is more oxidised and thus less suitable for hexavalent (or trivalent) chromium conversion treatment.

(a) **(b)**

Figure 2.11 SEM images of a hexavalent CCC on (a) zinc electrodeposit (b) hot dip galvanized surface [103].

- It is unknown whether or not micro-cracks penetrate completely through a conversion coating, if this was the case corrosive ions would have direct access to the zinc substrate and thus decrease the coating's corrosion resistance. In one study by Long et al. [44] using SEM-EDX of a hexavalent CCC Zn-Fe electrodeposited steel crack tip showed a stronger signal for Zn and Fe peaks than at a non-cracked region. In another SEM-EDX study by Zhang et al. [45] of a hexavalent CCC galvanised steel panel crack tip following heat treatment (210°C in an oven for 30 min) exhibited a lower content of Cr and O and rise in Zn in comparison to an uncracked region.
- Alternative reasons for cracking suggested by Zhang et al. [48], other than thickness, may be due to either a high water content or the nature of the chromium products in the

conversion coating. From an XPS survey scan study of elements present, the content of Cr and O at the surface was shown to not change significantly on increasing immersion time; see Table 2.6.

Table 2.6 XPS survey scan data of a hexavalent CCC on zinc (at. %), * the number in the parentheses refers to sequential measurements on the same sample with 1 h intervals. [48]**.**

Even with a micro-cracked surface morphology the corrosion protection for hexavalent CCCs does not appear to be undermined significantly. Most researchers are of the view that highly oxidising Cr(VI) ions can actually repair damaged regions, such as cracks, via a reduction mechanism to Cr(III) compounds and thus enable protection for in-service conditions in which a component may undergo scratching or damage.

2.5.2.2 High resolution analysis

A more in-depth characterisation of a hexavalent chromium based conversion coating surface morphology using SEM, albeit on an aluminium substrate, revealed that the coating is composed of spherical shaped particles in the order of 10-60 nm, with particle size becoming more uniform depending upon substrate condition (e.g. polished) [90]. Topographical AFM studies by Campestrini et al. [89], of hexavalent CCC on AA1050 also exhibited spherical particles. These particles were found to coalesce and lead to a more compact coating as a function of immersion time.

2.5.3 Chemical composition

2.5.3.1 Surface chemical composition

Chemical characterisation from XPS survey scans carried out by Zhang et al. [48] for a hexavalent CCC showed that on increasing immersion time (1 to 60 s) a decrease in the zinc content resulted (4 to < 1 at.%); see Table 2.6. The O and Cr contents remained approximately constant. Zhang et al. also carried out a non-monochromatic XPS high resolution scan of the Cr 2p peak. The Cr 2p spectrum exhibited both Cr(VI) and Cr(III) peak profiles. Curve fitting of the Cr $2p_{3/2}$ peak which is unaffected by $2p_{1/2,3/2}$ satellites [104] was carried out. Using the binding energy values of three standards (Cr_2O_3, $Cr(OH)_3$ or CrOOH, and Cr(VI)) with the chi-square value determining the quality of curve fit, it was shown that on increasing immersion time (1 to 60 s) the Cr(VI) content increased from 32 to 42%, $Cr(OH)_3$ decreased from 52 to 40% and Cr_2O_3 showed an overall increase; see Table 2.7.

Table 2.7 Curve fitted XPS Cr $2p_{3/2}$ spectra values (%) of hexavalent CCC on zinc surfaces. Curve fitting components included Cr(VI), Cr_2O_3 and $Cr(OH)_3$. * the number in the parentheses refers to sequential measurements on the same sample at 1 h intervals. [48]**.**

Biesinger et al. [66] have curve fitted a Cr $2p_{3/2}$ spectrum for a hexavalent CCC on zinc-galvanised steel and shown it to have a composition consisting of 25% Cr_2O_3, 60% $Cr(OH)_3$ and 15% Cr(VI); see Figure 2.12. It is important to note that no formulation or treatment time is stated for this composition, however, the researchers do utilise a more thorough and rigorous curve fitting procedure (e.g. peak BE position, FWHM and area ratios of Cr compounds to be fitted) along with data acquired from a monochromatic Al X-ray source.

Figure 2.12 Cr 2p spectrum for a hexavalent CCC on zinc-galvanized steel. Cr $2p_{3/2}$ envelope curve fitted using Cr_2O_3, $Cr(OH)_3$ and Cr(VI) standards. Spectrum charge referenced to O 1s ($Cr(OH)_3$) at 531.7 eV [66]**.**

Zhang et al. [48] also found that X-ray radiation during the XPS analysis of their hexavalent CCCs caused reduction of Cr(VI) to Cr(III); see Table 2.7, and suggested that an acquisition time below 45 min reduces this phenomenon. However, it should be noted that studies by Murase et al. [104] found little Cr(VI) reduction following 6 h X-ray radiation during analysis of a hexavalent CCC on a steel substrate; see Figure 2.13. X-ray Absorption Near Edge Spectroscopy (XANES) studies on hexavalent chromium conversion coated aluminum and its alloys have also been carried out by Kendig et al. [86]. It was noted that the sample's Cr(VI) content is less susceptible to photoreduction by the higher energy photons as in the case for XPS analysis. On increasing immersion time it was found that the percentage of Cr(VI) of the total Cr content detected increased before stabilising at ~10 to 20 %. It was proposed that more Cr(VI) is converted to Cr(III) compounds at the coating/substrate interface during the early stages of the film formation than at latter during which complete conversion never occurs. It was also proposed in these investigations that the trivalent chromium detected in the coating spectrum was not representative of a crystalline Cr_2O_3 standard spectrum but closer to that of an amorphous hydrated $Cr(OH)_3$ standard spectrum.

It is also important to note in this section the potential of Cr(VI)/Zn(II) or Cr(VI)/Al(III) compounds within a hexavalent chromium based conversion coating. Work carried out by Xia

et al. [100] using inductively coupled plasma analysis showed that Al(III)/Cr(VI) is not a major component.

Figure 2.13 High resolution Cr 2p spectra of hexavalent CCC on a steel substrate as a function of X-ray radiation for times of up to 6 h [104]**.**

2.5.3.2 Surface chemical composition before and after NaCl exposure

XPS survey scans carried out by Zhang et al. [48] on hexavalent CCCs following exposure to 0.01 M NaCl for 24 h showed that the Cr and O content decreased whilst that of Zn increased in comparison to an uncorroded sample; see Table 2.8. The increase in zinc was possibly attributed to zinc dissolution and the deposition of hydroxide/oxide on the surface via cracks or defects which were observed in earlier investigations carried out by Zhang et al. [48]. The ratio of Cr(VI) to total Cr content decreased from 0.4 to 0.25; see Table 2.8 and Figure 2.14. The decrease was possibly due to soluble Cr(VI) products having either reduced to Cr(III) insoluble products (e.g. chromium oxides/hydroxides) in regions of defects and cracks for self-repair or alternatively leached into the NaCl solution. It is interesting to note that no chloride species are identified as part of the upper layer of the conversion coating.

A XANES study of a hexavalent CCC on aluminium and its alloys following exposure in aerated 0.5 M NaCl found that on increasing exposure 0 to 29 days that the ratio of Cr(VI) to total Cr within the conversion coating declined approximately exponentially [86]. It was proposed that the decrease in Cr(VI) related to the solubility of this species in reacting with the Al substrate to form a Cr(III) compound at defects in the coating for repair. It is also important to note that Cr(VI) could have leached under a flooded solution environment. No

check for chromium in the 0.5 M NaCl solution was carried out. A study by Xia et al. [100,105], investigated the storage and release of Cr(VI) species within hexavalent CCC on AA1100 and AA2024 using ultraviolet-visible spectroscopy. The study showed that immersion of CCC in deionised water or 0.1 M NaCl solution resulted in the release of Cr(VI) before equilibrating. Factors associated with this included pH and exposed area to the solution. The absorption/desorption of Cr(VI) within a synthetic Cr(III) hydroxide was also studied with a potential covalent Cr(III)-O-Cr(VI) bond discussed.

Table 2.8 XPS survey scan data (element at.%) for hexavalent CCCs on zinc surfaces before and after 0.01 M NaCl solution exposure for 24 h. *Cr(VI)/Cr ratio derived from curve fitting of the respective high resolution Cr $2p_{3/2}$ peak envelope [48]**.**

Figure 2.14 Cr 2p spectra for the hexavalent CCCs (30 s immersion time) on zinc surfaces (a) before and (b) after immersion in 0.01 M NaCl solution for 24 h [48]**.**

2.5.3.3 Sub-surface chemical composition

An AES depth profile carried out by Zhang et al. [48] showed that the concentration of Cr decreases whilst that of Zn increases with depth within the conversion coating; see Figure 2.15. Overall, the hexavalent CCC appears to be a mixture of Cr and Zn oxides/hydroxides. Zinc oxide appeared to exist mainly at the interface between the conversion coating and zinc

substrate. Surface elemental composition showed that O and Cr were found to be present at 76 and 22 at.% respectively, with the remaining 2% contributed by Zn.

Figure 2.15 AES depth profiles for a hexavalent CCC on zinc with an immersion time of 60 s. The data points from the first 5 minutes of sputtering were omitted as a 40 nm gold layer was applied for improved conductivity [48]**.**

The identification of chemical oxidation states at depth within a coating is difficult using techniques such as XPS in conjunction with argon sputtering. In order to overcome this Murase et al. [104] investigated a hexavalent CCC on steel by varying the X-ray beam TOA used during XPS; see Figure 2.16. It was found that as the TOA increases the intensity of Cr(VI) increases in proportion to the Cr(III) signal.

Figure 2.16 Various high resolution angle resolved XPS Cr 2p spectra of the hexavalent CCC on steel (TOA are indicated on the spectra) [104]**.**

2.5.3.4 Sub-surface chemical composition before and after NaCl exposure

Treacy et al. [47] conducted XPS on hexavalent CCC on aluminium 2014 T-6 before and after exposure to a 24 h neutral salt fog. XPS high resolution scans showed that the form of chromium present on surface before and after exposure to salt fog did not change from the +3 oxidation state (578 eV); see Table 2.9. They also noted that the lack of Cr(VI) detected could be due to aluminium being oxidised easily by Cr(VI) species or even via X-ray induced photodecomposition. XPS survey scans showed that the Cr content was not detected after 48 h salt fog exposure; see Table 2.10.

Table 2.9 XPS Cr $2p_{3/2}$ binding energy values of hexavalent CCC on Al 2014 T-6 as a function of salt spray exposure (ASTM B117). All values charge corrected to C 1s at 284.6 eV. [47]**.**

Table 2.10 XPS survey scan data of hexavalent CCC on Al 2014 T-6 as a function of salt spray exposure (ASTM B117) [47]**.**

Similar XPS investigations have also been carried out by Raichevsky et al. [106] in which the hexavalent CCC on zinc electrodeposited steel chemistry changes following NaCl solution (5 wt-%) exposure for 6 days. It was found through observations of binding energy values that the chromium and zinc was more likely to be associated with chlorine ($CrCl_3$ and $ZnCl_2$) as opposed to oxygen, as in a non-corroded sample.

2.5.4 Corrosion characterisation

2.5.4.1 Influence of drying temperature on corrosion performance

Using electrochemical tests, such as open circuit potential (OCP) measurements it is possible to establish a potential to indicate the natural corrosion state of the specimen. Work carried out by Zhang et al. [45], for an untreated zinc panel has been shown to exhibit a lower potential value in comparison to a hexavalent CCC zinc panel i.e. it was less noble; see Figures 2.17 and 2.18. The OCP plots also show that for hexavalent CCCs, exposure to increasing post treatment drying temperatures (60, 110 and 210 °C), lowers the OCP values (i.e. they become less noble). Corresponding AFM studies of samples exposed to the same temperatures indicated micro-cracks whose width and depth increased for higher drying temperatures e.g. 60 °C 150 nm depth and 200-600 nm average width, 210 °C 300 nm depth and 300-800 nm average width. Zhang et al. concluded that aggressive chloride ions can access zinc through defects such as micro-cracks and thus lower the potential i.e. activating the zinc. Further to this, a rise in potential on increased NaCl exposure; see Figure 2.17, was related to the ability of absorbed soluble Cr(VI) species in defect regions to form reduced insoluble Cr(III) compounds consequently causing the potential to rise. Alternatively, zinc corrosion products, such as zinc oxide/hydroxide, could also have formed and filled defects to hinder further dissolution. For OCP values in de-aerated conditions; see Figure 2.18, there

was no subsequent rise in potential observed, possibly due to a limited oxygen concentration for ‘self-repair’ of active sites and / or zinc corrosion products. However, it must be noted that Cr(VI) is a highly oxidising agent without the aid of oxygen.

Figure 2.17 Open circuit potential for hexavalent CCC zinc panels and untreated electro-galvanised steel panels in quiescent 3.5% NaCl solution (pH 5.8) [45]**. Note legend abbreviations: EG - electro-galvanised steel, Cr10s - hexavalent CCC immersion treatment time (10 seconds), 60, 110 and 210 - post treatment oven temperatures (°C) for 30 minutes.**

Figure 2.18 Open circuit potential for hexavalent CCC zinc panels and untreated electro-galvanised steel panels in 3.5% NaCl solution (pH 6.9) de-aerated with N_2 [45]**. Note legend abbreviations: EG - electro-galvanised steel, Cr10s - hexavalent CCC immersion treatment time (10 seconds), 60, 110 and 210 - post treatment oven temperatures (°C) for 30 minutes.**

Similar OCP findings have also been noted by Chidambaram et al. [51] for hexavalent CCC on AA2024-T3 substrate. In this case, however, a defect in the form of a manual scratch was

introduced during OCP measurements; see Figure 2.19. A steady increase in potential was observed on increasing exposure time to 0.05 M NaCl solution following an initial decline upon introduction of the scratch, possibly due to 'self-repair'. Following OCP measurements SIMS analysis was carried out within the scratch region, with a few monolayers of absorbed chromium detected. Therefore indicating migration of Cr(VI) species from protected regions to the scratched region for repassivation and the observed increase in potential.

Figure 2.19 The open-circuit potential behaviour, showing repassivation of hexavalent CCC on aluminum alloy AA2024-T3 in 0.05 M NaCl solution before and after scratching. [51].

2.5.4.2 Influence of underlying substrate on corrosion performance

Work by Campestrini et al. [46] using Electrochemical Impedance Spectroscopy (EIS) has shown that the presence of intermetallic particles (IMC) and copper rich 'smut' on an aluminium alloy substrate (Al2024) reduces corrosion resistance. SEM and AFM surface morphology images illustrate these findings as CCC surface defects are found in close proximity to the IMCs. It was also found that removal of copper rich smut on the surface of IMCs improved adhesion of subsequent CCCs and improved overall corrosion protection.

2.5.4.3 Improving hexavalent CCC corrosion performance

An innovative method of improving hexavalent CCC on zinc coated steel is to introduce the active chromate species into a protein coating matrix such as albumin and gelatine. The idea was first proposed by Brenner et al. [107] and later utilised by Gao et al. [50] as a potential non-chromate replacement. It was shown through neutral salt spray tests and anodic

polarisation curves that chromated protein based conversion coatings exhibited superior corrosion resistance in comparison to a conventional hexavalent CCC as well as non chromate based systems (molybdate, tungstate and cerium trichloride). It was proposed that an improved coating thickness was a major factor for these findings.

2.5.5 Disadvantages of hexavalent CCCs

For all the positives noted previously for hexavalent CCCs, unfortunately, there are negative factors too. These negatives are based more on health and safety, environmental and legislative aspects. The key disadvantages are listed in the following sections.

2.5.5.1 Health and Safety

Chromium in its trivalent state is stable and is regarded to be of relatively low toxicity in comparison to a hexavalent state. A reflection of this, is the number and type of risk and safety phrases used in correspondence to EU legislation [108] to reference chemical compounds typically used in hexavalent and trivalent CCC treatment solutions; see Table 2.11. A health and safety issue potentially associated with hexavalent chromium conversion coated components is the exposure to soluble/insoluble hexavalent chromium on the surface of components as detected in XPS studies; see Section 2.5.3.1, during handling. It is important to note that trivalent CCC may not be entirely immune to the presence of Cr (VI) either as Cr (III) has the ability to oxidize to Cr (VI) under an oxidising conditions e.g. hydrogen peroxide.

2.5.5.2 Effluent disposal

The treatment process for chromate containing waste solutions is to reduce the sludge into a trivalent state using typically a reducing agent (e.g. sodium metabisulfite, sulfur dioxide, or ferrous sulphate [109] before precipitation and disposal. This consequently includes a cost factor for processing and disposal within a landfill site.

Table 2.11 Risk and safety phrases used in reference to chromium (VI) oxide and chromium (III) nitrate. Phrases in accordance to Chemical Hazard Information and Packaging (CHIP) regulations for materials data.

2.5.5.3 Legislation

With increasing pressure from public, governmental, industrial, and 'green' campaigning new directives have been brought in to improve sustainability of resources and reduce the impact on the environment. The following directives have Cr (VI) on the 'hit list'.

- The 'End of life vehicle' (ELV) 2000/53/EC directive, restricts the use of hexavalent chromium (no more than 0.1% by weight) in corrosion preventative coatings and came into effect in July 1st 2007. Annex II of the legislation also states that as part of the

coating treatment formulation, hexavalent chromium cannot be deliberately utilised as a component [5,53].

- The 'Waste of Electrical and Electronic Equipment' (WEEE) 2002/96/EC directive, restricts the use of hexavalent chromium (no more than 0.1% by weight) on electrical and electronic equipment, and came into effect in July 1st 2006 [54].
- The 'Restriction of hazardous substances' (RoHS) 2002/95/EC directive, restricts the use of hexavalent chromium (no more than 0.1% by weight) on electrical and electronic equipment, and came into effect in July 1st 2006 [110].

2.6 Alternatives to Hexavalent CCCs

The environmental and health and safety problems outlined above have resulted in hexavalent chromium containing coatings being phased out within industry. Therefore, the search for alternatives has been of high priority.

Alternatives which have been examined and suggested as possible replacements include tungstates, molybdates, cerium compounds, Zn-Cr alloys, cobalt complexes, zirconium based, Cr(III), phosphates [111]. Further alternatives have been outlined by Wynn et al. [8] for the replacement of Cr(VI) based treatment solutions; see Table 2.12.

Table 2.12 Passivation strategies to replace Cr (VI) [8]**.**

As a non-chromium treatment solution, molybdate based systems appear to be an ideal candidate since molybdenum belongs to the same periodic group as chromium, processed from a similar oxidation state (VI) and has been shown to have similar properties and

characteristics [112]. Since a patent in the 1940s for a electroplated molybdenum-oxygen compound as a protective and ornamental finish [113] many studies have been conducted into the suitability of molybdates as a conversion coating material. The surface morphology of molybdate conversion coatings has been shown to exhibit micro-cracking, as in the case of hexavalent CCC [114,115] and their film chemistry suggests a mixed metal oxide composition including molybdenum in a number of oxidation states [41,116,117]. However, their corrosion performance, like that of many other non-chromium based alternatives, has been shown to be inferior to that of hexavalent CCC [114,116,118-120].

Possibly the best alternatives to hexavalent CCC are trivalent CCC. These will be discussed in the following sections.

2.7 Trivalent CCCs

2.7.1 Trivalent CCC history

Trivalent CCCs are regarded by many as being the 'next best available technology' to hexavalent CCCs [6-8]. Overall, current trivalent CCCs meet legislation and fair well under corrosive environments if the treatment solutions used for their formation were formulated and operated correctly.

2.7.1.1 First generation

Trivalent CCC treatment solution formulations have typically utilised chromium nitrate as its chromium source. Industrially chromium nitrate is produced by firstly dissolving a hexavalent chromium source (e.g. sodium dichromate or chromic acid solution) in an acid solution of the desired anion (e.g. nitric acid) and then reducing it to a trivalent state following the addition of an reducing agent. This route is less expensive and easier than dissolving and oxidising from a pure chromium metal raw material, extracted initially from chromite. [78].

Historically, the first generation trivalent CCCs were thought to lack the necessary coating thickness required for adequate corrosion resistance of zinc coated steel [121,122]. Their basic composition was, industrially, based on inorganic chemistry with enhancements made through the addition of metal ions (e.g. cobalt) [123-125] and oxidising agents such as hydrogen peroxide [124,125], hypohalites and persulphates [126] to compensate the lack of Cr(VI) as an oxidising agent. Further developments were made with the addition of organic carboxylic acids [124] and increased treatment temperature up to 60 °C.

2.7.1.2 Second generation

Second generation trivalent system formulations are very much built upon first generation systems. The basis of the formulation is still chromium salts, organic acids, metal ions and oxidising agents. However, a move away from additives such as hydrogen peroxide on the basis of health and safety, high consumption/replenishment and potential decomposition of hydrogen peroxide under the presence of metal ions in solution (e.g. Zn, Fe, Co and Ni). Instead a greater emphasis has been paid towards the use of nitrates as oxidising agents [127], elevated solution temperature (55-65 °C), metal ions in the form of cobalt and complexants to aid film formation [122]. At this point in time there is also a consensus move away from fluoride forming ligands to organic based ligands such as malonic and oxalic acid on the grounds of environmental pollution problems [128]. Also, in a step to improve corrosion resistance, the concentration of trivalent chromium was increased up to 100 g/l [121,128]. All these changes enabled trivalent CCC to increase its coating thickness upto ~300 nm [122] and consequently rival hexavalent CCC for corrosion resistance. Commercially, with the addition of silicate based topcoats trivalent CCC's perform as well as hexavalent CCC's in some applications. A summary of additives and their function used for a typical second generation trivalent CCC are provided in Table 2.13.

Table 2.13 Second generation trivalent CCC additives [129]**.**

2.7.1.3 Third generation

Third generation trivalent CCC are very much tailored commercial products of second generation systems. Tripass LT1500 by MacDermid plc is one such commercially available product. Factors such as environmental legislation, processing and raw material costs are now major drivers. For instance, in order to reduce energy consumption trivalent CCC are now

being developed without the use of elevated treatment temperature [122]. Also to reduce cost and waste, lower concentrations of raw materials such as Cr are being used [128]. The ratio of additives used within the formulation for example Cr, complexing agents and nitrates, has also been better understood in terms of synergistic effects and making the system more efficient [128,130]. However, there are still fears for potential oxidising of Cr(III) to Cr(VI) species with the use of certain additives such as cobalt [131].

More novel methods of improving corrosion resistance of conversion coatings is through the addition of colloidal silica nano-particles [121]. When incorporated as part of the treatment solution this has been observed to increase coating thickness and subsequently improve corrosion resistance. Further improvements in wear resistance could also be envisaged as silica tends to collect at the surface of the conversion coating. This research has stemmed from the use of silica in topcoats for conversion coatings [132].

2.7.2 Film formation

2.7.2.1 Film formation mechanism

The film formation mechanism for trivalent CCC on zinc is thought to be in-line with an electrochemical dissolution-precipitation theory [81,129]. In this section potential film formation steps will be discussed for a typical second/third generation formulation including chromium nitrate, organic acids and cobalt nitrate

Before outlining a step by step chemical reaction path for trivalent CCC film formation the initial chemistry of the treatment solution will be discussed. Trivalent chromium nitrate, which is an ionic salt is expected to dissociate into its ions within deionised water; see Equation 2.23. Following ionisation, trivalent chromium could form an hexaaquachromium (III) complex ion; see Equation 2.24.

$$Cr(NO_3)_3 \rightarrow Cr^{3+} + 3NO_3^- \qquad \textbf{Equation 2.23}$$

$$Cr^{3+} + 6H_2O \rightarrow [Cr(H_2O)_6]^{3+} \qquad \textbf{Equation 2.24}$$

Oxalic and malonic organic acids, which are dicarboxylic acids, are expected to ionise within the treatment solution; see Equations 2.25 and 2.26. Upon ionisation the bi-dentate ligands are potentially able to attach onto chromium and other metal ion complexes following ligand

substitution reactions e.g. trisoxalatochromium (III) ion complex; see Equation 2.27. The substitution reactions, however, could be dependent upon the concentration of the reactant within solution, temperature, pressure and reaction time for a forward reaction to take place using 'Le Chatelier's principle'.

$$HOOC\text{-}COOH \leftrightarrow {}^{-}{:}OOC\text{-}COO{:}^{-} + 2H^{+} \quad \textbf{Equation 2.25}$$

$$HOOC\text{-}CH_2\text{-}COOH \leftrightarrow {}^{-}{:}OOC\text{-}CH_2\text{-}COO{:}^{-} + 2H^{+} \quad \textbf{Equation 2.26}$$

$$[Cr(H_2O)_6]^{3+} + 3C_2O_4^{2-} \leftrightarrow [Cr(C_2O_4)_3]^{3-} + 6H_2O \quad \textbf{Equation 2.27}$$

Hexaquachromium(III) to Trisoxalatochromium (III) ions

A step by step chemical reaction path for trivalent CCC film formation:

1) The acidic nature of the trivalent CCC treatment solution (pH ~1.8), similar to that of hexavalent CCC treatment solution, initiates zinc dissolution following submersion of a zinc coated steel panel, with the formation of hydrogen gas, consequently leading to a rise in solution pH at this region; see Equation 2.14, e.g. pH 3-4.5 [129]. Alternatively, nitrate ions (NO_3^-) may also reduce to NH_4^+ ions; see Equation 2.28 [129]. It is important to note that Cr(VI) is a stronger oxidising agent, in comparison to nitrate ions; see Equation 2.15.

$$4Zn + 10H^{+} + NO_3^{-} \rightarrow 4Zn^{2+} + NH_4^{+} + 3H_2O \quad \textbf{Equation 2.28}$$

2) For the formation of the trivalent CCC a rise in pH at the zinc/treatment solution interface is thought to result in the conditions in which chromium complexes can deposit as a chromium (III) deposit such as chromium hydroxide. This could potentially be from a chromium oxalic acid chelate; see Equation 2.29 [128]. In the case of the latter excess oxalic acid formed as a by-product may react with cobalt and deposit along with chromium hydroxide; see Equation 2.30 [128]. In general, deposition of chromium (III) compounds via a chromium complex is a characteristic of trivalent CCC film formation in comparison to hexavalent CCCs.

$$[CrC_2O_4.(H_2O)_4]^{+} \rightarrow Cr(OH)_3 + C_2O_4^{2-} + 3H^{+} + H_2O \quad \textbf{Equation 2.29}$$

$$C_2O_4^{2-} + Co^{2+} \rightarrow CoC_2O_4 \quad \textbf{Equation 2.30}$$

3) The deposition from a chromium complex to precipitate step is thought to be improved by increasing the processing solution temperature, chromium solution content and

accelerating the ligand replacement kinetics of the chromium (III) complex with the use of a less stable ligand complex e.g. malonic acid as opposed to fluoride base systems. The addition of metal ions in the treatment solution, e.g. cobalt, to catalyse the ligand replacement kinetics can also bring about improvements [130]. However, it should also be noted that as the Cr(III) precipitates form and provide coverage of the zinc surface, a limit in the coating thickness results as pores supplying zinc for electrochemical reactions are diminished [129].

4) Within the conversion coating zinc cations, as well as anions and complexes used in the treatment solution, could also be incorporated; see Equation 2.31 and 2.32 [81,129]. In such a case cobalt commonly added within trivalent CCC formulations could well be incorporated as an insoluble species. In comparison, hexavalent CCC film formation is thought to incorporate sulphate, zinc, water and Cr(VI) species. Water may also be incorporated within the trivalent CCC.

$Cr^{3+}(complex) + 3OH^- \rightarrow Cr(OH)_3 + complex$ **Equation 2.31**

$Cr(OH)_3 + complex + Zn^{2+} + A^- \rightarrow (Cr^{3+}, complex, 3OH^-, Zn^{2+}, A^-)$ **Equation 2.32**

2.7.2.2 Effect of treatment solution temperature on film formation

An important process parameter for trivalent chromium systems is temperature. Dikinis et al. [129] have shown that an increase in treatment solution temperature from 20 to 60 °C increases zinc dissolution and subsequently also increases the concentration of Cr(III) within the coating. Dikinis et al. also suggested that the rate of reaction was possibly greatest at the start of the immersion period and that the conversion coating grows ‘inside out’ as proposed for hexavalent CCCs i.e. diffusion and passage of film forming species through pores/defects within the conversion coating.

2.7.3 Chemical composition

Chemical characterisation using XPS has been carried out by Zhang et al. [43] to deduce the oxidation states present for a commercial trivalent CCC (Permapass Immunox 3K solution). As mentioned in Section 2.5.3.1 hexavalent CCCs contain chromium in two oxidation states Cr(VI) and Cr(III). Trivalent systems on the other hand, have been shown to exhibit no Cr(VI) peak observed specifically at 579.2 eV binding energy; see Figure 2.20b. The Cr content was deduced to be present as 60% $Cr(OH)_3$ and 40% in the form of Cr_2O_3 following

curve fitting analysis. It is important to note, however, that Cr(VI) has been detected for trivalent CCC using techniques based on UV colour analysis following the addition of 1,5 - diphenylcarbazide solution to a coating [9,131]. Potentially, certain additives or atmospheric oxygen may act as oxidising agents for conversion of Cr(III) to Cr(VI).

XPS survey scan data of trivalent CCCs; see Figure 2.20a, shows that elements detected include Cr, O and a strong signal for Zn. In comparison hexavalent CCC included elements O, S and Cr but not Zn.

a **b**

Figure 2.20 (a) XPS survey scan spectra (left image), and (b) XPS high resolution Cr 2p spectra (right image) for (a) a hexavalent CCC zinc surface and (b) a trivalent CCC zinc surface (immersion time 60 s) [43]**.**

2.7.4 Surface morphology

2.7.4.1 Surface morphology in comparison to hexavalent CCC

Research has indicated that hexavalent CCCs in general exhibit a 'dried cracked river bed morphology'; see Figure 2.10. To depict a general trivalent CCC surface morphology is somewhat difficult given the range of formulations used as well as commercial systems used. For example SEM images by Zhang et al. [43] on commercial Permapass Immunox 3K trivalent CCC; see Figure 2.21, shows a damaged morphology with no micro-cracked pattern visible. The morphology was suggested to be influenced by orientation of individual zinc grains and by etching. On the other hand trivalent CCC SEM studies by Cho et al. [133] for a formulation based on 50 mL/L $Cr(NO_3)_3$ (40%), 20 g/L $CoCl_2 \cdot 6H_2O$ and 3 mL/L H_2SO_4, observed an increased density of micro-cracks on increasing immersion time to a certain level. Further to which, micro-cracks decreased and were linked to coating thickness and tensile stress. Cho et al. also showed that pH has an influence upon both coating thickness and surface roughness. At a pH of 1.1 the surface appearance is rough whilst above pH 2.3

becomes smoother with the absence of micro-cracks in comparison. Treatment at pH 1.7 was shown to exhibit optimal coating thickness of ~1 μm for 40 s immersion time.

Zhang et al. [43] also carried out morphological studies of trivalent and hexavalent CCCs following exposure to 0.01 M NaCl solution for 5 h; see Figure 2.22. For hexavalent CCC, SEM images indicate white corrosion products in and around micro-cracked regions thus demonstrating localised corrosion. Trivalent CCC in comparison exhibited large white corrosion pits, possibly as a result of pores within the coating. Blistering and pitting was also observed by Cho et al. [133] for trivalent CCCs following exposure to 0.01 M NaCl solution for 80 h at pH 8.0; see Figure 2.23. For both hexavalent and trivalent CCC, corrosion has shown to begin at flaws within the conversion coating.

a **b**

Figure 2.21 SEM images (a) high and (b) low magnification images of a trivalent CCC (60 s immersion time) zinc surface dried in an oven at 70°C for 30 min at different magnifications [43]**.**

a **b**

Figure 2.22 SEM images of (a) a hexavalent CCC and (b) a trivalent CCC zinc surface after immersion in aerated 0.01 M NaCl solution exposure for 5 h [43]**.**

a **b**

Figure 2.23 SEM images of (a) a trivalent CCC (40 s immersion time, pH 1.7 at 30 °C) zinc surface before and (b) after 0.01 M NaCl solution exposure for 80 h (deaerated, pH 8.0 borate buffer, at 22±2 °C) [133].

2.7.4.2 Surface morphology following thermal treatment

Studies by Gardner et al. [6] on trivalent CCCs for zinc-iron electrodeposits demonstrated good corrosion resistance within a neutral salt spray cabinet following thermal shock treatment (150 ℃ for 1 h). This is the reverse of what happens with hexavalent CCCs. The loss of performance for hexavalent systems was suggested to be possibly due to deterioration of existing micro-cracks via enlargement of cracks, loss of water or soluble 'self-repair' hexavalent chromium species. Widening of cracks has also been observed by Zhang et al. [45] for hexavalent CCC on zinc surfaces. Studies also showed that at 210 ℃ white features were visible from within the cracks thought to be possibly zinc oxide corrosion products.

2.7.4.3 Effect of additives on surface morphology

The effect of additives used in trivalent treatment solutions on surface morphology has been observed by Dikinis et al. [129]. Table 2.14 summarises their findings.

Table 2.14 Effects of additives used in trivalent chromium solutions on conversion coating surface morphologies on zinc electrodeposited steel [129]**.**

.

2.7.5 Corrosion characterisation

2.7.5.1 Electrochemical corrosion performance

Electrochemical corrosion data can be used to compare and explain conversion coating corrosion protection mechanisms such as self-repair and barrier. An electrochemical corrosion performance comparison between hexavalent and trivalent CCC on zinc was carried out by Zhang et al. [43]. Open circuit potential plots as a function of time for bare zinc, hexavalent and trivalent chromium treated zinc specimens in aerated 0.01 M NaCl solution (open to air) are shown in Figure 2.24. They show that the potential values for untreated zinc are initially more negative than hexavalent and trivalent chromium but on increasing immersion time, the potential value becomes more positive i.e. more noble, possibly due to the formation of zinc corrosion products, which act as a temporary barrier against further zinc dissolution. The potential values for hexavalent and trivalent CCC remain fairly constant indicating no change in their corrosion behaviour. From the data one could speculate that in both cases corrosion is inhibited via a physical/chemical barrier coating. In addition, it is difficult to attribute self-repair properties for hexavalent CCC. Zhang et al. also carried out electrochemical impedance investigations (Bode and Nyquist plots). Overall, trivalent CCC on zinc was shown to exhibit a less effective corrosion resistance to hexavalent CCC even with the presence of a micro-cracked surface morphology in the latter case. The difference in corrosion resistance was attributed to a greater coating thickness and the availability of mobile, oxidising Cr(VI) species, which make possible the self-healing of flaws.

Figure 2.24 Open-circuit potential vs. time for bare zinc, trivalent and hexavalent CCCs in 0.01 M NaCl solution (pH 6) [43]**.**

2.7.5.2 Salt spray corrosion performance

A typical time to white rust formation (5% or onset) following exposure to neutral salt spray is somewhat difficult to specify given the range of processing and formulation parameters used for trivalent CCC. Factors such as formulation, treatment time, treatment pH, treatment temperature, zinc / zinc alloy substrate and coating thickness all contribute. Due to confidentiality most research papers and patents do not include specific formulations. However, in some cases examples are included. Studies by Dikinis et al. [129] reported a trivalent CCC formulation exhibiting similar corrosion resistance performance as that of a hexavalent CCC, a time of 240 h for the appearance of white zinc corrosion products following neutral salt spray (ISO 9227) was exhibited; see Table 2.15.

Table 2.15 Corrosion resistance for a trivalent and hexavalent CCC on zinc electrodeposited steel as used by Dikinis et al. Neutral salt spray carried out in accordance with ISO 9227. [129]**.**

Work carried out by Oshima et al. [128] appears to show that the addition of 2 g/l cobalt within the trivalent CCC formulation significantly affects corrosion resistance performance (i.e. time to 5% white rust); see Table 2.16. The base formulation is similar to that of a third generation trivalent CCC system; see Table 2.17. On increasing the treatment solution pH (1.4 to 2.0), a higher content of cobalt is incorporated within the coating and subsequently increases time to 5% white rust. The corrosion resistance appears to be proportional to cobalt content within the coating as opposed to any function of coating thickness; see Table 2.16. Also on increasing the cobalt content within the treatment solution an increase in corrosion resistance performance is observed for trivalent CCC following 2 h at 200 °C heat treatment; see Table 2.18.

The further addition of trivalent chromium within the base formulation increases coating thickness but does not improve corrosion resistance performance; see Table 2.19. However,

corrosion resistance performance is only increased if 2 g/l Co is included within the base formulation; see Table 2.19.

Table 2.16 Coating cobalt content, coating thickness and time to 5% white rust as a function of pH and the addition of 2 g/l cobalt to a base trivalent CCC formulation; see Table 2.17. Note: Treatment temperature of 30 °C, and 40 s immersion time. Neutral salt spray carried out in accordance with JIS-Z-2371 [128]**.**

Table 2.17 Base trivalent CCC formulation as used by Oshima et al. note: 40 s immersion time, treatment temperature 30 °C, [128]**.**

Table 2.18 Corrosion resistance as function of cobalt content within a trivalent CCC treatment solution of base formulation; see Table 2.17, after heating (2 h at 200 °C) as used by Oshima et al. Neutral salt spray carried out in accordance with JIS-Z-2371. [128]**.**

Table 2.19 Corrosion resistance as a function of chromium content and with the addition of cobalt within a trivalent CCC treatment solution as used by Oshima et al.. Note: treatment temperature 30 °C, immersion time 40 s, pH 2.2. Neutral salt spray carried out in accordance with JIS-Z-2371 [128]**.**

Preikschat et al. [130] also observed an increase in corrosion resistance performance following the inclusion of cobalt within a base formulation and operating parameters. The appearance of white rust was improved from 250 to 350 h. It was suggested that the inclusion of cobalt could act as a catalyst in ligand replacement reactions for film formation and that its presence within the coating could also improve corrosion resistance; see Table 2.20. Also included in Table 2.20 are times to white rust for similar base trivalent CCCs on zinc-iron / nickel substrates, on which superior corrosion resistance performance is observed.

Table 2.20 Time to appearance of white rust as a function of trivalent CCC formulation and substrate. Note: processing temperature 60 °C, pH 2, and immersion time 60 s. Carried out in accordance with ASTM B117-73 and DIN 50021 SS [130]**.**

2.8 Summary

A literature review has been carried out in general on the physical, chemical and corrosion protection properties of hexavalent and trivalent CCCs. Details of the techniques available to characterise conversion coatings has also been discussed. This information will provide a valuable insight and resource for subsequent test data and analysis carried out in this investigation. The aim of the investigation will be to compare a standard hexavalent CCC to a comerical third generation trivalent chromium system (Tripass LT1500) on zinc electrodeposited steel. Moreover the following areas will be investigated:

- Physical properties of the conversion coating
- Mechanism of film formation
- Mechanism of corrosion protection

In addition, organic topcoats for trivalent CCC and black trivalent CCC for acid and alkaline zinc surfaces will also be investigated. The sections that follow provide details of the experimental approach undertaken, results of the experiments carried out, discussions of data acquried, conclusions and further work.

3 Experimental methodology

3.1 Sample preparation

3.1.1 Substrate coupons

Galvanised mild steel polished Hull cell panels (100 x 75 mm) were supplied by OSSIAN Ltd. For these investigations the Hull cell panels were cut in half using tin shears. In order to strip the pre-galvanised film (which was used to protect the steel panels during storage) the panel was immersed for 30 s in 50% HCl (S.G. 1.18), and rinsed immediately with deionised water. Deionised water rinse helps to prevent further attack of acid before submersion of the panel in the zinc based electrolyte prior to electroplating. Note that HCl pickle was replaced weekly to ensure strength and to reduce contamination.

3.1.2 Zinc electrodeposition and procedure

Polished mild steel panels were bright zinc electroplated. Predominantly an acid-based electrolyte was used in this investigation, however, an alkaline electrolyte was also used in some cases. The formulations of the commercial acid and alkaline zinc baths are given in Tables 3.1 and 3.2, respectively.

Table 3.1 Acid zinc electrolyte formulation, Kenlevel, MacDermid plc. Note carrier and brightener were supplied by MacDermid plc. All other chemicals were purchased from Fisher Scientific.

Acid zinc electrolyte	
Chemical	**Concentration**
Zinc chloride	80.6 g/l
Potassium chloride	220 g/l
Boric acid	27.5 g/l
Kenlevel Ultima Carrier	40 ml/l
Kenlevel Ultima brightener	0.5 ml/l
Hydrogen peroxide (30% w/v)	2 ml/l

Zinc electroplating involved the following procedure: A polished mild steel panel was attached to a stainless steel cathode holder and placed into the zinc acid/alkaline electrolyte and connected to a Thurlby Thandar Instruments power supply for application of a direct current (15 V / 4 A). Two soluble zinc foil anodes were placed in front of and behind the polished mild steel panel using stainless steel electrode holders and connected to the power supply. The zinc foil anodes were 70 x 37.5 x 0.3 mm in size and purchased from Fisher Scientific. The application of a direct current to the cell activated deposition of zinc ions from

the electrolyte onto the mild steel substrate. Using an operating current density of 0.000275 A/mm^2 (or 2.75 A/dm^2) the required current and time for 8 µm electrodeposition of a 50 x 75 mm panel was calculated to be 2.063 A and 10.19 min. Calculations are provided in Appendix A. To prevent the build up of hydrogen on the substrate surface, continuous agitation was provided using a magnetic stirrer with the stirrer rotation speed set at approximately 120 rpm. Once the treatment time was met the panel was removed from the electrolyte, rinsed with deionised water and dried under a hot air dryer. A summary of the electroplating operating parameters are provided in Table 3.3.

Table 3.2 Alkaline zinc electrolyte formulation, Envirozin, MacDermid plc. Note all chemicals supplied by MacDermid plc, excluding sodium hydroxide which was purchased from Fisher Scientific.

Alkaline zinc electrolyte	
Chemical	**g/l or ml/l**
Zinc	12 g/l (added as 160 ml Isobrite solution containing 12 g Zn and 67.2 g NaOH)
Sodium hydroxide	65.05 g/l
Envirozin conditioner	27.5 g/l
Envirozin 120 Brightener	1.5 ml/l
Envirozin Base Additive	8 ml/l
Chemical 22	1 ml/l

Table 3.3 Acid and alkaline zinc electroplating operating parameters. Note pH was only adjusted for the acid zinc electrolyte using 10% NaOH and HCl purchased from Fisher Scientific. Note that for the alkaline zinc electrolyte no pH range was specified.

Operating Parameters	
pH	5.2 (for acid zinc only)
Temperature (°C)	20-30
Current Density (A/mm^2)	0.000275
Treatment Time (min) for 8µm thickness	10.19

3.1.3 Conversion coating treatment solution formulations and procedure

The surface of the bright zinc electrodeposited steel requires activation prior to conversion coating. A pretreatment step of deionised water rinse (60 s) followed by the immersion of the panel in 0.5% HNO_3 (S.G. 1.42) in 1 L deionised water for 30 s is recommended [134]. Following pretreatment, the panel was rinsed immediately with deionised water (30 s) and then immersed in the treatment solution, chromate A, B or Tripass LT1500, for the required treatment time. Treatment solution formulations and procedures are provided in Tables 3.4 and 3.5. Whilst immersed in solution, agitation was provided using a magnetic stirrer and manual shaking of the stainless steel holder. Following conversion coating, the specimen was

rinsed with deionised water (60 s) and dried using a hot air dryer to remove any residue. The samples were then left to stabilise at room temperature for 24 h in accordance with ASTM B201 [135] before any tests or analysis could be conducted.

Details of the two hexavalent CCC treatment solution formulations used in this investigation are provided in Table 3.4. Chromate A conversion coating is a commercial system (Iridite LY-4110, MacDermid plc) and was used predominately throughout the investigation. Chromate B conversion coating is the patented Cronak system [76]. The operating parameters for the two treatment solutions are provided in Table 3.5. Note that pH and immersion times selected are in relation to recommended operating parameters as specified in technical data sheet and patent.

Table 3.4 Formulations for hexavalent CCC treatment solutions.

Hexavalent CCC (chromate A)		**Hexavalent CCC (chromate B)**	
Chemical	**g/l**	**Chemical**	**g/l**
Chromic acid (H_2CrO_4)	0.72	Sodium dichromate ($Na_2Cr_2O_7$)	200
Sodium dichromate ($Na_2Cr_2O_7$)	0.64	Sulphuric acid (H_2SO_4)	10
Sulphuric acid (H_2SO_4) (77% w/v)	0.16		
Nitric acid (HNO_3) (59% w/v)	1.17		

Table 3.5 Operating parameters for hexavalent and trivalent CCC treatment solutions.

Operating Parameters	**Hexavalent Chromium (chromate A)**	**Hexavalent Chromium (chromate B)**	**Tripass LT 1500**
Temperature (°C)	21	21	21
pH	1.8	1.2	1.6-2.0
Immersion time (s)	20, 40, 80	10, 30, 60	45, 90, 180
Agitation	Mechanical	Mechanical	Mechanical

A commercial trivalent CCC treatment solution was used in this investigation, Tripass LT1500, MacDermid plc. The operating parameters and base formulation are provided in Table 3.5 and 3.6. Note that pH and immersion times selected are in relation to recommended operating parameters as specified in the technical data sheet. In most of the investigations the treatment solution was prepared from a concentrate supplied directly from MacDermid plc. In order to investigate the role of different additives the treatment solution was prepared in the laboratory, with the content of individual additives varied appropriately; see Table 3.7. As the treatment solution required a rigorous methodology, a step by step guide is provided in Table 3.8. Also to differentiate from the concentrate supplied directly from MacDermid plc, the

laboratory equivalent in terms of formulation will be acknowledged as Tripass LT1500 control as opposed to Tripass LT1500 in the thesis.

Table 3.6 Treatment solution formulation for trivalent CCC, Tripass LT1500.

Tripass LT 1500	
Chemical	**g/l**
Trivalent chromium nonahydrate ($Cr(NO_3)_3. 9H_2O$) (Added as 65% chromium nitrate nonahydrate solution)	106 (Cr 9 g)
Oxalic acid dihydate ($HOOCCOOH. 2H_2O$)	26
Malonic acid ($C_3H_4O_4$)	6.5
Cobalt (II) hexahydrate ($Co(NO_3)_2. 6H_2O$) (note: added as 60% cobalt nitrate hexahydrate solution)	7.3 (Co 0.9 g)
Sodium molybdate dihydrate ($Na_2MoO_4. 2H_2O$)	0.08 (Mo 0.032g)

Table 3.7 Trivalent CCC treatment solution formulations used for investigation into the role of additives. Note all individual chemicals were supplied by MacDermid plc. Treatment operating conditions 90 s immersion time / pH 1.8 / 21°C.

	Variables										
Tripass LT 1500	Control (g/l)	0 g/l malonic acid	13 g/l malonic acid	0 g/l oxalic acid	52 g/l oxalic acid	0 g/l cobalt nitrate	14.6 g/l cobalt nitrate	0 g/l sodium molybdate	0.4 g/l sodium molybdate	0 g/l chromium nitrate	212 g/l chromium nitrate
Malonic acid	6.5	0	13	6.5	6.5	6.5	6.5	6.5	6.5	6.5	6.5
Oxalic acid dihydrate	26	26	26	0	52	26	26	26	26	26	26
Cobalt nitrate hexahydrate	7.3	7.3	7.3	7.3	7.3	0	14.6	7.3	7.3	7.3	7.3
Sodium molybdate dihydrate	0.08	0.08	0.08	0.08	0.08	0.08	0.08	0	0.4	0.08	0.08
Chromium nitrate nonahydrate	106	106	106	106	106	106	106	106	106	0	212

Table 3.8 Methodology used for the preparation of the laboratory Tripass LT1500 control treatment solution.

Step	Tripass LT1500 control – methodology
1	To 500 ml of DI water add 106 g chromium nitrate nonahydrate solution and agitate.
2	Heat to 60°C.
3	Add 26 g of oxalic acid dihydrate and agitate.
4	To this add, with good stirring, 118.75 ml sodium hydroxide (10%).
5	Allow constituents to react for 1 h.
6	Add 6.5 g of malonic acid and agitate. Allow to react for 2 h.
7	Add the 7.3 g of cobalt nitrate hexahydrate solution and agitate.
8	Add 0.08 g of sodium molybdate dehydrate and agitate.
9	Make up to 1 litre and adjust solution pH to 2.0 with 10% NaOH or nitric acid as required.
10	Allow solution to equilibrate overnight. Cool solution down to room temperature.
11	Reheat solution and agitate for at least 5 h at 60°C, make up to 1 litre with DI water if required.
12	Following cooling to RT, check pH and adjust appropriately.

3.1.3.1 Black trivalent CCCs / Organic topcoats

Two different formulated black trivalent CCCs for acid and alkaline zinc electrodeposited steel were investigated. In addition, two different organic topcoats on a trivalent CCC (Tripass LT1500) on acid zinc electrodeposited steel were also investigated. The base formulations used for the acid and alkaline black trivalent CCC are provided in Table 3.9. Full details of their respective additive concentrations as well as operating parameters have not been included due to confidentiality requirements. The base formulation used for the two different organic topcoats applied onto Trivalent CCC on acid zinc electrodeposited steel were based on a colloidal silica solution. The two different topcoats differed in the size of silica nano-particle used (12 and 22 nm diameter). Again due to confidentiality additional details of this cannot be disclosed.

Table 3.9 Black trivalent CCC treatment solution formulations for acid and alkaline zinc surfaces.

Black trivalent CCC formulation for an alkaline zinc electrodeposited steel	Black trivalent CCC formulation for an acid zinc electrodeposited steel
Chromium nitrate $Cr(NO_3)_3$	Chromium nitrate $Cr(NO_3)_3$
Cobalt nitrate $Co(NO_3)_2$	Cobalt nitrate $Co(NO_3)_2$
Malonic acid (complexing agent)	Nickel nitrate $Ni(NO_3)_2$
Organosulphur (blacking agent)	Phosphoric acid
	Thiogamate
	Malonic acid (complexing agent)
	Colloidal silica

3.2 Surface morphology characterisation

Surface characterisation of conversion coatings and zinc electrodeposited steel was carried out using SEM, FEGSEM, FIBSEM and AFM.

3.2.1 Scanning Electron Microscopy (SEM)

3.2.1.1 Field Emission Gun Scanning Electron Microscope (FEGSEM)

A LEO 1530VP FEGSEM was used to obtain secondary electron images at low and high pressure modes in the variable pressure (VP) and InLens modes; see Section 2.4.1.1. An operating primary beam energy of either 20 or 5 kV was used. A larger primary beam energy for the low vacuum or VP mode was used to compensate for a longer working distance (~5 to 12 mm) between the electron beam aperture and sample surface in order to improve detection limits. Magnification used for the investigations ranged from 500 to 100,000X depending

upon the scale of resolution required e.g. InLens mode at 5 mm working distance and 100,000X magnification equated to approximately 200 nm on the annotated scale bar. In addition to surface morphological characterisation, Energy Dispersive X-ray (EDX) spectroscopy was carried out to characterise the general elemental composition of the coating and specific regions of interest. Note that the analytical depth was equivalent to 1 µm and thus beyond the conversion coating thickness. In some cases specimens were gold sputter coated in order to improve conductivity. In order to evaluate coating thickness using SEM, specimens were immersed in liquid nitrogen and then immediately fractured in one plane following treatment. Samples were cut to ~10 x 10 mm for all FEGSEM, SEM and AFM investigations.

SEM was used to evaluate hexavalent and trivalent CCCs and zinc substrates in the untreated state and following exposure to thermal and corrosive conditions. For thermal exposure the conditions were normal atmosphere in a circulating oven at 150 ˚C for 1 h followed by cooling at room temperature (21 ˚C). The corrosive exposure conditions were quiescent 5 wt.% NaCl solution (pH 6) for 18 h. In addition, SEM was used to evaluate hexavalent and trivalent CCCs following initial scratching and then exposure to quiescent 5 wt.% NaCl solution (pH 6) for 18 h. An Erichsen model 426 scratch pen according to van Laar (spherical tungsten carbide tip 0.5 mm in diameter) was used to scribe sample panels in accordance with ASTM D1654 [10]. Two scratch indentations were made with one being exerted at a greater manual force. Limitations of this method are noted in Section 4.1.3.5.

3.2.1.2 Cryo stage-SEM

A Cambridge Steroscan 360 instrument equipped with a cold stage was used in the secondary electron imaging mode to evaluate conversion coatings in a frozen state to potentially alleviate electron beam induced micro-cracking. An operating primary beam energy of 20 kV was used. Specimens were initially immersed in liquid nitrogen (-180°C) and then transferred under vacuum to a cryo stage-preparation chamber, where gold sputter coating could be carried out on the frozen sample. Following this, the specimen was then transferred to the SEM chamber for imaging where it remained in a frozen state. The specimens were imaged at -180 and 21°C following stabilisation. It is important to note that imaging of the specimens in the frozen state could also have been carried out at a higher temperature (-180 to -80°C).

3.2.2 Focused Ion Beam Scanning Electron Microscopy (FIBSEM)

A FEI Nova Nanolab 600 dual beam was used for focused ion beam and secondary electron imaging. Two imaging modes were utilised, secondary electron and gallium imaging. In the case of the latter, a primary beam of ~30 kV with a working distance of ~20 mm was used, with the detection of gallium ions. Secondary electron imaging was operated at 10 kV with a working distance of ~5 mm.

Focused gallium ion beam sputtering parameters are very much dependent upon the material and beam current used. In this investigation a voltage of 30 kV and 20 nA current was used.

3.2.3 Atomic Force Microscopy (AFM)

A TA instrument unit was used in the intermittent tapping mode to construct topographical images of conversion coatings and zinc electrodeposited steel. A silicon probe (10 nm diameter) attached to a vibrating cantilever of specific resonance frequency (~100-500 kHz) was rastered over the sample surface in a dry state. A magnitude of approximately 100 nm amplitude vibration was achieved with a tip force of the order of 10^{-12} N. AFM imaging has a resolution of ~10 nm based on the tip probe and is viable for resolving micro-cracks in CCCs. Note a typical crack width is ~100 nm. High and low resolution images were taken at 100 x 100, 10 x 10 and 1 x 1 µm raster widths. Surface roughness measurements were also established. Surface roughness measurements such as R_a were extrapolated from topographical data obtained in the intermittent tapping mode. R_a is the average deviation from the mean line given for surface irregularities. An algorithm was used in the software to establish statistical R_a values.

3.3 Chemical characterisation

Chemical characterisation of conversion coatings and zinc electrodeposited steel was carried out using AES, XPS, SEM-EDX and IR.

3.3.1 Auger Electron Spectroscopy (AES)

A JEOL 7100 Auger Spectrometer was used to provide chemical composition at the outermost atomic layers of the conversion coating surface (3-4 nm) in a lateral region of ~100 µm. A primary electron beam energy and beam current of ~10-20 keV and 2-5.00x10^{-7} A respectively was used. An argon ion etch rate of approximately 8 nm per min at a pressure of 5x10^{-2} Pa was used for depth profiling. SpecSurf software was used to generate intensity vs.

kinetic energy (0-1100 eV) plots. Atomic compositions of conversion coatings were quantified using derived peak heights from intensity vs. kinetic energy plots and reference relative sensitivity factors for individual elements. For consistency at least two different locations on the specimen surface were investigated using AES with one documented. Samples were cut to 5 x 5 mm, ensuring that a flat surface was preserved.

AES was used to investigate hexavalent CCC (chromate A) and trivalent CCC (Tripass LT1500) on acid zinc electrodeposited steel. To help elucidate film formation mechanism a range of hexavalent (chromate A - 1, 2, 5 and 40 s) and trivalent (Tripass LT1500 - 45, 60, 90 s) chromium conversion coating treatment times were investigated. Hexavalent CCC (chromate A - 20 s) and trivalent CCC (Tripass LT1500 - 90 s) samples exposed to quiescent 5 wt.% NaCl solution for 18 and 48 h were also investigated.

In order to identify the possibility of cobalt within a trivalent CCC AES spectrum, its major Auger peak at 775 eV had to be extracted from an overlapping minor zinc Auger peak at 773 eV. In order to achieve this a zinc oxide reference standard AES spectrum was obtained. Firstly, peak/trough measurements (mm) for zinc Auger peaks at 994 and 773 eV were taken, with a ratio being determined from the reference standard. The ratio could then be applied to the peak/trough 994 eV measurement (mm) for a trivalent CCC AES spectrum to determine contribution of the 773/775 eV peak/trough due to the presence of zinc the remainder being ascribed to the presence of cobalt. Thus determing the peak/trough value (mm) for cobalt Auger peak at 775 eV. A similar approach was also used for evaluating the presence of a major nickel Auger peak (848 eV) in black trivalent CCC AES spectrum, as it has a similar kinetic energy to that of a zinc Auger peak at 836 eV.

In addition to AES depth profile plots for black trivalent CCC and organic topcoat trivalent CCC are theoretical contributions of oxygen associated to silicon, chromium and zinc oxides. This has been established by firstly taking surface and bulk AES spectra for a number of relevant reference standards; silica (SiO_2), chromium oxide (Cr_2O_3) and zinc oxide (ZnO). Then calculating the relative sensitivity factor for surface and bulk of these using Equation 3.1. The relative sensitivity factor can then be applied to the AES software for deriving atomic % quantification.

$$\text{Sensivity}_{Zn} = \frac{\text{Sensitivity Oxygen } (S_O) \times \text{Concentration Oxygen } (C_O) \times \text{Height Zinc } (H_{Zn})}{\text{Height Oxygen } (H_O) \times \text{Concentration } (C_{Zn})} \quad \textbf{Equation 3.1}$$

Example for calculating sensitivity factor for Zn respective for ZnO

Height Zinc (H_{Zn}) (mm) – peak/trough height of main zinc auger peak (994 eV)

Height Oxygen (H_O) (mm) – peak/ trough height of main oxygen auger peak (503 eV)

Concentration Zinc (C_{Zn}) = 1 e.g. ZnO

Concentration Oxygen (C_O) = 1 e.g. ZnO

Sensitivity Oxygen (S_O) = 5 (arbitary random value)

3.3.2 X-ray Photoelectron Spectroscopy (XPS)

XPS was used to analyse hexavalent CCC (chromate A - 20 s) and trivalent CCC (Tripass LT1500 - 90 s) on acid zinc electrodeposited steel. XPS was also used to study hexavalent CCC (chromate A - 20 s) and trivalent CCC (Tripass LT1500 - 90 s) on acid zinc electrodeposited steel following exposure to quiescent 5 wt.% NaCl solution (pH 6) for 18 h. The role of additives used in Tripass LT1500 was also investigated; see Table 3.7.

3.3.2.1 Al Kα X-ray source (monochromatic)

All XPS monochromatic Al Kα X-ray source data was carried out at the National Centre for Electron Spectroscopy and Surface Analysis (NCESS), STFC Daresbury Laboratory, UK. A SCIENTA ESCA300 spectrometer interfaced with a monochromatic lens was used. The X-ray beam Take Off Angle (TOA) is the angle between the sample plane and the analyser. For the majority of the investigations this was set at 90°, with 10° and 30° used in specific cases for depth profiling of the uppermost surface regions. A pass energy of 150 eV and an analyser slit width of 0.8 mm were used for both survey and high resolution Al Kα scans. The Al Kα X-ray source anode voltage was set at 10 kV, with a filament current of 200 mA. Region spectra were recorded with a step interval of 0.05 eV, a step time of 0.1 s /eV and with co-addition of 5 to 10 scans.

The spectrometer energy scale was calibrated using the Fermi edge, $3d_{5/2}$ and M_4VV lines of a sputter cleaned sample of Ag foil. The measured binding energies came within 0.1 eV of the corresponding literature values (368.26 and 1128.78 eV respectively).

The XPS spectrometer was also equipped with a thermoionic emission electron flood gun which was used to facilitate charge compensation. This was achieved using a low energy

electron flood gun (Scienta FG300) with the gun settings adjusted for optimal spectral resolution.

To avoid the possibility of photoreduction of Cr(VI), all samples were analysed individually with spectrums acquired within 45 mins.

3.3.2.2 Al Kα X-ray source (non-monochromatic)

All XPS non-monochromatic Al Kα X-ray source data was obtained using a VG ESCALAB MkI spectrometer. A pass energy of 20 eV and an analyser slit width of 0.8 mm was used for both survey and high resolution scans. Al Kα X-ray source anode voltage was set at ~8 kV with a filament current of 200 mA. X-ray beam take off angle (TOA) was set at 90°.

3.3.2.3 Quantification of XPS data

Elemental quantification from survey scans was achieved using theoretically derived relative sensitivity factors and measuring element peak areas following subtraction of a Shirley type background [136]. This was carried out using ESCA300 DOS software (version 1.29) [137]. Atomic % quantification has been carried out for a range of chromium oxides and a zinc oxide standard.

Atomic % quantification values for individual elements detected within hexavalent and trivalent CCCs have not been included. This is because some chromium photoelectron peaks are overlapped by zinc Auger peaks. Therefore, survey scans have only been analysed for the identification of elements.

High resolution scans were analysed using XPSPEAK version 4.1 curve fitting software [138] based on a Gaussian-Lorentzian function. O 1s, C 1s and Cr 2p peaks were investigated.

In order to obtain fitting parameters for the high resolution Cr 2p data of hexavalent and trivalent CCCs, the peak envelopes of related chromium standards (e.g. CrO_3, Cr_2O_3 and $Cr(OH)_3$) were initially analysed. In addition as it was found that zinc Auger peaks ($L_3M_{23}M_{45}$) can overlap chromium photoelectron peaks (2p) for data retrieved from an Al Kα X-ray source a zinc standard was also investigated. It is important to note that the number of peaks assigned to the envelopes on each standard was dependent upon the number of inflections physically observed in their Cr $2p_{3/2}$ and Zn $L_3M_{23}M_{45}$ spectra. A Shirley

background was used to isolate the Cr $2p_{3/2}$ and Zn $L_3M_{23}M_{45}$ peak components. Their resulting parameters, such as: the peak maximum binding energy value, full width at half maximum (FWHM) and peak area were then fixed according to the data and constrained to the major peak within the standard. Only the peak area of the major peak was allowed to change during fitting with all other minor peaks constrained around it. As the chromium 2p photoelectron peak had the potential to be overlapped by the zinc Auger peak, their respective peak areas were calculated and subtracted against one another so that a peak area could be established for quantification. All derived peak maximum binding energy values were charge referenced to the main adventitious carbon peak of 285 eV. In the case of O 1s spectra, curve fitting peaks were added in relation to the number of physical inflections observed. Respective O 1s peak envelopes from chromium and zinc standards were not used as fitting parameters for the curve fitting chromium coatings, which was used in the case for Cr 2p data.

Chromium(VI) oxide (CrO_3) 99.99%, chromium(III) oxide (Cr_2O_3) 99.9% and zinc oxide (ZnO) were obtained from Sigma Aldrich. Chromium(III) chloride (sublimed anhydrous $CrCl_3$) 99%, was obtained from Fisher Scientific. Chromium hydroxide ($Cr(OH)_3$) was obtained via precipitation [66] of hydrous chromium chloride (1 M) with ammonia solution (0.1 M). All chromium and zinc compounds were obtained in a powder form and placed onto double sided adhesive tape (10 mm diameter) mounted on a stainless steel stub. In an effort to alleviate atmospheric contamination specimens were immediately transferred to the spectrometer following loading.

3.3.3 Infra-red (IR) spectroscopy

A SHIMADZU FTIR machine was used to analyse KBr discs containing the conversion coatings, Tripass LT1500 and chromate A, chromium standards (CrO_3, Cr_2O_3, $Cr(OH)_3$), Zinc oxide (ZnO) and organic acids used as part of the Tripass LT1500 formulation (malonic and oxalic acid). The KBr disc in each case was prepared as ~1-2 mg of the sample with ~200 mg of KBr following grounding with a pestle and mortor, and shaped into a disc under pressure within a die. All IR spectra were produced within the range of 4000 to 400 cm^{-1}, with a resolution of 4 cm^{-1} and 64 number of scans.

In addition, reflectance absorption infra-red investigations were carried out on hexavalent and trivalent CCCs (chromate A and Tripass LT1500) using a FTIR SPECTRA-TECH unit with a model 500 attachment. OMNIC software was used to subtract sample spectra against potential

background data such as atmospheric contamination and actual beam spectra. IR spectra were produced within the range 650 to 4000 cm^{-1}, with a resolution of 2 cm^{-1} and 1024 as the number of scans.

3.4 Corrosion characterisation

In order to characterise the corrosion properties of the hexavalent and trivalent CCCs, electrochemical Linear Polarisation Resistance (LPR) data and polarisation curves were produced.

3.4.1 Linear Polarisation Resistance (LPR) and polarisation curves

Electrochemical LPR was carried out broadly in accordance with ASTM G59 and G102 [11,139]. An ACM Instrument AutoTafel potentiostat unit and computer software was used to apply a potential of +/- 20 mV around the rest potential (E_{corr}) at a sweep rate of 6 mV/min. For polarisation curves, potential was applied at +/- 1500 mV around the rest potential at a sweep rate of 10 mV/min to establish anodic and cathodic branches for the specimen (4 cm^2 cell area). Note that two samples, one for each for the individual cathodic and anodic potential current plots were used to prevent any prior physical or chemical changes in the conversion coating and untreated zinc coating state. The coupon was immersed in quiescent 5 wt.% NaCl solution (pH 6) at room temperature for 40 min so that a rest potential could be established for both LPR and polarisation curves. A platinum auxiliary (4 cm^2 cell area) and reference saturated calomel electrode (SCE) were used to complete the cell. Potential vs. current density was plotted with polarisation resistance determined by graphical interpretation. A line was drawn for the data slope intersecting at 0 mV and 0 mA/cm^2, with the gradient taken as the polarisation resistance value ($\Omega.cm^2$). In order to evaluate the influence of oxygen within the NaCl solution upon the corrosion process determined from polarisation curves, the solution was purged with high purity nitrogen gas for 1 h prior to introduction of the specimen. Note no measurements were taken of the NaCl solution oxygen concentration before and after purging.

LPR measurements were also conducted with increasing exposure time at regular intervals (24 to 462 h) within quiescent 5 wt.% NaCl solution (pH 6) for hexavalent CCC (chromate A - 40 s) and trivalent CCC (Tripass LT1500 - 90 s) specimens.

4 Results

4.1 Surface characterisation

4.1.1 Untreated

4.1.1.1 Acid zinc electrodeposited steel

A low magnification FEGSEM image of an acid zinc electrodeposited steel coupon appears to show a relatively smooth surface topography in which there are no visible grain-like structures or boundaries; see Figure 4.1a. At higher magnification the surface morphology appears rough with the appearance of very small deposit structures (>50 nm) coalesced on top of one another; see Figures 4.1b-c. Where there is strong agglomeration of these deposits a white contrast appears to the general background.

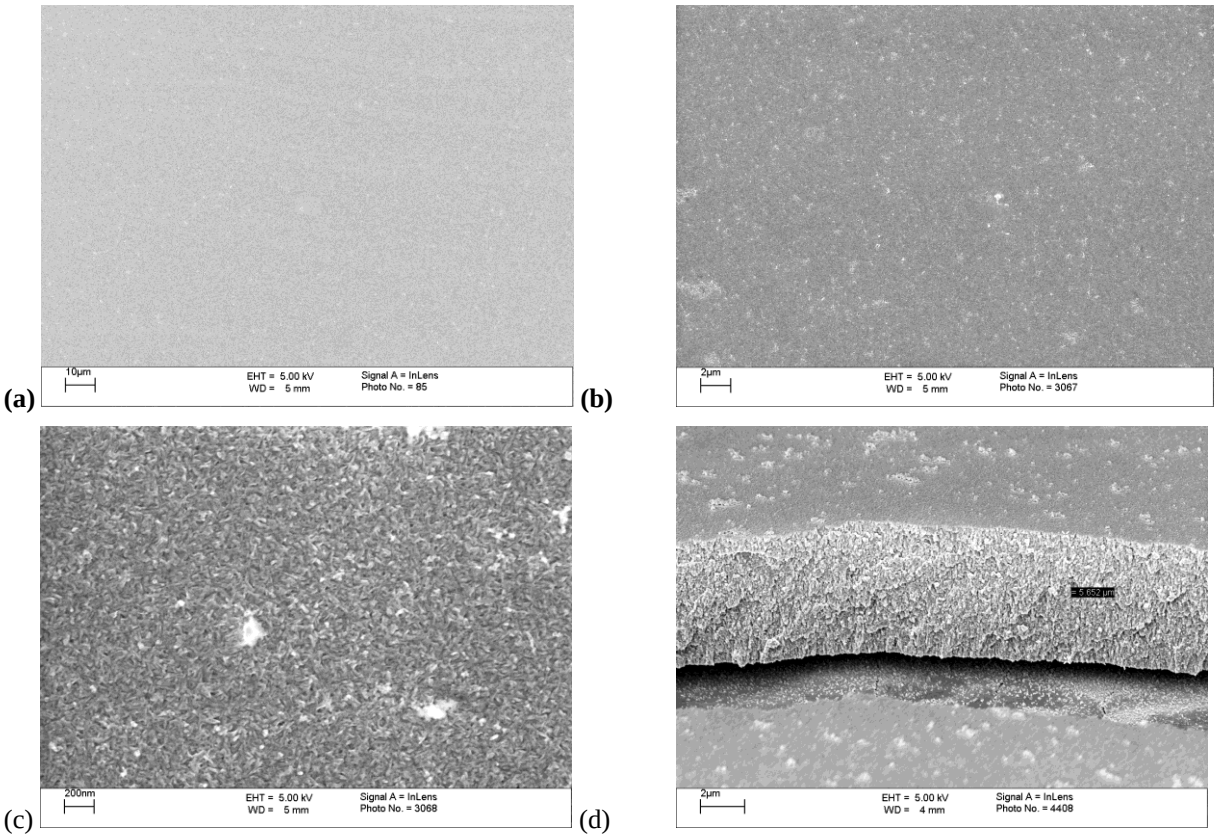

Figure 4.1 FEGSEM micrographs of acid zinc electrodeposited steel taken at low (a) and high magnification (b,c). FEGSEM micrograph of cryo fracture acid zinc electrodeposited steel (d). Samples were gold coated.

Complementary to top plane images, cryo-freeze fracture specimen preparation was carried out to observe the cross-section and thickness of the zinc electrodeposited steel. Figure 4.1d shows small peaks protruding from the zinc electrodeposit surface and could be related to deposit agglomeration observed in top plane images. AFM images of the surface also exhibit protrusions from the surface in the z axis (~250 nm); see Figure 4.2. This minor phenomenon could be related to levelling, a function of the organic brightener additives or initial corrosion products as a result of atmospheric exposure. The cross-section of the zinc electrodeposit reflects an irregular structure construed of tiny deposits coalesced together. The average thickness of the acid zinc electrodeposit was 5167 nm; see Table 4.1. As a portion of the cathode holder was also immersed in the electrolyte during electroplating, a lower coating thickness than the expected 8 µm resulted. In hindsight the exposed region could have been blanked off using non-conductive tape or a longer plating time could have been used. From an electrochemical point of view, hydrogen evolution during the electroplating process could also have contributed to a reduction in coating thickness.

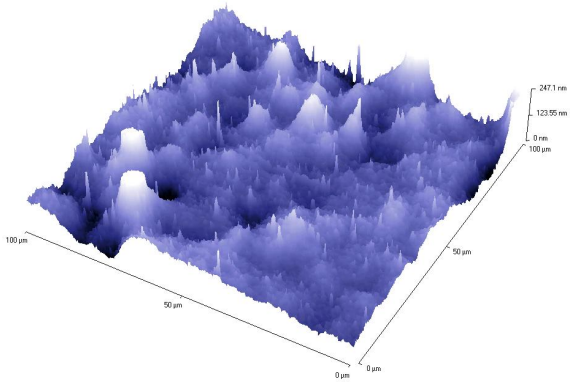

Figure 4.2 AFM micrograph of an acid zinc electrodeposited steel.

4.1.1.2 Alkaline zinc electrodeposited steel

FEGSEM micrographs; Figure 4.3a, of an alkaline zinc electrodeposited steel reveal a similar surface topography in comparison to acid zinc electrodeposits. On closer observation, however, the general deposit differs in that an 'intertwined mesh' is exhibited; see Figure 4.3b. The single deposit features are in the order of ~ 200 and 50 nm in length and thickness. No coating thickness measurements of the alkaline zinc electrodeposited steel were undertaken. AFM topographical image depicts a relatively flat surface with only one or two protruding features in the z-axis; see Figure 4.4. These again could be agglomerate features. Surface roughness of alkaline zinc electrodeposits were found to have a higher R_a value in comparison to acid zinc electrodeposits; see Table 4.2. This can be related to differences in

deposit structure observed in FEGSEM micrographs; Figures 4.1c and 4.3b. In the case of acid zinc electrodeposited steel a finer deposit structure was observed.

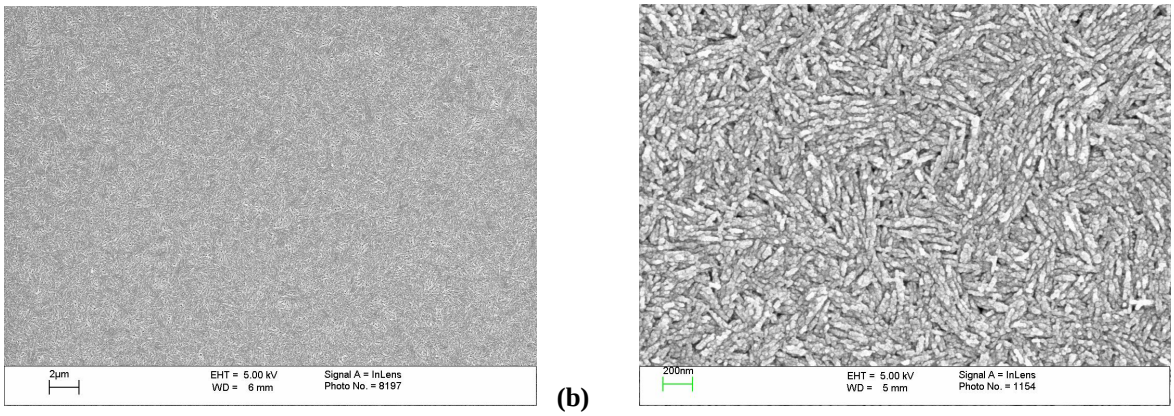

Figure 4.3 FEGSEM micrograph of an alkaline zinc electrodeposited steel taken at low (a) and high magnification (b). Samples were gold coated.

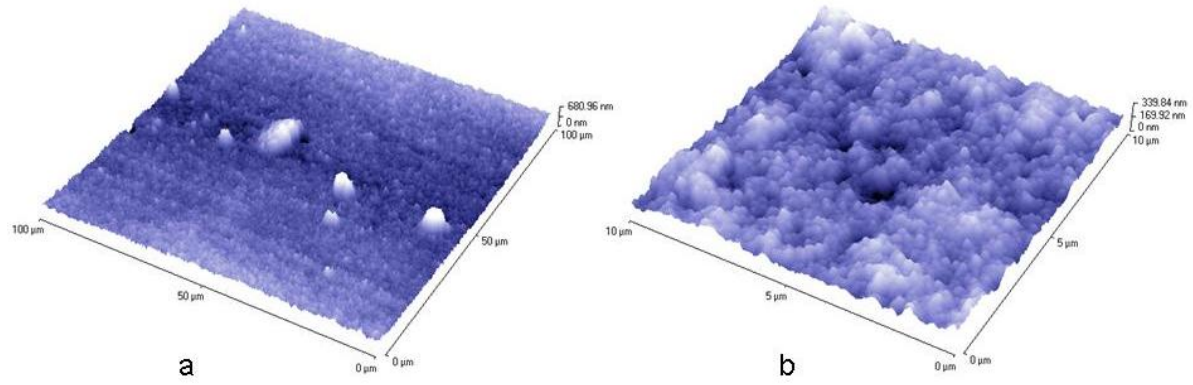

Figure 4.4 AFM micrographs of an alkaline zinc electrodeposited steel taken at low (a) and high (b) magnification.

Table 4.1 FEGSEM cryo-fracture conversion coating and acid zinc electrodeposit coating thickness measurements.

Coating	Thickness (nm)			
	Reading 1	Reading 2	Reading 3	Average
Acid zinc electrodeposit	5102	4750	5650	5167
Chromate A 20 s	140	105	120	122
Chromate A 40 s	166	200	170	179
Chromate A 80 s	280	320	330	310
Tripass LT1500 45 s	170	170	157	166
Tripass LT1500 90 s	210	200	200	203
Tripass LT1500 180 s	290	280	270	280

Table 4.2 AFM surface roughness values for conversion coating and zinc substrate (at 100 µm magnification), R_a is the average deviation from the mean line given for surface irregularities.

Sample	Roughness (R_a)
Acid zinc electrodeposited steel	31
Alkaline zinc electrodeposited steel	77.4
Zinc foil	311.4
Chromate A 20 s on acid zinc electrodeposited steel	16.4
Chromate A 40 s on acid zinc electrodeposited steel	10.8
Chromate A 80 s on acid zinc electrodeposited steel	19.3
Chromate B 10 s on alkaline zinc electrodeposited steel	67.8
Chromate B 30 s on alkaline zinc electrodeposited steel	94.7
Chromate B 60 s on alkaline zinc electrodeposited steel	33
Chromate B 30 s on zinc foil	313.1
Tripass LT1500 45 s on acid zinc electrodeposited steel	14.8
Tripass LT1500 90 s on acid zinc electrodeposited steel	16.1
Tripass LT1500 180 s on acid zinc electrodeposited steel	14.5

4.1.1.3 Zinc foil

FEGSEM micrographs; Figure 4.5a-b, of a zinc foil substrate reveal an uneven and inferior surface morphology in comparison to acid and alkaline zinc electrodeposits. Rolling lines are clearly evident from secondary processing as are crater defects. These findings are also exhibited in the AFM images; see Figure 4.6. Therefore zinc foil has a significantly higher surface roughness value in comparison to both acid and alkaline zinc electrodeposits; see Table 4.2.

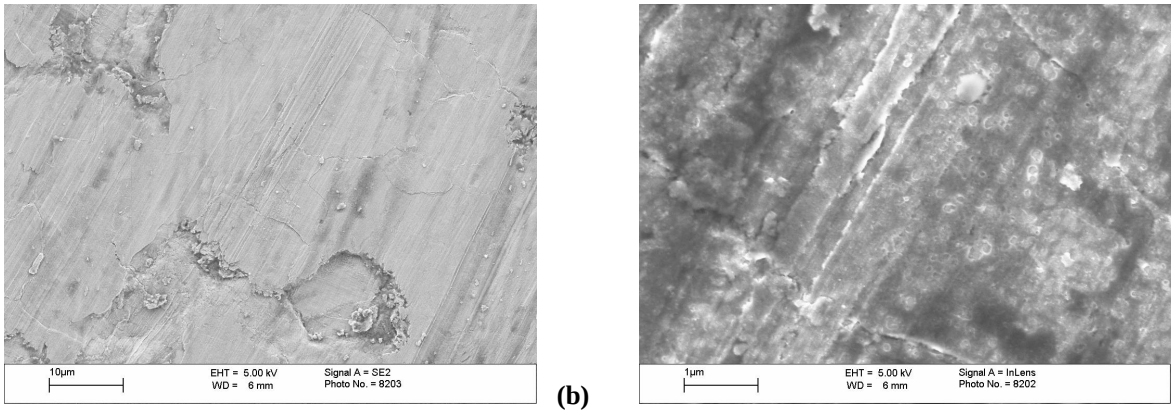

Figure 4.5 FEGSEM micrographs of a zinc foil taken at low (a) and high (b) magnification. Samples were gold coated.

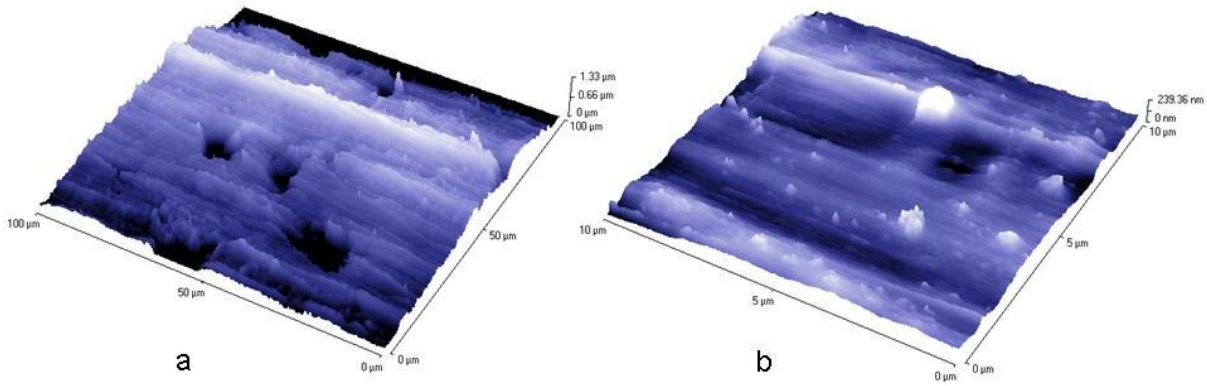

Figure 4.6 AFM micrographs of a zinc foil taken at low (a) and high (b) magnification.

4.1.1.4 Chromate A conversion coating on acid zinc electrodeposited steel

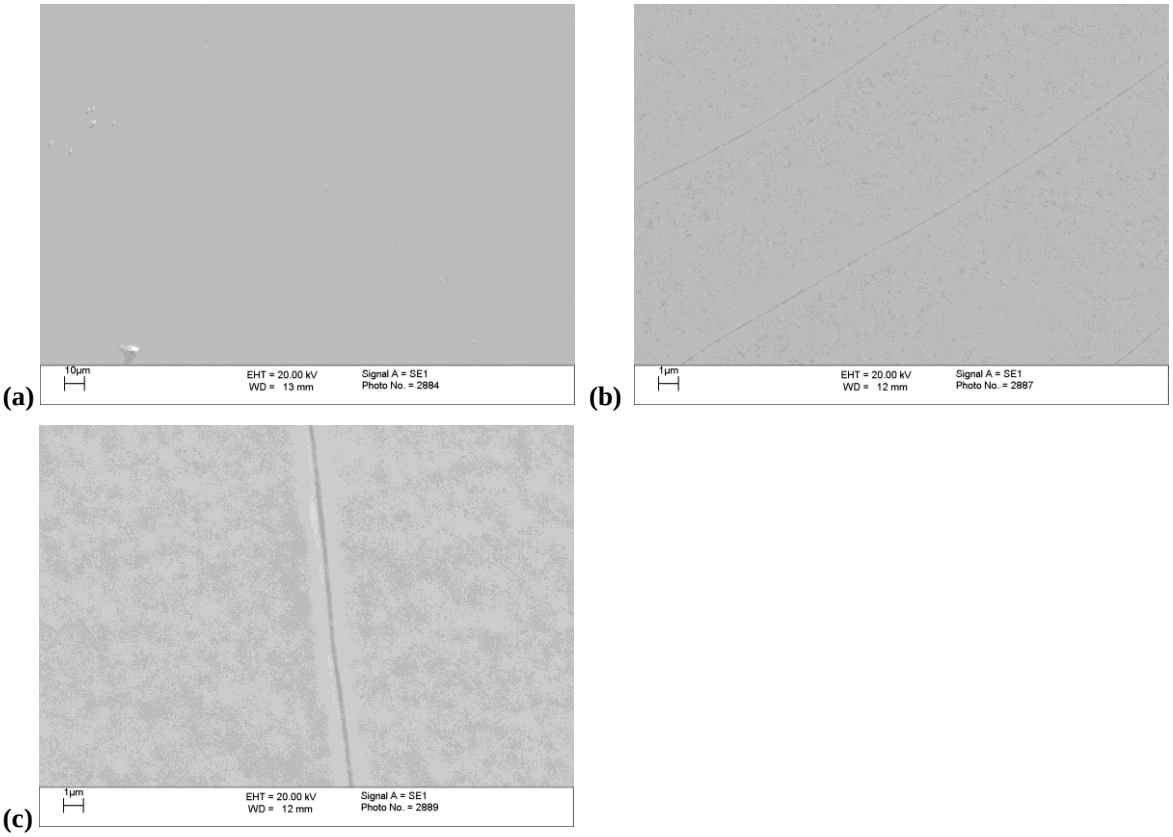

Figure 4.7 FEGSEM low vacuum micrographs of chromate A conversion coatings on acid zinc electrodeposited steel illustrating the effect of increasing immersion time a – 20, b – 40 and c - 80 s.

FEGSEM low vacuum images of a chromate A conversion coating on acid zinc electrodeposited steel without gold sputter preparation are shown in Figure 4.7 a-c. It can be seen that as the conversion coating treatment time increases from 20 to 40 s micro-cracks become visible. The ability of the FEGSEM to resolve the micro-cracks is improved using the InLens mode; see Figure 4.8 a-b. The morphology of the crack lines appear parallel without

intersection. The crack pattern is not characteristic of a ‘cracked river bed’ morphology as observed by other researchers [45,48,88,90,98,99]. As the conversion coating treatment time increases from 40 to 80 s a lower crack density is observed. This is somewhat unexpected. As it would be expected that a greater coating thickness; see Table 4.1, would in theory increase tensile stress and the opportunity for crack formation in the coating; see Section 2.5.2.1 and Figure 2.10.

Bar the appearance of micro-cracks, in general, the surface topography is flat and smooth. This is also supported by the surface roughness values of chromate A treated acid zinc electrodeposited steel being lower than that of the untreated acid zinc electrodeposited steel; Table 4.2. Higher magnification FEGSEM images appear to show some porous structure; Figure 4.8c. Porosity could be characterised by changes in constrast in which dark spots (~>50 nm diameter) appear to be scattered randomly across the surface topography. Figure 4.8c also shows that crack widths were approximately 100 nm.

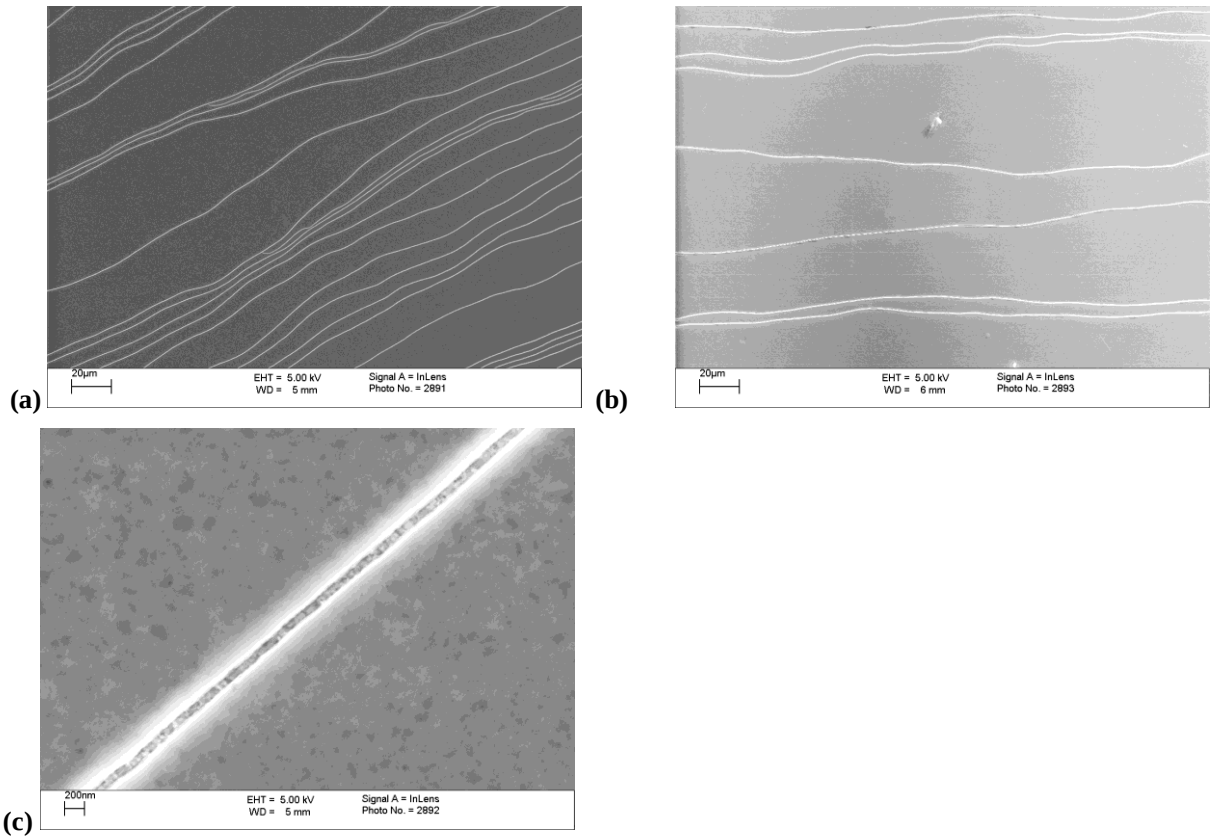

Figure 4.8 FEGSEM InLens mode micrographs of chromate A conversion coatings on acid zinc electrodeposited steel formed at different immersion times a - 40, b - 80 and c – 40 s.

To analyse the effect of sputter coating preparation, chromate A conversion coatings (formed at different immersion times 20, 40 and 80 s) on acid zinc electrodeposited steel samples were gold coated prior to FEGSEM analysis. Under the InLens mode, a chromate A 20 s conversion coating exhibited no micro-cracks as in previous studies; Figure 4.9a. However, chromate A 40 s conversion coating, in instances, and 80 s, in most cases exhibited regions of blistering in addition to micro-cracking; Figures 4.9b, c and d. An Energy Dispersive X-ray spectroscopy (EDX) investigation of a blistered region, as shown in Figure 4.10a, reveals that the blistered film (area B) is that of the conversion coating and the underlying area (area A) is that of the zinc substrate; see spectra in Figures 4.10b and c. It is possible that the vacuum used during gold coating produced the blistering.

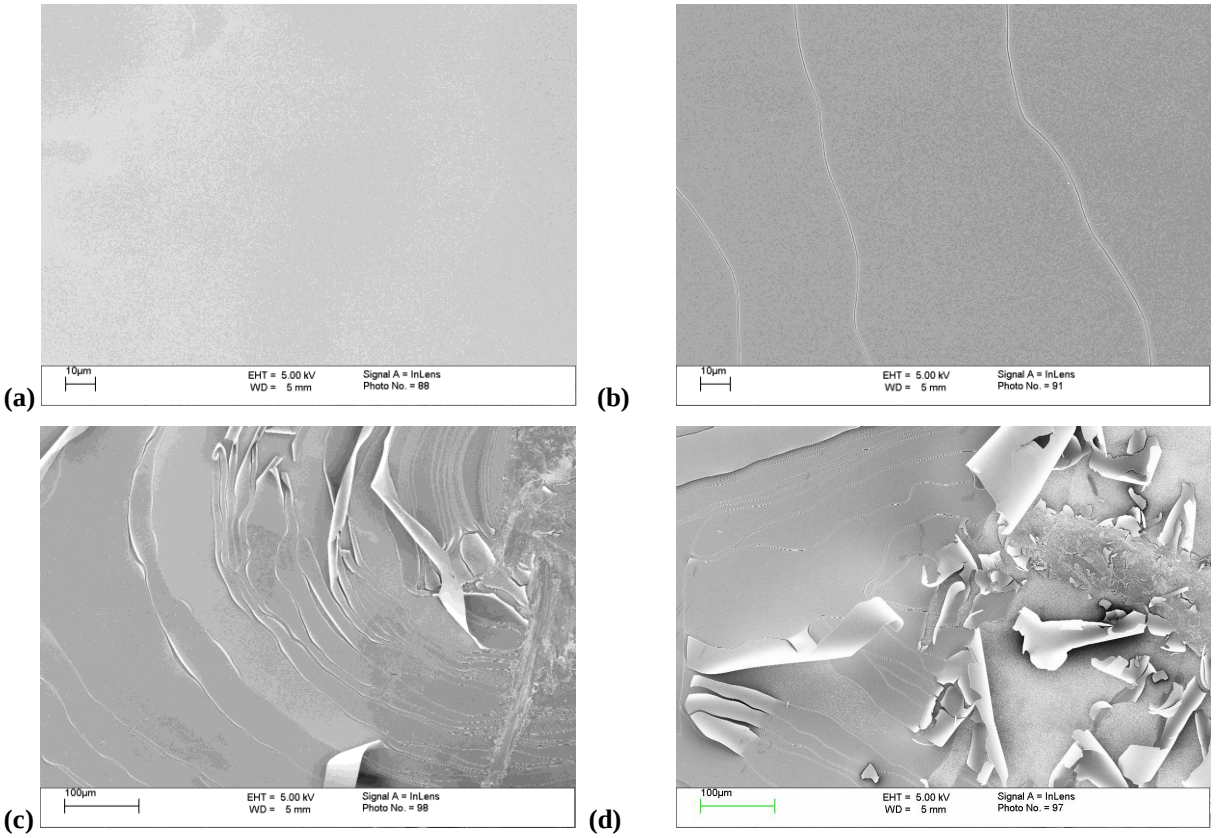

Figure 4.9 FEGSEM micrographs of chromate A conversion coatings on acid zinc electrodeposited steel formed at different immersion times (a – 20, b, c - 40 and d – 80 s). Samples were gold coated.

FEGSEM images of chromate A 20 s conversion coating following cryo fracture preparation; Figures 4.11a, reveal a thin conversion coating well adhered onto the underlying zinc electrodeposit substrate. As the specimens were prepared with a gold coating for conductivity, surface detail of the conversion coating is enhanced in comparison to the top plane images mentioned earlier. The conversion coating surface appears to be composed of spherical-like

particulate structures, tightly bonded and adjoined to one another. Some cracks can be observed within the conversion coating, however, these are most likely to be a function of the freeze fracture method. The average thickness of a chromate A 20 s conversion coating was 122 nm; see Table 4.1.

On increasing immersion times 40 & 80 s and following cryo fracture preparation, the conversion coating in certain regions appeared to delaminate from the zinc substrate; Figure 4.11b-g. Large cracks observed represent fracture of the zinc electrodeposit. For chromate A 80 s conversion coating the micro-cracked morphology appears slightly different to that of 40 s in that the coating crack pieces are larger in width. High magnification images of chromate A 40 & 80 s; Figure 4.11d,g, exhibit a similar spherical-like particulate conversion coating structure as observed for chromate A 20 s conversion coating; Figure 4.11a.

The average thickness of 40 and 80 s chromate A conversion coating was 179 and 310 nm respectively; Table 4.1. The increased coating thickness for 40 and 80 s in comparison to 20 s immersion time could be a major factor for micro-cracking and delamination.

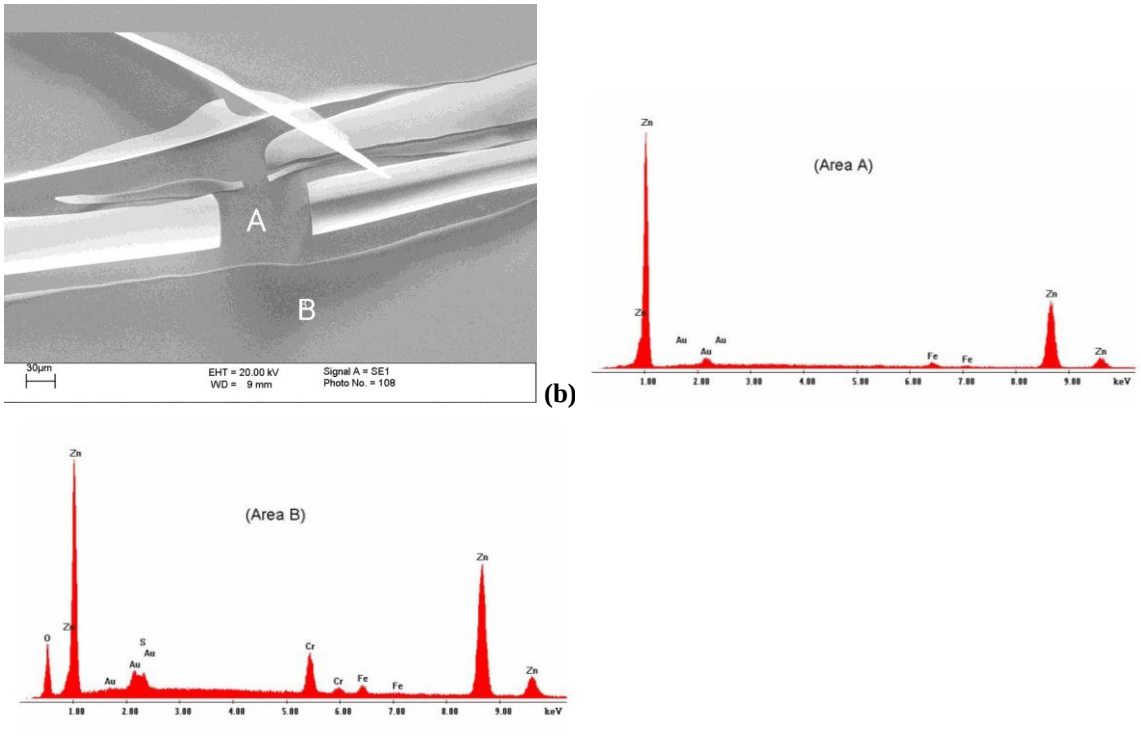

Figure 4.10 FEGSEM micrograph of chromate A conversion coating on acid zinc electrodeposited steel formed at 80 s immersion time (a), along with EDX spectra of corresponding areas A and B (b-c). Sample was gold coated.

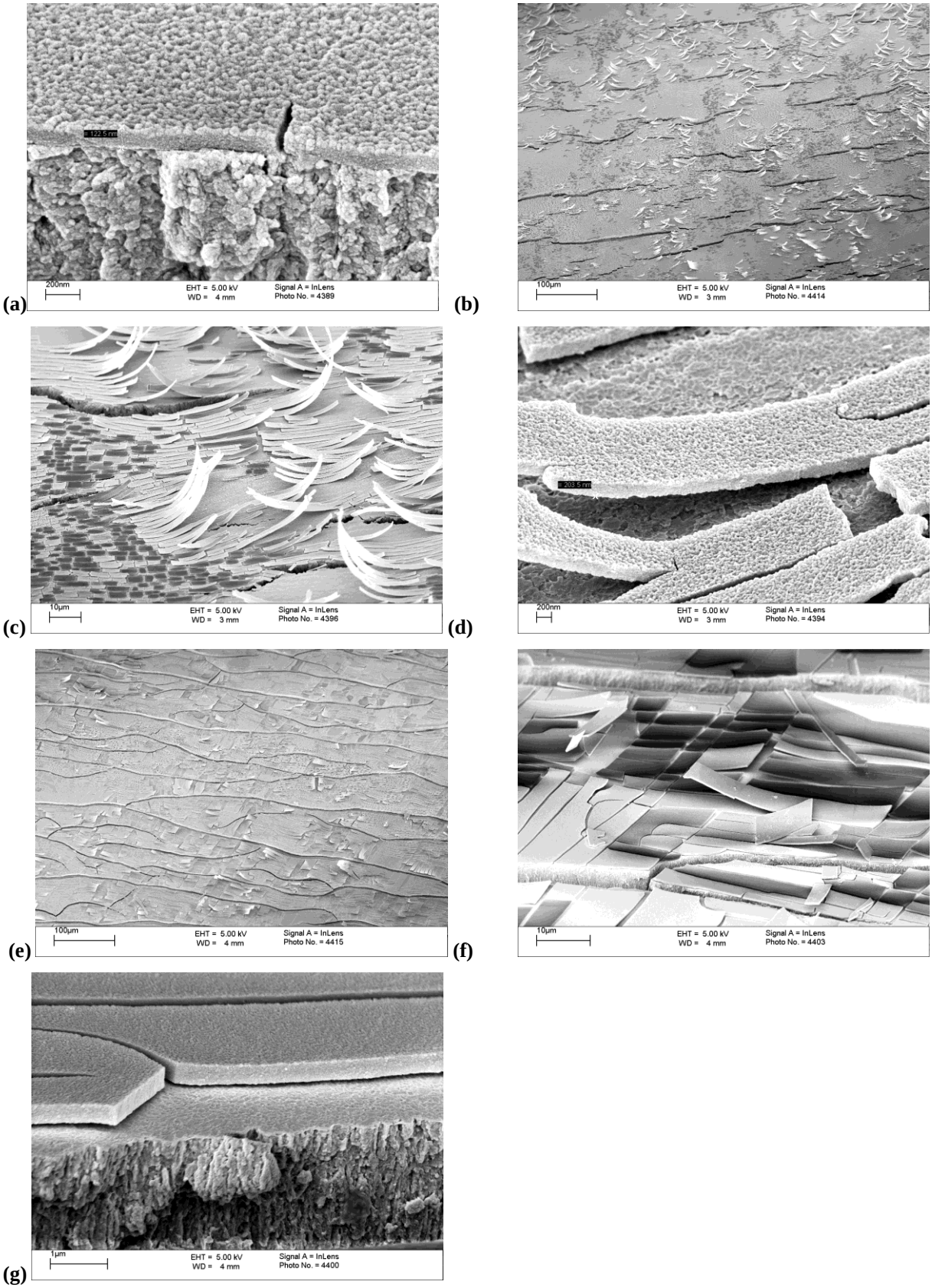

Figure 4.11 FEGSEM micrographs of cryo fractured chromate A conversion coatings on acid zinc electrodeposited steel formed at different immersion times a – 20, b, c, d - 40, and e, f, g – 80 s. Samples were gold coated.

AFM topographical studies on chromate A conversion coatings; Figure 4.12, exhibit no micro-cracking or blistering as observed during FEGSEM studies; Figure 4.8 and 4.9. AFM analysis does not expose the conversion coating samples to a vacuum or electron beam as in the case of SEM analysis and therefore reduces the opportunity for water to be lost from the conversion coating and subsequent micro-cracks to form; see Sections 5.2. As in the case of FEGSEM studies; see Figure 4.11, the conversion coating surface does appear to resemble a fused spherical-like particulate structure. One might also refer to such a surface morphology as nodular.

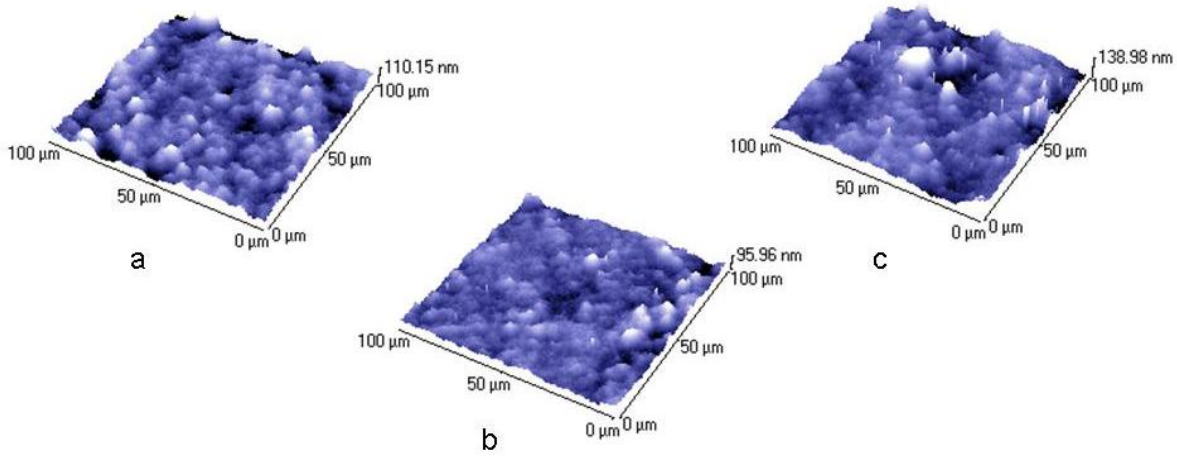

Figure 4.12 AFM micrographs of chromate A conversion coatings on acid zinc electrodeposited steel illustrating the effect of increasing immersion time a-20, b-40, c-80 s.

4.1.1.5 Chromate A conversion coating on alkaline zinc electrodeposited steel

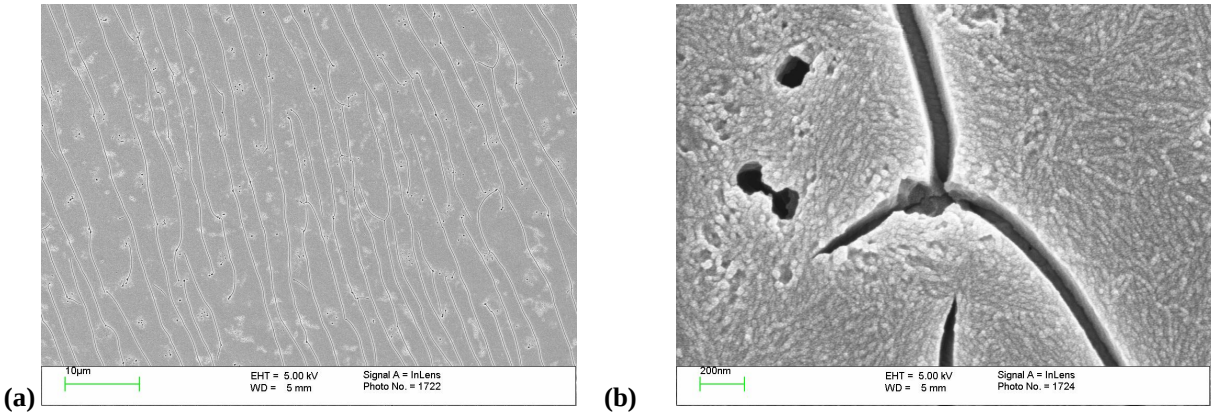

Figure 4.13 FEGSEM micrographs of chromate A 20 s conversion coating on alkaline zinc electrodeposited steel taken at increased magnification (a-b). Samples were gold coated.

Chromate A conversion coatings were also applied onto alkaline zinc electrodeposited substrates. FEGSEM images of chromate A 20 and 40 s conversion coatings following gold sputter coating are shown in Figures 4.13 and 4.14. In both cases micro-cracking is observed. Again like that of chromate A conversion coating applied to acid zinc electrodeposits, micro-cracks generally run parallel to one another. In the case of chromate A 20 s conversion coating, cracks appear to initiate and end from pores within the coating. However, for chromate A 40 s conversion coatings these sparsely populated pores act as intersecting crack junctions. The pores evident in these coatings act as defects and hence stress concentrators for crack formation. It is interesting to note that no micro-cracks were observed for chromate A 20 s conversion coatings on acid zinc electrodeposited steel; Figure 4.9a. In this case the critical coating thickness for micro-cracking to occur may have been reached.

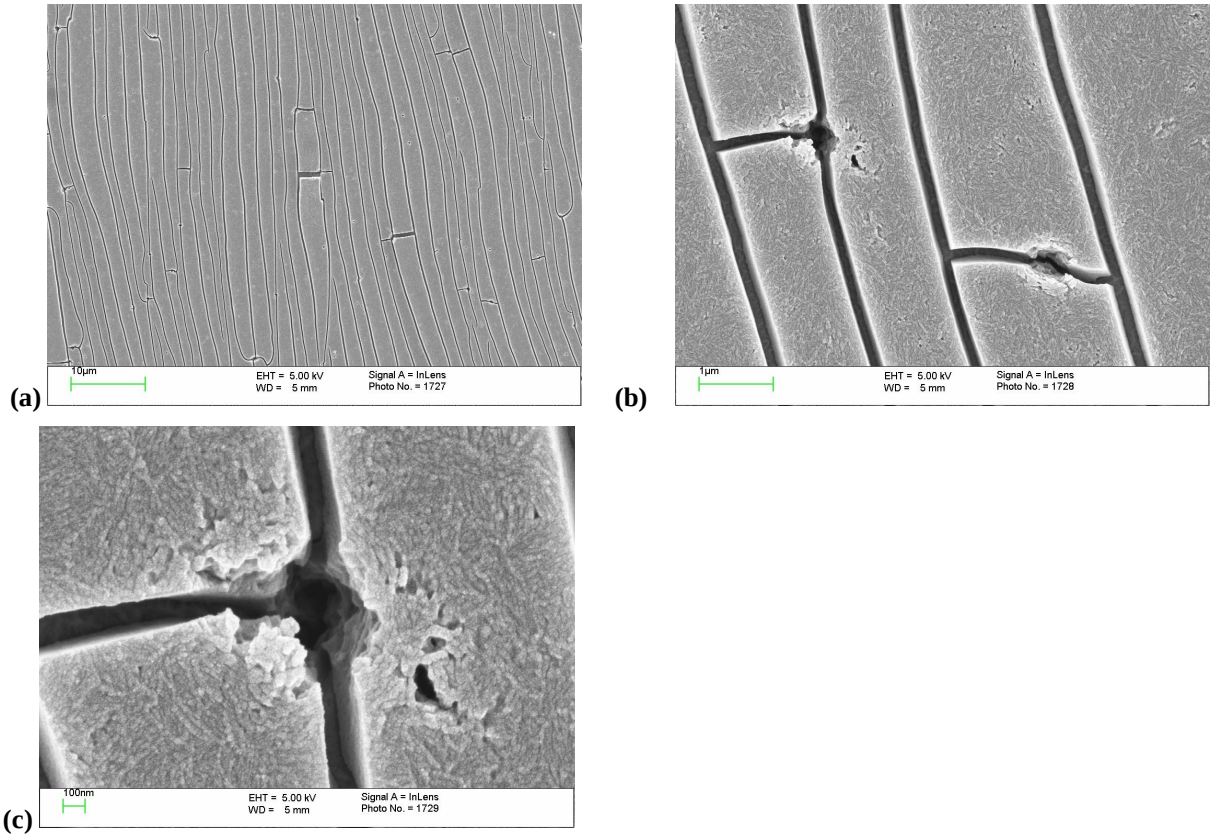

Figure 4.14 FEGSEM micrographs of chromate A 40 s conversion coating on alkaline zinc electrodeposited steel taken at increased magnification (a-c). Samples were gold coated.

4.1.1.6 Chromate B conversion coating on zinc electrodeposited steel

In order to investigate the effect of hexavalent chromium chemistry on surface morphology a different formulated treatment bath was used, chromate B. Chromate B conversion coating was applied onto both acid and alkaline zinc electrodeposit substrates and characterised using FEGSEM following gold sputter coating preparation; Figure 4.15 and 4.16. As in the case of

chromate A conversion coating on acid zinc electrodeposits, increased immersion time resulted in blistering. Also, as with chromate A conversion coatings it is clear to see that micro-cracks appear to propagate mainly in one direction. The crack pattern could have been influenced by the underlying surface morphology. Further discussions on this can be found in Section 5.2.2. Micro-cracking is prominent at 10 s immersion time and thus possibly beyond the critical coating thickness for micro-cracking to occur. The surface morphology for chromate B conversion coatings on alkaline zinc electro-deposits, in general, is similar to that applied onto acid zinc electrodeposits, with the exception that no blistering is observed for 30 s immersion. In contrast to FEGSEM studies, AFM surface morphology images exhibit no major signs of micro-cracks or blistering; Figure 4.17a-c. There are some indications of uneven topography across all immersion times, represented by peak and tough structures in the z-axis. However, again like that of chromate A conversion coatings applied onto acid zinc electrodeposited steel, the surface roughness for chromate B conversion coatings on alkaline zinc in general is less; Table 4.2.

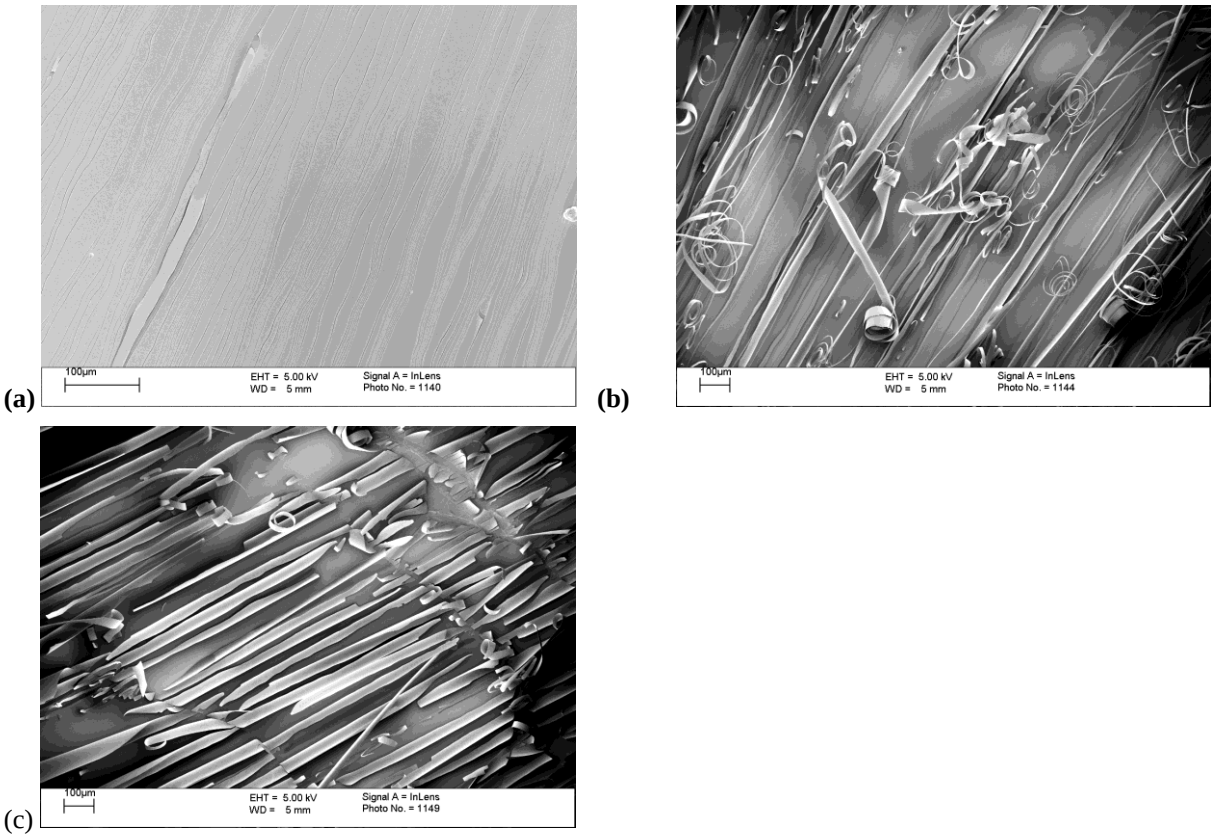

Figure 4.15 FEGSEM InLens mode micrographs of chromate B conversion coatings on acid zinc electrodeposited steel illustrating the effect of increasing immersion time a – 10, b – 30 and c – 60 s. Samples were gold coated.

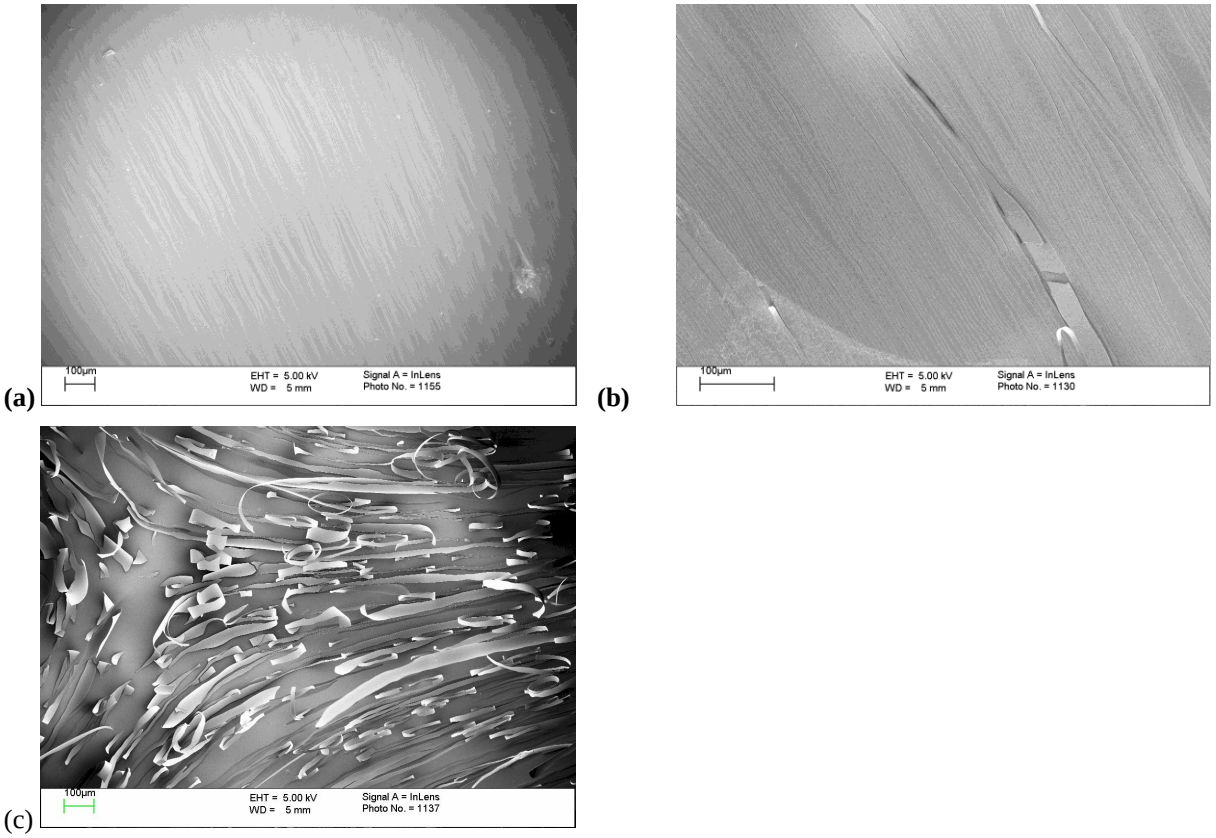

Figure 4.16 FEGSEM InLens mode micrographs of chromate B conversion coatings on alkaline zinc electrodeposited steel illustrating the effect of increasing immersion time a – 10, b – 30 and c – 60 s. Samples were gold coated.

To observe whether or not micro-cracking is influenced by operating conditions of the SEM e.g. thermal induction via the electron beam. Chromate B conversion coating on alkaline zinc electrodeposit specimens were imaged on a cold stage at -180°C. The surface morphology did not exhibit micro-cracking or blistering on increasing immersion time; Figure 4.18a-c. The micrographs show no real details apart from dust particles. Upon stage stabilisation to room temperature (21°C) the surface morphology had changed, with micro-cracking and blistering present with increasing immersion time; Figure 4.19a-c. These images are similar to FEGSEM images mentioned earlier; Figure 4.15 and 4.16. These results indicate that the SEM operating conditions influence chromate B conversion coating micro-cracking; see Section 5.2.1.

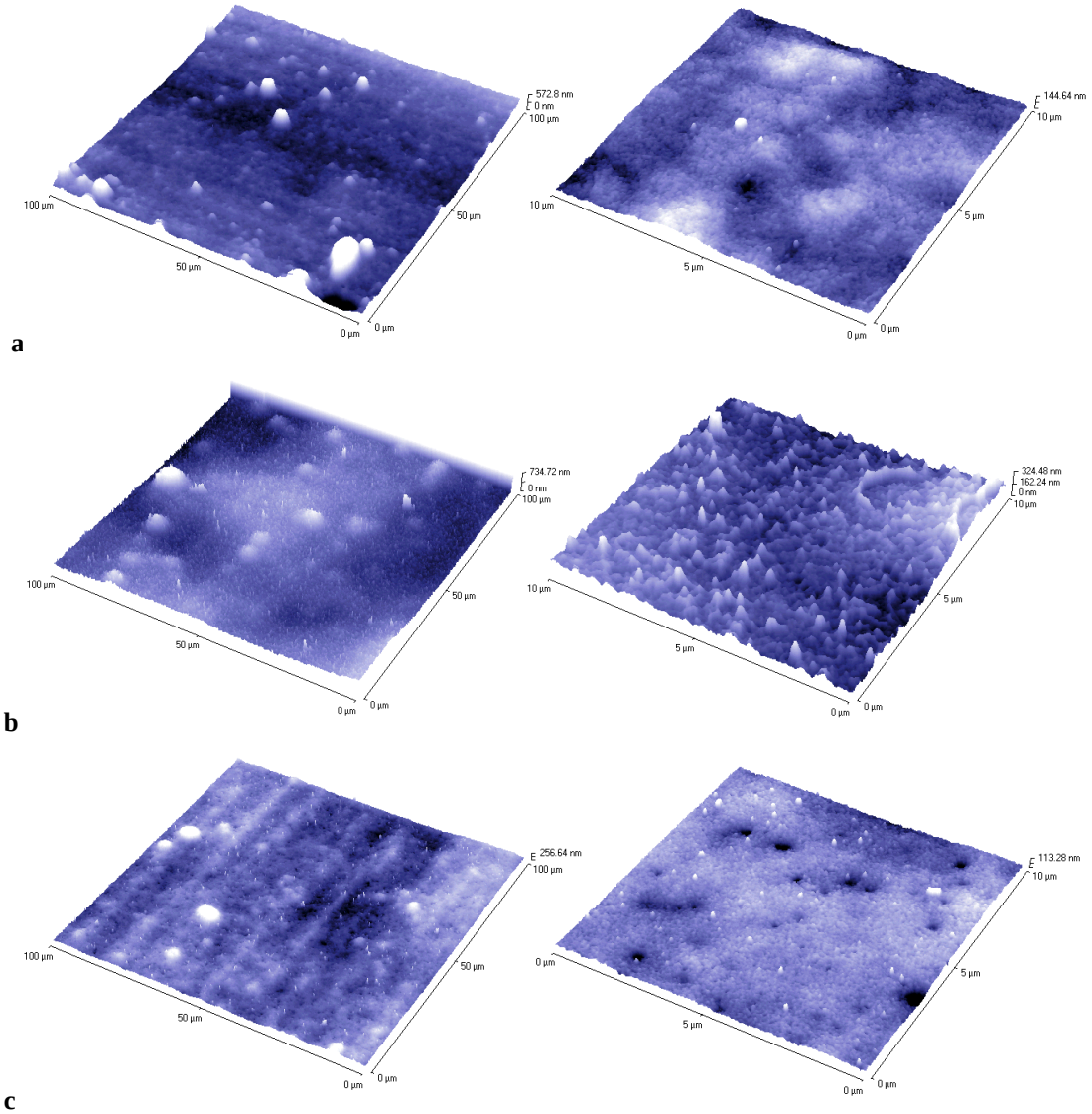

Figure 4.17 AFM micrographs of chromate B conversion coatings on alkaline zinc electrodeposited steel illustrating the effect of increasing immersion time a – 10, b – 30 and c – 60 s.

(a)

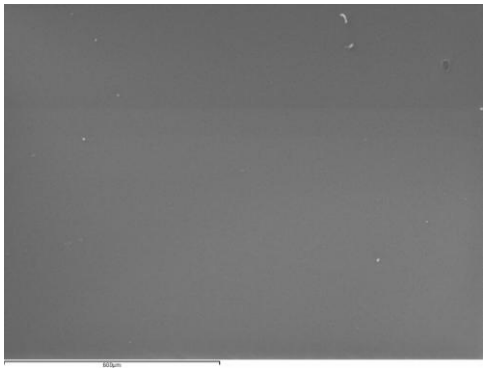

(b)

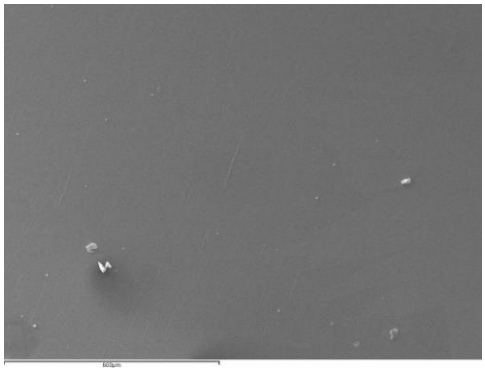

(c)

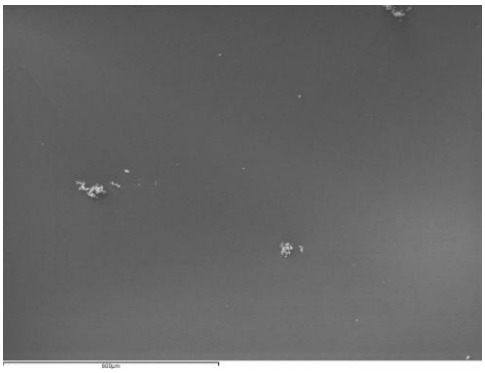

Figure 4.18 SEM micrographs imaged at a stage temperature of -180°C showing chromate B conversion coatings on alkaline zinc electrodeposited steel formed at a-10, b-30 and c-60 s immersion times. Samples were gold coated.

(a)

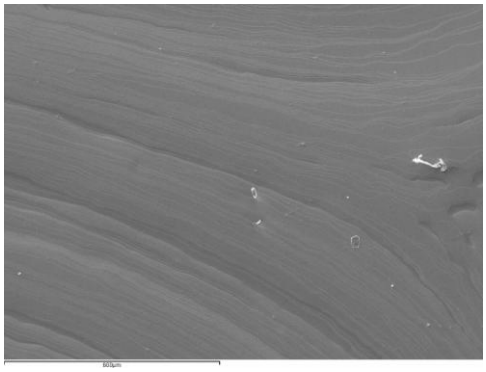

(b)

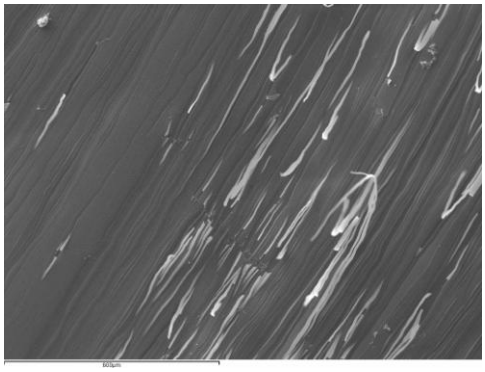

(c)

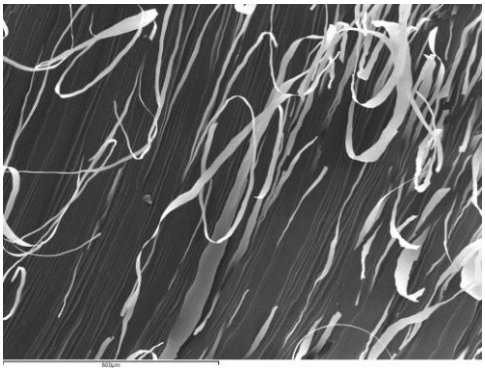

Figure 4.19 SEM micrographs imaged at a stage temperature of 21°C showing chromate B conversion coatings on alkaline zinc electrodeposited steel formed at a-10, b-30 and c-60 s immersion times. Samples were gold coated.

4.1.1.7 Chromate B conversion coating on zinc foil

Figure 4.20a-c, illustrates FEGSEM images of chromate B 30 s conversion coatings on zinc foil substrate following gold sputter coating. The surface morphology is that of a characteristic cracked river bed morphology as observed by other researchers [45,48,88,90,98,99]. The high density crack pattern may be proliferated as a result of the underlying zinc foil surface defects as illustrated in Figures 4.5 and 4.6.

AFM surface morphology images exhibit a rough topography for all immersion times of chromate B conversion coatings on zinc foil; Figure 4.21a-c. As well as peak and tough structures exhibited in the z-axis of images, deep cracks can also be seen for high magnification images, possibly representative of defects observed with FEGSEM studies. Consequently, it is not surprising that surface roughness measurements for zinc foil and chromated specimens on zinc foil are similar in R_a value; Table 4.2.

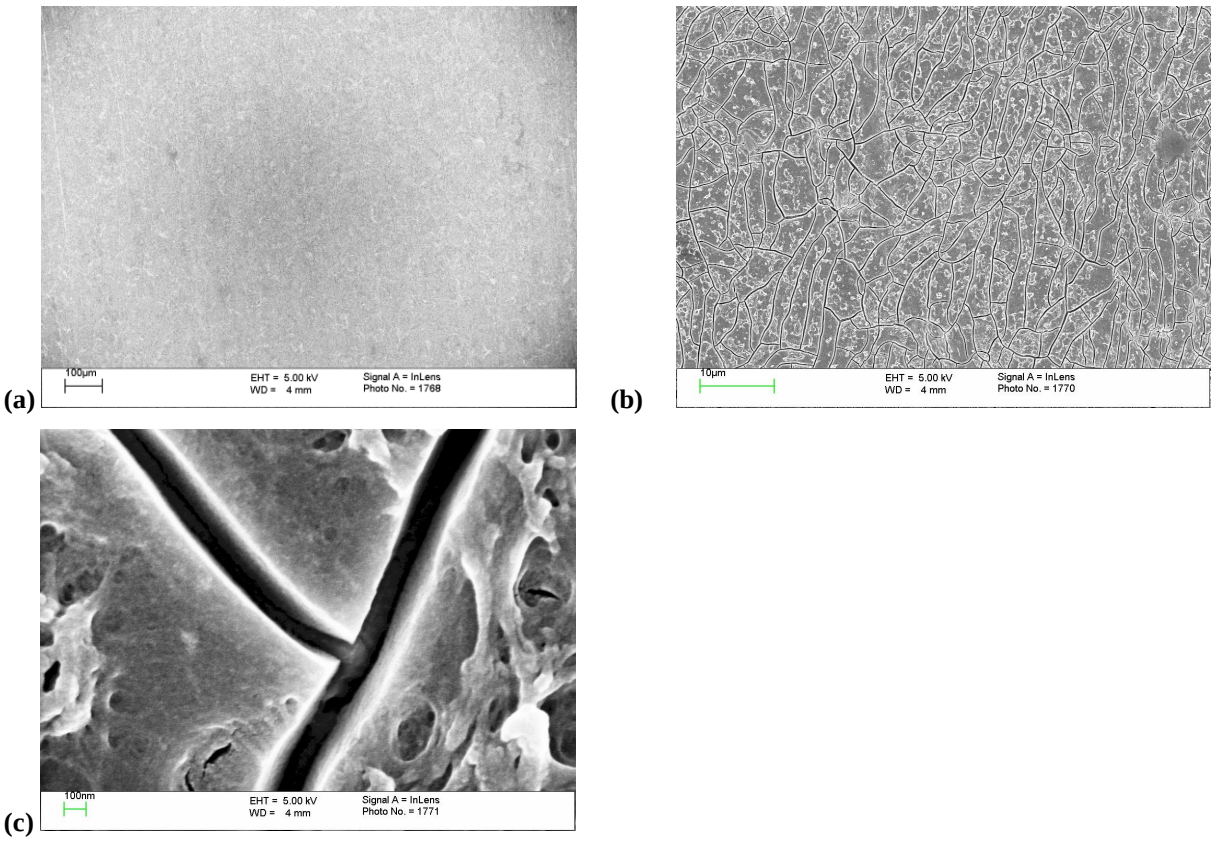

Figure 4.20 FEGSEM InLens micrographs of chromate B 30 s conversion coating on zinc foil taken at increased magnification (a-c). Samples were gold coated.

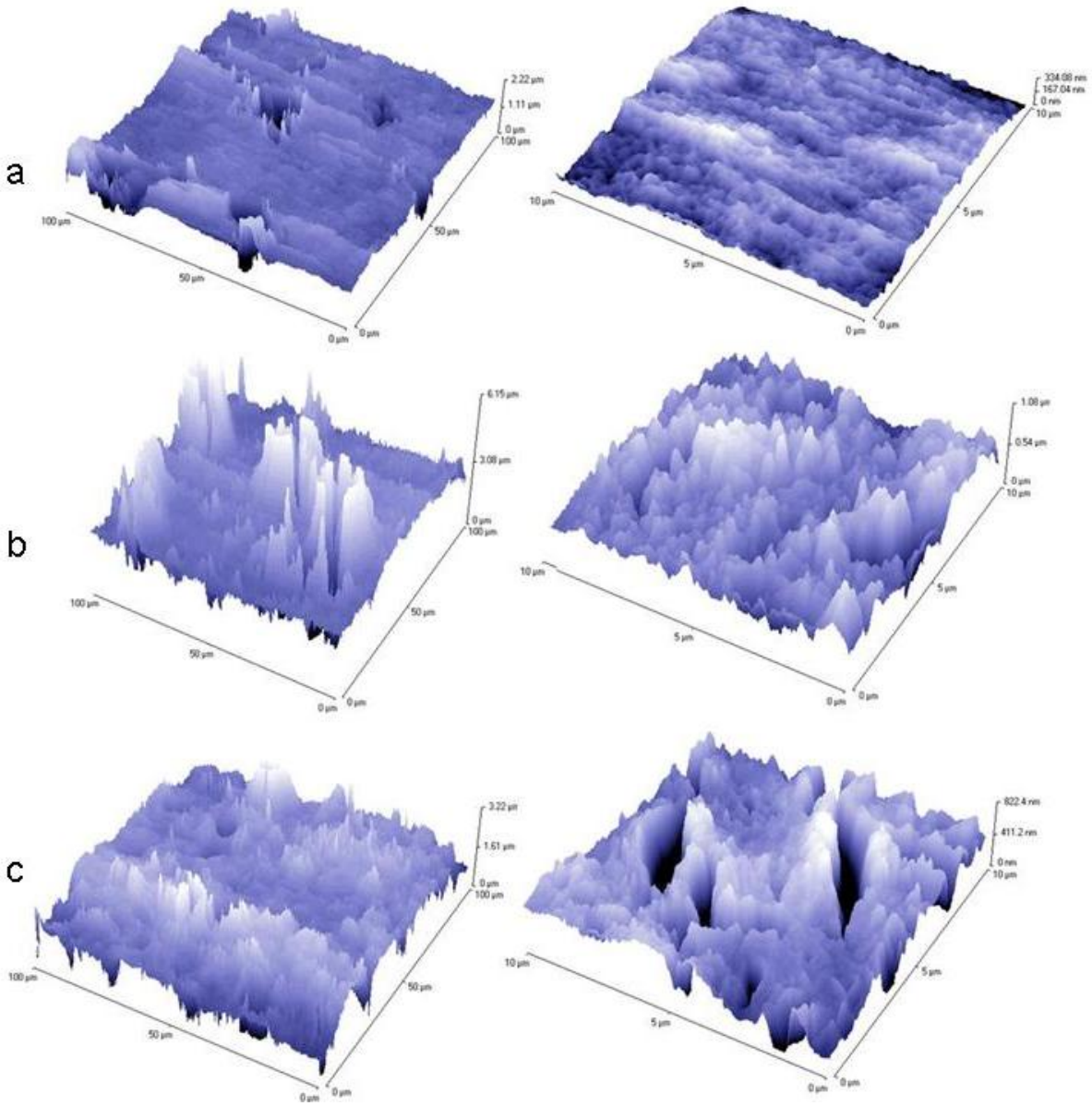

Figure 4.21 AFM micrographs of chromate B conversion coating formed on zinc foil illustrating the effect of increasing immersion time 10 (a), 30 (b) and 60 s (c) taken at increased magnification.

4.1.1.8 Trivalent CCC (Tripass LT1500) on acid zinc electrodeposited steel

FEGSEM micrographs of trivalent CCC on acid zinc electrodeposits exhibit a flat and smooth surface topography for all immersion times (45, 90 and 180 s); Figure 4.22 a,c,e. The morphology is absent of any micro-cracks or any of the other physical defects observed for hexavalent CCCs. At higher magnification the surface appears to be composed of overlapping particulate structures; Figure 4.22 b, d, f, similar to that observed for hexavalent CCC.

In general, cryo fracture prepared trivalent CCCs show only cracking of the zinc electrodeposit; Figure 4.23. No micro-cracking or blistering is evident for trivalent CCCs

prepared at 45 and 90 s immersion times. Trivalent CCCs prepared at 180 s do show additional micro-cracking and blistering of the conversion coating in localised areas, but these are not as widespread as those observed for hexavalent CCC 40 and 80 s. It is important to also note that no micro-cracks were observed for top plane images of trivalent CCC 180 s and therefore all micro-cracks were a function of the cryo fracture specimen preparation process.

High magnification images of the conversion coating cross-sections appear to be similar to the particulate structure observed for hexavalent CCCs. The underlying zinc morphology is also similar to that underlying the hexavalent CCC. The average conversion coating thickness for trivalent CCCs was found to increase on increasing immersion time; Table 4.1.

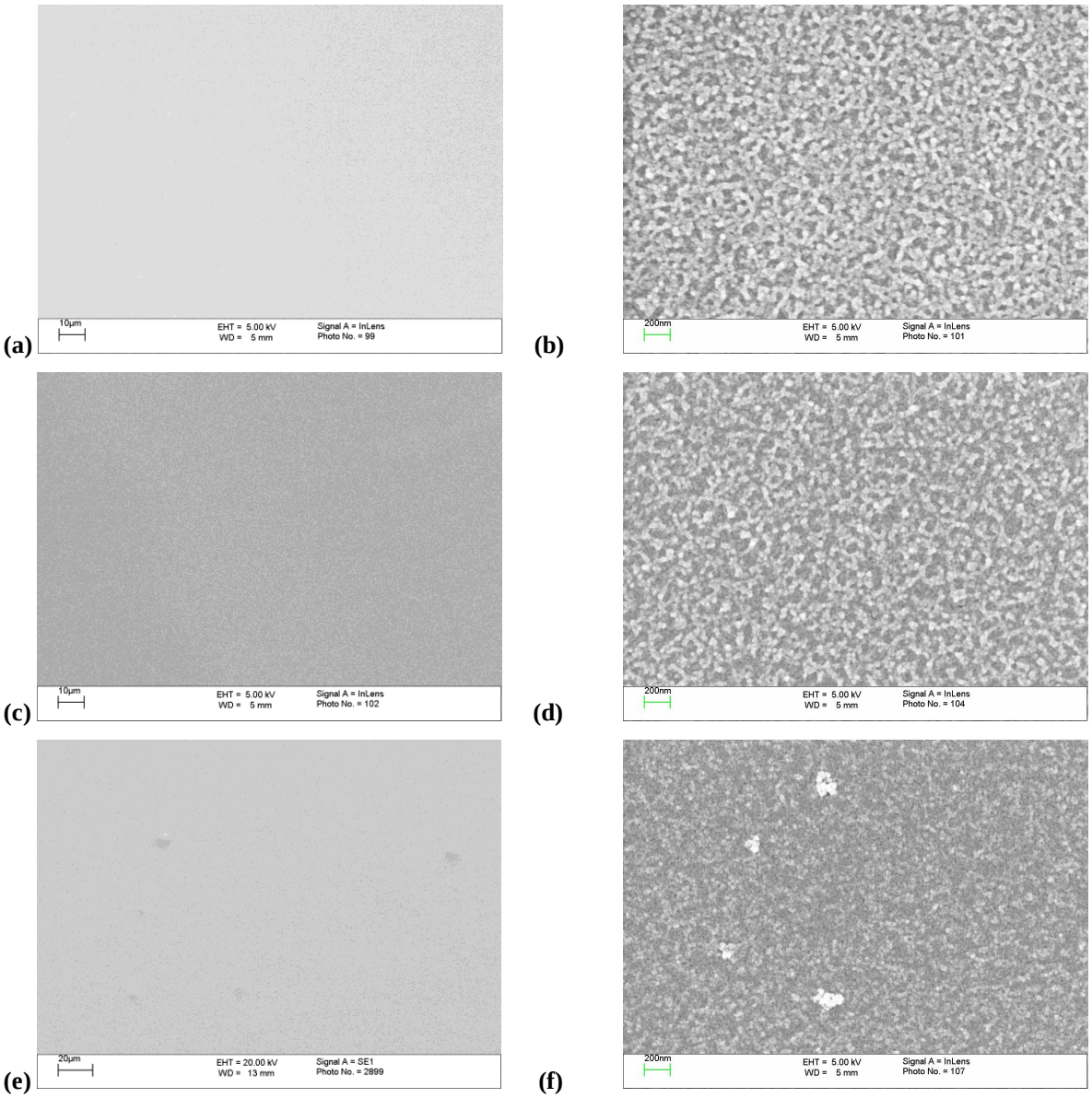

Figure 4.22 FEGSEM micrographs of trivalent CCCs on acid zinc electrodeposited steel illustrating the effect of increasing immersion time 45 (a-b), 90 (c-d) and 180 s (e-f). Samples were gold coated.

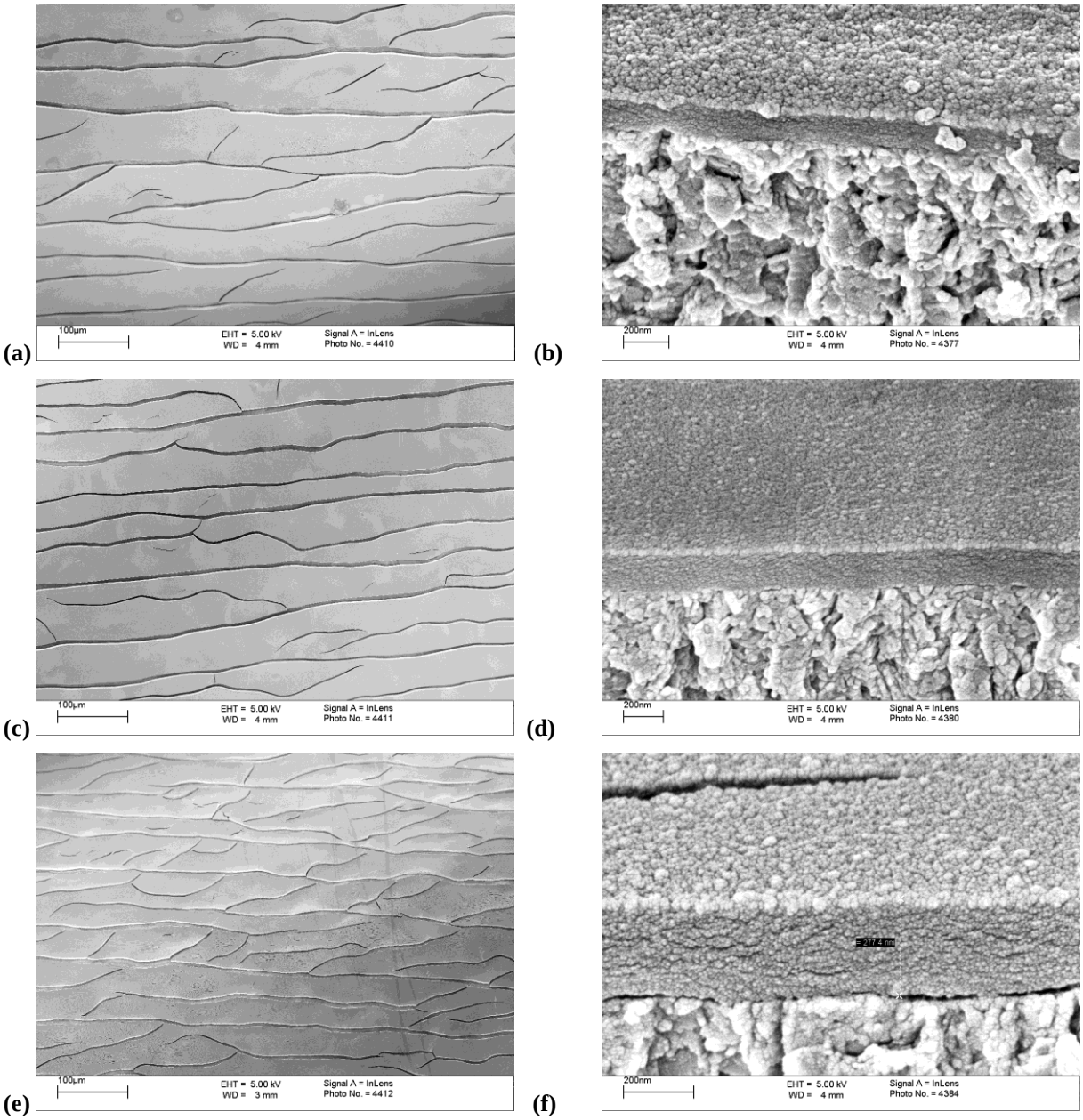

Figure 4.23 FEGSEM InLens micrographs of cryo fracture trivalent CCC on acid zinc electrodeposited steel illustrating effect of immersion time 45 (a-b), 90 (c-d) and 180 s (e-f). Samples were gold coated.

AFM topographical micrographs of trivalent CCCs; Figure 4.24, exhibit no micro-cracking or blistering and exhibit a fused particulate surface structure for all immersion times complementing FEGSEM studies. Note that the crack observed for Trivalent CCC 180 s was a result of AFM specimen preparation.

Surface roughness values for all trivalent CCC treatment times on acid zinc electrodeposited steel resulted in a reduction in R_a value compared to an untreated acid zinc electrodeposited steel substrate; Table 4.2.

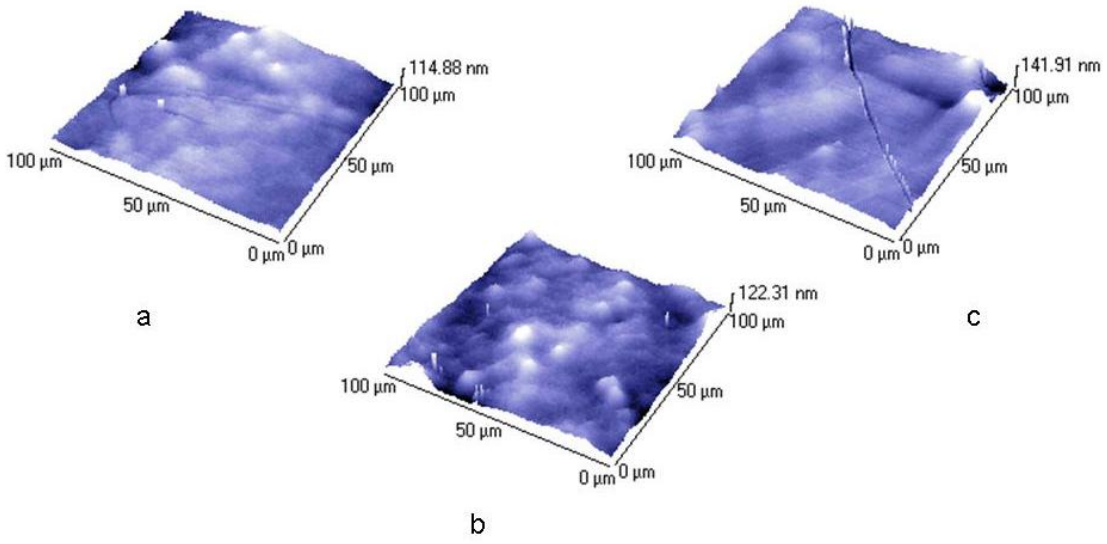

Figure 4.24 AFM micrographs of trivalent CCC on acid zinc electrodeposited steel illustrating the effect of immersion time (a) 45, (b) 90 and (c) 180 s.

4.1.2 Effect of heat treatment exposure

4.1.2.1 Acid / alkaline zinc electrodeposited steel

The effect of elevated temperatures upon the surface morphology of acid and alkaline zinc electrodeposits were investigated using FEGSEM and FIB-SEM. The exposure conditions were normal atmosphere in a circulating oven at 150°C for 1 h followed by cooling to room temperature (21°C). FEGSEM analysis of acid zinc electrodeposit specimens exposed to 150°C for 1 h displays a surface covered with random nodular shaped eruptions, characteristic of zinc whiskers [140-143] approximately 2-8 µm in lateral size; Figure 4.25a-b. As part of the eruption, filament type growth (mm) may also occur over time. Zinc whiskers were not evident for non-heat treated samples; Figure 4.1. Proposed mechanisms for whisker formation are outlined in Section 5.3.1.

As well as FEGSEM studies, EDX spectroscopy was also carried out on and around a typical zinc whisker to identify whether there were any significant differences in elemental composition. In both cases Zn and Fe were identified at similar levels; Table 4.3.

Table 4.3 EDX at. % composition at and around a zinc whisker.

Element	Zinc (general area) at. %	Zinc (whisker) at. %
Fe	2.7	2.2
Zn	97.4	97.8

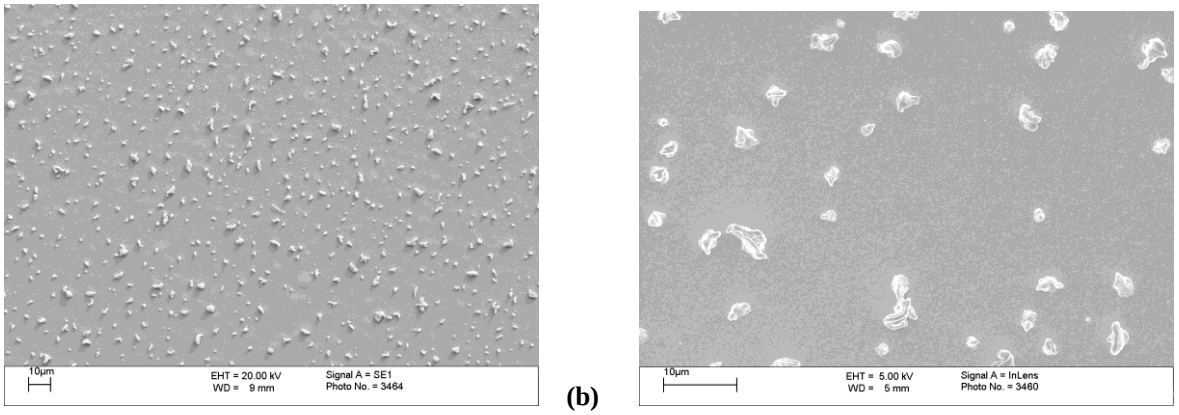

Figure 4.25 FEGSEM micrographs of acid zinc electrodeposited steel surface following exposure at 150°C for 1 h in a circulating oven, taken at low (a) and high (b) magnifications.

FIBSEM is a method by which grain structure could be established in and around the whisker and its root through microscopic sectional examination. The identification of grain patterns could help to identify the cause of whisker formation.

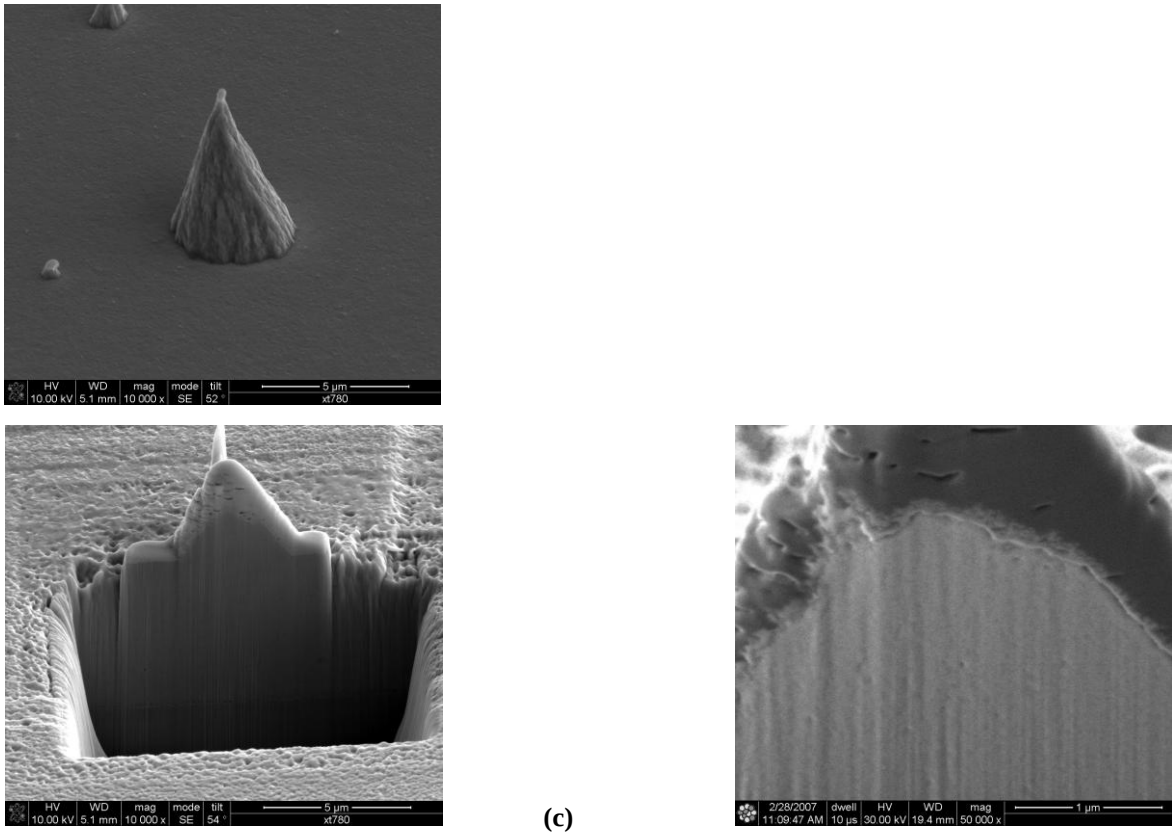

Figure 4.26 (a) FIB secondary electron micrograph of a zinc cone on an acid zinc electrodeposited steel surface following exposure at 150°C for 1 h. (b & c) low and high magnification FIB electron micrographs of a zinc cone & electrodeposit cross-section.

Figure 4.26a, illustrates an acid zinc electrodeposit zinc whisker. Its morphology is of a conical shape. Figure 4.27a, illustrates an alkaline zinc electrodeposit zinc whisker. In constrast, its morphology is spherical in shape. In both cases the features could well be regarded as the early stage of growth for a filamentous or random nodular shaped zinc whisker. Figure 4.26b-c and 4.27b-c provide cross-sectional images of the whiskers following FIB milling and cleaning. It is difficult to establish clear, definitive, grain patterns within the whisker or electrodeposit. Columnar structures may be present in both cases; Figure 4.26c and 4.27c, however, given what appears to be vertical lines this could well be an artefact of the milling and cleaning process created during sectioning. Reynolds et al. [61], also found it difficult to observe grain patterns using FIBSEM and TEM with whiskers growing from zinc electroplated specimens. The specimens used in their study were taken from a data centre floor tile thought to be ~ 15 to 20 years old. No additional information regarding the history of the tile was provided.

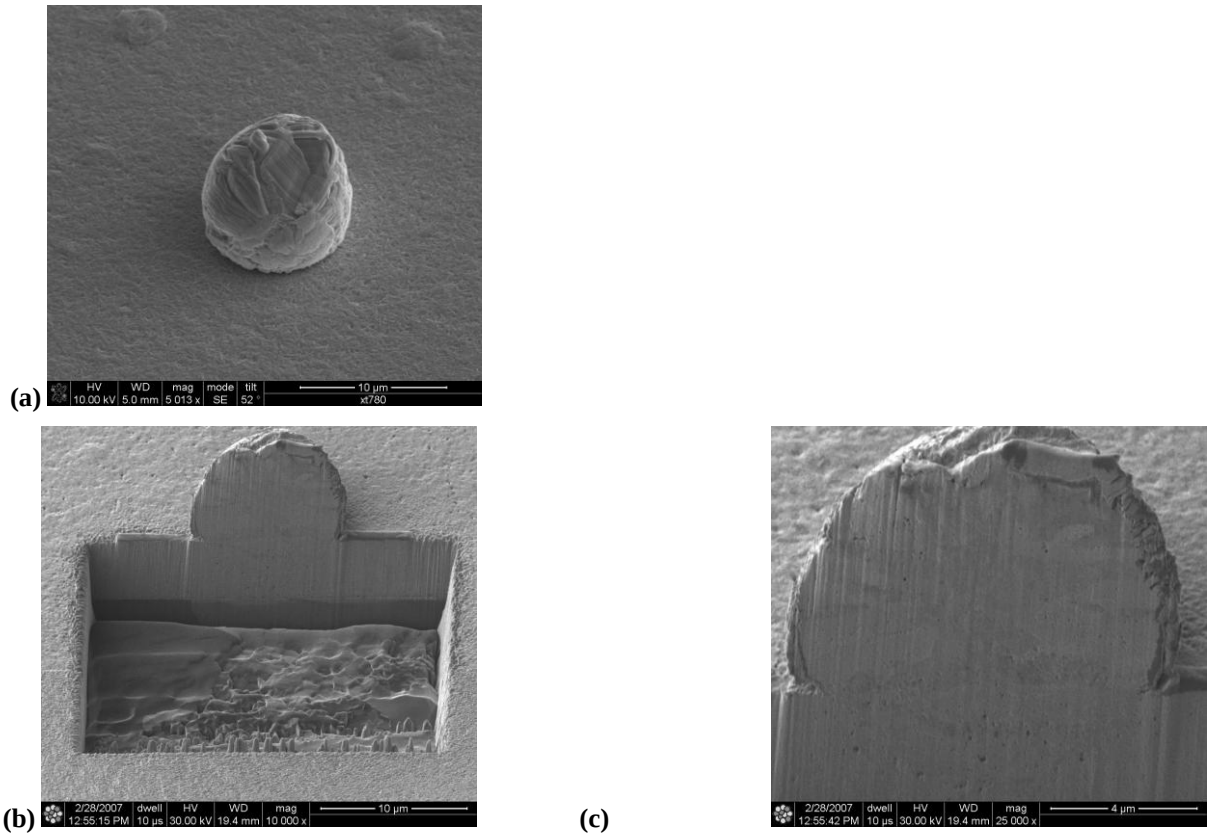

Figure 4.27 (a) FIB secondary electron micrograph of a zinc sphere on an alkaline zinc electrodeposited steel surface following exposure at 150°C for 1 h. (b & c) low and high magnification FIB electron micrographs of a zinc sphere & electrodeposit cross-section.

4.1.2.2 Hexavalent and trivalent CCCs on acid zinc electrodeposited steel

Low magnification FEGSEM micrographs; Figures 4.28 a & c, of chromate A 40 s conversion coating on acid zinc electrodeposited steel following heat treatment also exhibit a micro-cracked surface morphology comparable to those of non-heat treated specimens; Figure 4.8. However, within the surface micro-cracks, zinc whiskers are displayed showing similar characteristics to that seen for heat treated uncoated zinc electrodeposits. Higher magnification images; Figure 4.28 b & d, show that the zinc whiskers appear to protrude from cracks, from which point their growth seems both lateral and perpendicular. It is important to note that hexavalent CCCs are reported to be under tensile stress [98,99] and therefore the presence of underlying zinc whiskers could result in further localised stressing and perhaps the growth of cracks essentially perpendicular (often in a 'cross') to the original crack format as illustrated in Figures 4.28a & c. It is interesting to speculate as to whether zinc whiskers have formed in pre-existing passive coating crack sites as a result of exposure to 150°C for 1 h or whether the widespread cracking was enhanced as a result of the whisker growth.

Low and high magnification FEGSEM images; Figure 4.28e-f, of trivalent CCC 90 s exhibit a similar surface morphology to that of an non-heat treated specimen; Figure 4.22. There are no surface micro-cracks or protruding zinc whiskers in contrast to hexavalent CCC. The conversion coating is clearly well adhered to the zinc substrate and resists the potential of protruding whiskers during exposure to 150°C for 1 h. An increased exposure time (24 h) in which zinc whiskers have been observed to protrude out of the trivalent CCC is discussed in Section 5.3.2.

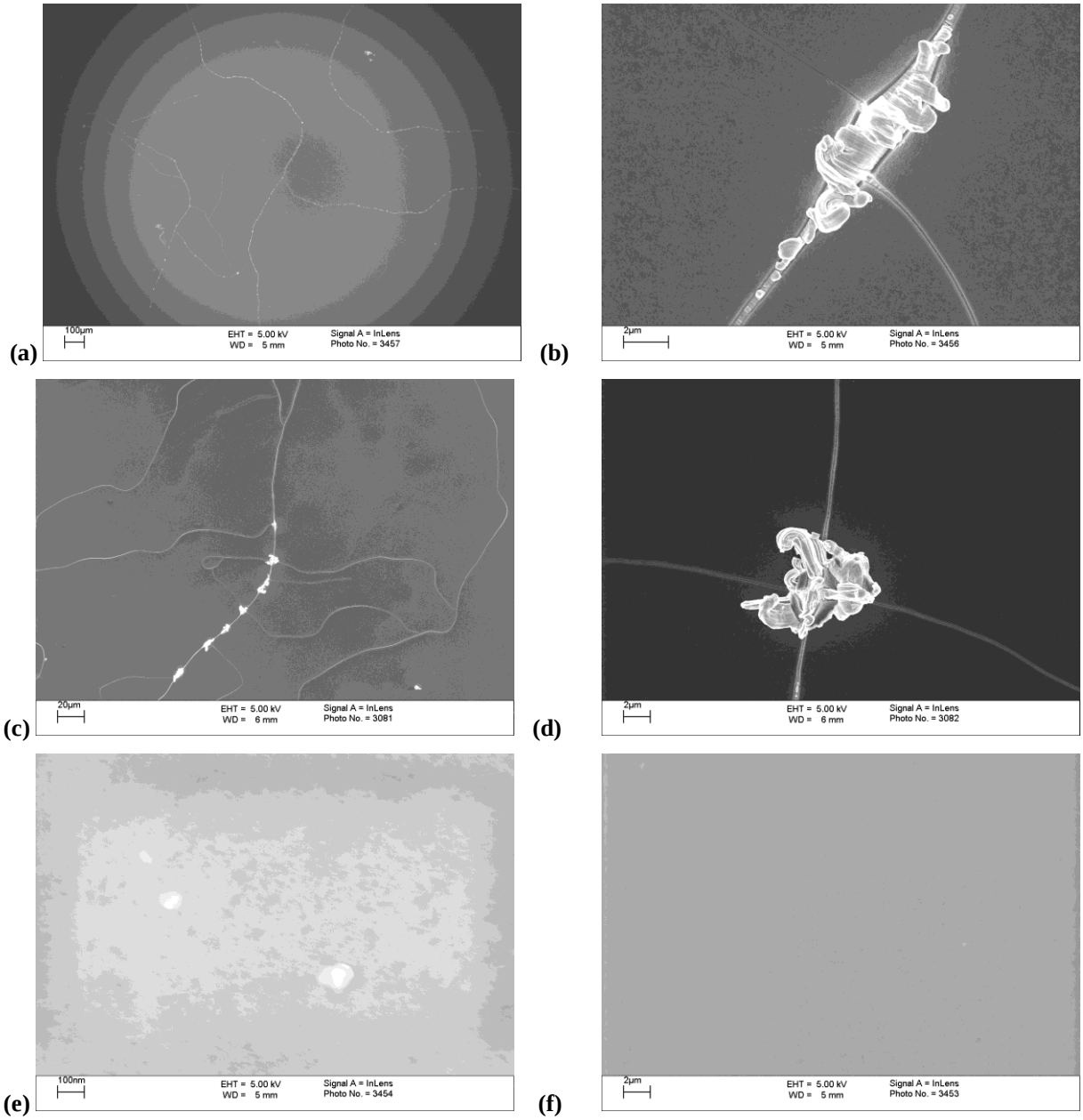

Figure 4.28 FEGSEM micrographs of chromate A 40 s conversion coating and trivalent 90 s CCC on acid zinc electrodeposited steel following exposure at 150°C for 1 h in a circulating oven. Low (a & c) and high (b and d) magnification micrographs of chromate A conversion coating surfaces. Low (e) and high (f) magnification micrographs of trivalent CCC surfaces.

4.1.3 Effect of 5% NaCl solution exposure

4.1.3.1 Acid zinc electrodeposited steel

To observe the effect of a corrosive environment on the surface morphology of an acid zinc electrodeposited steel, specimens were exposed to 5% NaCl solution for 18 h before FEGSEM analysis. A low magnification SEM image; Figure 4.29a, appears to show a surface topography which is clearly different in comparison to that of an untreated acid zinc

electrodeposited specimen; see Figure 4.1. It appears that some regions are of a darker tone than others, possibly indicating an advanced level of corrosion. Higher magnification images of the white regions; Figures 4.29b-c, appear to show a large ‘nettle-like’ structure possibly indicating initial corrosion products. High magnification images of the dark regions; Figures 4.29d-e, shows a mixture of ‘nettle’ and ‘bead-like’ structure which could indicate a more advanced level of corrosion. The dark regions could be indicative of more anodically active regions.

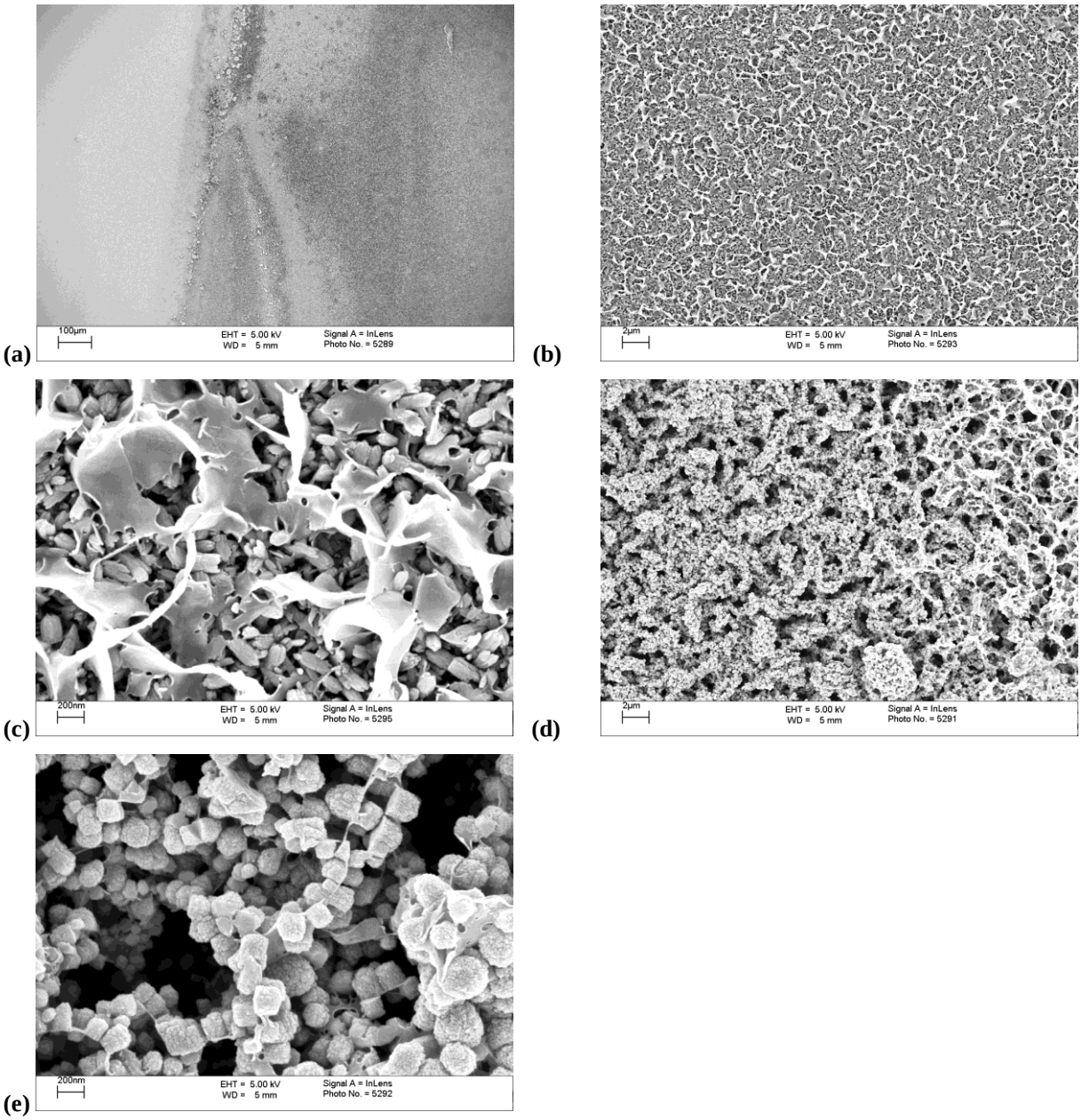

Figure 4.29 FEGSEM micrographs of acid zinc electrodeposited steel following exposure to 5% NaCl solution for 18 h. Low magnification image (a), high magnification images of white region (b-c) and dark region (d-e).

EDX data from the white and dark regions; Table 4.4, clearly shows that the content of oxygen and chlorine is significantly higher for the dark region, whilst that of zinc content is lower following normalisation of the data to 100%. The presence of oxygen and chlorine could possibly indicate zinc dissolution, which is a fundamental mechanism for corrosion. Consequently, secondary corrosion products may be formed such as $ZnCl_2$, ZnO or $Zn(OH)_2$. It is important to note that some corrosion products formed may have entered into the NaCl solution or been lost during the DI rinse process.

Table 4.4 EDX at. % for white and dark regions on zinc electrodeposited steel following exposure to 5% NaCl solution for 18 h.

Element	White region at. %	Dark region at. %
O	8.4	25.9
Cl	0.5	13.8
Fe	2.6	2.9
Zn	88.5	57.4

4.1.3.2 Chromate A conversion coating on acid zinc electrodeposited steel

A low magnification FEGSEM image of a chromate A 20 s conversion coating appears to exhibit some blistering of the conversion coating from the zinc substrate; Figure 4.30a-b. At higher magnification; Figure 4.30c, it appears that residual flakes of the conversion coating remains. EDX investigations of the underlying region (area A) indicate a lower Cr and higher zinc content in comparison to the upper conversion coating region (area B); Table 4.5. This indicates some residual conversion coating in this case. It is important to note that the approximate analysis depth for EDX is ~1-10 µm and therefore enables the detection of zinc from the underlying zinc substrate at a high level in addition to that present in the conversion coating; see Section 2.4.1.1.

Table 4.5 EDX at. % data for areas A & B of a chromate A 20 s conversion coating on acid zinc electrodeposited steel following exposure to 5% NaCl solution for 18 h from Figure 4.30b.

Element	Area A at. %	Area B at. %
O	5.1	7.5
Cl	0.8	-
Cr	0.7	2.5
Fe	3.0	2.6
Zn	90.4	87.4

FEGSEM analysis of exposed chromate A 40 and 80 s conversion coatings illustrates a greater number of defect regions (e.g. peeling and blistering across the conversion coatings) in comparison to the chromate A 20 s conversion coating; Figure 4.31a and c. Also in high magnification FEGSEM images of blistered regions, the underlying zinc morphology is different; Figure 4.31b and d. EDX data of a chromate A 80 s conversion coating blistered interface region shows that for area A (underlying zinc substrate) oxygen and chromium levels decrease whilst that of zinc increases in comparison to area B (conversion coating); Table 4.6. Also there is no detection of chlorine.

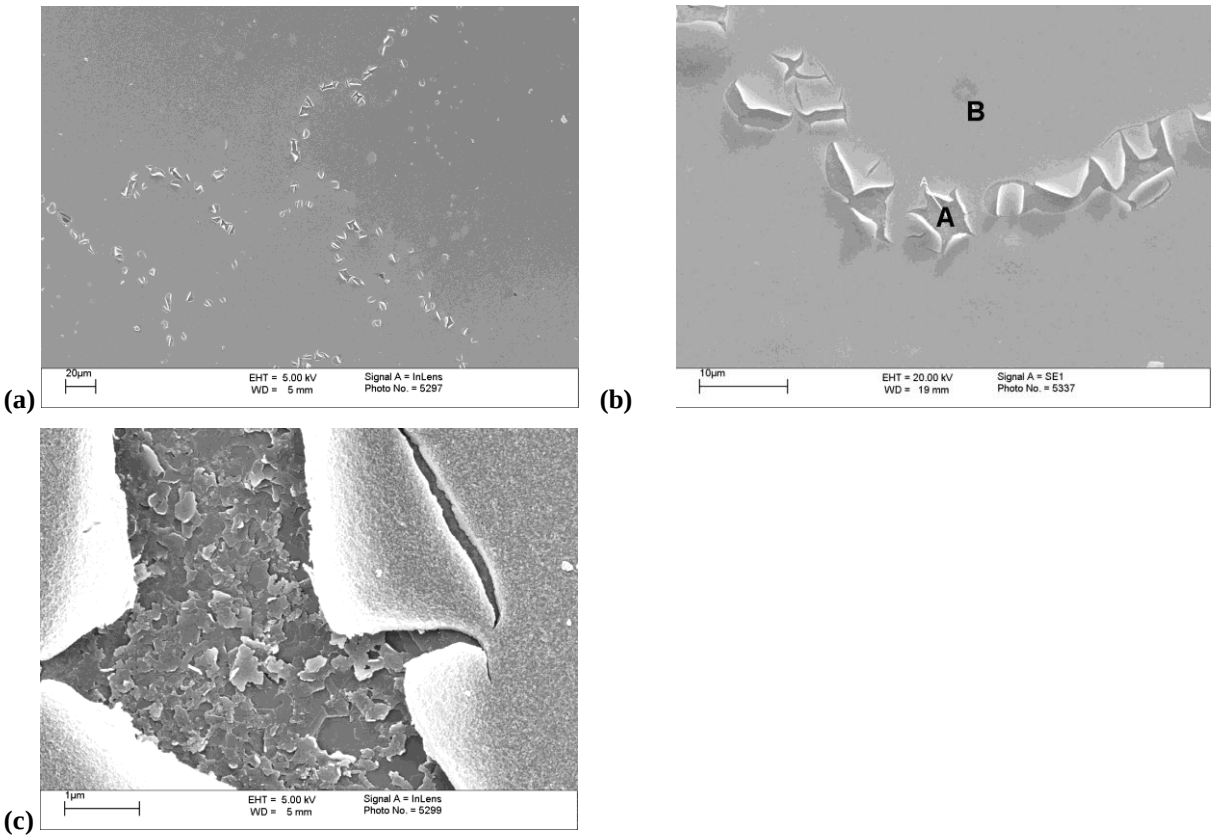

Figure 4.30 FEGSEM micrographs of a chromate A 20 s conversion coating on acid zinc electrodeposited steel following exposure to 5% NaCl solution for 18 h.

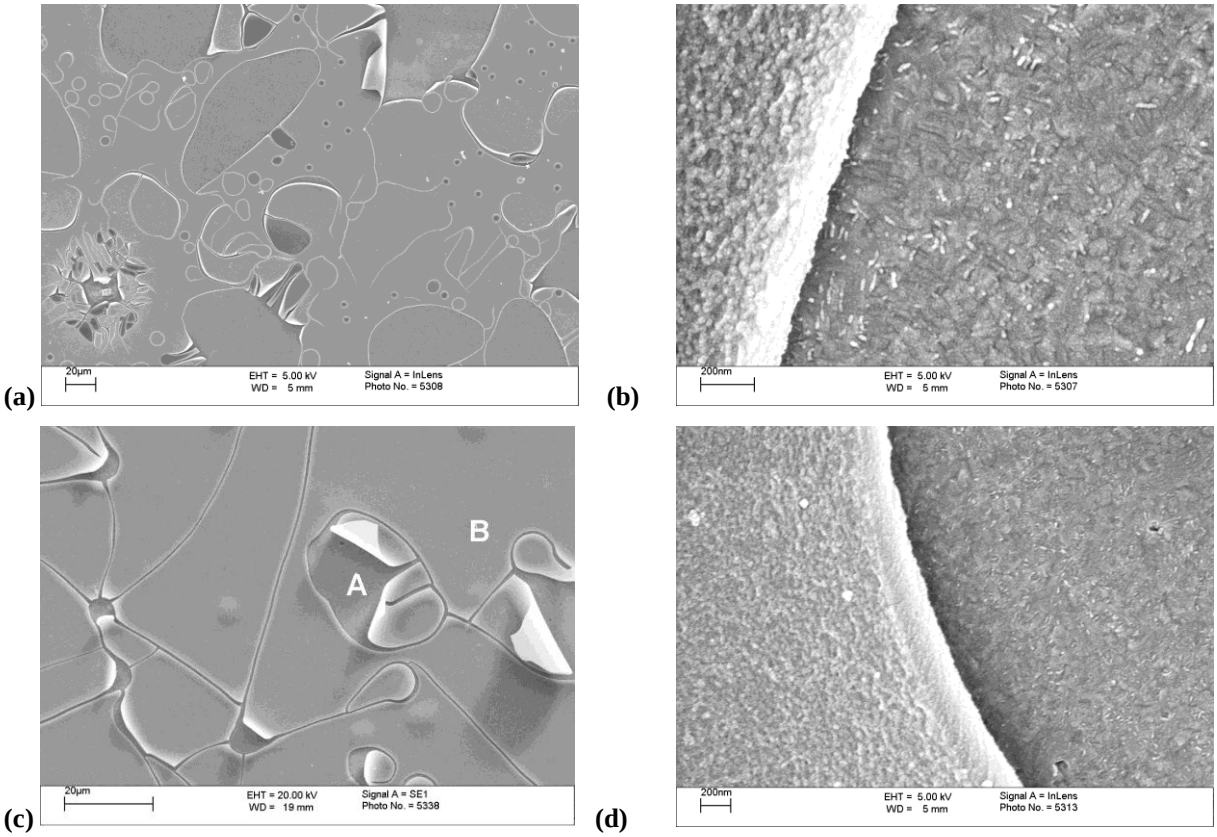

Figure 4.31 FEGSEM micrographs of chromate A conversion coating 40 s (a-b) and 80 s (c-d) on acid zinc electrodeposited steel following exposure to 5% NaCl solution for 18 h.

Table 4.6 EDX at. % data for areas A and B of chromate A conversion coating 80 s on acid zinc electrodeposited steel following exposure to 5% NaCl solution for 18 h, from Figure 4.31c.

Element	Area A at. %	Area B at. %
O	1.4	17.6
Cl	-	1.1
Cr	0.7	6.1
Fe	2.8	2.2
Zn	95.1	73.0

In order to deduce the effect of exposure to the NaCl solution through a conversion coating, cryo fracture was carried out on a conversion coating and underlying zinc substrate followed by analysis using FEGSEM. Cross-sectional analysis at high magnification for chromate A 20 and 40 s conversion coatings shows a gap between the interface of the conversion coating and that of the zinc substrate which could indicate initial loss of adhesion following exposure; Figure 4.32a-b. The morphology of the underlying zinc substrate is different to that observed for an untreated specimen; Figure 4.11, possibly as a result of penetration of corrosive ions.

For the case of chromate A 80 s conversion coating, a FEGSEM micrograph reveals total stripping of the conversion coating from the zinc substrate and therefore no high magnification interface analysis could be carried out. Digital images of the specimen within the NaCl solution shows stripping of conversion coating into solution; see Figure 4.33b. This is almost certainly advanced during the freeze fracture specimen preparation. In comparison chromate A 20 s conversion coating, trivalent 45 s and 180 s CCC showed no stripping of the conversion coating following the same time of exposure; see Figure 4.33 a, c-d. Stripping of chromate A (80s) conversion coating could be linked to a low content of zinc within the conversion coating; see Section 5.2.4.

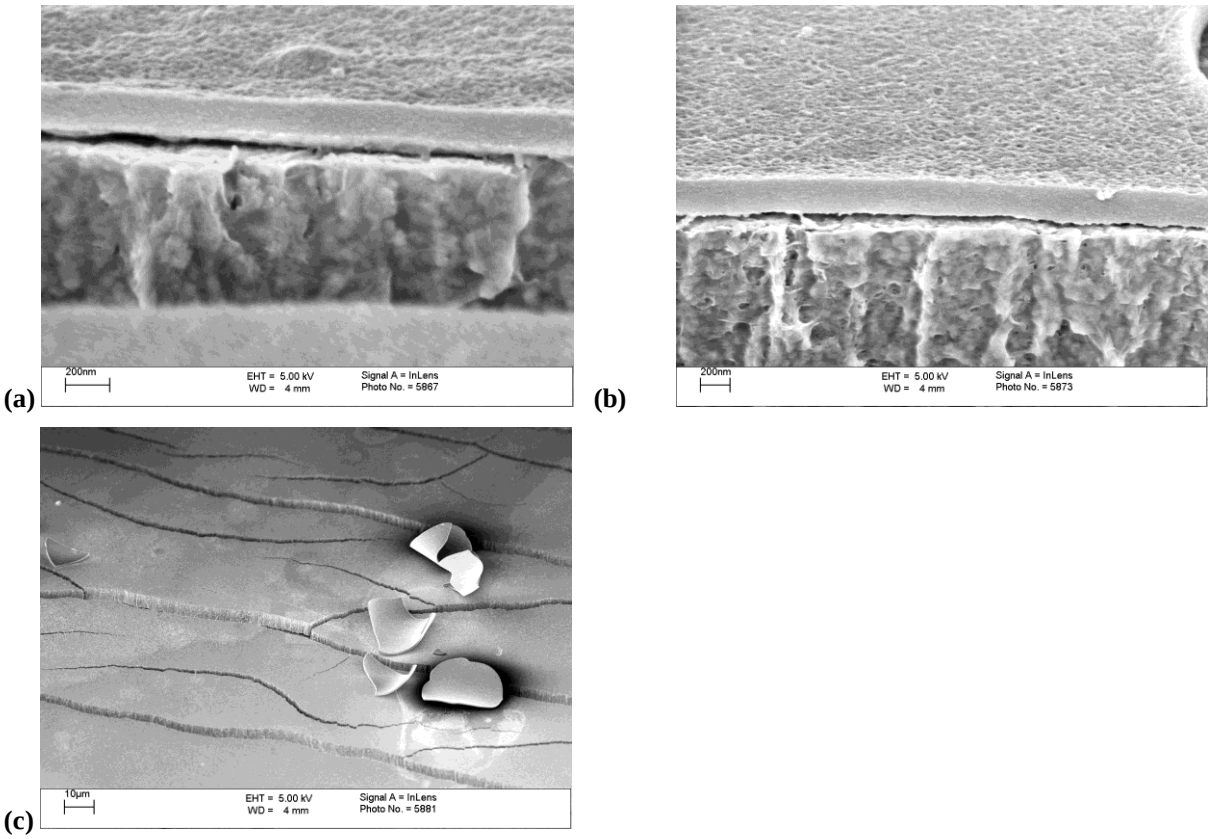

Figure 4.32 FEGSEM micrographs of cryo fractured chromate A conversion coating 20 (a), 40 (b) and 80 s (c) following exposure to 5% NaCl solution for 18 h.

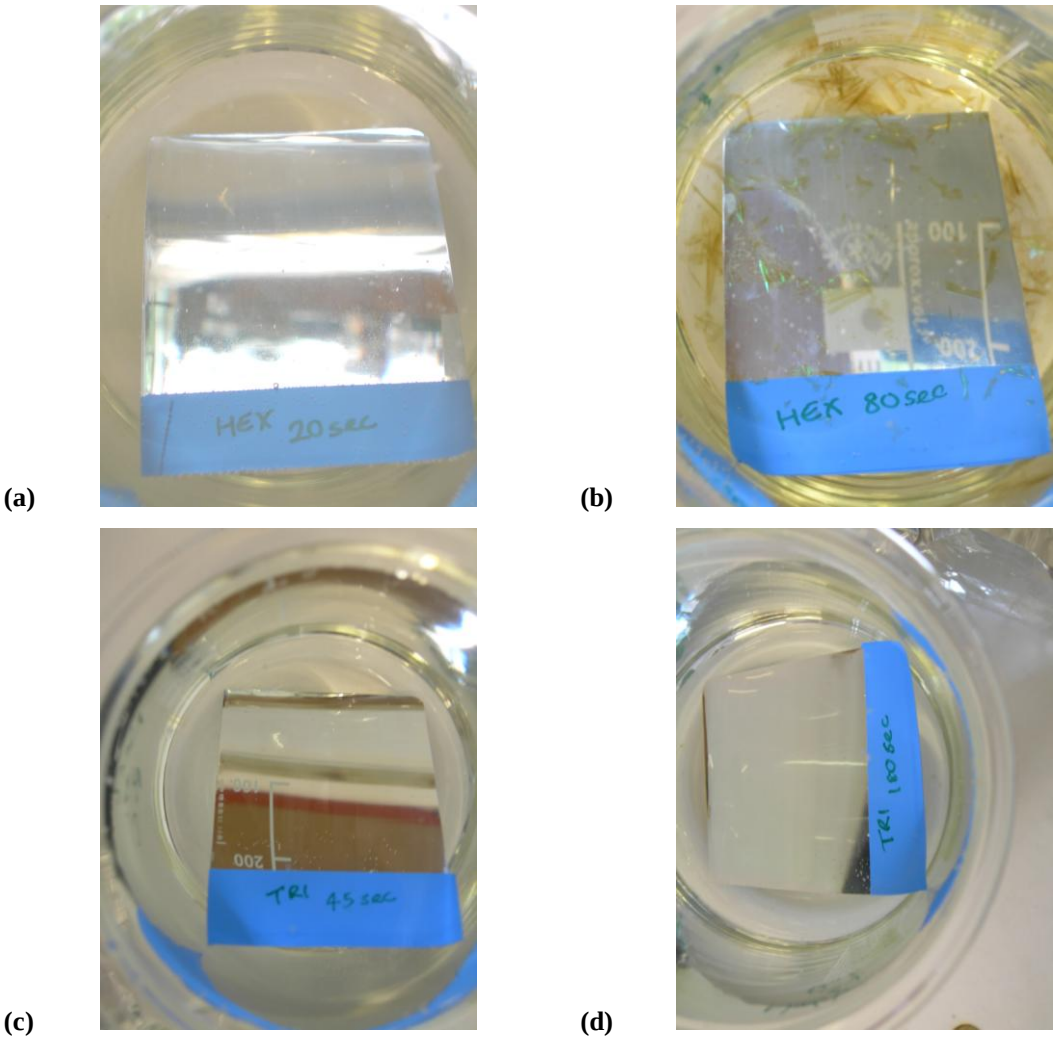

Figure 4.33 Actual appearance of chromate A conversion coating 20 s (a), 80 s (b) and trivalent CCC 45 s (c), 180 s (d) on acid zinc electrodeposited steel in 5% NaCl solution following 18 h exposure.

4.1.3.3 Trivalent CCC on acid zinc electrodeposited steel

FEGSEM micrographs of trivalent 45 s CCC following exposure to 5% NaCl solution for 18 h appears to show surface deterioration of the conversion coating including a scatter of debris; Figure 4.34a-c. EDX scans of the debris objects (area A Figure 4.34b) exhibit a high content of chlorine which supports the view that surface debris could be zinc chloride corrosion products, salt crystals or simply chloride products from the NaCl solution; Table 4.7. This could simply be a result of insufficient rinsing following exposure. In comparison trivalent CCC 90 and 180 s show minimal surface deterioration; Figure 4.35. Any minor surface defect features are possibly the result of adsorbed chloride products as observed for trivalent CCC 45 s.

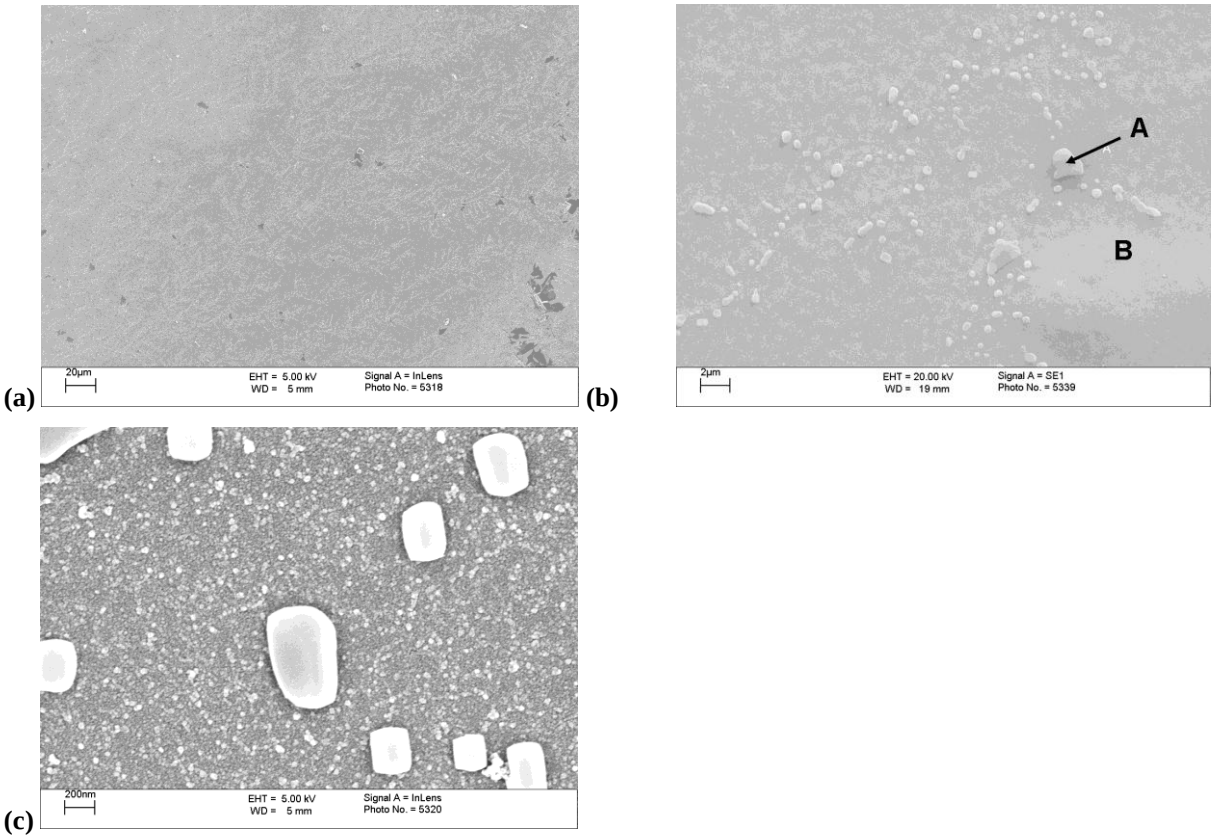

Figure 4.34 FEGSEM micrographs of trivalent CCC 45 s on acid zinc electrodeposited steel following exposure to 5% NaCl solution for 18 h.

Table 4.7 EDX at. % data of Areas A & B of trivalent CCC 45 s on acid zinc electrodeposited steel following exposure to 5% NaCl solution for 18 h. From Figure 4.34b.

Element	Area A at. %	Area B at. %
O	5.1	5.8
Cl	6.2	0.8
Cr	1.2	1.1
Fe	2.8	2.7
Zn	84.7	89.6

High magnification cyro freeze fracture FEGSEM micrographs of the interface between trivalent CCC 45, 90 and 180 s and the underlying acid zinc electrodeposited steel exhibits no gaps, peeling or blistering; Figure 4.36a-c. The zinc substrate, like that coated with chromate A conversion coating, has undergone a change in morphology. The morphology of the conversion coating appears to remain unchanged by the corrosive environment.

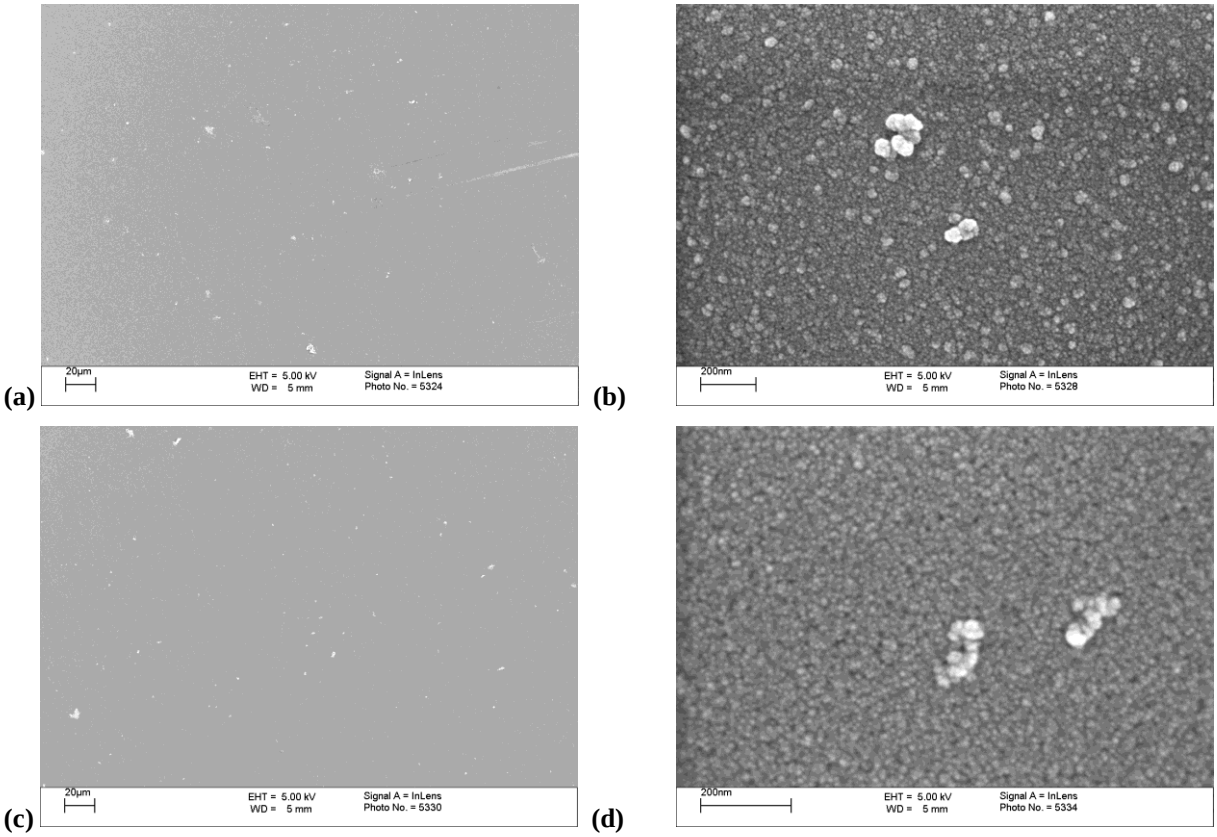

Figure 4.35 FEGSEM micrographs of trivalent CCC 90 (a-b) and 180 s (c-d) on acid zinc electrodeposited steel following exposure to 5% NaCl solution for 18 h.

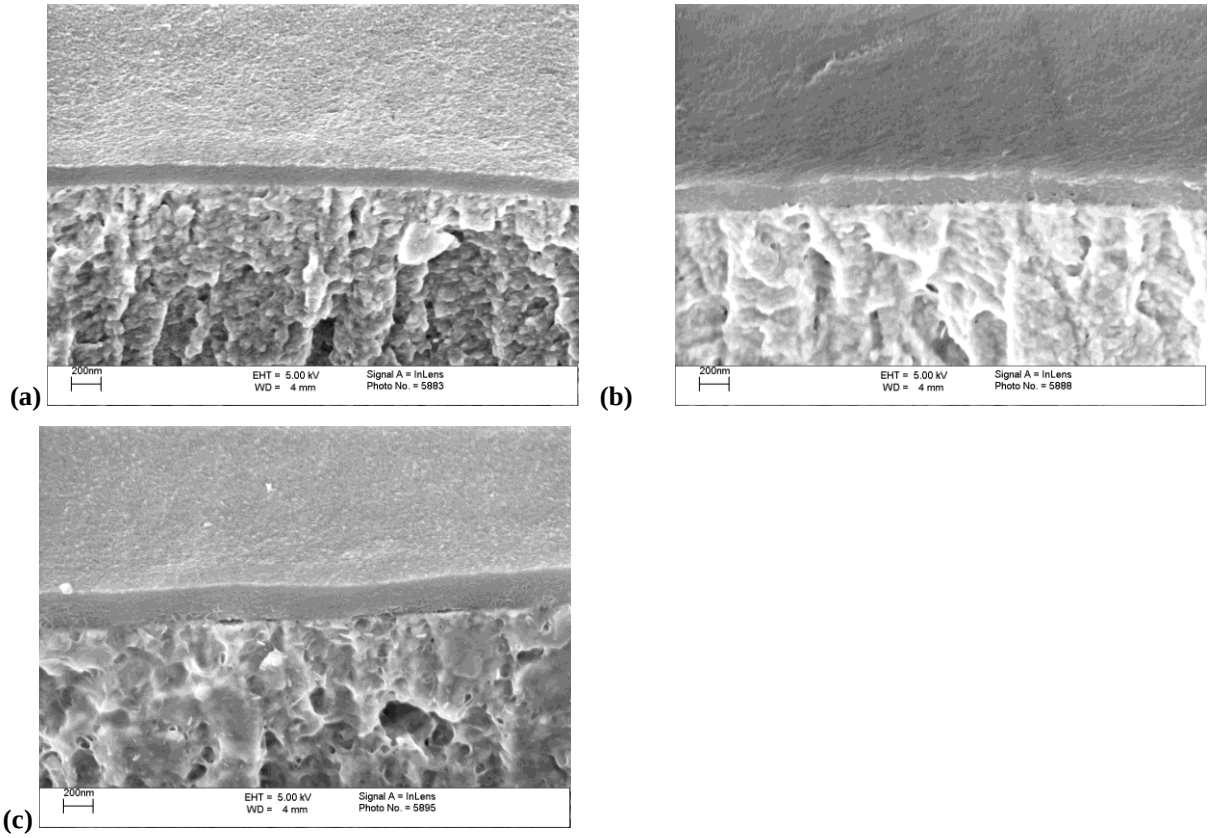

Figure 4.36 FEGSEM micrographs of cryo fractured trivalent CCC 45 (a), 90 (b) and 180 s (c) on acid zinc electrodeposited steel following exposure to 5% NaCl solution for 18 h.

4.1.3.4 Conversion coating thickness following exposure

Following exposure to 5% NaCl solution for 18 h the trivalent CCC average thickness measurements; Table 4.8, shows a decrease in comparison to those of untreated specimens; see Table 4.1. This could indicate dissolution of the conversion coating into solution via corrosion products or shrinkage of the conversion coating following internal corrosion reactions. It is important to note that SEM surface morphological studies show minimal corrosion activity.

Alternatively, for chromate A conversion coatings the average thickness measurements following 18 h exposure to NaCl solution; Table 4.8, show an increase in comparison to those of untreated specimens; Table 4.1, of up to 112 nm. The rise is different to trivalent CCCs and may have resulted due to internal/external corrosion products i.e. swelling.

Table 4.8 FEGSEM cryo-fracture conversion coating thickness measurements for chromate A conversion coating and trivalent CCC on acid zinc electrodeposited steel following exposure to 5% NaCl solution for 18 h.

Conversion coating	Thickness (nm)			
	Reading 1	Reading 2	Reading 3	Average
Trivalent CCC 45 s	130	140	125	132
Trivalent CCC 90 s	190	200	185	193
Trivalent CCC 180 s	223	230	240	231
Chromate A 20 s	240	210	200	217
Chromate A 40 s	270	230	250	250
Chromate A 80 s	410	427	430	422

4.1.3.5 Effect of scratching CCC surfaces followed by exposure

A carbide tipped pen was used to manually scratch a chromate A 40 s conversion coating and trivalent 90 s CCC, before immersion of the panels in 5% NaCl solution for 18 h. This method of scratching samples was carried out in accordance with ASTM D1654 [10]. Two scratch indentations were made with one being exerted at a greater manual force, this being scratch no.1. Scratch no.2 was merely to provide a grazed surface.

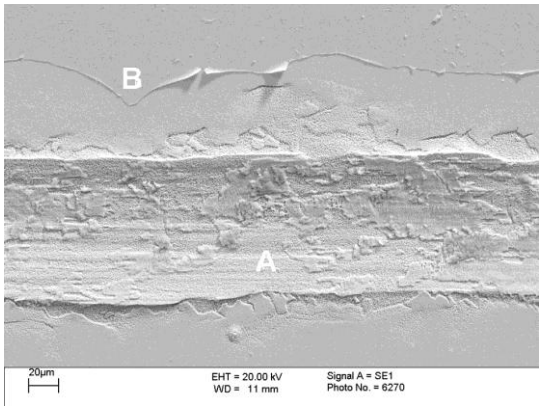

(a)

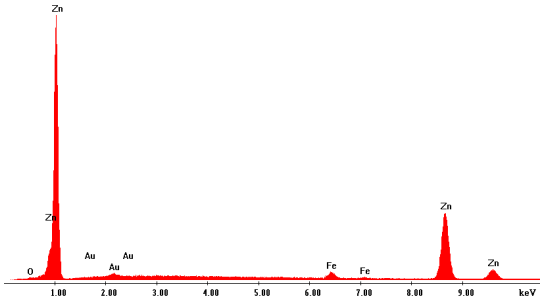

(b)

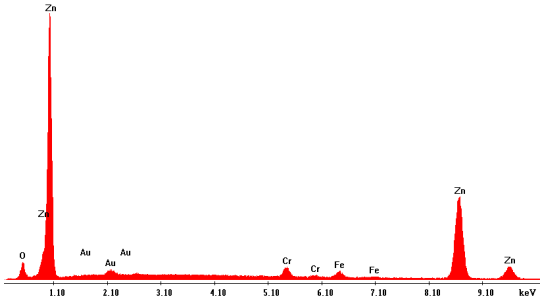

(c)

Figure 4.37 FEGSEM micrograph (a) and EDX spectra ((b) - area A), (c) area B)) of scratch no. 1 on chromate A 40 s conversion coating on acid zinc electrodeposited steel following exposure to 5% NaCl solution for 18 h.

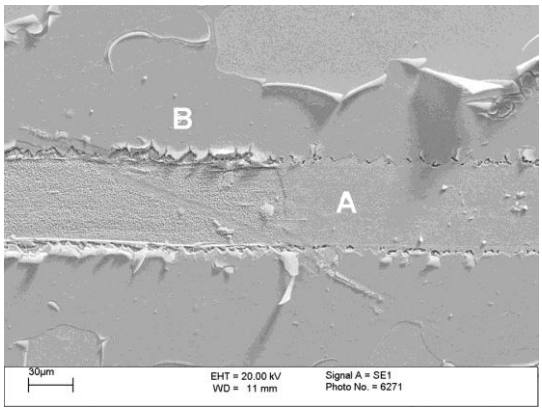

(a)

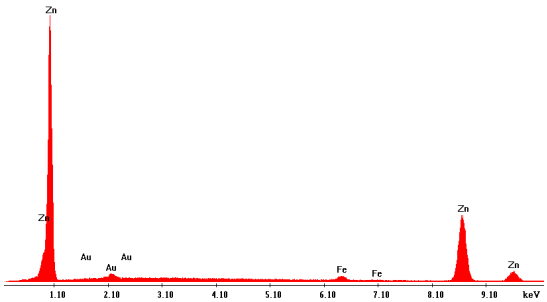

(b)

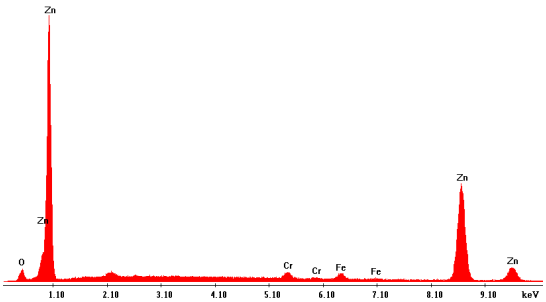

(c)

Figure 4.38 FEGSEM micrograph (a) and EDX spectra ((b) -A), (c) area B)) of scratch no. 2 on chromate A 40 s conversion coating on acid zinc electrodeposited steel following exposure to 5% NaCl solution for 18 h.

FEGSEM images of scratches no.1 and 2 for chromate A 40 s conversion coating can be observed in Figures 4.37a and 4.38a. It is clear to see that the scratch width is greater for scratch no.1 (~53 - 93 µm). EDX analysis within the scratch profiles of both shows no detection of chromium; Figure 4.37b and 4.38b, indicating an absence of self-repair properties as there appears to be removal of the conversion coating. Higher magnification FEGSEM micrographs; Figure 4.39a-c, of the scratch no.2 panel i.e. location area A; Figure 4.38a, indicates regions of partial conversion coating removal.

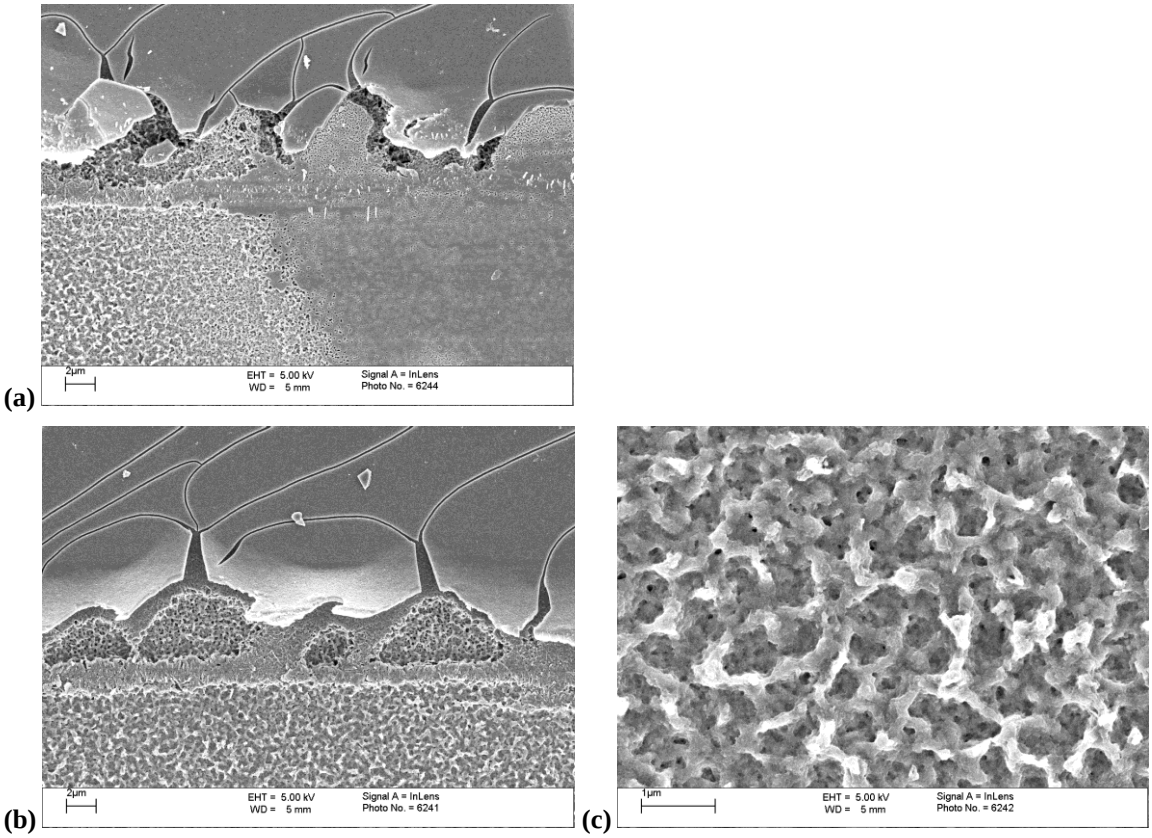

Figure 4.39 Higher magnification FEGSEM micrographs of scratch no 2 on chromate A 40 s conversion coating following exposure to 5% NaCl solution for 18 h. (a, b) conversion coating and zinc interface, (c) scratched zinc surface.

FEGSEM micrographs of scratch no 1 and 2 for trivalent CCC can be observed in Figures 4.40a and 4.41a. Scratch width dimensions are greater for scratch no.1 (~50 - 86 µm). EDX analysis within the profile of scratch no. 2 detected some chromium; Figure 4.41b. Higher magnification images of scratch no.2; Figure 4.42a-b, suggest that the conversion coating was merely grazed as opposed to being removed as in the case of scratch 1. This suggests that the adhesion between the conversion coating and zinc substrate is strong. Also, unlike chromate A 40 s conversion coating, there is no additional peeling and micro-cracking.

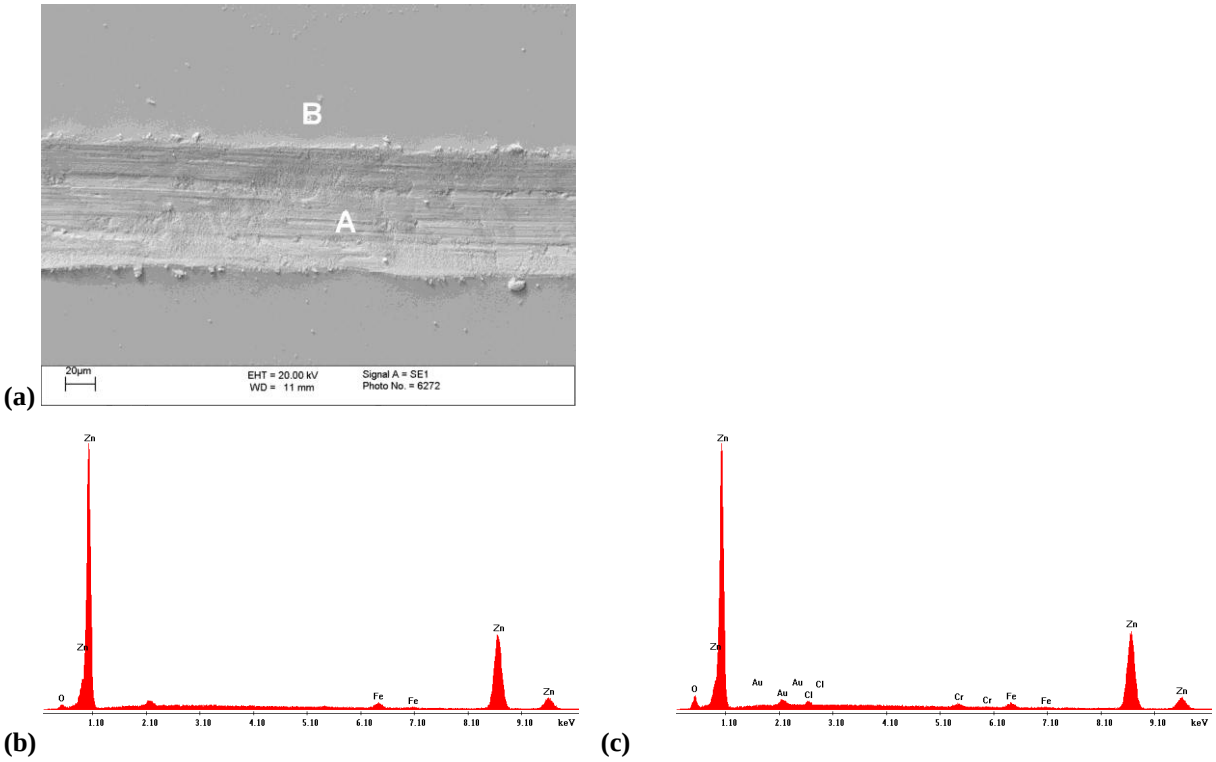

Figure 4.40 FEGSEM micrograph (a) and EDX spectra ((b) - area A), (c) area B)) of scratch no. 1 on trivalent 90 s CCC following exposure to 5% NaCl solution for 18 h.

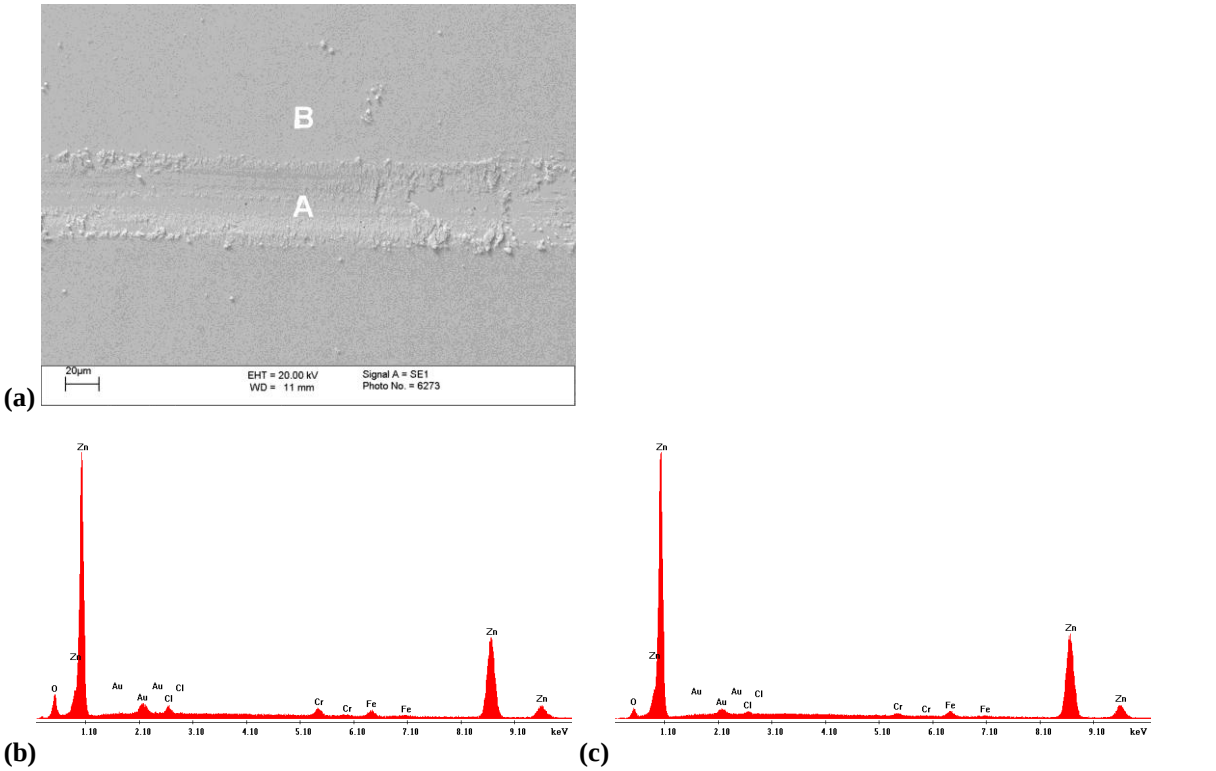

Figure 4.41 FEGSEM micrograph (a) and EDX spectra ((b) - area A), (c) area B)) of scratch no. 2 on trivalent 90 s CCC following exposure to 5% NaCl solution for 18 h.

(a) 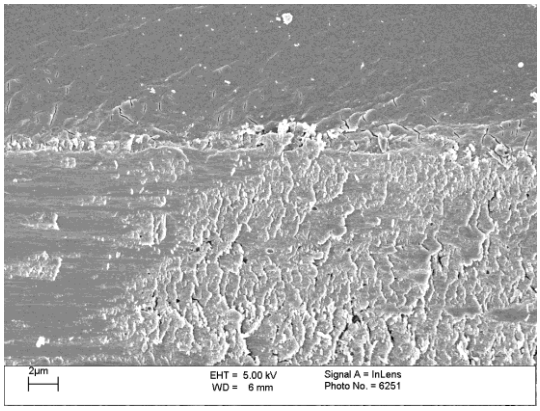

(b) 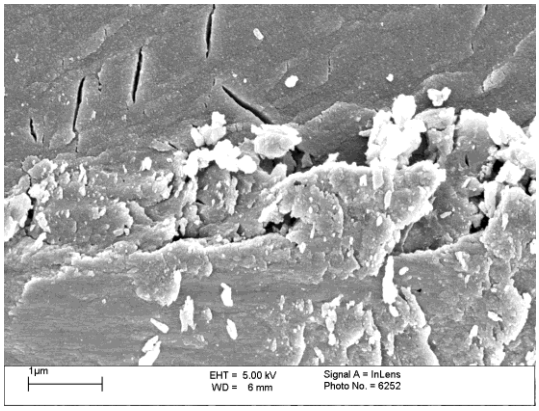

Figure 4.42 Higher magnification FEGSEM micrographs of scratch no 2 on trivalent 90 s CCC following exposure to 5% NaCl solution for 18 h.

The method of using a carbide tipped pen (to ASTM D1654 standard) to induce a scratched surface has limitations in that the surface debris can be transferred from one region to another during the scratch process. Also, as the profile and scratch depth is difficult to control via manual operation, there may be reproducibility issues using this manual scratch method.

4.1.4 Effect of Tripass LT1500 additives on conversion coating surface morphology

4.1.4.1 Tripass LT1500 – control

The Tripass LT1500 control treatment solution, was prepared 'in-house' from constituent chemicals as opposed to Tripass LT1500 prepared from a proprietary concentrate, from MacDermid plc. FEGSEM images of Tripass LT1500 control are very similar to those of Tripass LT1500; Figure 4.43a-b and 4.22. A cross-sectional FEGSEM image of the conversion coating and underlying zinc electrodeposited steel is also similar; Figure 4.43c. Average conversion coating thickness is, however, slightly thinner at 175 nm for Tripass LT1500 control; Table 4.9, in comparison to 203 nm for Tripass LT1500; Table 4.1.

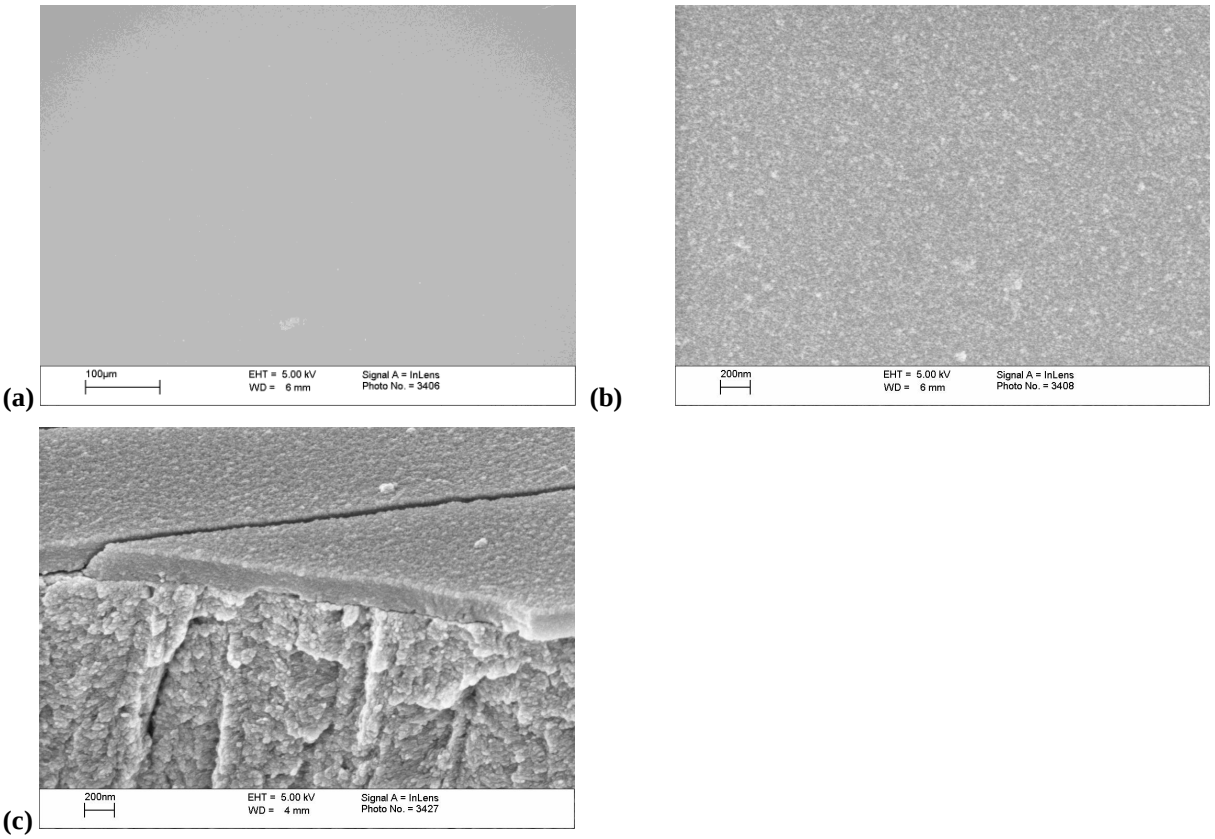

Figure 4.43 FEGSEM micrographs of Tripass LT1500 control on acid zinc electrodeposited steel (a, b), cross-sectional image following cryo fracture (c). Samples were gold coated.

4.1.4.2 Effect of sodium molybdate

FEGSEM images of Tripass LT1500 modified both with the addition (0.4 g/l) and the exclusion of sodium molybdate exhibited surface morphologies which were free of micro-cracks or other physical defects; Figure 4.44a & c. High magnification and cross-sectional FEGSEM images appear to exhibit a fine particulate structure for both variables; Figure 4.44b

& d-f. This is similar to that of the Tripass LT1500 control as is the structure of the underlying zinc electrodeposited steel. The addition of sodium molybdate appears to have reduced the overall coating thickness in comparison to Tripass LT1500 control; Table 4.9.

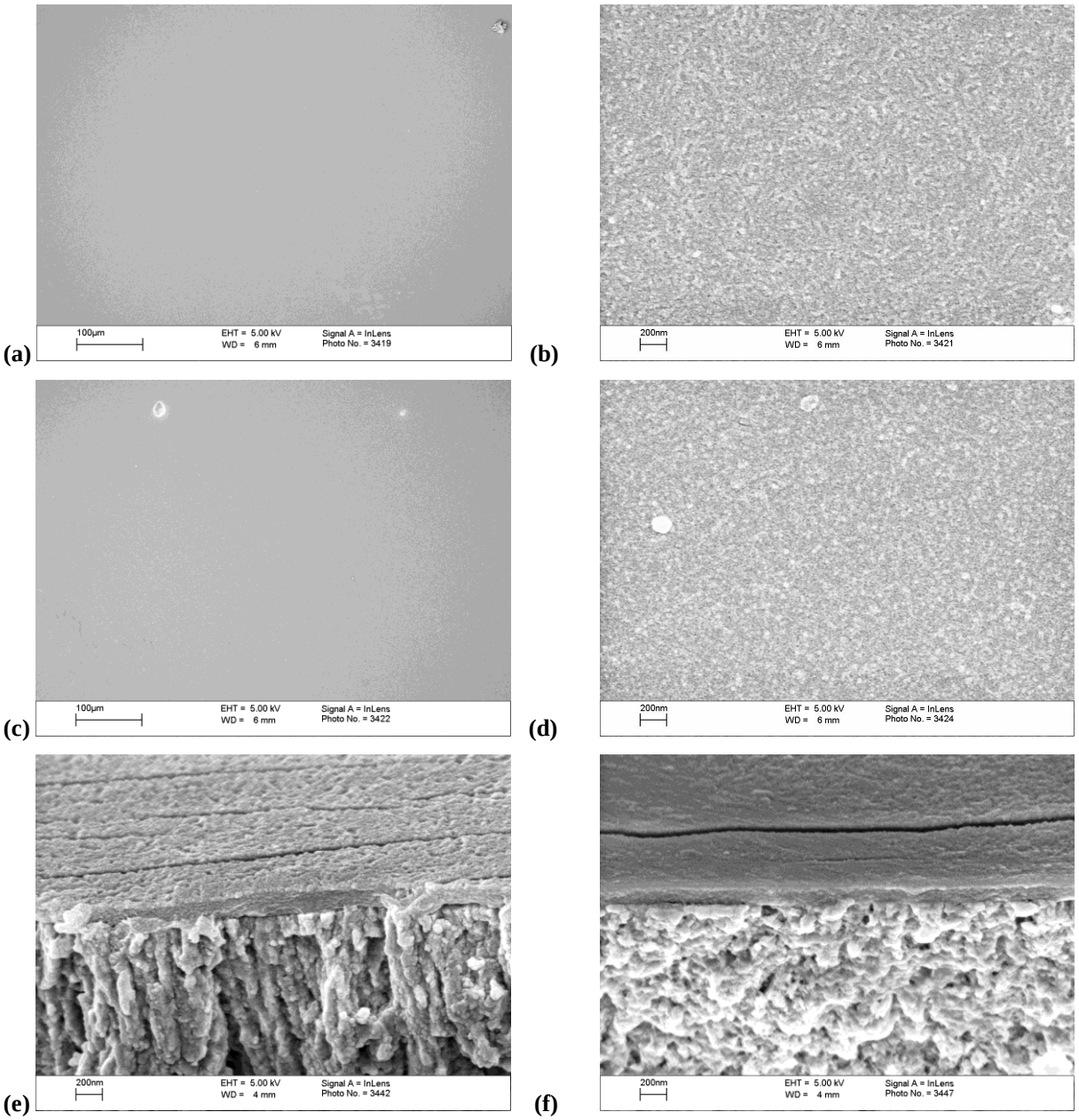

Figure 4.44 FEGSEM micrographs of Tripass LT1500 with no (a-b) and 0.4 g/l (c-d) sodium molybdate on acid zinc electrodeposited steel. FEGSEM cryo fractured Tripass LT1500 including no (e) and 0.4 g/l (f) sodium molybdate. Samples were gold coated.

Table 4.9 FEGSEM cyro-fracture conversion coating thickness measurements. *Note: Tripass LT1500 - 52 g/l oxalic acid conversion coating thickness measurements taken from individual precipitate products which formed.

Sample	Thickness measurements (nm)			
	1	2	3	Average (nm)
Tripass LT1500 – control	145	200	180	175
Tripass LT1500 - no sodium molybdate	191	176	170	179
Tripass LT1500 - 0.4 g/l sodium molybdate	173	140	120	144
Tripass LT1500 - no cobalt nitrate	170	180	190	180
Tripass LT1500 - 14.6 g/l cobalt nitrate	195	180	194	190
Tripass LT1500 - no malonic acid	212	185	200	199
Tripass LT1500 - 13 g/l malonic acid	190	150	190	177
Tripass LT1500 - 13 g/l malonic acid (+ 1 day further solution heating)	180	160	160	167
Tripass LT1500 - no oxalic acid	210	200	190	200
Tripass LT1500 - 52 g/l oxalic acid*	100	105	90	98
Tripass LT1500 - no chromium nitrate	-	-	-	-
Tripass LT1500 – 212 g/l chromium nitrate	250	270	260	260

4.1.4.3 Effect of cobalt nitrate

FEGSEM images of Tripass LT1500 modified with the addition (14.6 g/l) and exclusion of cobalt nitrate exhibited surface morphologies generally free of micro-cracks or other physical defects; Figure 4.45a & c. There are some superficial cracks for the 14.6 g/l specimen, however, these are not representative of the entire surface and thus could have occurred during specimen preparation. The conversion coating cross-sections and high magnification FEGSEM images appear to resemble a fine particulate structure in both cases; Figure 4.45e-f. The conversion coatings are compact and well adhered to the zinc electrodeposited steel. The structure of the latter is similar to that of the Tripass LT1500 control.

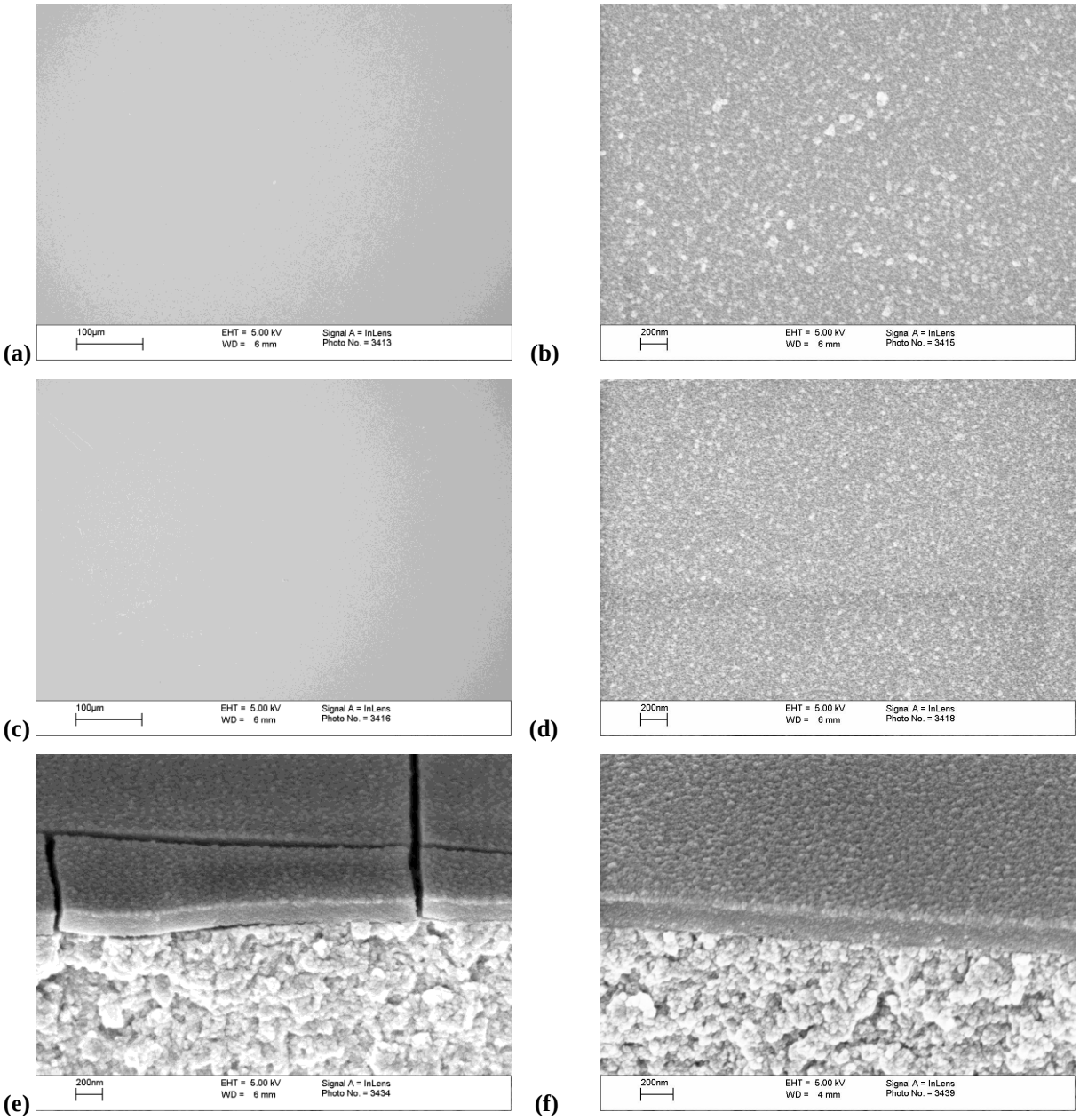

Figure 4.45 FEGSEM micrographs of Tripass LT1500 with no (a-b) and 14.6 g/l (c-d) cobalt nitrate on acid zinc electrodeposited steel. FEGSEM cryo fractured Tripass LT1500 including no (e) and 14.6 g/l (f) cobalt nitrate. Samples were gold coated.

4.1.4.4 Effect of malonic acid

FEGSEM images of Tripass LT1500 modified with the addition of malonic acid (13 g/l) exhibits a surface morphology laden with micro-cracks; Figure 4.46c-d. The micro-cracks are random in their orientation and do not run parallel to one another. They appear to propagate to the underlying zinc electrodeposited steel surface; Figure 4.46d. However, when the same treatment solution was allowed to age with additional heating, the surface morphology

changes to that exhibiting no micro-cracks or any other physical imperfections; Figure 4.46e-f. This is also true for a treatment solution without any malonic acid; Figure 4.46a-b.

Cross-section and high magnification FEGSEM images of conversion coatings show in all variables a fine particulate structure; Figure 4.47a-c. This, along with the underlying zinc electrodeposited steel, appears to be similar to a Tripass LT1500 control morphology. The conversion coating thickness for all variables are similar to that of the control; Table 4.9.

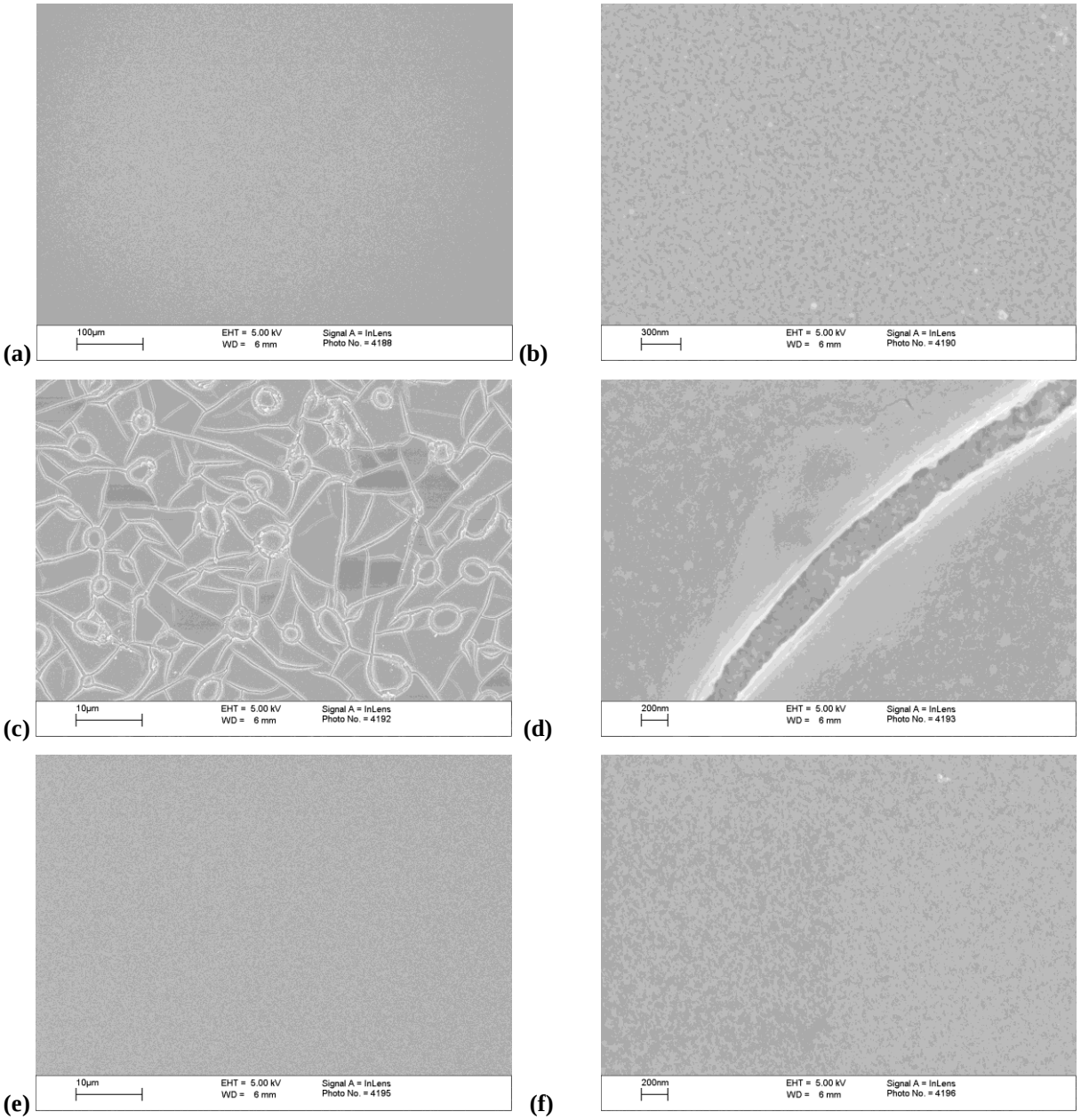

Figure 4.46 FEGSEM micrographs of Tripass LT1500 with no (a-b), 13 g/l (c-d), 13 g/l (with further solution heating) (e-f) malonic acid on acid zinc electrodeposited steel. Samples were gold coated.

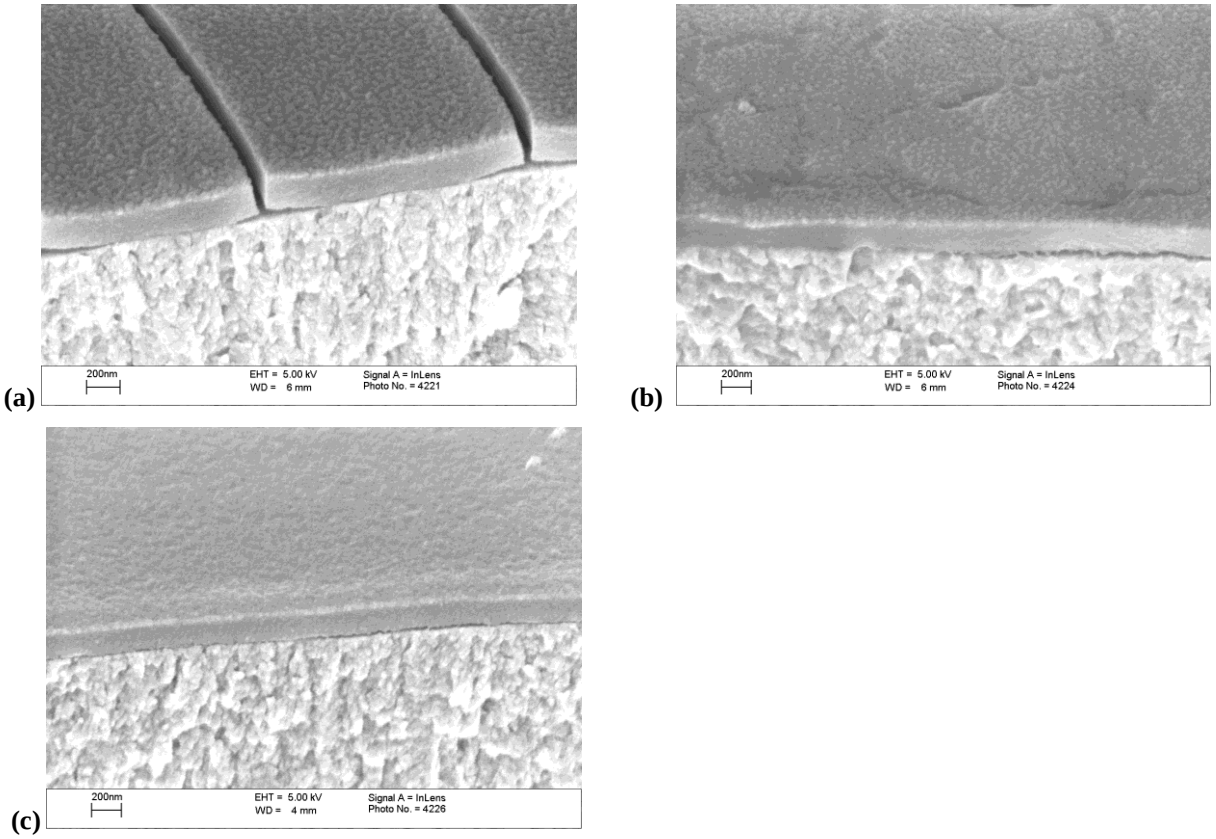

Figure 4.47 FEGSEM micrographs of cryo fractured Tripass LT1500 including no (a), 13 g/l (b) and 13 g/l with further solution heating (c) malonic acid on acid zinc electrodeposited steel. Samples were gold coated.

4.1.4.5 Effect of oxalic acid

FEGSEM images of Tripass LT1500 modified by the exclusion of oxalic acid exhibits a surface morphology with a scattering of tiny micro-cracks orientated in a random fashion; Figure 4.48a-b. In addition, there is extensive blistering of the conversion coating from the zinc electrodeposited steel, however, this is not representative of the entire surface morphology. The addition of oxalic acid (52 g/l) to a control formulation results in an extensive network of micro-cracks. On closer observation these cracks appear to be regions in which there is no coagulation of the spherical-like particulate structures (~100 nm); Figure 4.48d. These structures are confirmed in cross-sectional FEGSEM images; Figure 4.48f. The conversion coating appears less compact and significantly different to that of the control Tripass LT1500. The conversion coating cross-section is composed of 3-4 particles in terms of thickness (~100 nm). The average coating thickness for this variable was difficult to establish. FEGSEM images of the cross-section for no oxalic acid, exhibit a similar morphology for conversion coating and underlying zinc electrodeposited steel as that of Tripass LT1500 control. In addition, there is a distinct gap between the conversion coating

and the zinc electrodeposited steel, which may suggest a loss of adhesion or alternatively due to the freeze fracture specimen preparation method.

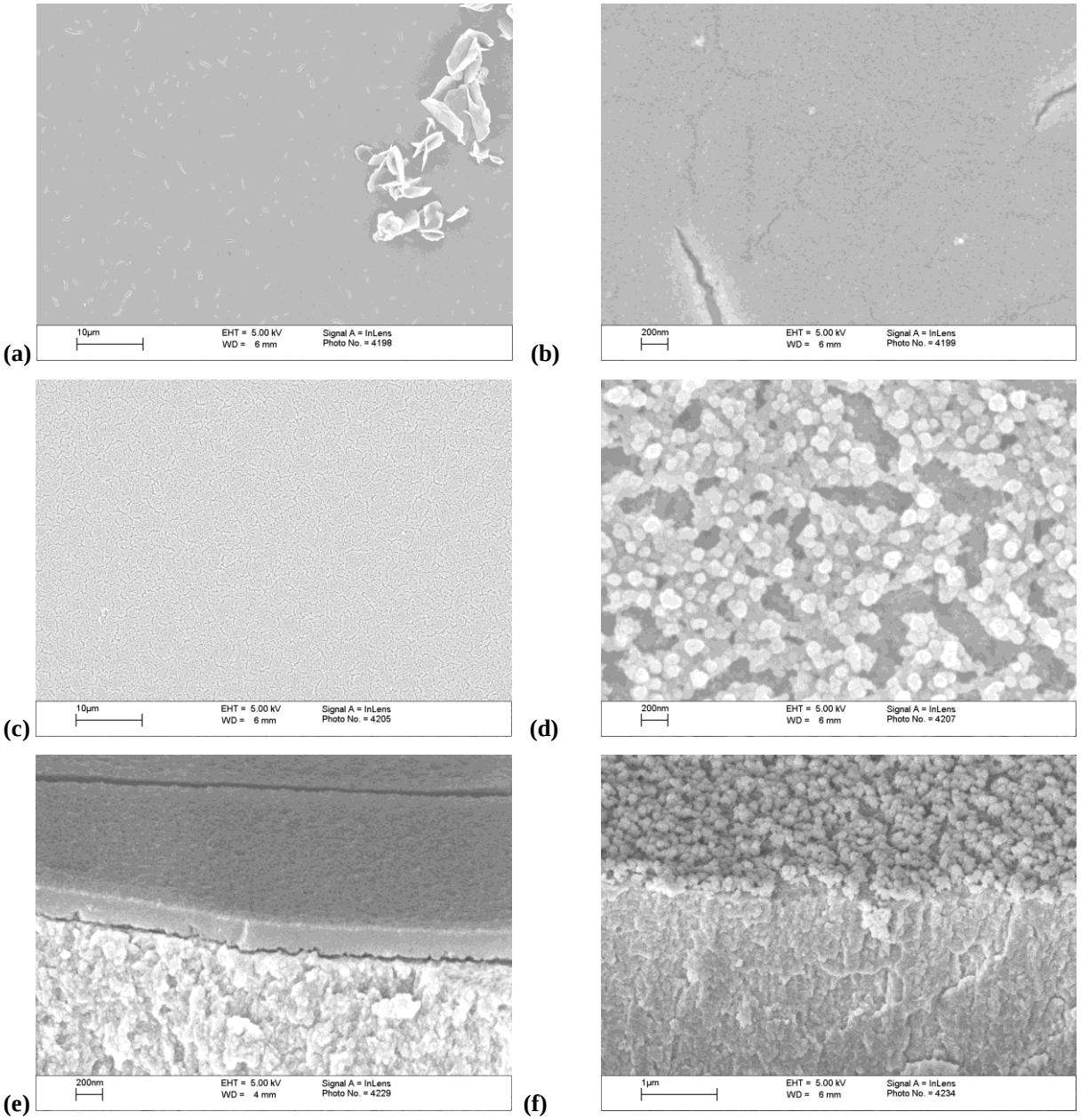

Figure 4.48 FEGSEM micrographs of Tripass LT1500 with no (a-b), 52 g/l (c-d) oxalic acid, FEGSEM micrographs of cryo fractured Tripass LT1500 including no (e), 52 g/l (f) oxalic acid. Samples were gold coated.

4.1.4.6 Effect of chromium nitrate

FEGSEM images of Tripass LT1500 modified by the exclusion of chromium nitrate exhibit a surface morphology containing ‘rod-like’ structures across the surface; Figure 4.49a. These are randomly orientated and have a higher concentration of oxygen in comparison to a ‘non-

rod' region, possibly indicating ZnO products; Table 4.10. On closer observation there appear to be pyramidal shaped structures protruding from a flat porous underlying surface, possibly that of the zinc electrodeposited steel; Figure 4.49b-c. Observation of FEGSEM cross-sectional images of the variable do not appear to exhibit a conversion coating and thus no coating thickness was taken; Figure 4.49d-e. Also the zinc electrodeposited steel cross-section appears different to that of the control Tripass LT1500.

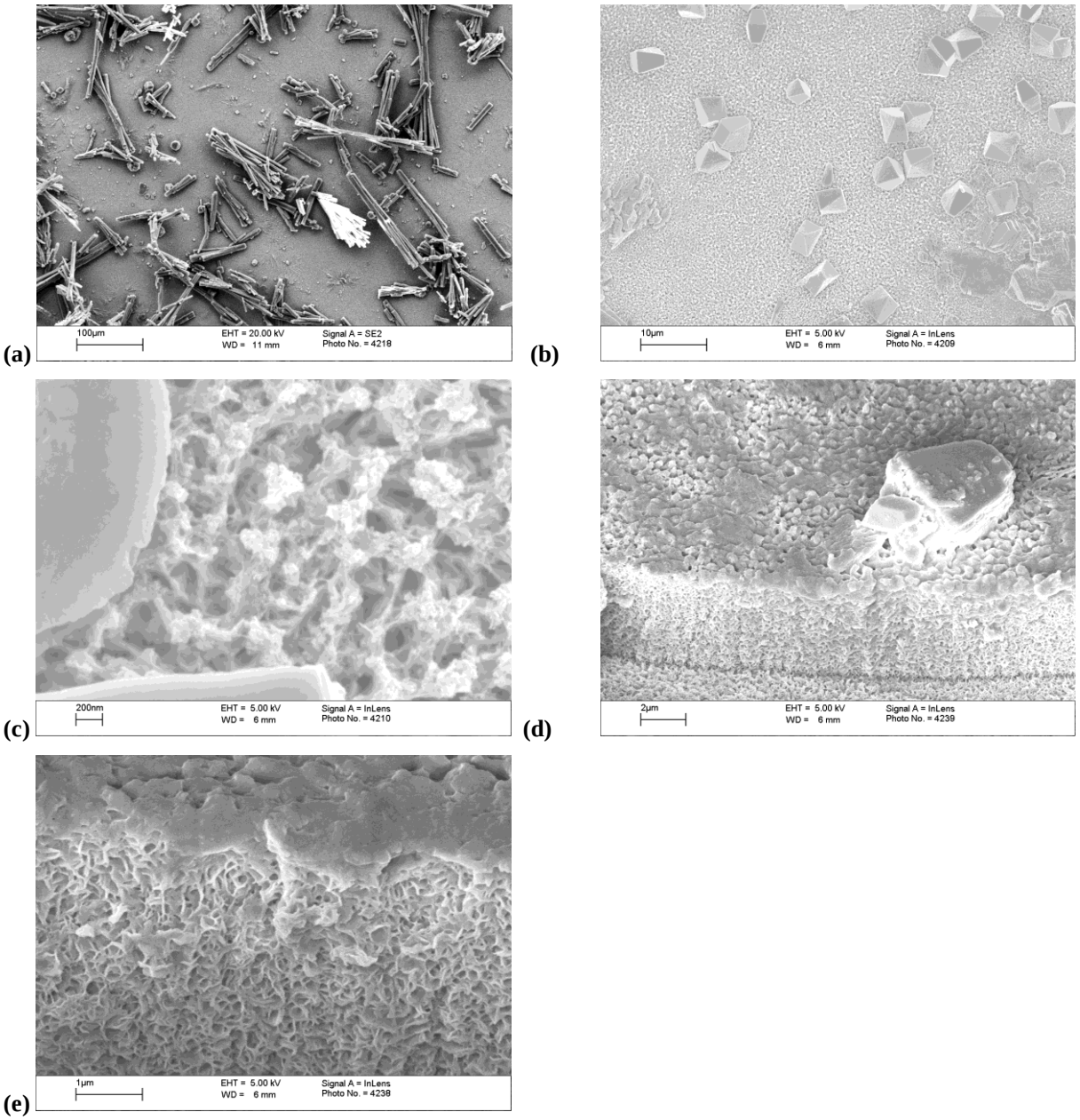

Figure 4.49 FEGSEM micrographs of Tripass LT1500 with no chromium nitrate on acid zinc electrodeposited steel (a-c), cryo fractured images (d-e). Samples were gold coated.

Table 4.10 EDX at. % values for Tripass LT1500 conversion coating containing no chromium nitrate. From Figure 4.49a.

Element	Non rod feature region at. %	Rod feature region at. %
O	12.1	44.4
Au	0.8	0.7
Fe	2.0	1.6
Co	0.6	4.0
Zn	84.5	49.3

FEGSEM images of Tripass LT1500 modified with the inclusion of chromium nitrate (212 g/l) exhibit a surface morphology with some micro-cracks scattered across the surface; Figure 4.50a and c. The micro-cracks are unusually circular in shape. On closer observation of the conversion coating cross-section it appears well adhered to the zinc electrodeposited steel and reveals a fine particulate structure; Figure 4.50d. The conversion coating thickness was found to be greater than that of the control Tripass LT1500. Overall with chromium nitrate incorporation even at the higher level, the conversion coating as well as the underlying zinc electrodeposited steel resembles the morphology to that of the Tripass LT1500 control.

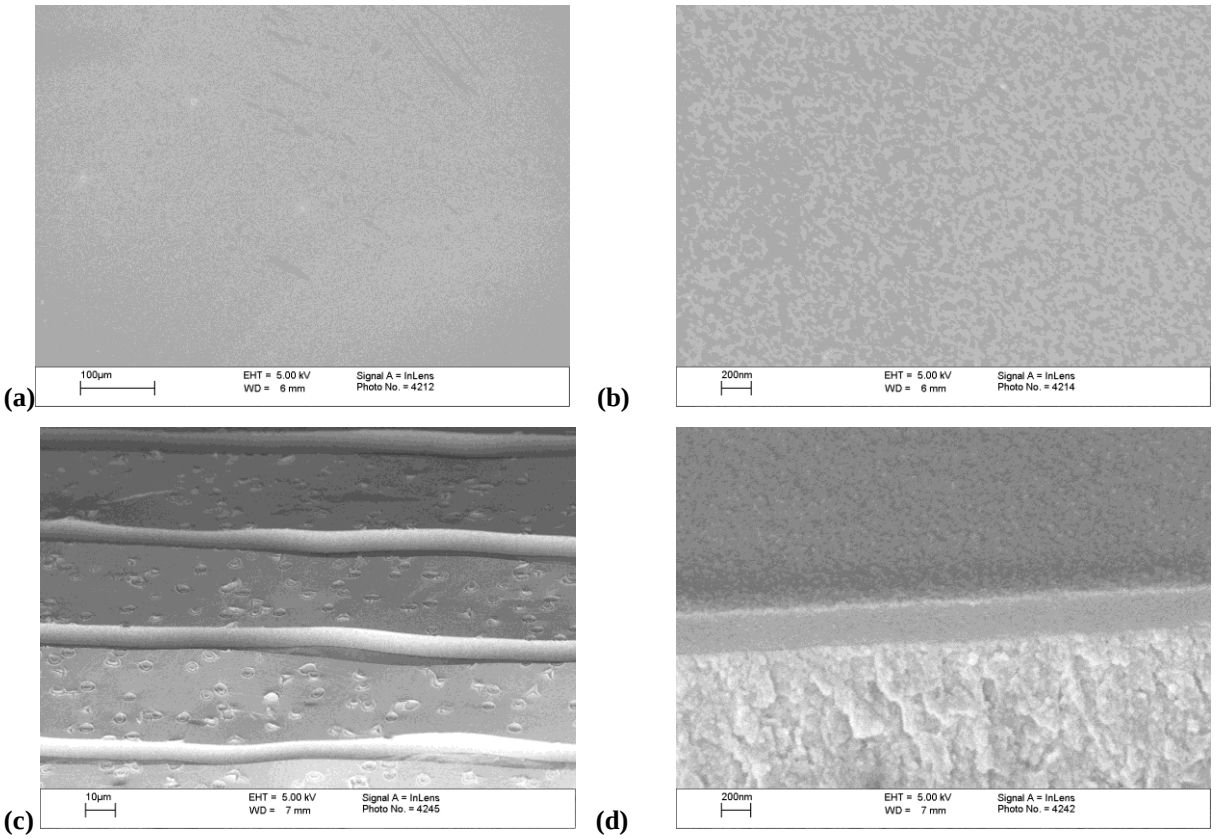

Figure 4.50 FEGSEM micrographs of Tripass LT1500 with 212 g/l chromium nitrate (a-b) on acid zinc electrodeposited steel, cryo fractured images (c-d). Samples were gold coated.

4.1.5 Black trivalent CCC surface morphologies

4.1.5.1 Black trivalent CCC on acid zinc electrodeposited steel

FEGSEM images of a black trivalent CCC on acid zinc electrodeposited steel exhibit a surface morphology with tiny micro-cracks (~1 μm) orientated in a random fashion; Figure 4.51a-b. In a cross-sectional FEGSEM image, the interface between the conversion coating and zinc electrodeposited steel is difficult to distinguish; Figure 4.51c. Conversion coating thickness was determined by measuring the length of the micro-cracks in the z-axis. The average conversion coating thickness of 407 nm is almost double that for Tripass LT1500; see Tables 4.11 and 4.1. This may be due to a difference in treatment time or a different film formation mechanism.

Table 4.11 FEGSEM cryo-fracture black trivalent CCC and organic topcoat coating thickness measurements.

Sample	Coating thickness measurements (nm)			
	1	2	3	Average (nm)
Black trivalent CCC on acid zinc electrodeposited steel	370	425	425	407
Black trivalent CCC on alkaline zinc electrodeposited steel	870	816	890	859
Organic topcoat (based on 12 nm silica particles) on a trivalent CCC (Tripass LT1500) on acid zinc electrodeposited steel	500	468.2	537	502
Organic topcoat (based on 12 nm silica particles)	292	300.8	303.5	299
Organic topcoat (based on 22 nm silica particles) on a trivalent CCC (Tripass LT1500) on acid zinc electrodeposited steel	538	566	558.8	554
Organic topcoat (based on 22 nm silica particles)	346	417	410.7	391

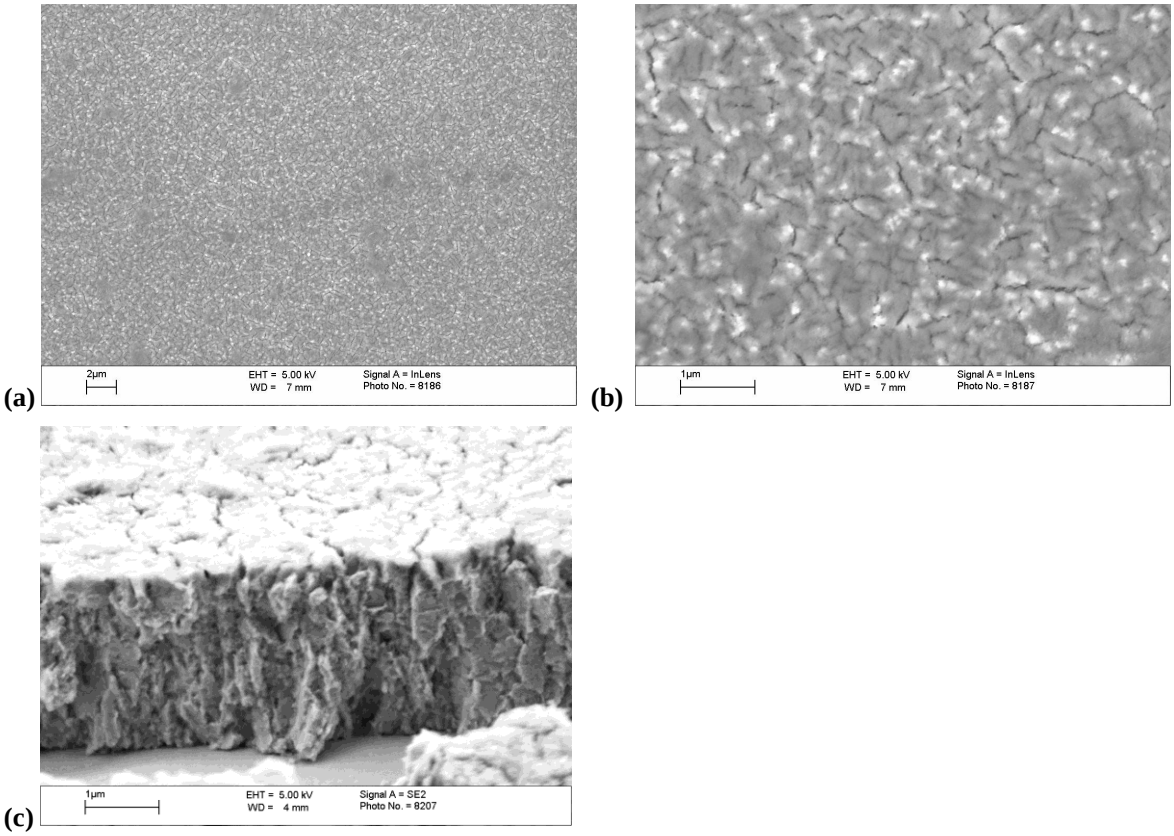

Figure 4.51 FEGSEM micrographs of black trivalent CCC on acid zinc electrodeposited steel (a-b), cryo fractured image (c). Samples were gold coated.

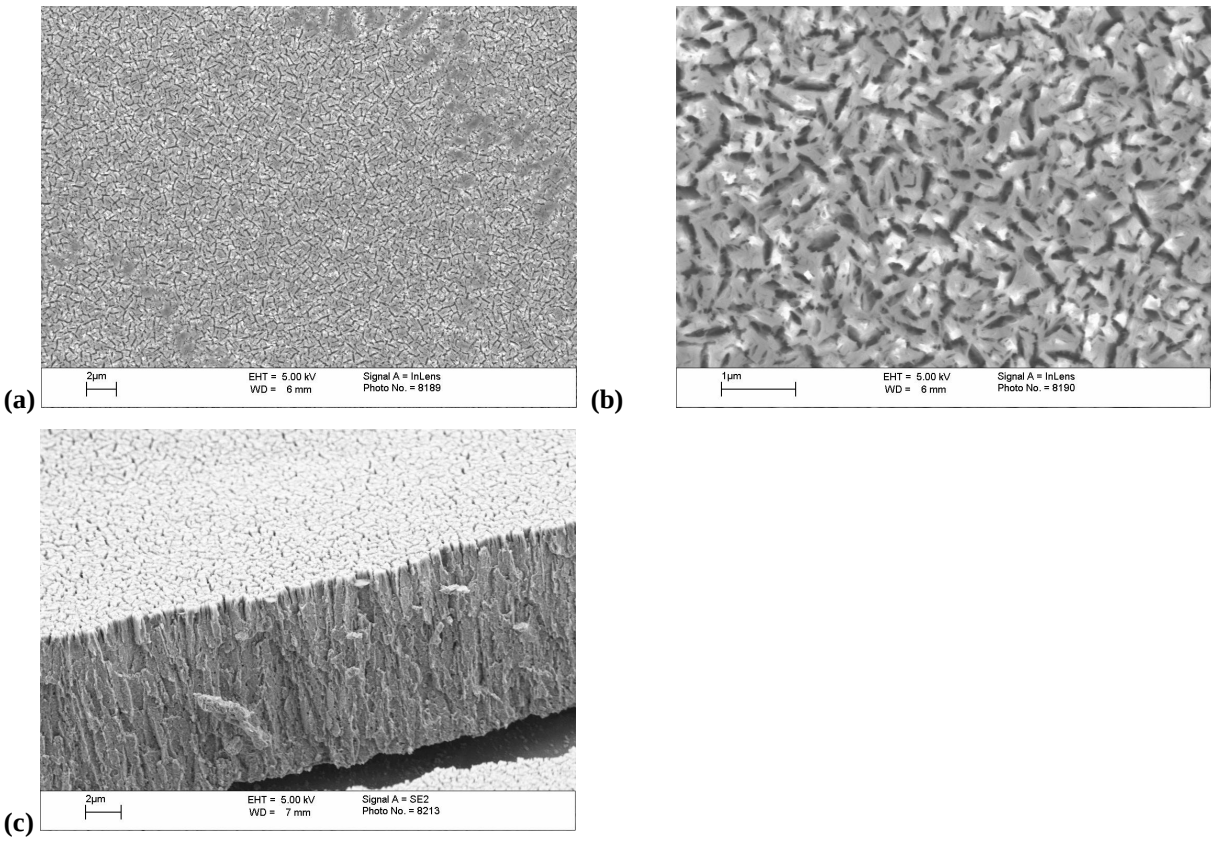

Figure 4.52 FEGSEM micrographs of black trivalent CCC on alkaline zinc electrodeposited steel (a-b), cryo fractured image (c). Samples were gold coated.

4.1.5.2 Black trivalent CCC on alkaline zinc electrodeposited steel

FEGSEM images of black trivalent CCC on alkaline zinc electrodeposited steel surface morphology exhibit an extensive network of randomly orientated micro-cracks; Figure 4.52a-b. Crack widths are larger than that of black trivalent CCC formed on acid zinc electrodeposited steel and hence are easily distinguished. Again, as with the black trivalent CCC formed on acid zinc electrodeposited steel, the interface between the conversion coating and underlying zinc electrodeposited steel is difficult to distinguish and hence the conversion coating thickness was taken as the length of cracks in the z-axis direction and was found to be 859 nm; Figure 4.52c.

4.1.6 Organic topcoat surface morphologies on a trivalent CCC

FEGSEM images of a trivalent CCC (Tripass LT1500) on acid zinc electrodeposited steel with the inclusion of a 12 nm size nano-silica based topcoat exhibit a surface morphology free from micro-cracks and any other physical defects; Figure 4.53a-b. A FEGSEM cross-section of the topcoat, conversion coating and zinc electrodeposited steel reveals distinct regions between the different interfaces; Figure 4.53c. The average conversion coating and topcoat thicknesses were measured to be 203 and 299 nm respectively; Table 4.11.

For a 22 nm size nano-silica based topcoat FEGSEM images reveal a rough surface morphology; Figure 4.54 a-b. The dark regions (area a) exhibited in FEGSEM backscatter mode; Figure 4.54a, were originally thought to be pores, however, a high magnification image of this region; Figure 4.54b, and EDX scans of this region (area A); Table 4.12, indicates that this is possibly a cluster of silica based nano-particles. A FEGSEM image of the coating's cross-section appears to be similar to that of the coating using a 12 nm particle size with the exception that the topcoat based on 22 nm particles is thicker (391 nm); Table 4.11.

Table 4.12 EDX at. % values of Area A and B of Figure 4.54a.

Element	Area A at. %	Area B at. %
C	5.6	8.0
O	26.4	18.3
Al	0.7	0.8
Si	30.3	15.1
Cr	0.9	1.2
Zn	36.1	56.6

(a)

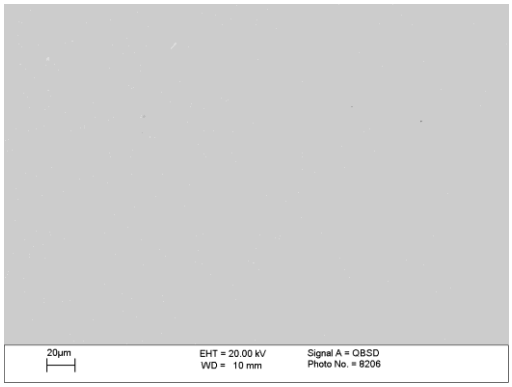

(b)

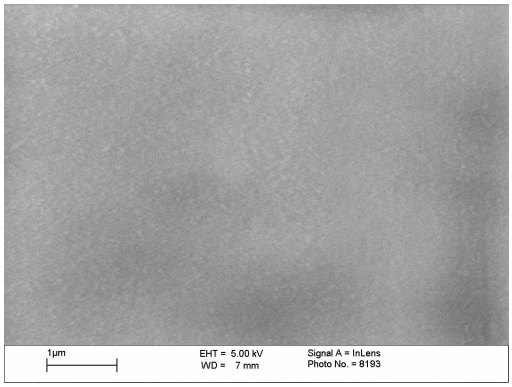

(c)

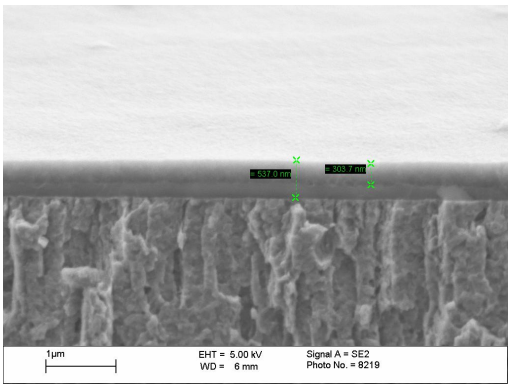

Figure 4.53 FEGSEM micrographs of Tripass LT1500 with an organic topcoat (based on 12 nm sized silica particles) on acid zinc electrodeposited steel (a-b), cryo fractured image (c). Samples were gold coated. Note annotations on (c) are unintended surplus measurements.

(a)

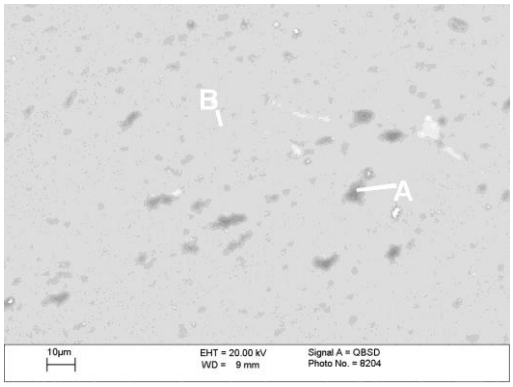

(b)

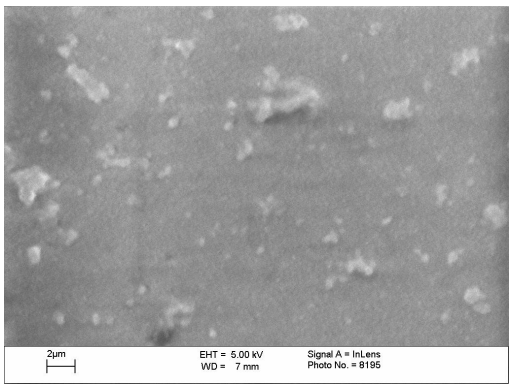

(c)

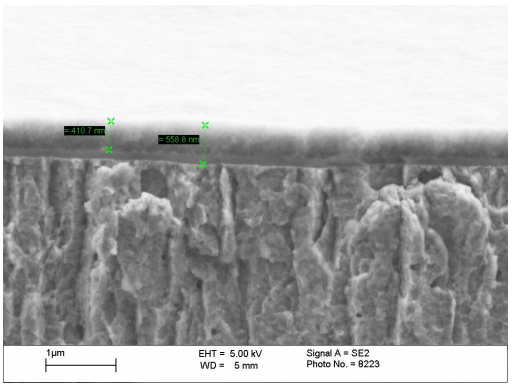

Figure 4.54 FEGSEM micrographs of Tripass LT1500 with an organic topcoat (based on 22 nm sized silica particles) on acid zinc electrodeposited steel (a-b), cryo fractured image (c). Samples were gold coated. Note annotations on (c) are unintended surplus measurements.

4.2 Chemical characterisation

4.2.1 X-ray Photoelectron Spectroscopy (XPS)

In order to determine the precise oxidation states of selected conversion coatings, high resolution XPS data of hexavalent CCCs, trivalent CCCs and a number of reference chromium compounds were investigated. The methodology used for the curve fitting of both Cr 2p and O 1s spectra is provided in Section 3.3.2.3. Both monochromatic and non-monochromatic Al X-ray sources were used, to compare data from both types of instrument. To avoid the possibility of photoreduction of Cr(VI), all samples were analysed individually with spectra acquired within 45 mins.

4.2.1.1 Reference chromium compounds

4.2.1.1.1 Chromium compounds : Survey scan data

XPS survey scan results were obtained using both monochromatic and non-monochromatic Al X-ray sources for the following reference chromium compounds: chromium trioxide (CrO_3), chromium oxide (Cr_2O_3), chromium chloride ($CrCl_3$) and chromium hydroxide ($Cr(OH)_3$). These quantitative results are provided in Tables 4.13 and 4.14. From the atomic percentages it is possible to calculate the ratio of O to Cr and Cl to Cr, and compare these to the nominal ratios of these compounds. In the case of monochromatic Al X-ray source data the $Cr(OH)_3$, CrO_3 and Cr_2O_3 ratios are very much in line with expected values. With the exception of a slightly higher than expected O level for $Cr(OH)_3$. The non-monochromatic Al X-ray source data for Cr_2O_3 and CrO_3 is also in line with expected values. In both X-ray source data, the Cl to Cr ratio for $CrCl_3$ compound, is significantly higher than expected. It is important to note that the O:Cr ratios from CrO_3 and Cr_2O_3 compounds may also be influenced by small levels of reduction and oxidation of chromium, particularly for the former. For $Cr(OH)_3$, some of the additional oxygen may be associated with strongly absorbed water, which may not have desorbed under vacuum and or X-ray beam exposure.

Table 4.13 Survey scan at. % data for reference chromium compounds using monochromatic Al X-ray source.

	Element at.%				Chromium Ratios	
	C 1s	O 1s	Cr 2p	Cl 2p	O:Cr	Cl:Cr
CrO_3	15.1	60.4	24.5	0.0	2.5	
Cr_2O_3	13.7	53.9	32.4	0.0	1.7	
$CrCl_3$	25.5	0.0	13.0	61.5		4.7
$Cr(OH)_3$	30.3	51.8	15.6	2.3	3.3	

Table 4.14 Survey scan at. % data for reference chromium compounds using non-monochromatic Al X-ray source.

	Element at.%				Chromium Ratios	
	C 1s	O 1s	Cr 2p	Cl 2p	O:Cr	Cl:Cr
CrO_3	27.8	52.8	19.4		2.7	
Cr_2O_3	13.5	54.9	31.6		1.7	
$CrCl_3$	18.0	3.4	14.6	64.0		4.4
$Cr(OH)_3$	33.7	50.6	13.3	2.4	3.8	

4.2.1.1.2 Chromium (III) oxide (Cr_2O_3) : High resolution XPS data

Figure 4.55 illustrates the difference in high resolution XPS data acquired from both monochromatic and non-monochromatic Al X-ray sources for the Cr 2p peak envelope of this sample. From the data it appears that the monochromatic Al X-ray source exhibits a greater detail of variations in the binding energy to intensity for this sample.

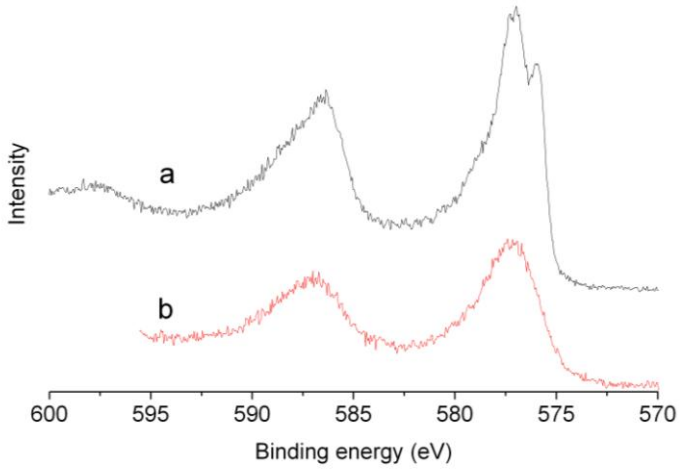

Figure 4.55 Monochromatic (a) and non-monochromatic (b) Al X-ray source Cr_2O_3 Cr 2p high resolution spectra.

A high resolution Cr 2p spectrum from the Cr_2O_3 control sample is provided in Figure 4.56a. The spectrum resembles the peak envelope observed by Biesinger et al. [66], Unveren et al. [67] and Ilton et al. [144]. Multiplet splitting is clearly evident on the $2p_{3/2}$ peak envelope as is a $2p_{1/2}$ satellite located around 597 eV. The corresponding $2p_{3/2}$ satellite may be overlapped by the Cr $2p_{1/2}$ peak envelope. The $2p_{3/2}$ peak envelope was fitted with four peaks in correspondence with distinct physical shoulders and general overall broadening. The full details of these peaks such maximum peak binding energy, FWHM and area percentage values are provided in Table 4.15. It is important to note that the introduction of peaks within curve fitting can be highly subjective. The use of a quantitative method, namely using a chi-square value which gives a degree of best fit, was attempted. It was felt that this value can be manipulated depending upon the number of peaks used within the model. First derivative plots of the data were also carried out, these appear to highlight noticeable physical inflections but does not take into account broadening of the peak envelope; see Figure 4.57a. The first derivative plots were also found to require prior smoothing [145] in order to improve the signal-to-noise of the data, thus potentially altering the data; see Figure 4.57b.

A high resolution Cr_2O_3 O 1s spectrum is provided in Figure 4.56b. A sharp peak and a shoulder are observed at around 530.45 and 531.56 eV respectively. Quantified data from this Figure are presented in Table 4.16.

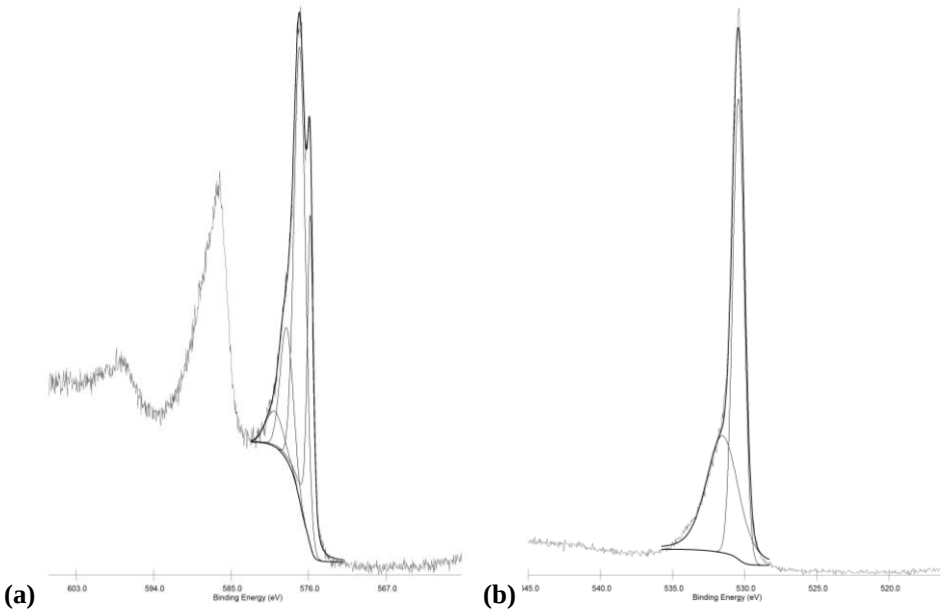

Figure 4.56 High resolution Cr 2p (a) and O 1s (b) spectra of Cr_2O_3 compound.

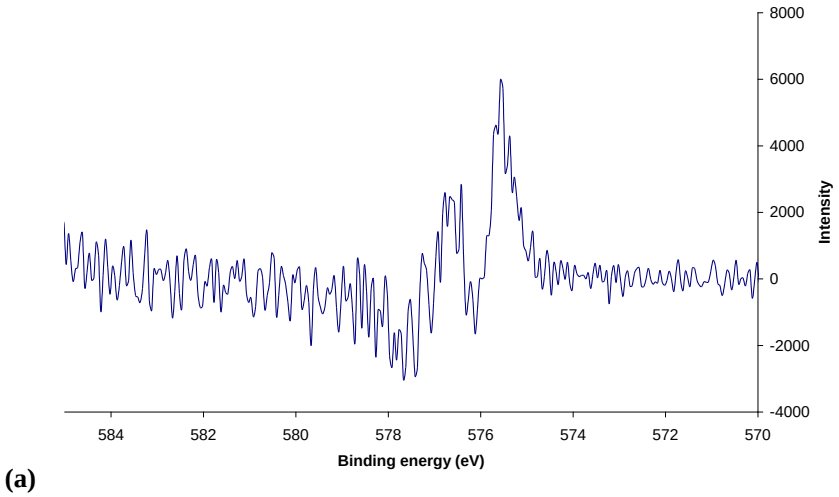

(a)

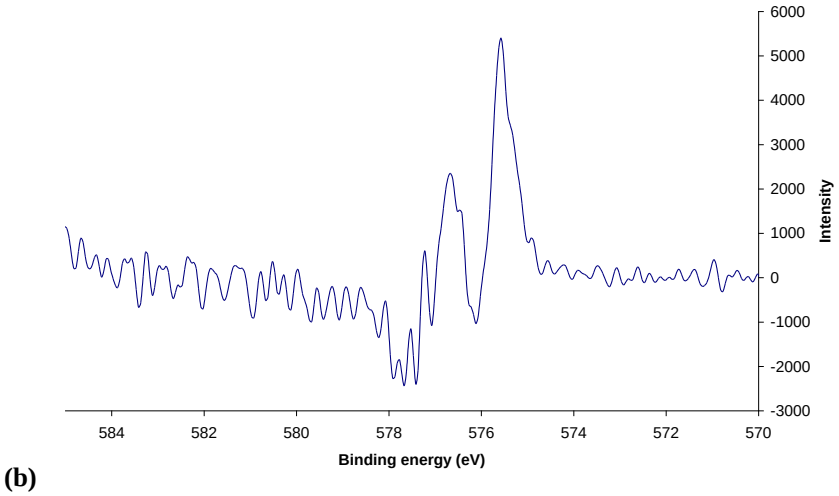

(b)

Figure 4.57 (a) A first derivative plot of Cr_2O_3 high resolution Cr 2p data, without smoothing, (b) First derivative plot of Cr_2O_3 high resolution Cr 2p data, with prior smoothing using Savitsky and Golay least squares central point smoothing method [145]**.**

4.2.1.1.3 Chromium (VI) oxide (CrO_3) : High resolution XPS data

A high resolution Cr 2p spectrum from the CrO_3 control is provided in Figure 4.58a. The peak envelope again is similar to the Cr(VI) spectrum peak envelope observed by Biesinger et al. [66]. The main peak maximum of 579.96 eV from the $2p_{3/2}$ spectrum is, however, higher than that cited by Biesinger et al. [66] for a $PbCrO_4$ crocoite compound (578.9 eV) and the average value based on National Institute of Standards and Technology (NIST) XPS database for Cr(VI) compounds which is 579.5 eV [66,146]. It is important to note that although the chromium compounds referred to may be similar in oxidation state to that used in this investigation, their respective chemical environment i.e. groups present in different compounds could also contribute towards slightly different binding energy values.

In this instance the Cr $2p_{3/2}$ peak envelope does not show any evidence of multiplet splitting, or additional satellite structures. Additional peaks either side of the main $2p_{3/2}$ maximum peak may be due to reduction under vacuum and/or X-ray beam exposure of Cr(VI). Such artefacts have previously been reported by Chidambaram et al. [64], Kagwade et al. [65] and Zhang et al. [48]. Using the peak maximum binding energy (BE) values 578.30 and 581.06 eV from curve fitting data in Table 4.15 it may be possible to ascribe $Cr(OH)_3$ to the former, whilst the latter could be associated with a compound impurity or background contribution.

A high resolution O 1s spectrum, from the CrO_3 control, is provided in Figure 4.58b. The peak envelope is similar to that observed for Cr_2O_3; see Figure 4.56b, however, the shoulder is less pronounced and is reflected by its reduced relative peak area; see Table 4.16. The binding energy values for the main and shoulder peaks, in comparison to Cr_2O_3, are ~0.3 eV higher.

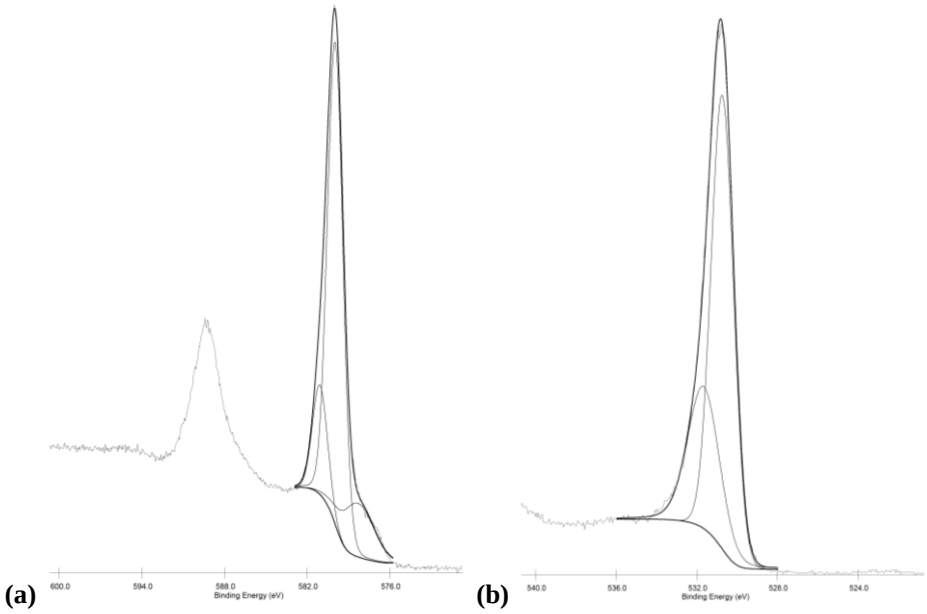

Figure 4.58 High resolution Cr 2p (a) and O 1s (b) spectra of CrO_3 compound.

4.2.1.1.4 Chromium (III) chloride ($CrCl_3$) : High resolution XPS data

A high resolution Cr 2p spectrum from the $CrCl_3$ control is provided in Figure 4.59 and has been curve fitted with four peaks. The peak envelope is again similar to that observed by Biesinger et al. [66]. In this case multiplet splitting of the Cr $2p_{3/2}$ peak is evident as is a separate small peak observed around 583.50 eV, thought to be due to a shake up peak [62].

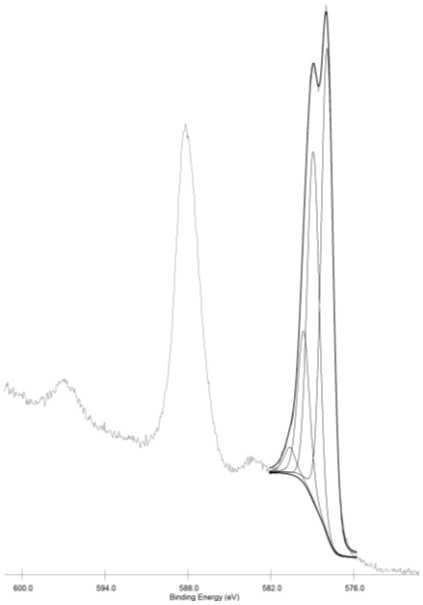

Figure 4.59 High resolution Cr 2p spectrum of $CrCl_3$ compound.

4.2.1.1.5 Chromium hydroxide $Cr(OH)_3$: High resolution XPS data

A high resolution Cr 2p spectrum from the $Cr(OH)_3$ control is shown in Figure 4.60a. The $2p_{3/2}$ peak maximum binding energy value was established as 577.79 eV; see Table 4.15. This, in fairly good agreement with binding energy values listed by other researchers, is high (c.f. 577.3 eV) [48,66]. It could be that the slightly higher binding energy value observed in this investigation is a function of the remaining $CrCl_3$ from the preparation process of $Cr(OH)_3$ which has a value of 577.93 eV. However, on inspection of survey scan results only 2.3% Cl was detected and the absence of $2p_{3/2}$ peak splitting, in Figure 4.59 suggests that this is unlikely. The binding energy value also indicates that the drying method used for the preparation of this standard did not have the effect of transforming $Cr(OH)_3$ to Cr_2O_3; see Table 4.15.

It is important to note that a $2p_{1/2}$ satellite can be observed on the spectra at around 598 eV. The corresponding $2p_{3/2}$ satellite may be overlapped by the Cr $2p_{1/2}$ peak envelope.

A high resolution O 1s spectrum from this sample is provided in Figure 4.60b. The binding energy value of the major peak at 531.91 eV is at least 1 eV higher than that observed in the case of Cr_2O_3 and CrO_3; see Table 4.16. Peak shoulders are clearly observed either side of the major peak maximum. Their peak maximum positions of 533.07 and 530.39 eV could be representative of water containing species as well as oxygen associated with other forms of chromium such as Cr_2O_3 or CrO_3.

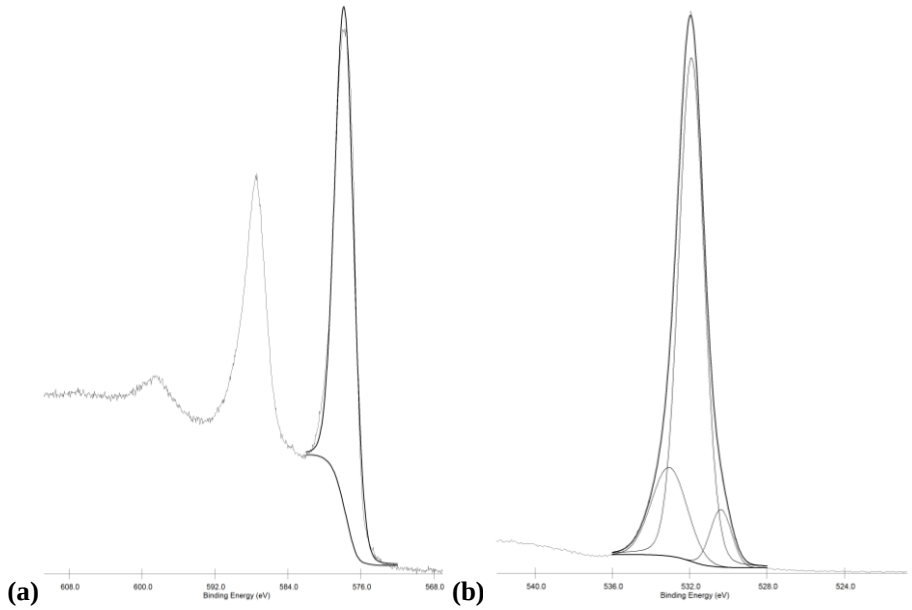

Figure 4.60 High resolution Cr 2p (a) and O 1s (b) spectra of $Cr(OH)_3$ compound.

4.2.1.1.6 Zinc oxide (ZnO) : High resolution XPS data

In this present investigation it was found that Zn $L_3M_{23}M_{45}$ Auger peaks at ~576 eV and ~585 eV have the potential of overlapping the Cr 2p photoelectron peaks at ~577 and ~586 eV for a chromium conversion coated zinc substrate. This problem is only observed for data acquired using an Al X-ray source. Therefore, in order to take account of these Auger peaks within the XPS spectra from CCC on zinc high resolution Zn Auger were acquired in the LMM region from a ZnO standard. Figure 4.61a provides the corresponding high resolution Zn LMM spectrum from a ZnO control with curve fitting carried out on the ~576 eV $L_3M_{23}M_{45}$ envelope. The distinctive broad slope of this peak merited the use of two peaks for curve fitting. The respective peak maximum binding energy, FWHM and area percentage values are provided in Table 4.15. It is important to note that Auger peaks have been charge referenced to C 1s, to take into account of charging as a conversion coating is semi-conducting and is not entirely a flat topography. A similar approach has been taken on all chromium compound control samples.

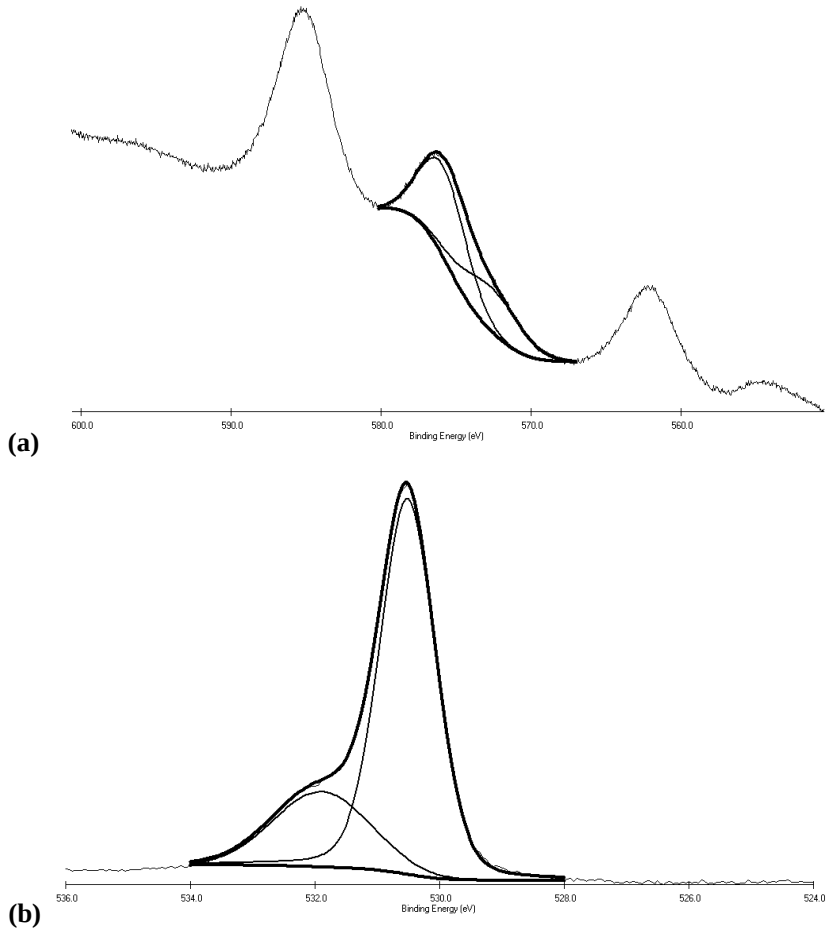

Figure 4.61 High resolution Zn LMM (a) and O 1s (b) spectra of ZnO compound.

A high resolution O 1s spectrum from the ZnO control is provided in Figure 4.61b. The binding energy value of the major peak at 530.52 eV is similar to that of Cr_2O_3 and CrO_3; see Table 4.16. A peak shoulder is observed to the left of the major peak maximum at 531.89 eV and is similar to that of Cr_2O_3 or CrO_3.

Table 4.15 Cr $2p_{3/2}$ and Zn LMM curve fitted peak maximum BE, FWHM and area % values. All binding energy values are charge corrected to C 1s at 285 eV.

Standard	Peak 1 (eV)	FWHM	%	Peak 2 (eV)	FWHM	%	Peak 3 (eV)	FWHM	%	Peak 4 (eV)	FWHM	%
Cr_2O_3	575.83	0.8	24.59	577.03	1.55	52.16	578.56	1.74	17.02	579.97	2.4	6.24
CrO_3	578.30	2.70	15.40	579.96	1.33	69.59	581.06	1.28	15.01	-	-	-
$CrCl_3$	577.93		48.10	578.93		33.19	579.63		15.39	580.63		3.32
$Cr(OH)_3$	577.79	2.44	100	-	-	-	-	-	-	-	-	-
ZnO	573.49	4.45	37.13	576.72	3.59	62.87						

Table 4.16 O $1s_{1/2}$ curve fitted peak maximum BE, FWHM and area % values. All binding energy values are charge corrected to C 1s at 285 eV.

Sample	O 1s (left peak) (eV)	FHWM	Area %	O 1s (main) (eV)	FHWM	Area %	O 1s (right peak) (eV)	FHWM	Area %
$Cr(OH)_3$	533.07	2.15	17.6	531.91	1.54	75.4	530.39	1.30	6.9
CrO_3	531.81	1.58	30.4	530.74	1.31	69.6			0.0
Cr_2O_3	531.56	2.79	42.9	530.45	0.93	57.1			0.0
ZnO	531.89	1.83	24.04	530.52	1.05	75.96			

Table 4.17 Summary of relative peak area % for Cr $2p_{3/2}$ of chromium coating data curve fitted using Cr_2O_3, $Cr(OH)_3$ and CrO_3 as reference compounds as well as ZnO LMM. All energy values are charge corrected to C 1s at 285 eV. Full details of related peak maximum BE, FWHM presented in Appendix B.

Sample	CrO_3 (%)	$Cr(OH)_3$ (%)	Cr_2O_3 (%)	ZnO (%)
Hexavalent CCC	27.47	69.34	1.13	2.06
Trivalent CCC	0.00	24.52	32.33	43.15
Hexavalent CCC 10° TOA	30.54	69.46	0.00	0.00
Hexavalent CCC 30° TOA	33.48	64.39	0.00	2.13
Hexavalent CCC + NaCl	8.69	79.20	9.24	2.87
Trivalent CCC + NaCl	0.00	44.39	35.03	20.58

Table 4.18 Hexavalent and trivalent CCC O $1s_{1/2}$ curve fitted peak maximum BE, FWHM and area % values. All binding energy values are charge corrected to C 1s at 285 eV.

Sample	O 1s BE (left peak (eV)	FHWM	Area %	O 1s BE (main) (eV)	FHWM	Area %	O 1s BE (right peak) (eV)	FHWM	Area %
Hexavalent CCC	533.23	1.98	19.6	531.92	1.44	67.5	530.69	1.29	12.9
Hexavalent CCC (flood gun)	533.33	2.01	21.7	532.10	1.46	64.9	530.85	1.35	13.4
Trivalent CCC			0.0	531.53	1.96	94.6	529.72	1.36	5.4
Hexavalent CCC (10° TOA)	533.30	2.05	25.4	532.14	1.58	62.7	530.88	1.54	11.9
Hexavalent CCC (+ NaCl exposure)	532.72	2.08	30.3	531.85	1.28	54.8	530.87	1.67	14.9
Trivalent CCC (+ NaCl exposure)			0.0	531.70	1.77	96.4	529.93	1.15	3.6

4.2.1.2 Hexavalent and trivalent CCC

4.2.1.2.1 Untreated : Survey scan XPS data

XPS survey scans for an hexavalent and trivalent CCC are provided in Figures 4.62 and 4.63. These were obtained using a monochromatic Al X-ray source. Atomic % quantification values for individual elements detected have not been included. This is because the most intense chromium photoelectron peaks used for quantification are overlapped by zinc Auger peaks. Therefore, survey scans have only been analysed for the identification of elements. The values listed on the Figures are only approximate, given the resolution.

Analysis of the hexavalent and trivalent CCCs exhibited carbon photoelectron and Auger peaks at 285 eV (C 1s) and 1226 eV (C $KL_{23}L_{23}$). The presence of carbon could be the result of atmospheric contamination and / or absorbed organic constituents from the base formulation. The latter is likely to be associated more with the trivalent CCC; see Section 5.4 and 5.4.1. Chromium photoelectron peaks are also observed in both conversion coatings at 45/46 eV (Cr $3p_{1/2}$ and Cr $3p_{3/2}$) and 577/586 eV (Cr $2p_{3/2}$ and Cr $2p_{1/2}$). The intensity of both photoelectron peaks is less pronounced for trivalent CCC in comparison to the hexavalent CCC. There is also a tiny chromium Auger peak observed at 962 eV indicative of the Cr $L_3M_{23}M_{45}$ line for hexavalent CCC.

A major oxygen photoelectron peak is observed at ~531 eV, O 1s, for both conversion coatings. In addition, a small photoelectron peak is observed at 23 eV, O 2s, for the hexavalent CCC. Oxygen KLL Auger peaks are also observed at 1012, 997 and 976 eV, with the latter most intense in both conversion coatings.

Major zinc photoelectron peaks at 1022 eV Zn $2p_{3/2}$, and 1045 eV Zn $2p_{1/2}$, are observed for both conversion coatings, with a greater intensity for trivalent CCC. In addition other zinc photoelectron peaks at 140 eV Zn 3s, 92/89 eV Zn $3p_{1/2}$ / Zn $3p_{3/2}$ and 10 eV Zn 4d were also observed for trivalent CCC. Zinc LMM Auger peaks are observed for trivalent CCC at 662, 655, 585, 576, 562, 498 and 475 eV. Some of these peaks are intense and overlap Cr 2p photoelectron peaks which are located in similar energy positions. In the case of hexavalent CCC zinc Auger peaks are less intense and only some are observed.

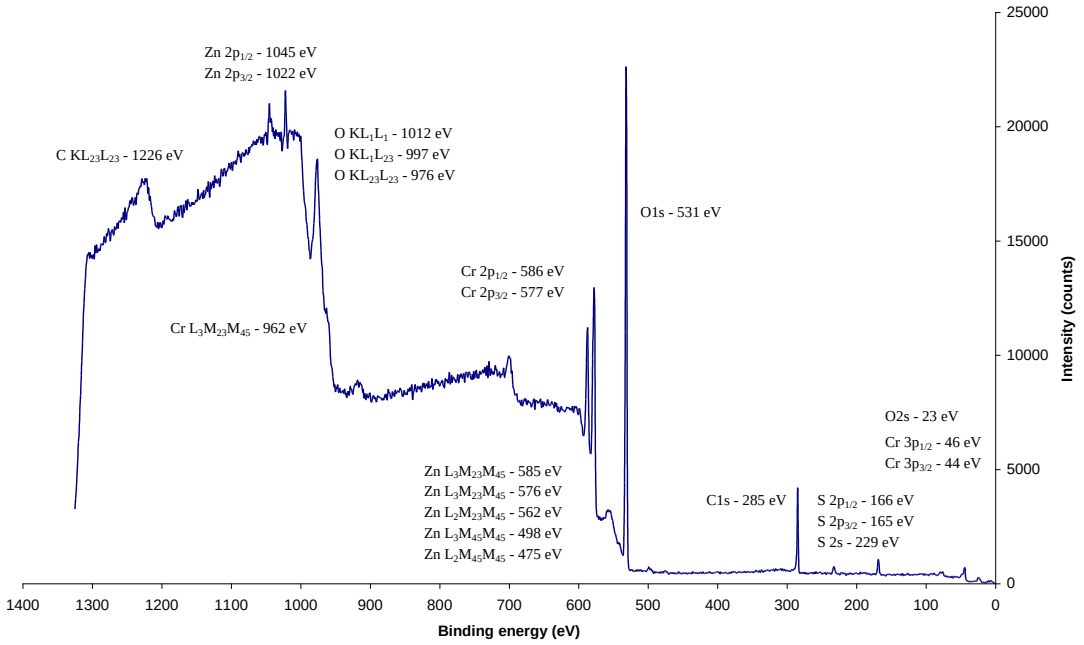

Figure 4.62 Monochromatic Al X-ray source XPS survey scan of a chromate A conversion coating (20 s) on acid zinc electrodeposited steel. BE values listed are approximate.

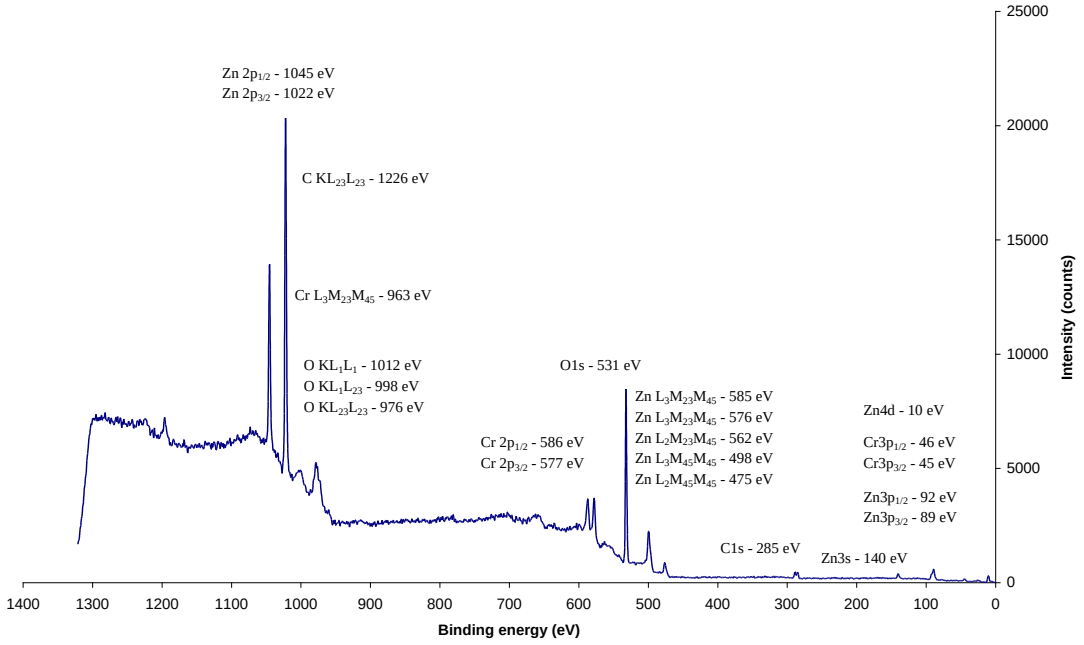

Figure 4.63 Monochromatic Al X-ray source XPS survey scan of a trivalent CCC (90 s) on acid zinc electrodeposited steel. BE values listed are approximate.

In the case of the hexavalent CCC, in addition to carbon, oxygen, zinc and chromium photoelectron peaks, sulphur peaks were also observed at 166/165 eV S $2p_{1/2}$ and S $2p_{3/2}$ and at 229 eV S 2s. Sulphur is expected given that sulphuric acid was used as part of the

hexavalent CCC treatment solution formulation. It is important to note, however, that no cobalt or molybdenum photoelectron peaks were observed for the trivalent CCC which included these elements as part of its treatment solution formulation. The lack of cobalt and molybdenum may indicate that these elements are not present at the surface of the coating, that these elements play no part in the film formation process, or that the levels of cobalt nitrate and sodium molybdate added as part of the formulation is insufficient for incorporation of cobalt or molybdenum.

4.2.1.2.2 Effect of 5% NaCl solution exposure : Survey scan XPS data

To evaluate the chemistry of the conversion coatings following simulation of a corrosive environment, samples were exposed to 18 h 5% NaCl solution exposure. XPS survey scans of the hexavalent and trivalent CCC are provided in Figures 4.64 and 4.65, with analysis only of the elements present. In both spectra carbon photoelectron (C 1s) and Auger (C $KL_{23}L_{23}$) peaks were identified as previously seen in untreated sample spectra. Chromium photoelectron peaks (Cr 2p and Cr 3p) are clearly present in the conversion coating spectra, with the intensity of both Cr 2p and Cr 3p photoelectron peaks being more pronounced for hexavalent CCC in comparison to that of trivalent CCC. There is, however, significant 2p peak envelope increase for trivalent CCC compared with the zinc indicating either loss of zinc or migration of chromium or both.

Oxygen photoelectron (O 1s / O 2s) and Auger (KLL) peaks are again exhibited for both conversion coating spectra. Similar zinc photoelectron and Auger peaks as exhibited in untreated spectra of the respective conversion coatings are again exhibited. It may be that the change in Cr $2p_{1/2}$ peak envelope size for trivalent CCC is related to a decrease in intensity of an overlapping zinc (Zn $L_3M_{23}M_{45}$) Auger peak.

In the case of hexavalent CCC the sulphur photoelectron peaks observed are less pronounced in comparison to the untreated spectrum.

Within both conversion coatings only a very small signal for chlorine (2p) was observed, and therefore the curve fitting of high resolution Cr 2p hexavalent and trivalent CCC spectra was not fitted with the Cr 2p $CrCl_3$ reference peak.

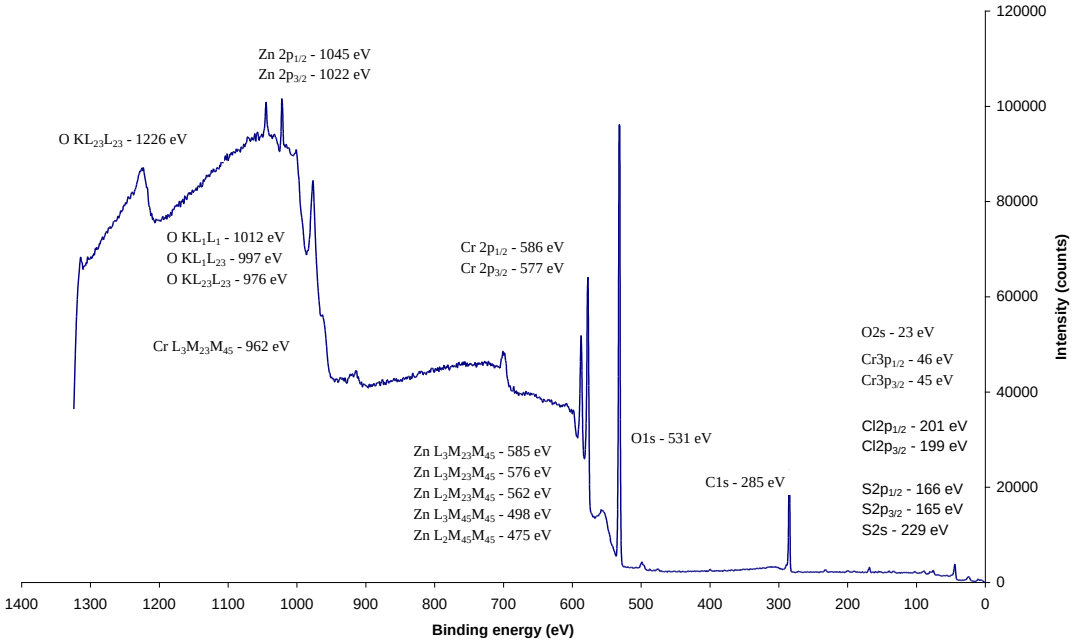

Figure 4.64 Monochromatic Al X-ray source XPS survey scan of a chromate A conversion coating (20 s) on acid zinc electrodeposited steel following exposure to 18 h 5% NaCl solution. BE values listed are approximate.

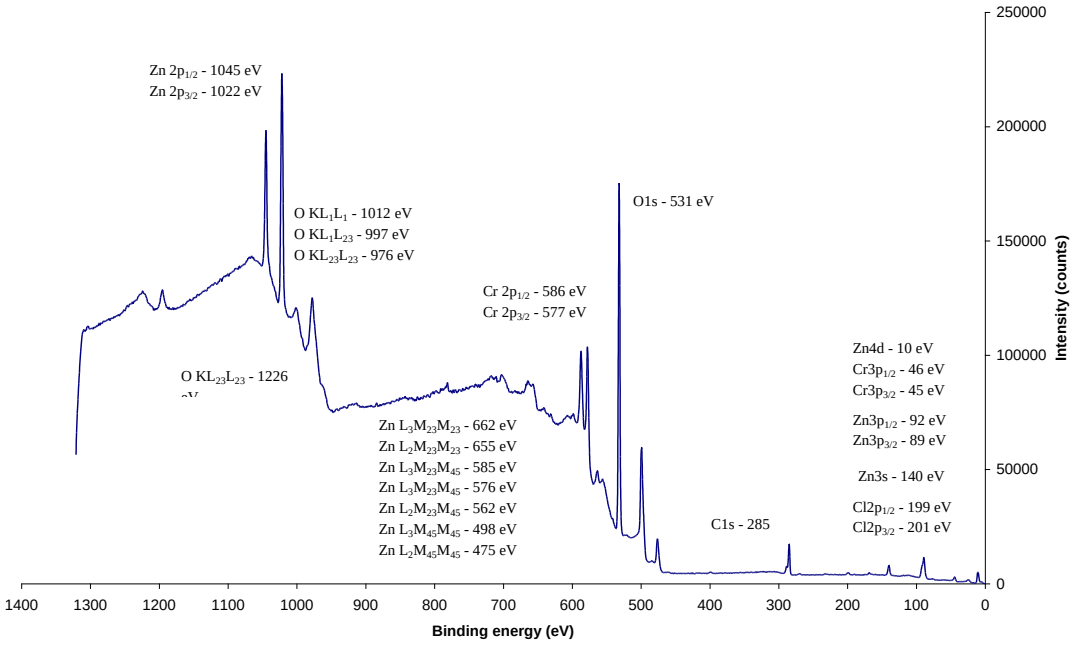

Figure 4.65 Monochromatic Al X-ray source XPS survey scan of a trivalent CCC (90 s) on acid zinc electrodeposited steel following exposure to 18 h 5% NaCl solution. BE values listed are approximate.

4.2.1.2.3 Untreated : High resolution XPS data

The Cr $2p_{3/2}$ peak, was chosen for curve fitting analysis as it provides the most intense photoelectron peak for chemical state evaluation. Hexavalent and trivalent CCC Cr 2p peak

envelope data for both are provided in Figures 4.66a and b. A marked difference between the two peak envelopes is a shoulder present on the $2p_{3/2}$ peak for the hexavalent CCC. Similar envelope shapes were also observed by other researchers [48,66]; see Figure 2.12 and 2.14.

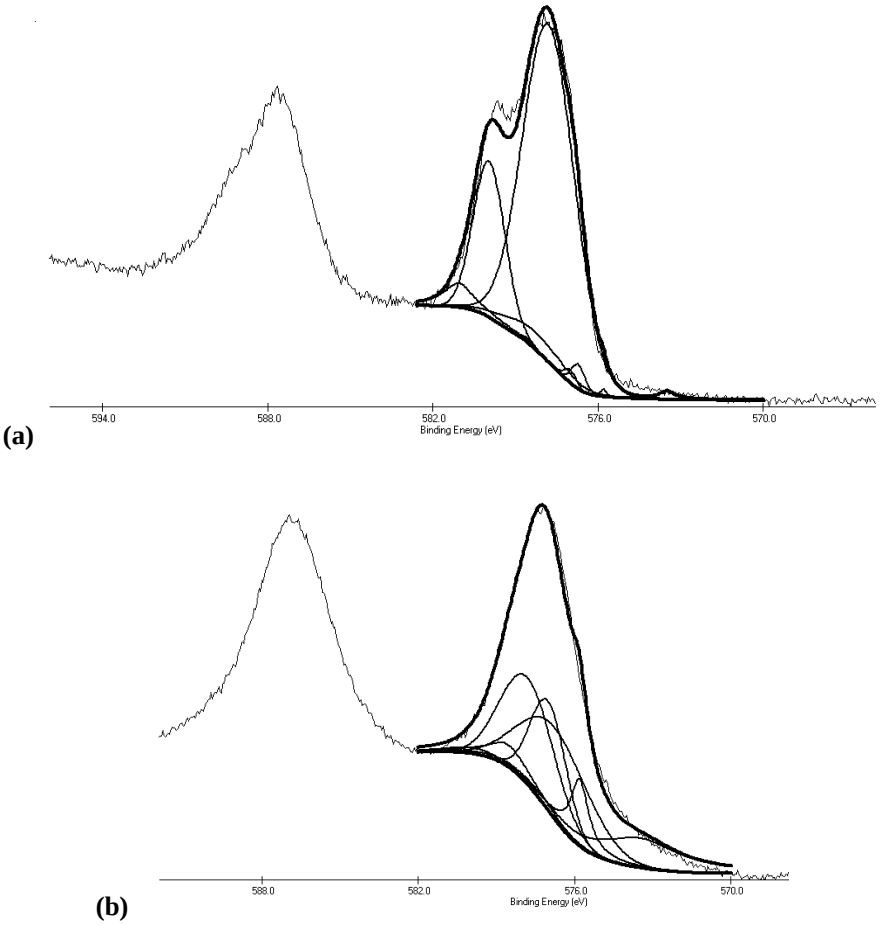

Figure 4.66 High resolution Cr 2p chromate A conversion coating (20 s) (a) and trivalent CCC (90 s) (b) on acid zinc electrodeposited steel spectra.

Curve fitting of the spectrum with CrO_3, Cr_2O_3, $Cr(OH)_3$ and ZnO reference peaks indicates that the shoulder region is associated with CrO_3 or of a similar chromium oxidation state species; see Table 4.17 and Appendix B. Curve fitting data also indicates that the remaining chromium content for hexavalent CCC is largely composed of $Cr(OH)_3$, with the remainder attributed to Cr_2O_3. The curve fitting model also indicated the presence of ~ 2% ZnO. This is consistent with the relatively small Zn 2p peak observed in Figure 4.62. In the case of trivalent CCC, curve fitting indicated a much larger contribution of ZnO within the envelope also indicated in Figure 4.63. This is further supported by a larger peak area for Cr $2p_{1/2}$, which clearly indicates an overlapping zinc Auger peak (Zn $L_3M_{23}M_{45}$). This zinc Auger peak area is proportionately larger than the overlapping Auger peak residing in the region of the Cr $2p_{3/2}$ peak, hence the large contribution of ZnO through curve fitting. Another characteristic of

the zinc Auger peak in this region is its distinctive slope as illustrated in Figure 4.61a, which is also observed in the trivalent CCC spectra. Even though measures have been taken to account for potential zinc within the curve fitting model, an ideal scenario would have been to use a monochromatic Mg X-ray source for the XPS analysis. This was not available in the present study. XPS data using this source would have ensured that overlapping zinc Auger peaks rest at different energy positions in correspondence to Equation 2.5. Importantly, curve fitting of the trivalent CCC indicates that no CrO_3 is detected and that the chromium layer is composed of $Cr(OH)_3$ and Cr_2O_3.

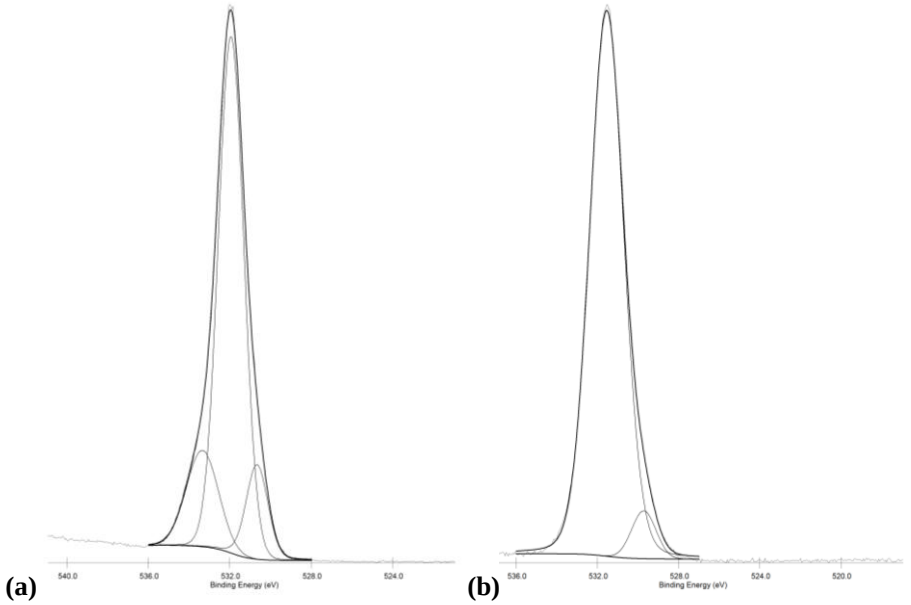

Figure 4.67 High resolution O 1s chromate A conversion coating (20 s) (a) and trivalent CCC (90 s) (b) on acid zinc electrodeposited steel spectra.

Oxygen 1s spectra for the coatings are shown in Figures 4.67a & b. The hexavalent CCC differs to that of the trivalent CCC peak envelope in that shoulders can be observed either side of the main peak maximum as opposed to just one side. Curve fitting of the O 1s peak envelope on the hexavalent CCC provides similar peak maximum binding energy positions to that of $Cr(OH)_3$ O 1s; see Tables 4.16 and 4.18. The $Cr(OH)_3$ sample spectrum also exhibits shoulders either side of the main peak maximum. This result confirms the previous conclusion that the hexavalent CCC is principally composed of $Cr(OH)_3$ and includes potential water containing species. In the case of the trivalent CCC curve fitting of the O 1s spectrum main oxygen peak maximum and shoulder peak binding energy value is difficult to ascribe to a given reference standard; Tables 4.16 & 4.18. This analysis is therefore indicating a complex mixture of chemistry. Given the high zinc content of the trivalent CCC this is somewhat expected.

4.2.1.2.4 Untreated hexavalent CCC depth profile : High resolution XPS data

Hexavalent CCC Cr 2p spectra taken at 10° and 30° TOA are shown in Figure 4.68a & b. The peak envelopes are very similar to that of the hexavalent CCC Cr 2p spectrum taken at 90° TOA; see Figure 4.66a. In all cases these spectra exhibit a shoulder region off the main peak maximum. Curve fitting once again indicates that the shoulder region is associated with CrO_3 or of a similar chromium oxidation state species; see Table 4.17. Curve fitting data also appears to show that at 10° and 30° TOA a slightly higher CrO_3 content and a reduction of Cr_2O_3 content is produced in comparison to the 90° TOA. However, variation between 10° and 30° TOA appears to be minimal, indicating a reasonably uniform composition within the sampling depth of this technique.

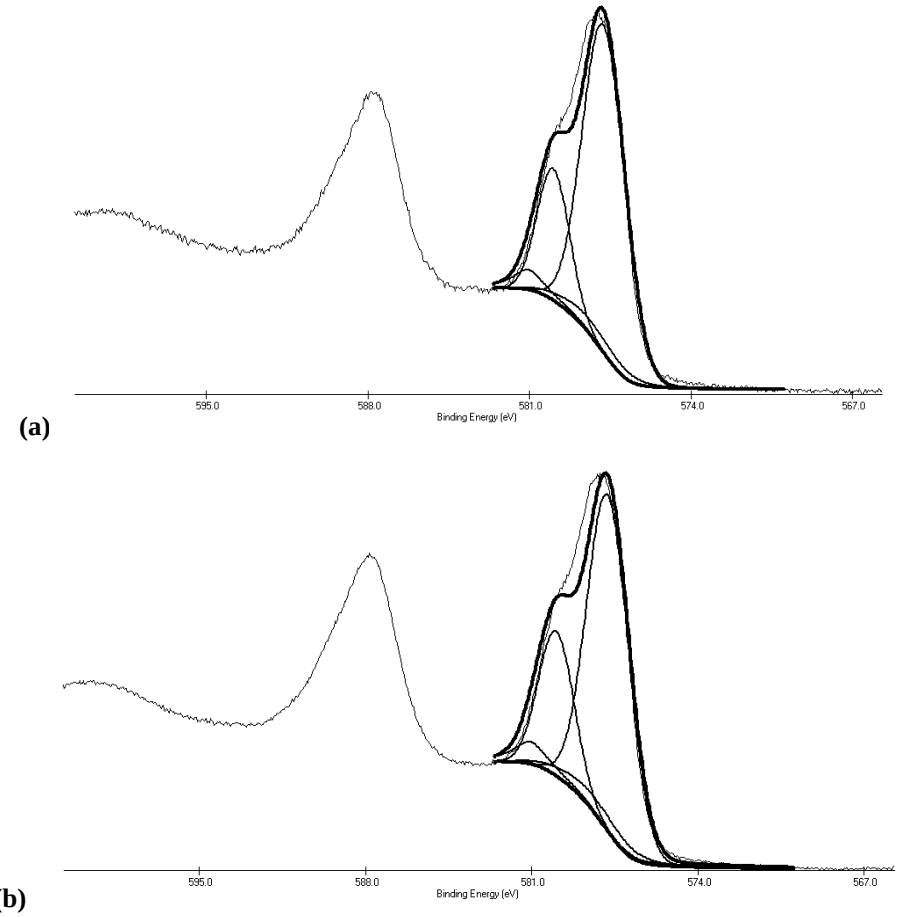

Figure 4.68 High resolution Cr 2p chromate A conversion coating (20 s) on acid zinc electrodeposited steel spectra taken at 10° (a) and 30° (b) TOA.

An O 1s spectrum of a hexavalent CCC taken at 10° TOA is shown in Figure 4.69. The peak envelope is similar to that of the hexavalent CCC 90° TOA spectrum peak envelope in which shoulders either side of the main peak maximum are present. Curve fitting of their respective

binding energy positions and area percentage are also similar; see Table 4.18. This confirms the above conclusion.

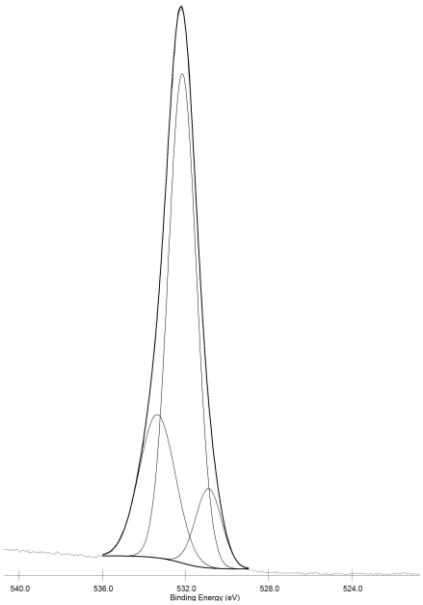

Figure 4.69 High resolution O 1s chromate A conversion coating (20 s) on acid zinc electrodeposited steel spectrum taken at 10° TOA.

4.2.1.2.5 Effect of 5% NaCl solution exposure : High resolution XPS data

Cr 2p spectra from both hexavalent and trivalent CCC, following exposure to 18 h 5% NaCl solution are provided in Figures 4.70a and b. Compared with the untreated coating, the Cr 2p peak envelope for the hexavalent CCC spectrum differs, with a reduction in the shoulder size associated with Cr(VI). This change in oxidation state was also observed by Zhang et al. [48]; see Figure 2.14. Curve fitting highlights a reduction in CrO_3 content, along with an increase in Cr_2O_3 and $Cr(OH)_3$; see Table 4.17. Curve fitting data from exposed trivalent CCC revealed an increase in the $Cr(OH)_3$ component and a decrease in the ZnO contents post salt solution exposure; see Table 4.17. The significant reduction in Zn:Cr ratios indicated in Table 4.17 is illustrated by comparing Figures 4.63 with 4.65.

Oxygen 1s spectra for the exposed coatings are provided in Figures 4.71a & b. The exposed hexavalent CCC, like that of the untreated spectra peak envelope exhibits shoulders either side of the main peak maximum. O 1s curve fitting of peak maximum binding energy positions shows that one of the shoulders has a reduced binding energy value from 533.23 to 532.72 eV, however, it also has an increased relative peak area from 19.6 to 30.3%. Curve fitting O 1s data of the exposed trivalent CCC shows relatively minor differences to that of the untreated coating.

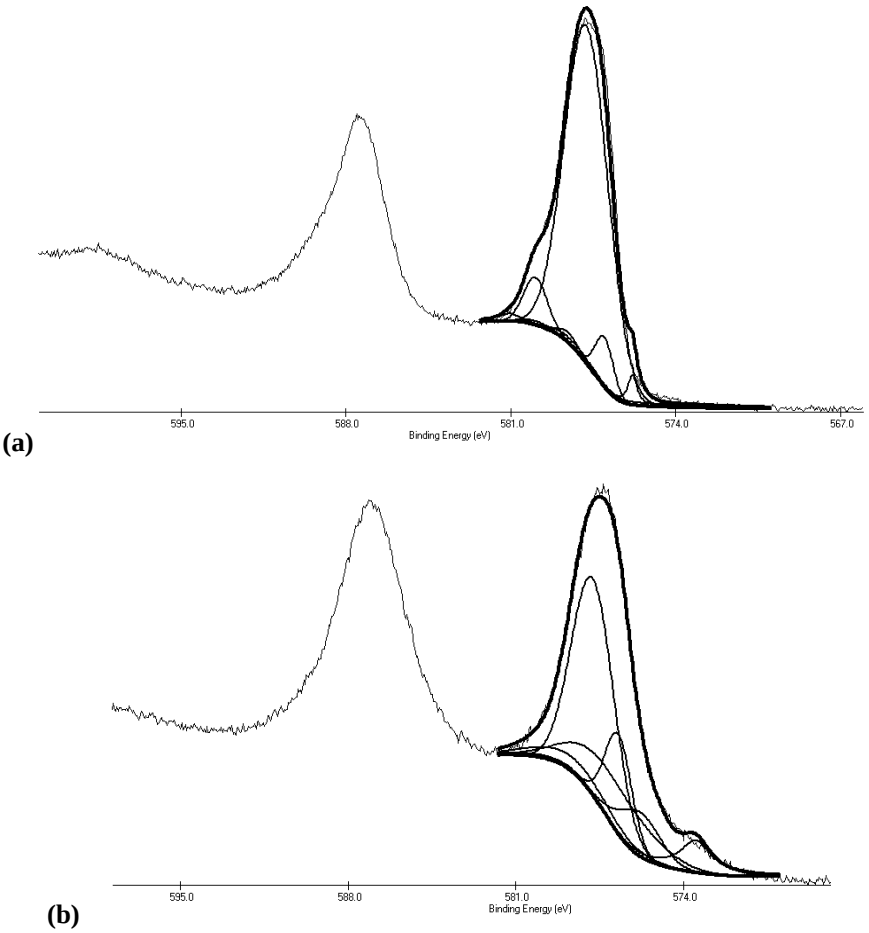

Figure 4.70 High resolution Cr 2p chromate A conversion coating (20 s) (a) and trivalent CCC (90 s) (b) on acid zinc electrodeposited steel spectra taken after 18 h 5% NaCl solution exposure.

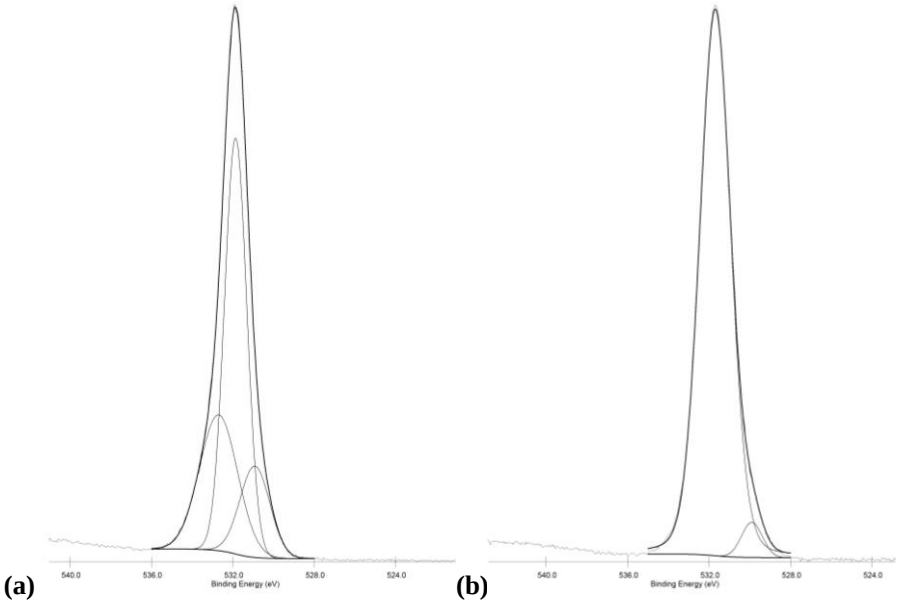

Figure 4.71 High resolution O 1s chromate A conversion coating (20 s) (a) and trivalent CCC (90 s) (b) on acid zinc electrodeposited steel spectra taken after 18 h 5% NaCl solution exposure.

4.2.1.3 Effect of Tripass LT1500 additives on conversion coating chemical composition

XPS was used to investigate the role of additives such as sodium molybdate, cobalt nitrate, malonic acid, oxalic acid and chromium nitrate within a trivalent CCC (Tripass LT1500) on a acid zinc electrodeposited steel substrate; see Table 3.7. Survey scans were carried out using a non-monochromatic Al X-ray source. Due to potential overlapping of zinc Auger peaks (576 eV $L_3M_{23}M_{45}$ and 585eV $L_3M_{23}M_{45}$) with photoelectron peaks of chromium (577 eV $2p_{3/2}$ and 586 eV $2p_{1/2}$) quantification results of survey scans are not presented, but rather the identification of elements was carried out from raw data only.

4.2.1.3.1 Tripass LT1500 control : Survey scan XPS data

Analysis of the XPS survey scan; see Figure 4.72, for the Tripass LT1500 control reveals the presence of a carbon photoelectron peak at 285 eV (C 1s) and possibly an Auger peak at 1226 eV ($KL_{23}L_{23}$), however, identification of the latter is difficult given it is overlapped by a Zn $2p_{3/2}$ photoelectron peak at 1022 eV. The presence of carbon could be related to atmospheric contamination and / or absorbed organic constitutes from the base formulation. Infrared spectra of the trivalent CCC, discussed later, may help in this conclusion; see Section 4.2.3.2.

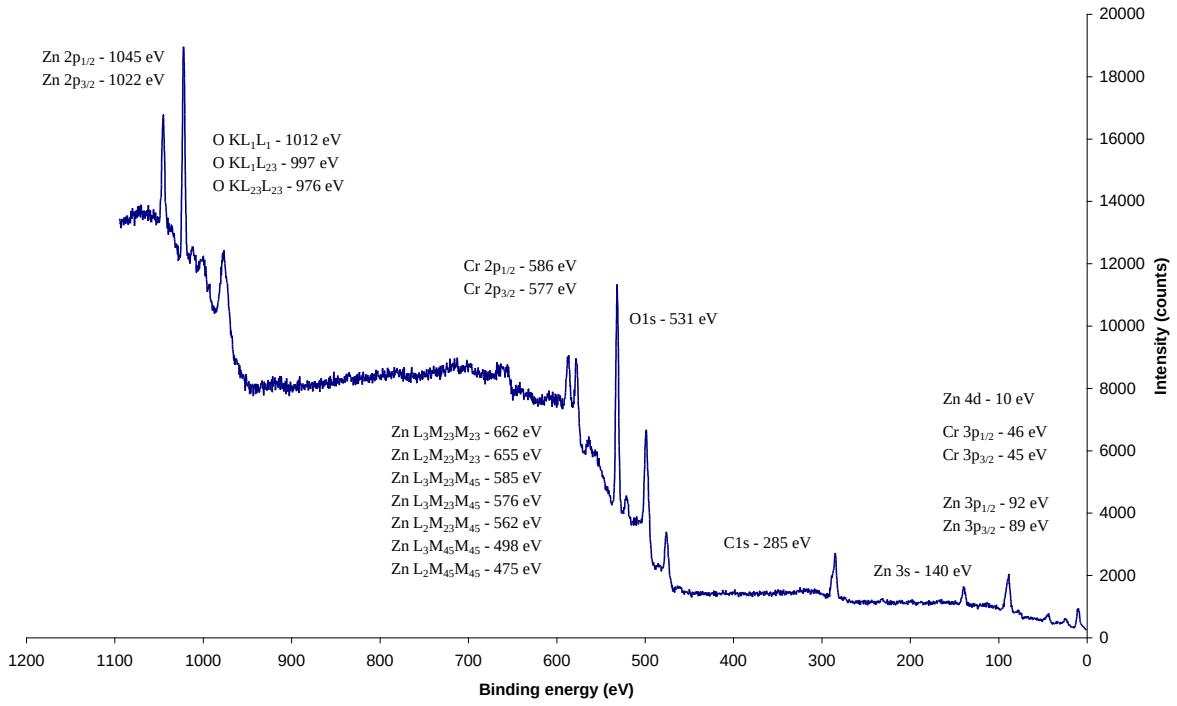

Figure 4.72 Non-monochromatic Al X-ray source XPS survey scan of Tripass LT1500-control (trivalent CCC) on acid zinc electrodeposited steel. BE values listed are approximate.

Also detected in the survey spectra are zinc and oxygen photoelectron and Auger peaks, with their main photoelectron peaks situated at 1022 and 531 eV. As mentioned above, a zinc

Auger peak (576 eV) overlaps a main chromium photoelectron peak (577 eV), however, at 45-46 eV Cr $3p_{1/2}$ and Cr $3p_{3/2}$ peaks have been identified and thus support the view that chromium is present within the conversion coating.

4.2.1.3.2 Effect of sodium molybdate : Survey scan XPS data

An XPS survey scan of Tripass LT1500 without sodium molybdate; see Figure 4.73, does not appear to differ from that of the Tripass LT1500 control. Chromium, oxygen, zinc and carbon still appear to be the main elements within the conversion coating.

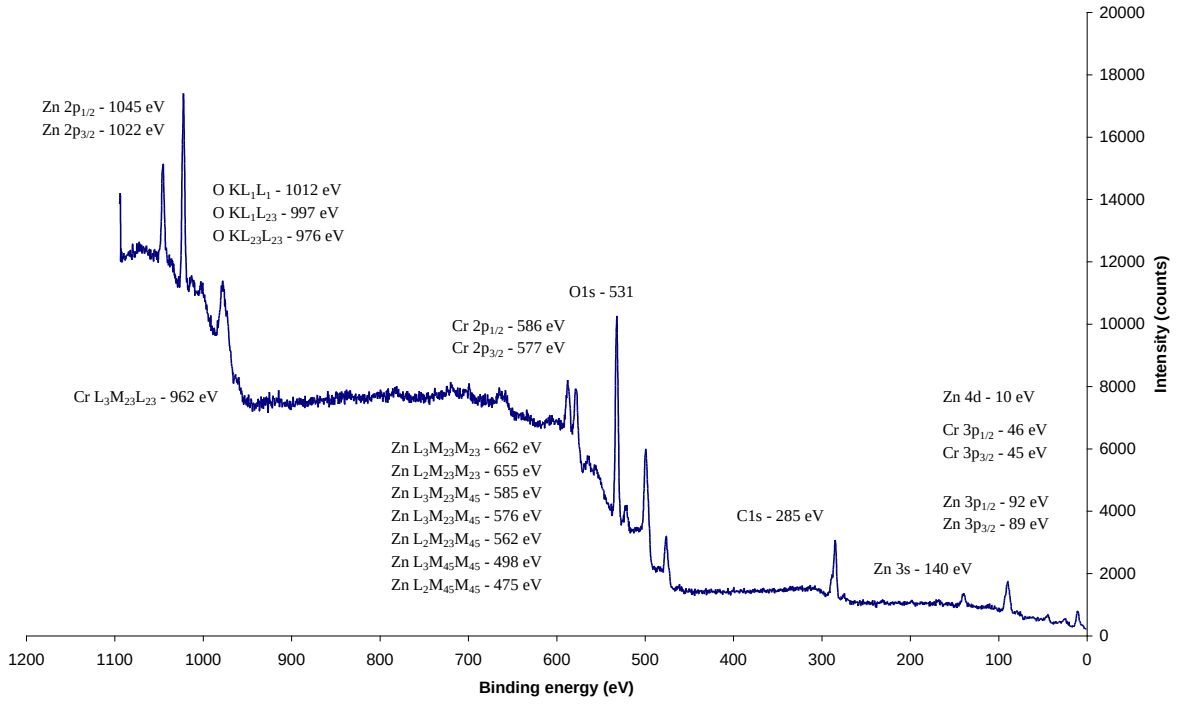

Figure 4.73 Non-monochromatic Al X-ray source XPS survey scan of Tripass LT1500 not containing sodium molybdate (trivalent CCC) on acid zinc electrodeposited steel. BE values listed are approximate.

An XPS survey scan of Tripass LT1500 with the inclusion of additional sodium molybdate (0.4 g/l) indicates the presence of molybdenum, along with the common elements detected; see Figure 4.74. The main molybdenum photoelectron peak at 230 eV (Mo $3d_{5/2}$), as well as those at 413 and 396 eV (Mo $3p_{1/2}$ and Mo $3p_{3/2}$), were identified within the XPS survey scan.

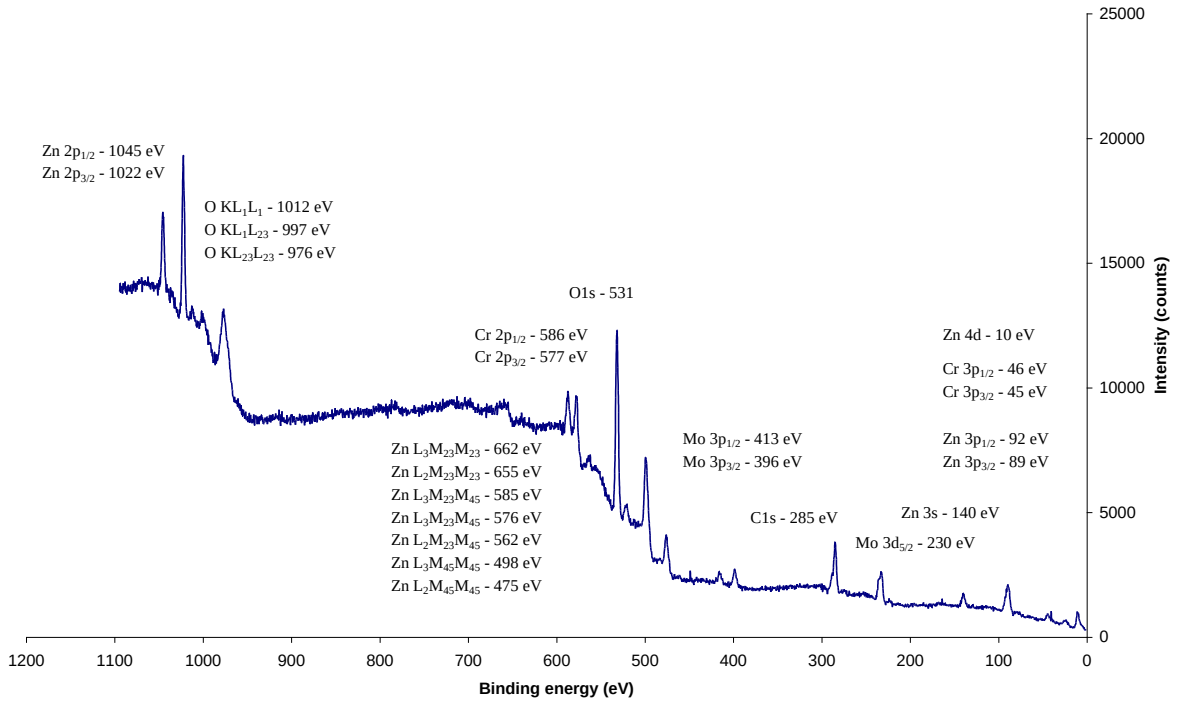

Figure 4.74 Non-monochromatic Al X-ray source XPS survey scan of Tripass LT1500 including 0.4 g/l sodium molybdate (trivalent CCC) on acid zinc electrodeposited steel. BE values listed are approximate.

4.2.1.3.3 Effect of cobalt nitrate : Survey scan XPS data

An XPS survey scan of Tripass LT1500 without cobalt nitrate; see Figure 4.75, resulted in the detection of chromium, oxygen, zinc and carbon as exhibited for a standard Tripass LT1500. In the case of the latter solution with the additional inclusion of cobalt nitrate (14.6 g/l) the additional presence of cobalt is revealed in the survey scan; see Figure 4.76. The main cobalt photoelectron peak at 781 eV has been identified (Co $2p_{3/2}$). It is also possible the corresponding Co $2p_{1/2}$ photoelectron peak at 796 eV is also present given its close location. It is also important to note there may also be possible signals, but not conclusive evidence, for further cobalt Auger lines at 701 ($L_2M_{23}M_{45}$), 716 ($L_3M_{45}M_{45}$), 779 eV ($L_3M_{23}M_{45}$) within the XPS survey scan. Signal-to-noise of the spectra make it difficult to assign these additional peaks.

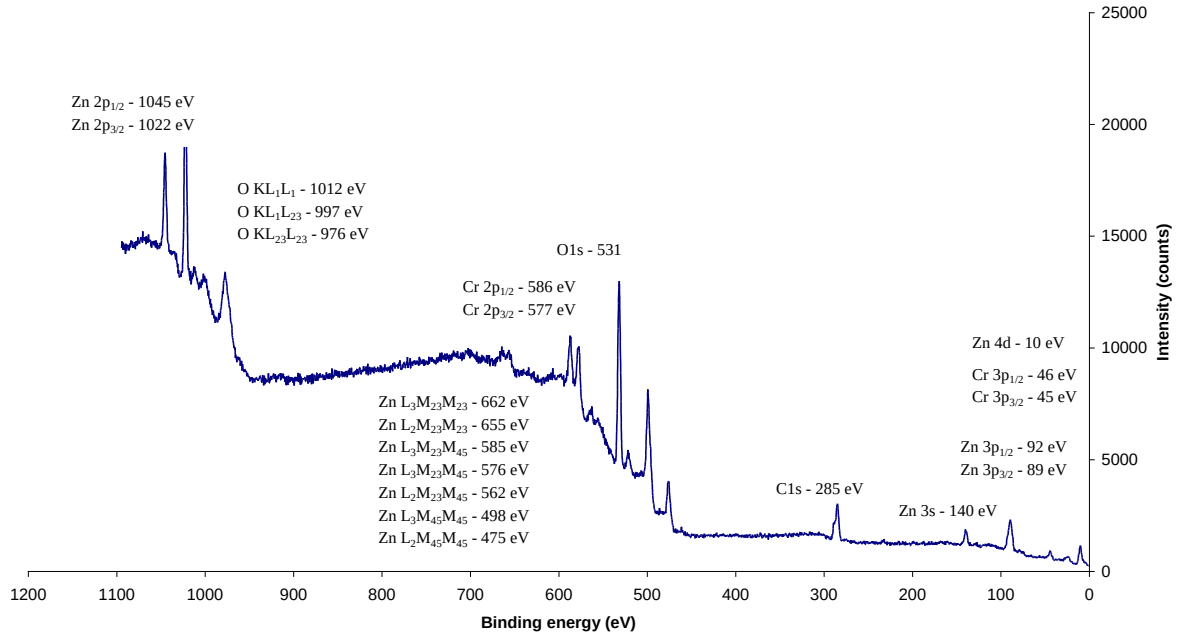

Figure 4.75 Non-monochromatic Al X-ray source XPS survey scan of Tripass LT1500 not containing cobalt nitrate (trivalent CCC) on acid zinc electrodeposited steel. BE values listed are approximate.

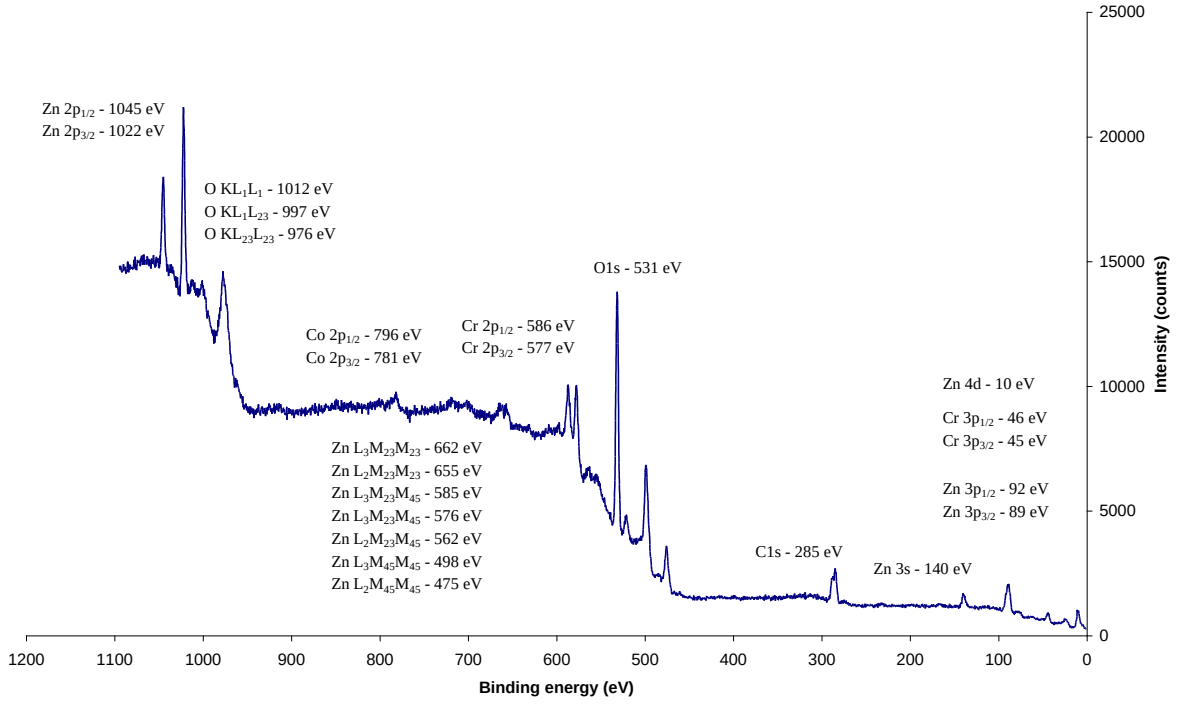

Figure 4.76 Non-monochromatic Al X-ray source XPS survey scan of Tripass LT1500 including 14.6 g/l cobalt nitrate (trivalent CCC) on acid zinc electrodeposited steel. BE values listed are approximate.

4.2.1.3.4 Effect of malonic acid : Survey scan XPS data

An XPS survey scan of Tripass LT1500 without malonic acid; see Figure 4.77, indicates the presence of chromium, oxygen, zinc and carbon as in the case of Tripass LT1500 control. There is also the indication of peaks at 230 eV indicative of molydenuem (Mo $3d_{5/2}$) and at 165-166 eV indicative of sulphur (S $2p_{3/2}$ and S $2p_{1/2}$). The presence of sulphur is possibly a contaminant absorbed during the specimen preparation or analysis stage. The detection of molybdenum is unusual since Tripass LT1500 control did not show a clear peak at that energy.

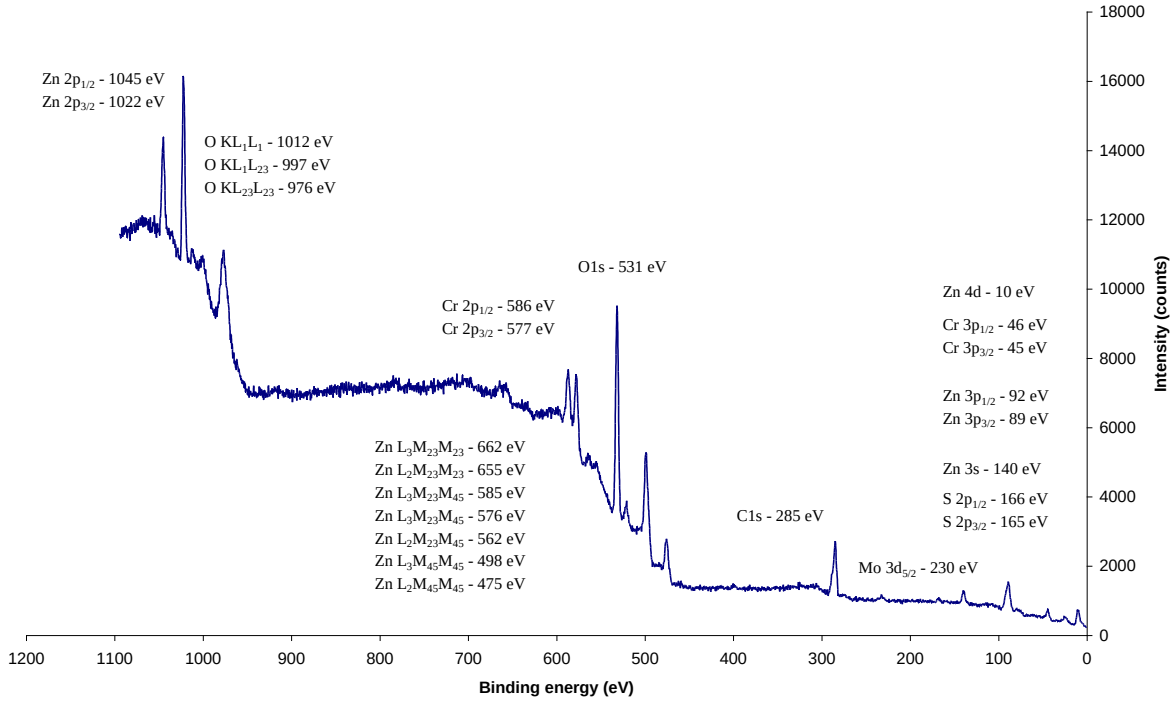

Figure 4.77 Non-monochromatic Al X-ray source XPS survey scan of Tripass LT1500 not containing malonic acid (trivalent CCC) on acid zinc electrodeposited steel. BE values listed are approximate.

An XPS survey scan of Tripass LT1500 with the inclusion of additional malonic acid (13 g/l) does not result in the detection of additional elements such as molybdenum or sulphur but does exhibit the common elements chromium, oxygen, zinc and carbon; see Figure 4.78. When Tripass LT1500 treatment solution with additional malonic acid (13 g/l) was allowed to age with additional heating prior to conversion coating no significant difference in the XPS survey scan data was observed; see Figure 4.79, in comparison to the standard 13 g/l malonic acid variable.

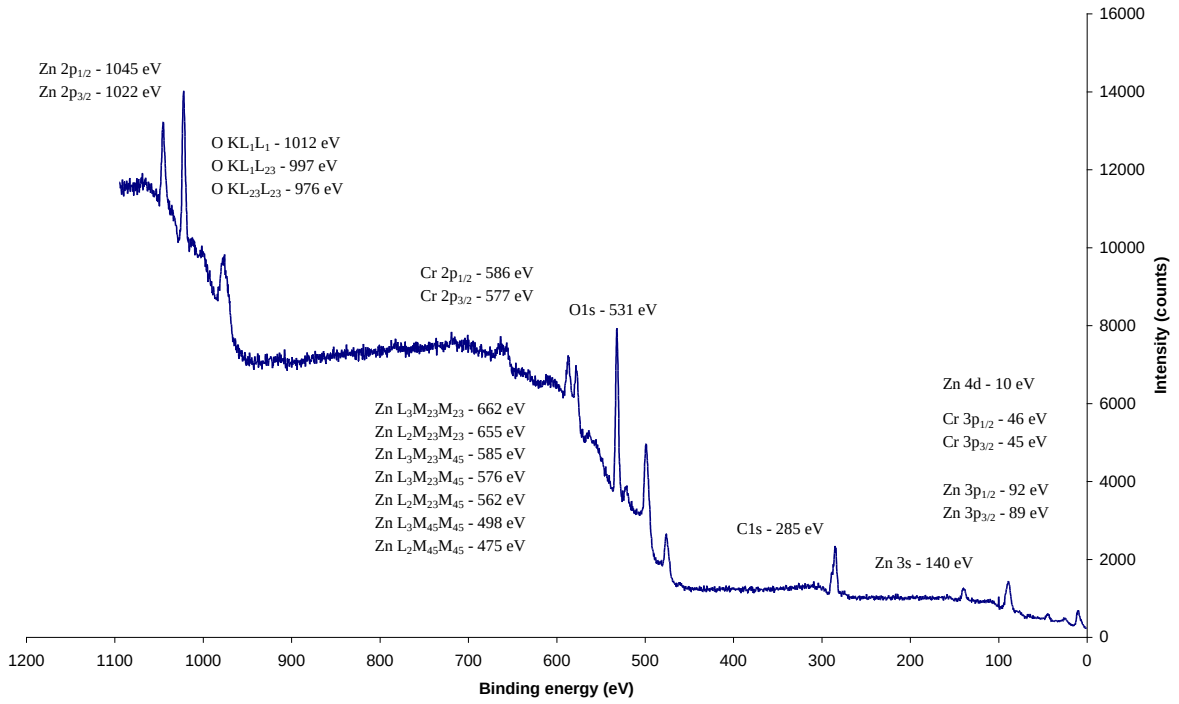

Figure 4.78 Non-monochromatic Al X-ray source XPS survey scan of Tripass LT1500 including 13 g/l malonic acid (trivalent CCC) on acid zinc electrodeposited steel. BE values listed are approximate.

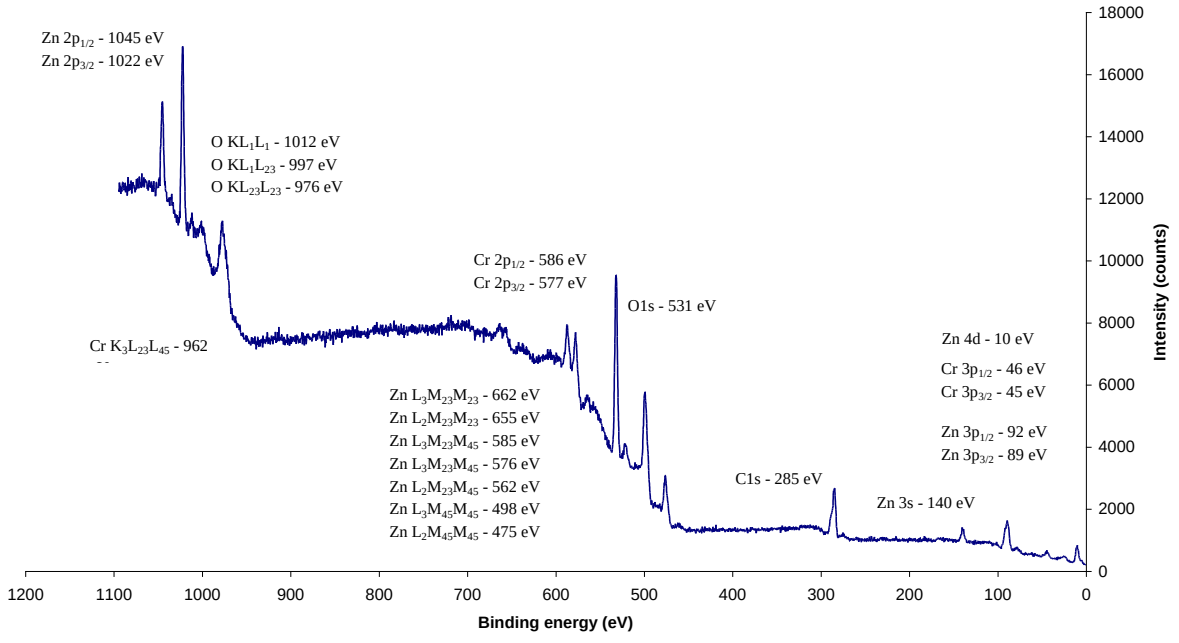

Figure 4.79 Non-monochromatic Al X-ray source XPS survey scan of Tripass LT1500 including 13 g/l malonic acid (treatment solution allowed to age with additional heating prior to conversion coating process) (trivalent CCC) on acid zinc electrodeposited steel. BE values listed are approximate.

4.2.1.3.5 Effect of oxalic acid : Survey scan XPS data

An XPS survey scan of Tripass LT1500 without oxalic acid; Figure 4.80, exhibits a similar chemical composition as that of Tripass LT1500 control in which elements such as chromium, oxygen, zinc and carbon are detected. There are also indications of additional peaks such as sulphur (S $2p_{3/2}$ and S $2p_{1/2}$) and molybdenum (Mo $3d_{5/2}$) at 165-166 and 230 eV.

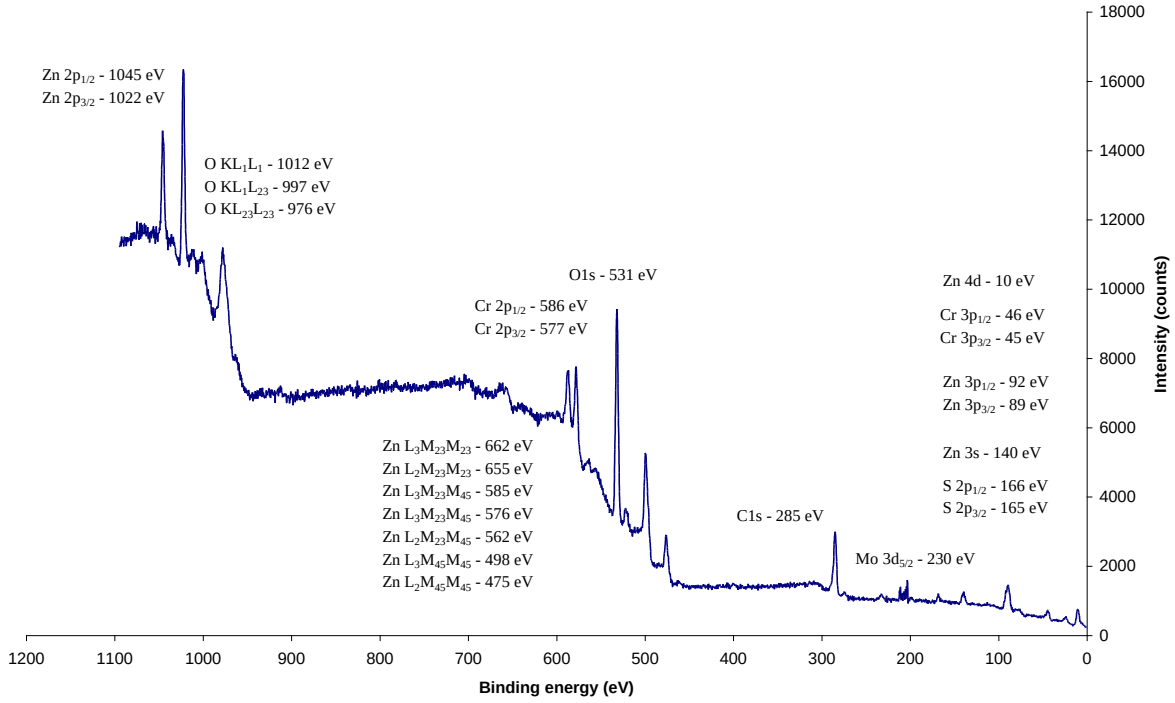

Figure 4.80 Non-monochromatic Al X-ray source XPS survey scan of Tripass LT1500 not containing oxalic acid (trivalent CCC) on acid zinc electrodeposited steel. BE values listed are approximate.

An XPS survey scan of Tripass LT1500 with the inclusion of additional oxalic acid (52 g/l) results in the detection of elements such as oxygen, zinc and carbon; Figure 4.81. However, the detection of chromium is somewhat less clear given that no chromium peaks (Cr $3p_{1/2}$ and Cr $3p_{3/2}$) at 45-46 eV are evident. Also the profile of the peaks exhibited at 577 and 586 eV do not represent the typical Cr 2p profile but that for zinc Auger peaks 576 eV $L_3M_{23}M_{45}$ and 585eV $L_3M_{23}M_{45}$ in terms of area and size. It is typically expected that the Cr $2p_{3/2}$ peak envelope in terms of height and size is greater than that of the Cr $2p_{1/2}$, however, with the overall level of chromium being proportionately less within the trivalent CCC as well as the contribution of a zinc Auger peak ($L_3M_{23}M_{45}$) the Cr $2p_{3/2}$ peak envelope can be made to look similar in height and size to the peak envelope located at ~586 eV i.e. Cr $2p_{1/2}$.

Also in this XPS survey scan it is important to note that the peak profile intensity for carbon is not as pronounced as exhibited in other XPS survey scans such as that for the Tripass LT1500 control.

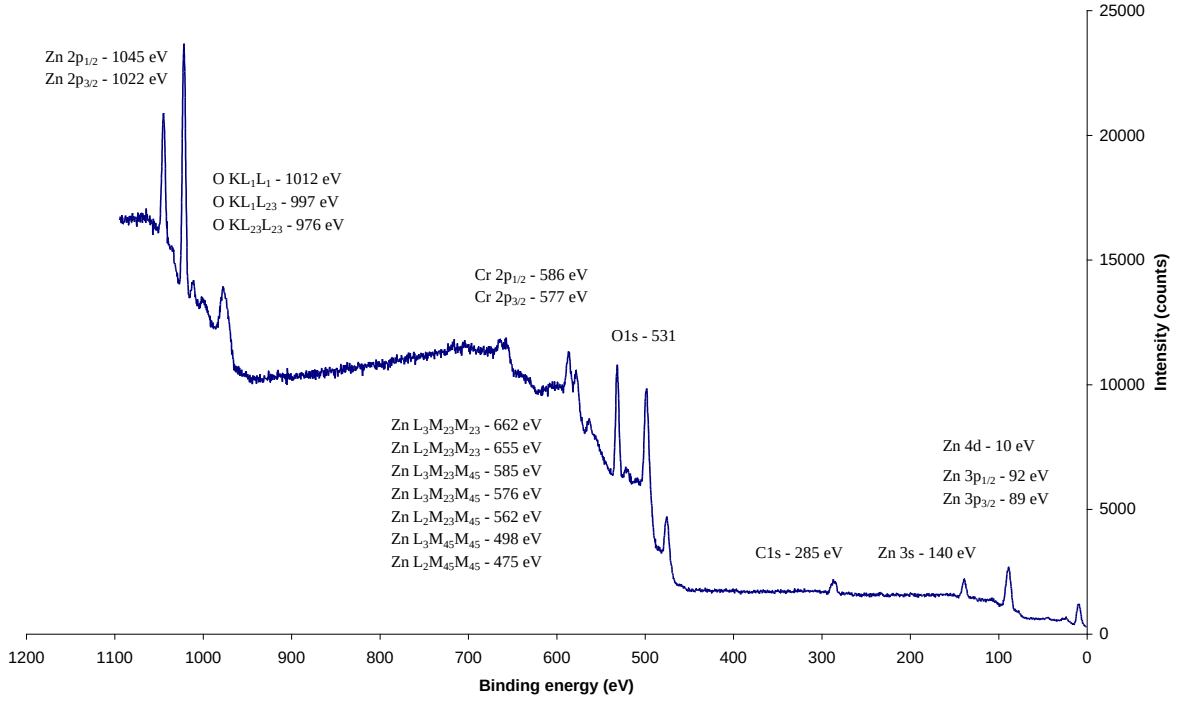

Figure 4.81 Non-monochromatic Al X-ray source XPS survey scan of Tripass LT1500 including 52 g/l oxalic acid (trivalent CCC) on acid zinc electrodeposited steel. BE values listed are approximate.

4.2.1.3.6 Effect of chromium nitrate : Survey scan XPS data

An XPS survey scan of Tripass LT1500 with the exclusion of chromium nitrate, not surprisingly, results in the detection of only the elements oxygen, zinc and carbon; Figure 4.82. The peak profile intensity, like that of the Tripass LT1500 - 52 g/l oxalic acid variable, is not as pronounced as that exhibited in other XPS survey scans.

An XPS survey scan of Tripass LT1500 with the inclusion of additional chromium nitrate (212 g/l) chromium peaks (Cr $3p_{1/2}$ and Cr $3p_{3/2}$ and Cr $2p_{1/2}$ and Cr $2p_{3/2}$) are evident once more; see Figure 4.83. There is also an indication of a sulphur peak at 165-166 eV (S $2p_{3/2}$ and S $2p_{1/2}$).

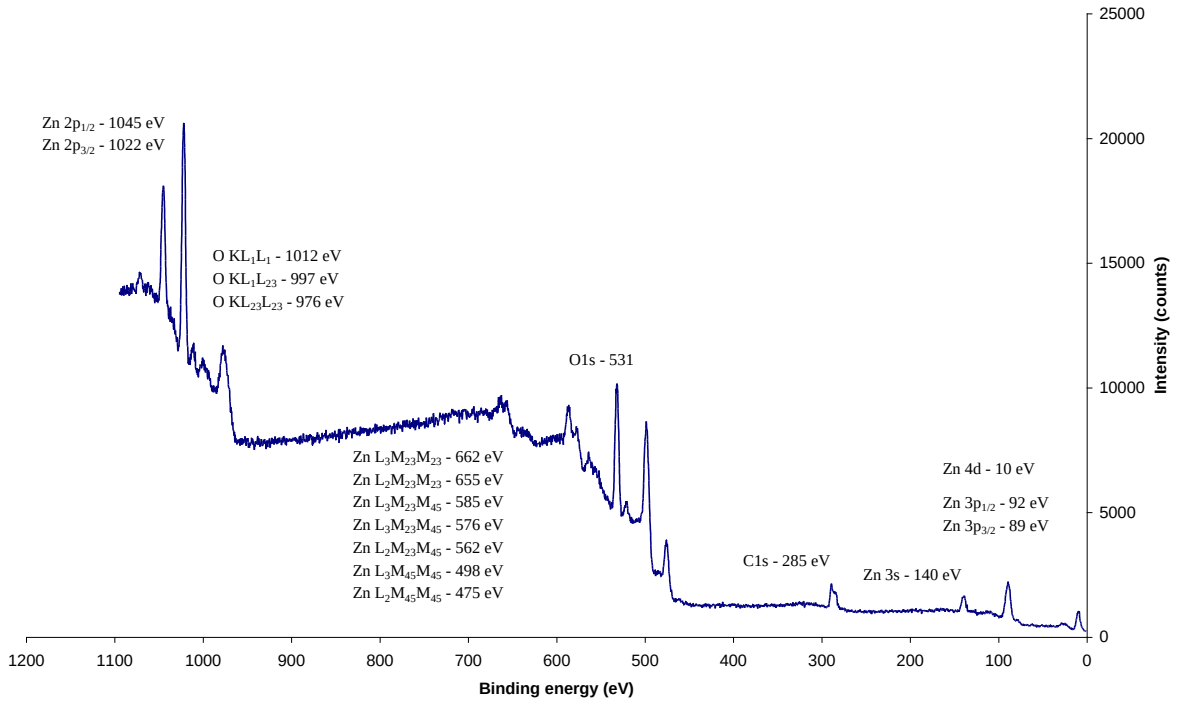

Figure 4.82 Non-monochromatic Al X-ray source XPS survey scan of Tripass LT1500 not containing chromium nitrate (trivalent CCC) on acid zinc electrodeposited steel. BE values listed are approximate.

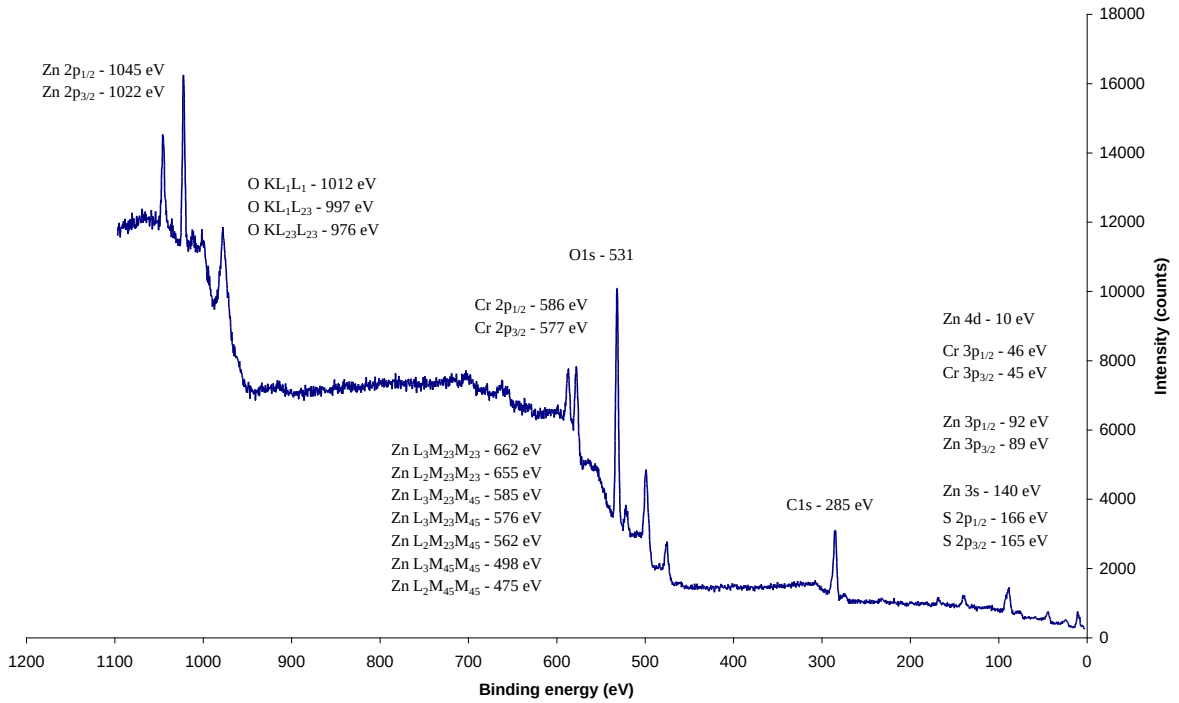

Figure 4.83 Non-monochromatic Al X-ray source XPS survey scan of Tripass LT1500 including 212 g/l chromium nitrate (trivalent CCC) on acid zinc electrodeposited steel. BE values listed are approximate.

4.2.2 Auger Electron Spectroscopy (AES)

4.2.2.1 Hexavalent CCC : Untreated

AES was used to determine surface and sub-surface chemical compositions of hexavalent (chromate A) and trivalent (Tripass LT1500) CCCs on acid zinc electrodeposited steel after various immersion times; see Section 3.3.1. Surface compositions are given in Table 4.19. The carbon content observed for hexavalent and trivalent CCCs indicates a monolayer or sub monolayer coverage of contamination, most likely the result of atmospheric exposure. From a consideration of zinc:chromium ratios, on increasing immersion time it is clear that the surface zinc content for hexavalent CCCs decreases, whilst that of chromium, oxygen and sulphur generally increase. Surface compositions of trivalent CCCs indicate an overall higher level of zinc within the conversion coating and at longer immersion times in comparison to hexavalent CCC. It is important to note that the zinc content was also found to be higher for trivalent CCCs than hexavalent CCC from XPS surface compositional analysis. Trivalent CCCs also have sulphur and chlorine present, possibly as a result of contamination from the treatment bath or during sample preparation. The surface chromium content for the trivalent CCC appears to indicate a degree of variation.

Table 4.19 Surface chemical compositions (at. %) from AES data for chromate A conversion coating and trivalent CCC (Tripass LT1500) on acid zinc electrodeposited steel formed at different immersion times.

Sample	Immersion time (s)	Element at. %					
		S	Cl	C	O	Cr	Zn
Chromate A conversion coating	1	2.8	0.0	67.9	20.2	3.9	5.2
	2	5.5	0.0	53.6	24.0	6.5	10.4
	5	6.0	4.5	19.6	45.3	18.0	6.6
	40	3.7	0.0	36.5	51.3	8.5	0.0
Trivalent CCC	45	2.1	7.5	33.9	43.1	2.7	10.7
	60	0.0	0.0	18.9	55	11.3	14.8
	90	1.7	8.2	27.4	40.9	2.7	19.1

Figures 4.84-4.87 illustrate depth profiles for hexavalent CCC after 1, 2, 5 and 40 s immersion. These all confirm that carbon is present only as a contaminant of the surface as it is not present in the sub-surface region. Also present only as a contaminant of the surface is chlorine in the case of 5 s conversion coating treatment time; see Figure 4.86. Contamination may have occurred during specimen preparation. In general, the zinc content for hexavalent

CCCs remains low with depth, with a sharp rise only at the conversion coating / zinc electrodeposit interface, as might be expected.

The general oxygen content within hexavalent CCC was shown to increase on increasing immersion time up to 40 s this is in anticorellation with the surface carbon. For all immersion times oxygen content at sub-surface was shown to increase sharply and stabilise from the content exhibited at the surface before declining at depth. The decline in oxygen also corresponds to an increase in zinc content at depth which signifies the conversion coating / zinc electrodeposited interface.

The sulphur content within hexavalent CCCs, in general, decreases from the level exhibited at the surface/subsurface region with depth. For the thicker films its reducing content stabilises before the conversion coating / zinc electrodeposited interface. It is likely that sulphur has an influence upon the film formation mechanism possibly as an initiator of the corrosion process (i.e. zinc dissolution) and as a result is absorbed within the conversion coating. Other researchers have also noted that sulphur appears to have some role in the film formation mechanism of hexavalent CCCs [79,82].

The depth profiles of chromium content within hexavalent CCC 1, 2, 5 and 40 s initially increases from the level exhibited at the surface, before stabilising and declining at the conversion coating / zinc electrodeposited interface.

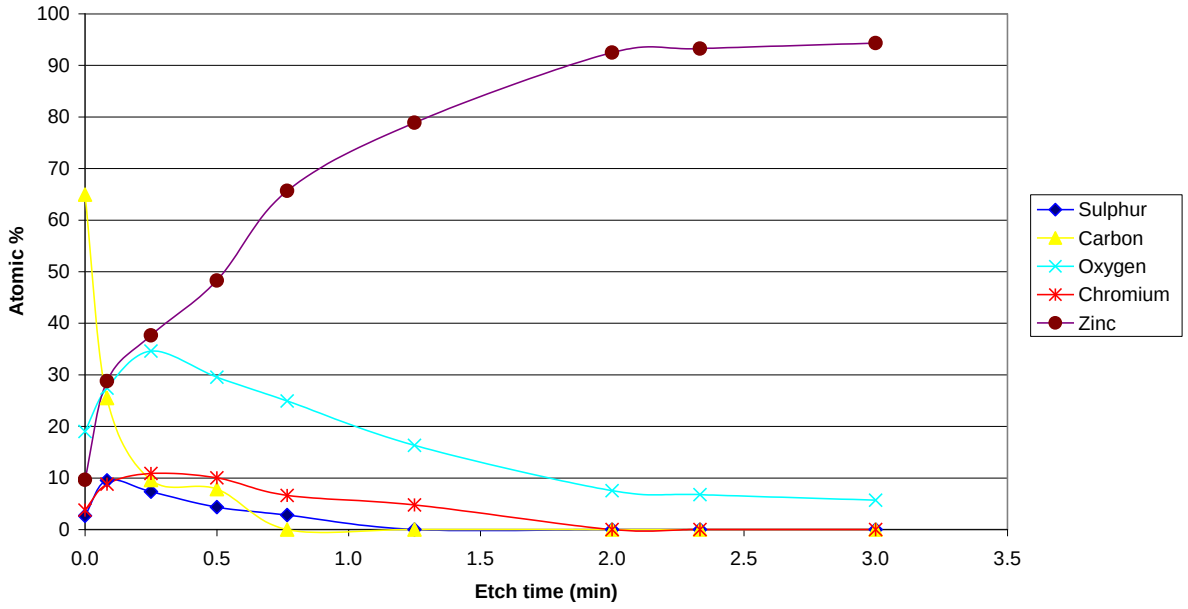

Figure 4.84 AES depth profiles for a chromate A conversion coating (1 s) on acid zinc electrodeposited steel.

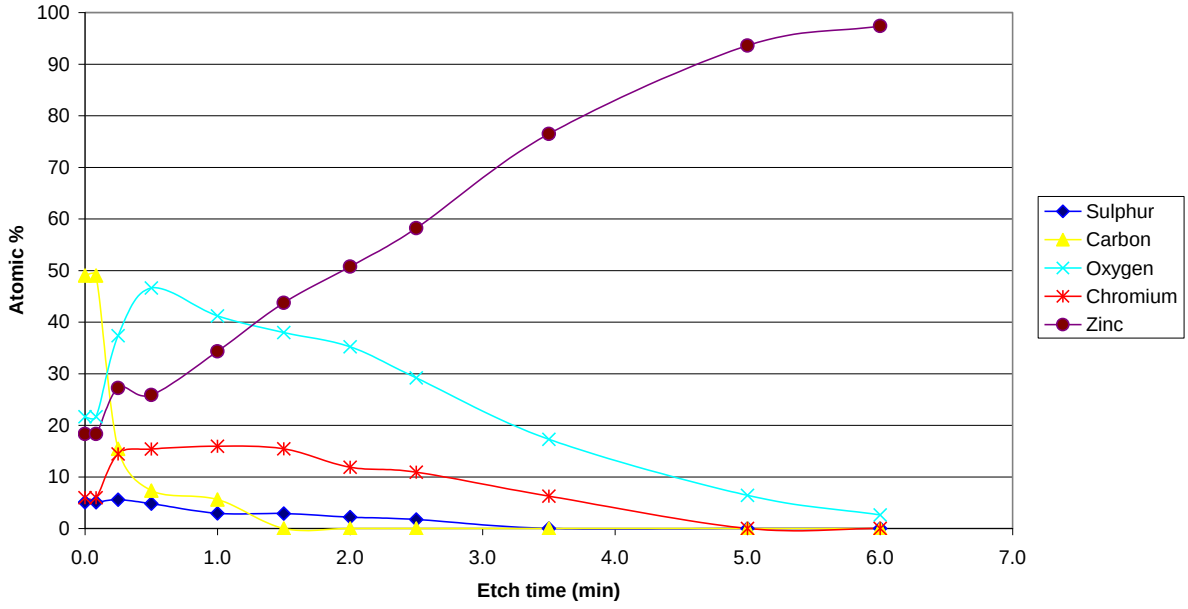

Figure 4.85 AES depth profiles for a chromate A conversion coating (2 s) on acid zinc electrodeposited steel.

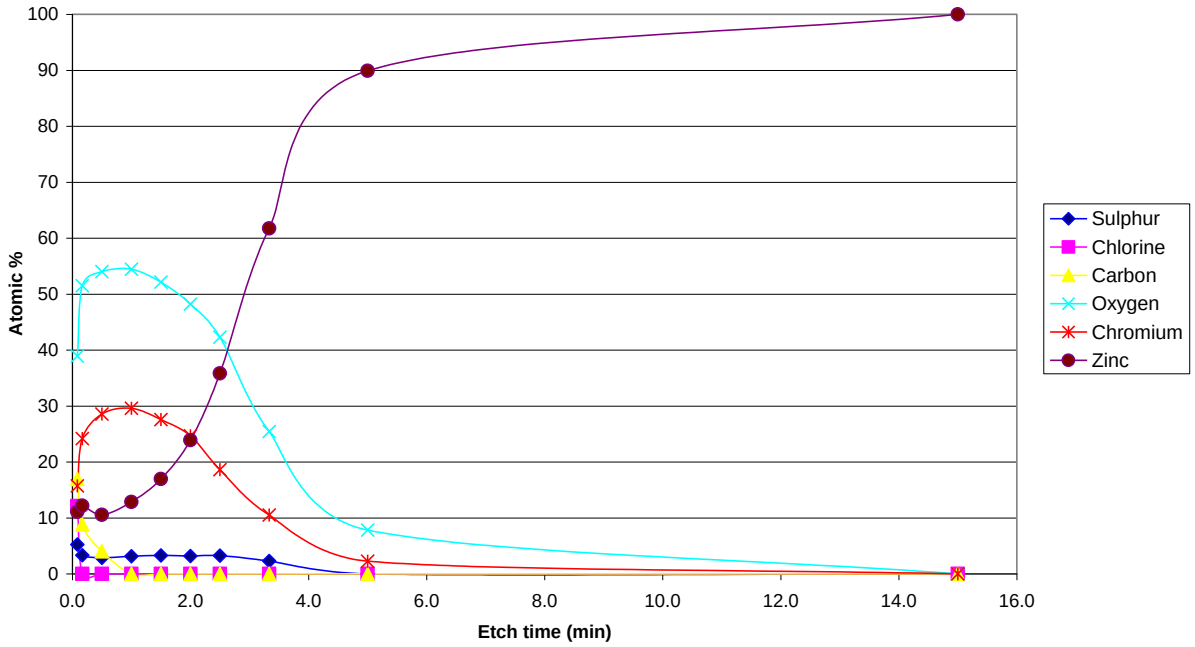

Figure 4.86 AES depth profiles for a chromate A conversion coating (5 s) on acid zinc electrodeposited steel.

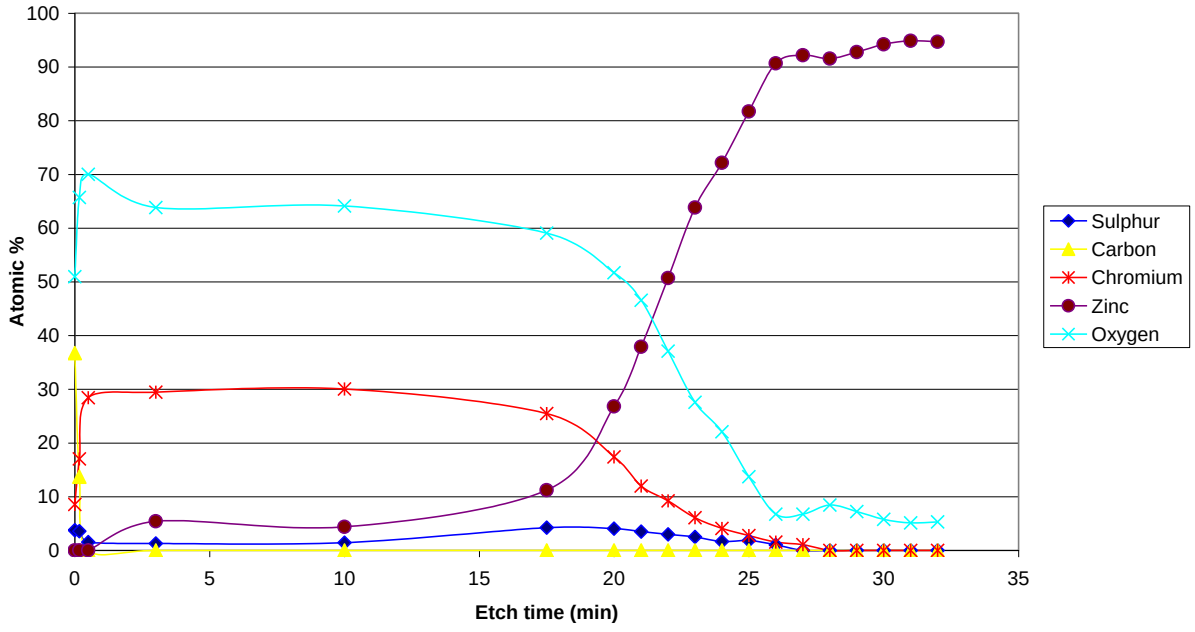

Figure 4.87 AES depth profiles for a chromate A conversion coating (40 s) on acid zinc electrodeposited steel.

4.2.2.2 Trivalent CCC : Untreated

Figure 4.88 and 4.89 illustrate depth profiles for trivalent CCC after 60 and 90 s treatment time, with the former being a full depth profile. In both plots carbon is present only on the surface as its presence at sub-surface is lacking following initial ion etching. In comparison to hexavalent CCC the content of zinc within the conversion coating at surface and sub-surface is significantly greater, possibly indicating a higher zinc dissolution rate during the conversion coating film formation process. It is important to note that there is no zinc included within the trivalent CCC treatment solution formulation; see Table 3.6.

Oxygen content within the trivalent CCC was shown to increase initially from the level exhibited at the surface and stabilise before declining at depth in correspondence to an increase in zinc content (i.e. conversion coating / zinc electrodeposited interface). This oxygen content appears to be similar to that exhibited in the thicker hexavalent CCC depth profile (40 s).

The content of chromium within trivalent CCC 60 and 90 s in general was found to initially increase from the level exhibited at the surface, before stabilising and finally declining as the conversion coating / zinc electrodeposited interface approached. In comparison to the hexavalent CCC (40 s) the level of chromium within the trivalent CCC (60 s) was found to be much lower, ~30 to ~15%.

Sodium molybdate was added as part of the trivalent CCC treatment solution formulation, however, the presence of the most intense molybdenum Auger peak at 186 eV was not detected. Cobalt nitrate was also added as part of the treatment solution formulation. Its presence within the Auger spectrum was more difficult to detect. This is because the major cobalt Auger peak at 775 eV falls under a similar kinetic energy position to that of a minor zinc Auger peak at 773 eV. Therefore, zinc Auger peaks (773 and 994 eV) peak/trough measurements (mm) for a zinc oxide reference standard and that for the trivalent CCC were evaluated. Following subtraction the presence of cobalt within the trivalent CCC data was difficult to positively ascribe; see Table 4.20 and 4.21. This therefore indicates that cobalt is unlikely to be present or there is very little within the converision coating. The methodology used for this subtraction method is provided in Section 3.3.1. Further work could have been to use alternative elemental depth profile techniques such as Dynamic Secondary Ion Mass Spectroscopy (DSIMS) or Glow Discharge Optical Emission Spectroscopy (GDOES).

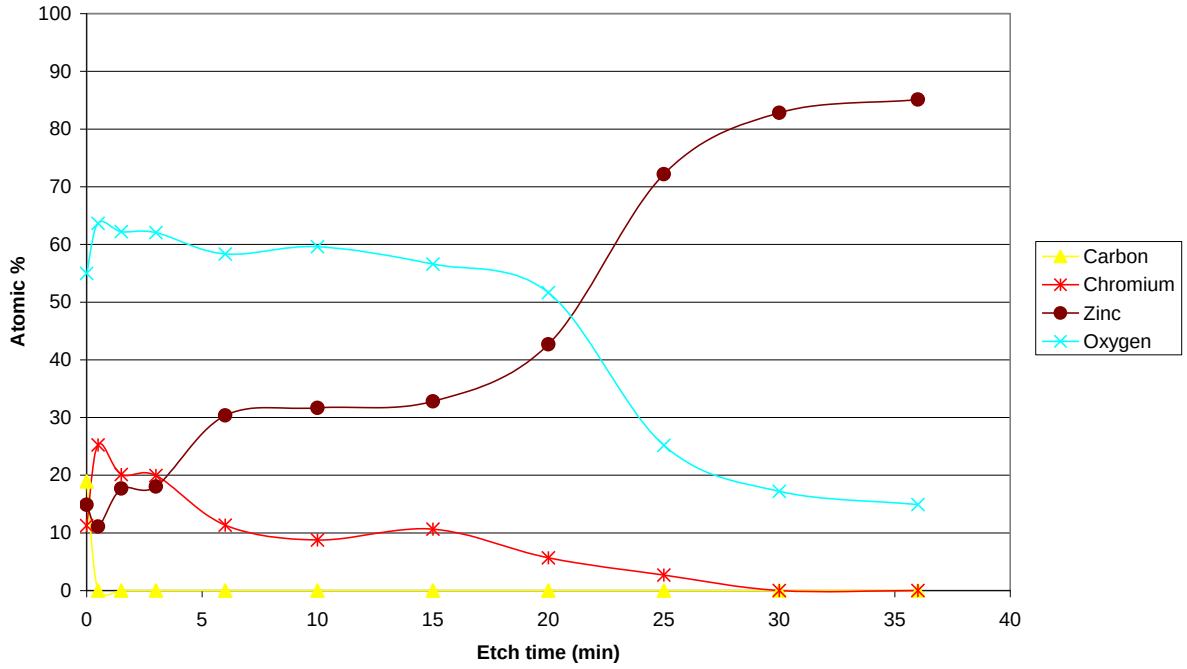

Figure 4.88 AES depth profiles for a trivalent CCC (60 s) on acid zinc electrodeposited steel.

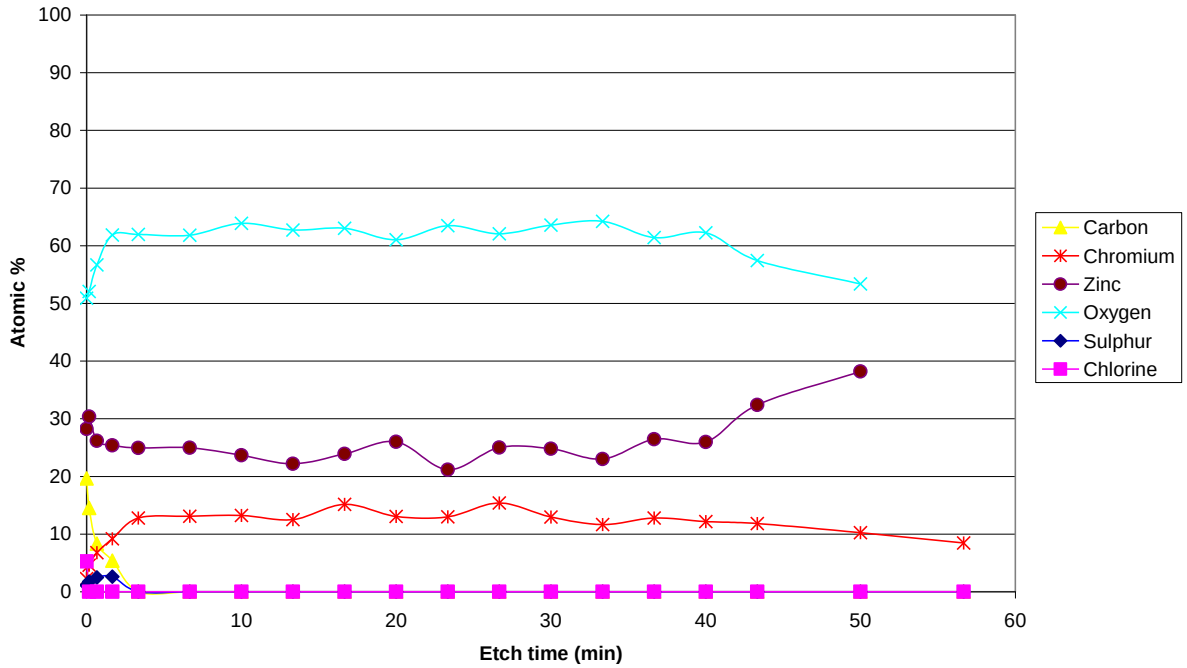

Figure 4.89 AES depth profiles for a trivalent CCC (90 s) on acid zinc electrodeposited steel.

Table 4.20 AES spectrum data for a trivalent CCC (60 s) on acid zinc electrodeposited steel including potential cobalt Auger peak contribution.

Etch time (min)	Zn - 994eV (mm)	Co – 775 eV and Zn – 773 eV (mm)	Potential overlapping cobalt Auger peak at 775 eV (mm)
0	6	0	
0.5	6	0	
1.5	10	0	
3	10	0	
6	20	0	
10	20	0	
15	20	0	
20	44	4	+ 2.1
25	79	5	+ 1.6
30	83	5.5	+ 1.9
36	88	5	+ 1.2

Table 4.21 AES spectrum data for a trivalent CCC (90 s) on acid zinc electrodeposited steel including potential cobalt Auger peak contribution.

Etch time (s)	Zn – 994eV (mm)	Zn - 773eV (mm)	Potential overlapping cobalt Auger peak at 775 eV (mm)
0	23	0	
10	26	0	
40	32	0	
100	26	0	
200	15.5	0	
400	26	0	
600	27	0	
800	16	0	
1000	20	0	
1200	25	0	
1400	26	0	
1600	17	0	
1800	24.5	0	
2000	18	0	
2200	17	0	
2400	24	0	
2600	20	0	
3000	35	4	+ 2.50
3400	44	4	+ 2.11

4.2.2.3 Hexavalent CCC : Effect of 5% NaCl solution exposure

AES depth profiles of hexavalent CCC (chromate A 20 s) following 18 and 48 h 5% NaCl solution exposure are provided in Figures 4.90 and 4.91. In comparison to an untreated AES depth profile plot in Figure 4.87 albeit a 40 s film, there is significantly more zinc and correspondingly less chromium content detected within the conversion coatings following exposure. On increasing exposure the zinc content detected increased. This could indicate dissolution of the conversion coating, micro-cracking exposing the underlying zinc substrate or increased zinc corrosion products within the conversion coating. Note that analysis was carried out in an area in which no cracking was visible in the SEM image generated by the AES instrument. Also in comparison to the untreated sample the content of chromium and oxygen detected within the conversion coating is at a reduced level. This also decreases with increasing exposure time. In the case of 48 h exposure chlorine appears to have been absorbed and penetrated into the conversion coating. The exact explanation for the presence of chlorine at 48 h and not at 18 h is somewhat unclear. It may be that increased exposure time increased the number of defects within the conversion coating e.g. pores and cracks thus allowing penetration of chloride anions. However, given that AES analysis was carried out on a non-cracked region the presence of chlorine may actually be due to chloride attack of the mixed metal oxide conversion coating. Once penetrated chloride ions may have reacted with zinc to form zinc chloride in addition to zinc oxide / hydroxide corrosion products. Alternatively, the chlorine detected may be as free chloride ions or possibly with chromium ($CrCl_3$). On increased exposure time 18 to 48 h no sulphur was detected. The mechanism for this is unclear as it is not unentirely known as to what or if sulphur is associated with in the hexavalent CCC e.g. $Cr_2(SO_4)_3$ or $ZnSO_4$. It may have been possible that on increased exposure time that sulphur was simply leached out of the conversion coating.

4.2.2.4 Trivalent CCC : Effect of 5% NaCl solution exposure

AES depth profile plots of trivalent CCC following 18 and 48 h 5% NaCl exposure are provided in Figure 4.92 and 4.93. Both plots exhibit similar elemental profiles at depth for O, Zn, Cr and C, which in general is similar to an untreated sample in Figure 4.88. The only significant difference is an increased level of Cl detected within the conversion coating following 48 h exposure which is similar to that exhibited in the hexavalent CCC, see Figure 4.91. It is possible that at a longer exposure time chloride ions are able to penetrate and permeate through the conversion coating. The absence of Na within the coating suggests that Cl could be associated with Cr or Zn. Note that low levels of Na are difficult to detect in the

presence of high Zn due to peak overlaps. In comparison to hexavalent CCC the trivalent CCC chemistry appears to demonstrate much less change following NaCl solution exposure.

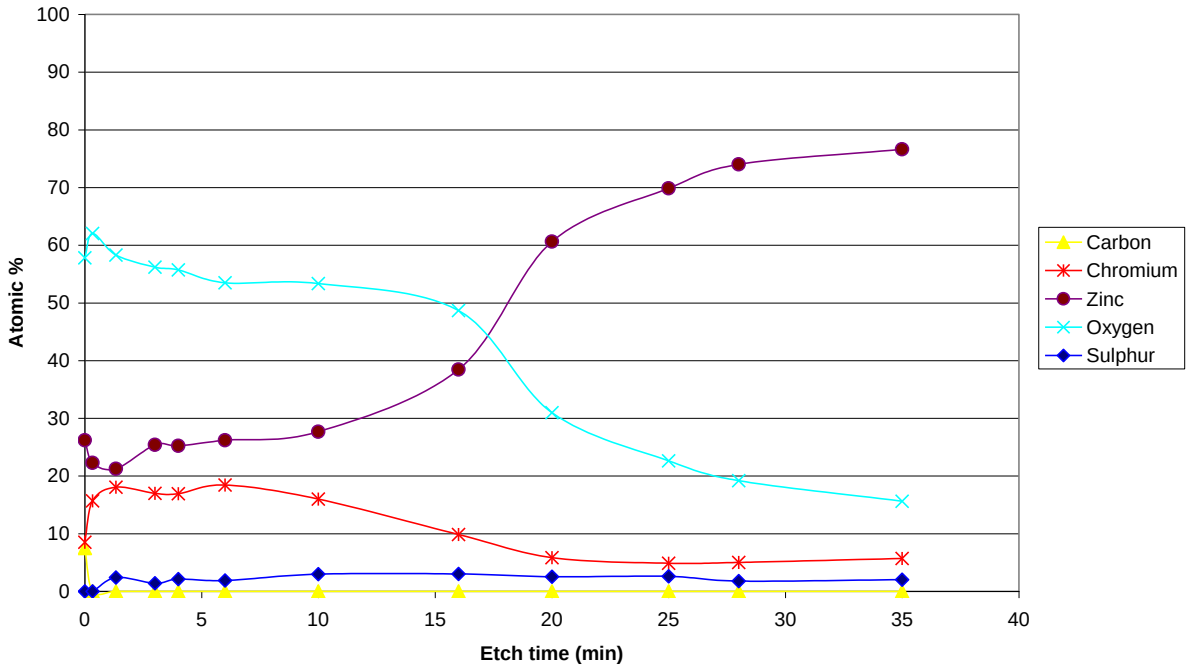

Figure 4.90 AES depth profiles for a chromate A conversion coating (20 s) on acid zinc electrodeposited steel following 18 h 5% NaCl solution exposure.

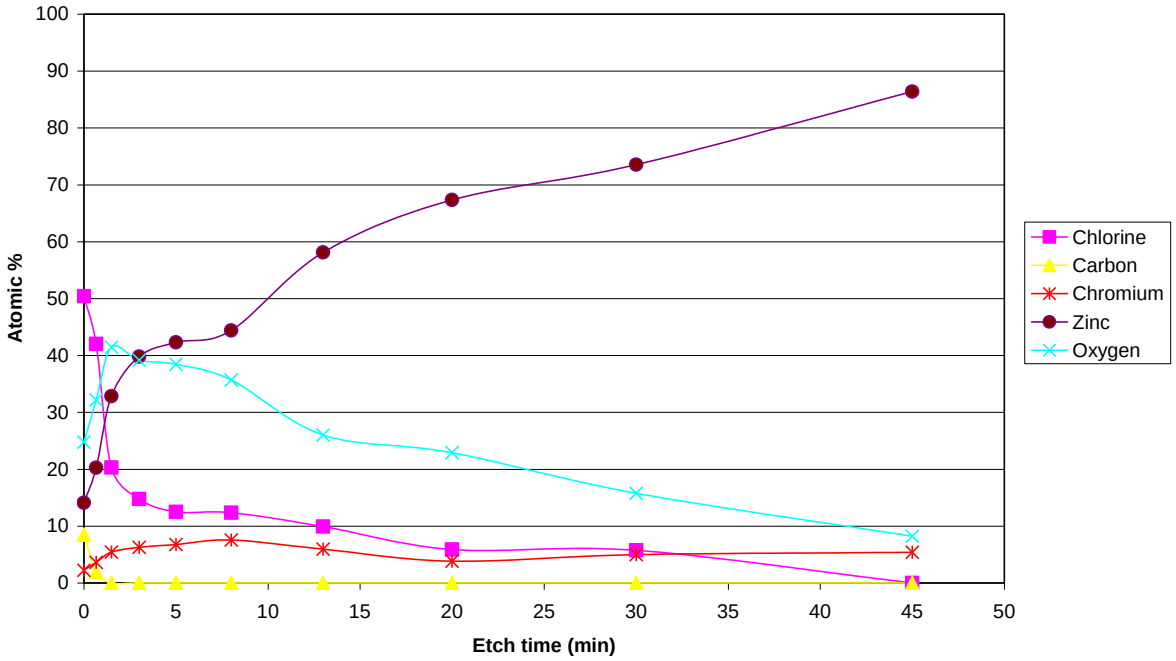

Figure 4.91 AES depth profiles for a chromate A conversion coating (20 s) on acid zinc electrodeposited steel following 48 h 5% NaCl solution exposure.

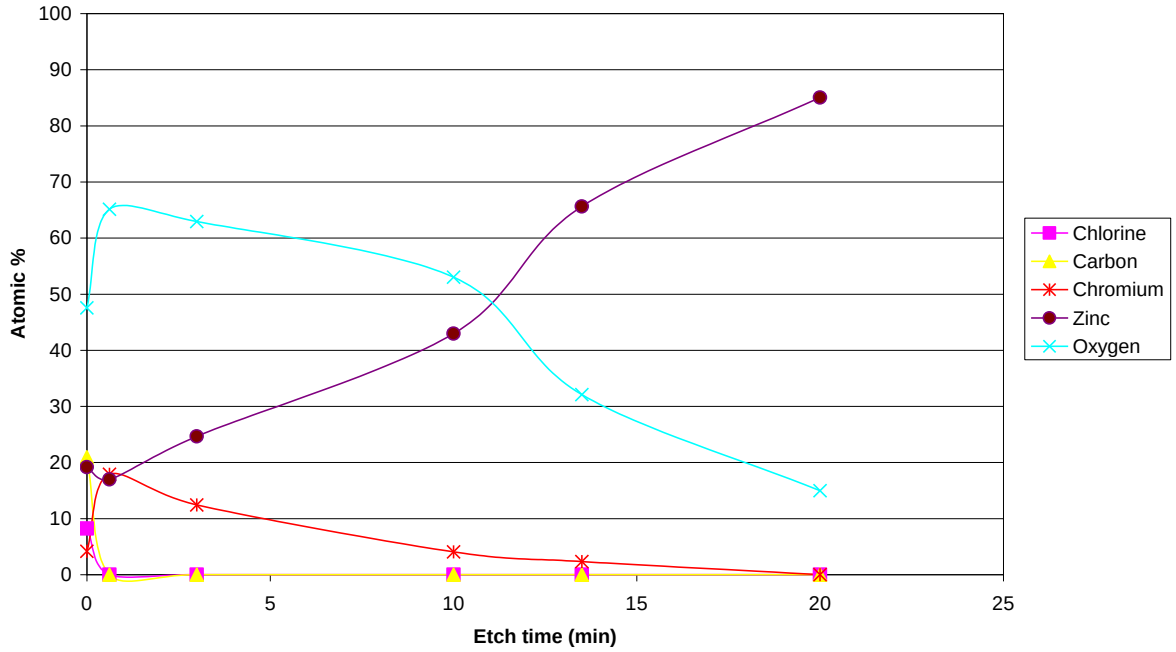

Figure 4.92 AES depth profiles for a trivalent CCC (90 s) on acid zinc electrodeposited steel following 18 h 5% NaCl solution exposure.

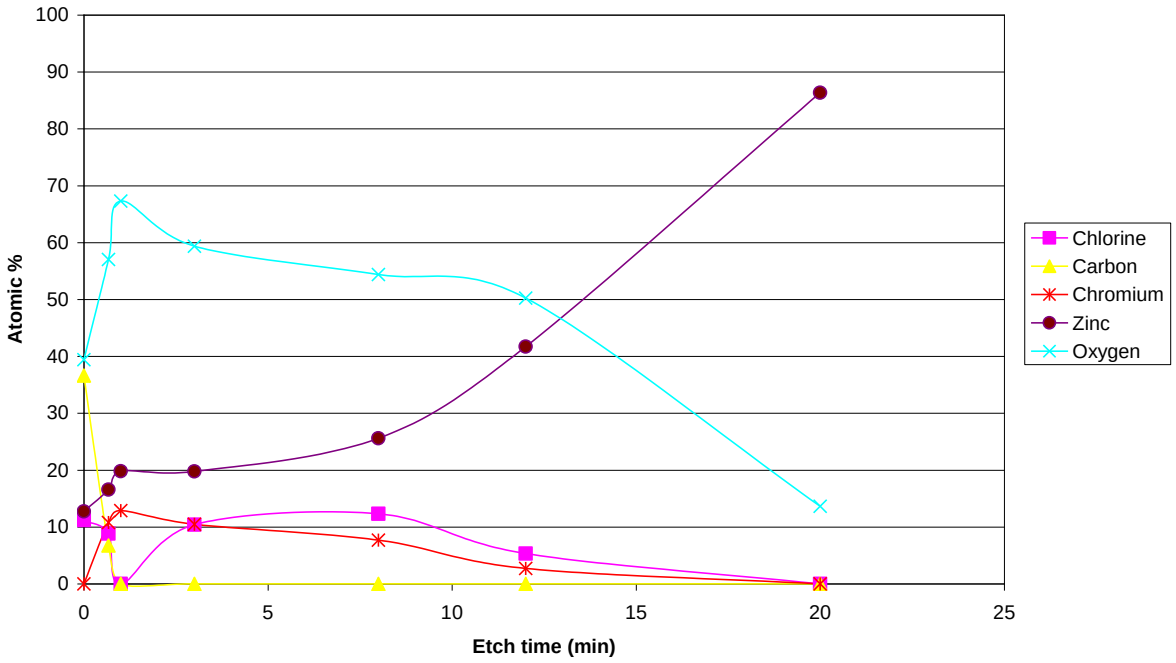

Figure 4.93 AES depth profiles for a trivalent CCC (90 s) on acid zinc electrodeposited steel following 48 h 5% NaCl solution exposure.

4.2.2.5 Black trivalent CCC

4.2.2.5.1 Black trivalent CCC on acid zinc electrodeposited steel

An AES depth profile plot of a black trivalent CCC on acid zinc electrodeposited steel substrate is shown in Figure 4.94. The basic constitutes of this conversion coating comprises of carbon, silicon, chromium, zinc and oxygen. In order to evaluate the relative contribution of oxygen associated with chromium, zinc and silicon a further plot is provided in Figure 4.95. The methodology used in the characterisation of this data is provided in Section 3.3.1. From this AES plot it is clear to see that upon initial argon ion etching silicon is present in the form of silica (SiO_2) as firstly the oxygen to silicon ratio is approximately 2 to 1 and that the kinetic energy of silicon was found to be 76 eV similar to that found for a SiO_2 standard in comparison to 92 eV for pure silicon. Silicon in this form appears to be the mainstay of the conversion coating following initial etching. As the silica levels deplete at depth a rapid increase in zinc content from ~0 to 30% is observed. Also detected at this region is chromium at relatively low concentrations (~5%). Unassociated oxygen ($O_{Remainder}$) between approximately 5 and 17 min etch time may be due to residual water within the conversion coating.

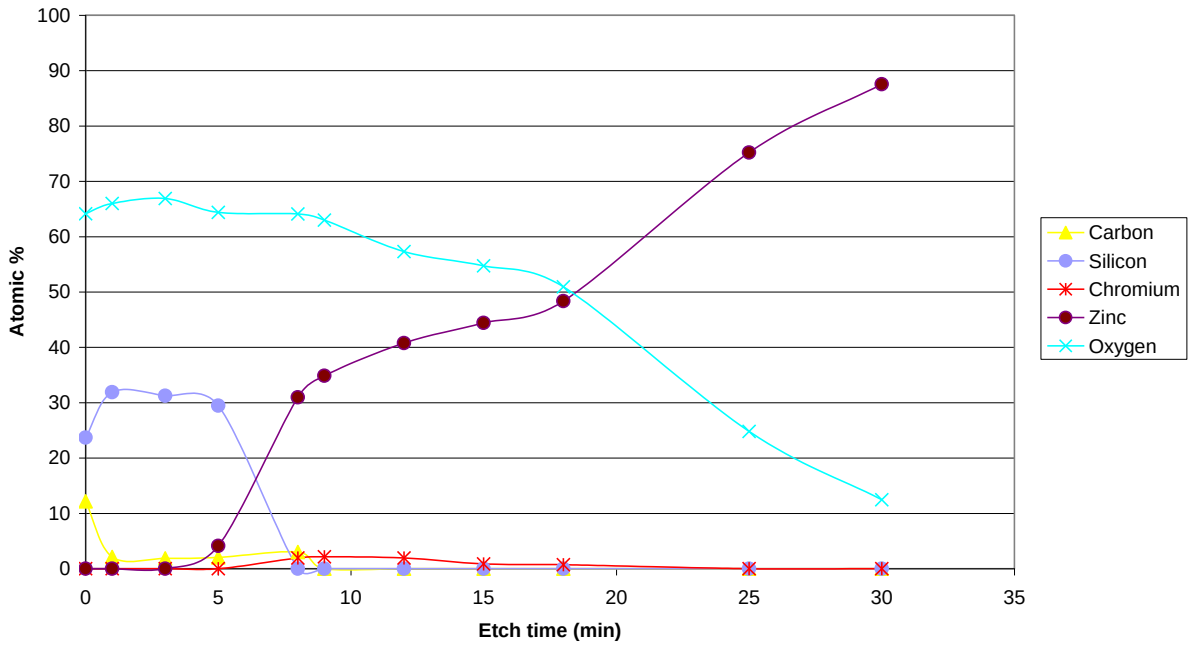

Figure 4.94 AES depth profiles for a black trivalent CCC on acid zinc electrodeposited steel.

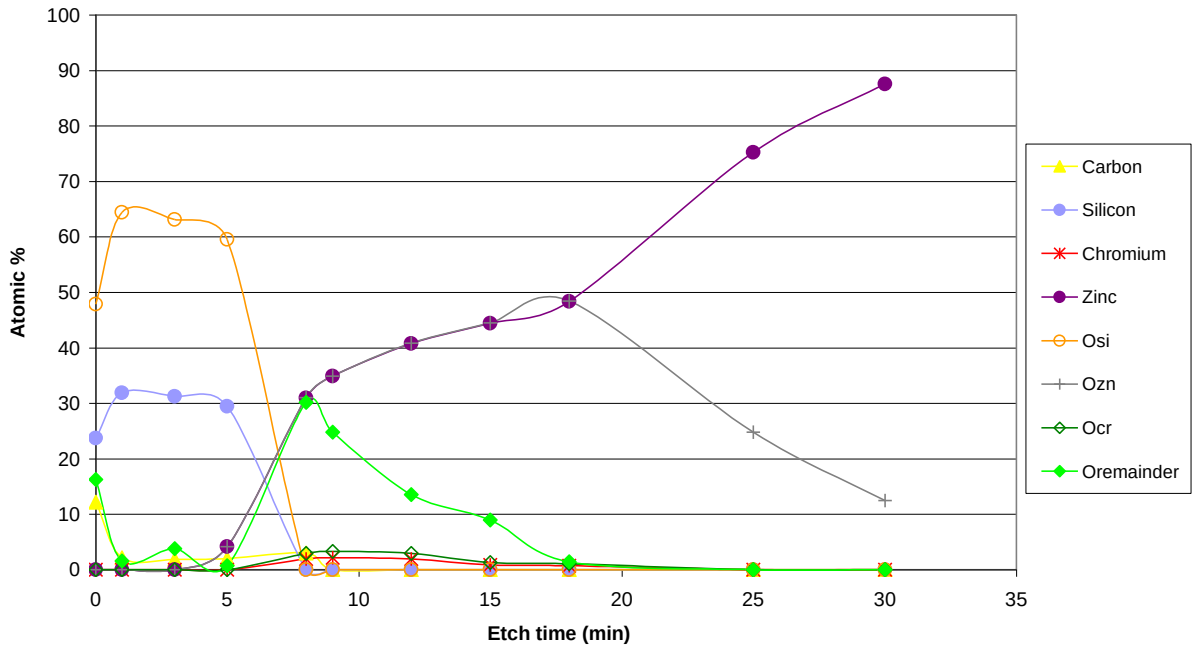

Figure 4.95 AES depth profiles for a black trivalent CCC on acid zinc electrodeposited steel including proportionate associations of oxygen to chromium, zinc and silicon. Note: O_{Si}, O_{Zn}, O_{Cr} and $O_{Remainder}$ listed in the legend are short for oxygen association with silicon, zinc, chromium and unassociated oxygen.

At further depth zinc content rises gradually (30 to 50%) before significantly increasing at the zinc substrate interface, taken as the point at which the total oxygen content falls below that of zinc (~18 min etch time); see Figure 4.94. At the point at which there is significant zinc content increase at the zinc substrate interface the small contribution of chromium detected within the bulk of the coating depletes. Carbon was also detected at the surface region but most likely only present as a contaminant possibly following atmospheric exposure.

Trace amounts of cobalt and nickel may also be present within the conversion coating given that both were included as part of the treatment solution formulation. Analysis of their intense Auger peaks (775 and 848 eV) fall under similar kinetic energy positions to that of minor zinc Auger peaks (773 and 836 eV), consequently zinc Auger peak/trough measurements (mm) for a zinc oxide reference standard at 773 and 994 eV and that for the black trivalent CCC were evaluated. The methodology used for this subtraction evaluation is provided in Section 3.3.1. Following subtraction, it was concluded that there was some indication of the presence of Co and Ni; Table 4.22. However, this information must be treated with a degree of suspicion as peak/trough measurements (mm) equated from the spectrum may have a

contribution from background noise and dependent upon the overall resolution of spectra i.e. signal-to-noise and number of scans taken. In short, it was not possible to unambiguously or positively identify the presence of Ni/Co.

Table 4.22 AES spectrum data of black trivalent CCC (Tripass black for acid zinc electrodeposit) including potential overlapping Ni and Co Auger peak contributions.

Etch time (min)	Zn - 994eV (mm)	Zn - 836eV (mm)	Zn - 773eV (mm)	Potential overlapping nickel Auger peak at 848 eV (mm)	Potential overlapping cobalt Auger peak at 775 eV (mm)
0					
1					
3					
5	7				
8	31.5	8	7	2.0	5.6
9	42	10	6	2.0	4.2
12	55	13	7	2.5	4.6
15	68	15	7	2.0	4.1
18	88	18	5	1.2	1.2
25	99	24		5.1	
30	99.5				

4.2.2.5.2 Black trivalent CCC on alkaline zinc electrodeposited steel

An AES depth profile from a black trivalent CCC on alkaline zinc electrodeposited steel substrate is shown in Figure 4.96. The basic constitutes of this conversion coating comprise of carbon, sulphur, chromium, zinc and oxygen. In order to evaluate the relative contribution of oxygen associated with chromium and zinc a further plot is provided in Figure 4.97, with the characterisation method used provided in the Section 3.3.1. In the surface to sub-surface region (~0 to 10 min) the concentration of sulphur detected reduces from ~40 to below 30% and reduces steadily thereafter as the zinc electrodeposited interface approaches. Overall the relative concentration of sulphur detected is considerable throughout the conversion coating and thus suggests functionality in the film formation mechanism. The relative chromium concentration throughout the conversion coating is low (up to ~ 5%). In comparison zinc concentration is considerable at the surface (~30%) and rises steadily at depth. So much so that the point at which the zinc electrodeposited interface is reached is difficult to determine. The corresponding oxygen to zinc indicates that oxygen is not in the ratio of 1:1 as what would be expected for ZnO at any point thus possibly indicating the presence of metallic zinc. Once again carbon is detected at the surface of the conversion coating via possible atmospheric contamination. The presence of cobalt and nickel Auger peaks within the conversion coating were sought using the procedures previously described, however, there

was no conclusive evidence of such species; Table 4.23, as in the case of cobalt within black trivalent CCC on acid zinc electrodeposited steel; Table 4.22.

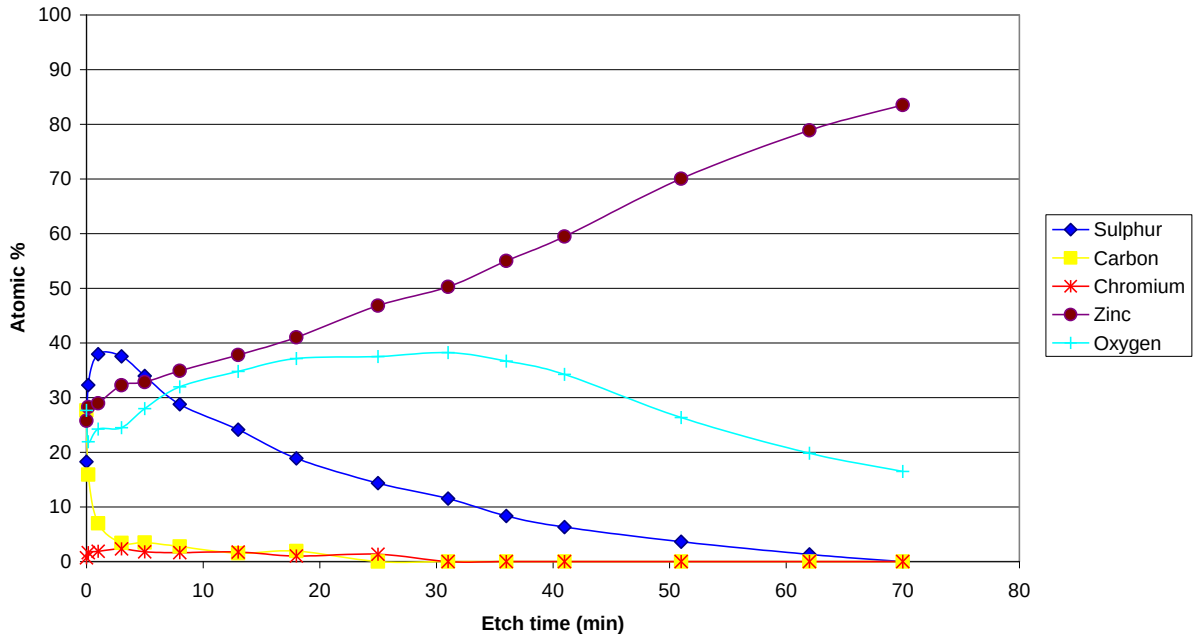

Figure 4.96 AES depth profiles for a black trivalent CCC on alkaline zinc electrodeposited steel.

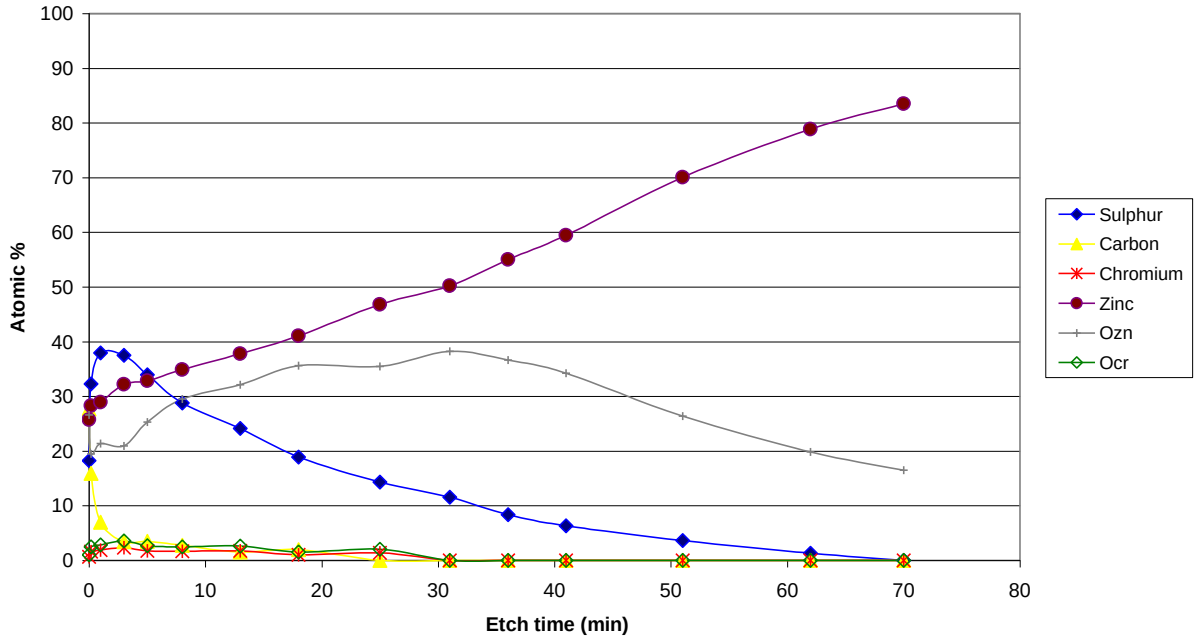

Figure 4.97 AES depth profiles for a black trivalent CCC on alkaline zinc electrodeposited steel including proportionate associations of oxygen to chromium and zinc. Note: O_{Zn} and O_{Cr} listed in the legend are short for oxygen association with zinc and chromium.

Table 4.23 AES spectrum data for trivalent black CCC on alkaline zinc electrodeposited steel including potential overlapping Ni and Co Auger peak contributions.

Etch time (min)	Zn - 994eV (mm)	Zn – 836eV (mm)	Zn - 773eV (mm)	Potential overlapping nickel Auger peak at 848 eV (mm)	Potential overlapping cobalt Auger peak at 775 eV (mm)
0	49.5	10.5	5	1.0	2.9
0.16	34	7	2.5	0.5	1.0
1	30	6	2.5	0.3	1.2
3	36	7.5	4	0.6	2.5
5	36	7	3	0.1	1.5
8	48.5	9.5	4	0.2	1.9
13	56.5	12	5	1.2	2.6
18	65	13	5	0.6	2.2
25	78.5	16	5	1.0	1.6
31	68	16		3.0	
31	67	12	5.5		2.6
36	61	11.5	4		1.4
41	92	17.5	5		1.0
51	113	22	5.5	0.4	0.6
62	98	18	4		
70	106	21	5.5	0.7	0.9

4.2.2.6 Organic topcoat

Figure 4.98 provides an AES depth profile of a silica based topcoat applied onto a trivalent CCC acid zinc electrodeposited steel substrate. Figure 4.99 provides information on oxygen attributed to chromium, silicon, zinc oxides and possible unassociated oxygen e.g. residual water within the coating. The AES depth profiles clearly indicate three different chemical regions in respect to the sample. The first region is composed entirely of silicon and oxygen (0 to ~12 min etch time). The kinetic energy position of the major Auger peak for silicon is 76 eV, indicating that the silicon is in a high oxidation state e.g. SiO_2. The remainder of the oxygen (up to ~10%) is possibly related to hydroxyl groups attached to the edge of core silica particles. The relative low levels of carbon detected within the topcoat indicates that a silica only treatment solution was possibly used for the preparation of this film.

As the concentration of the silica from the topcoat decreases, following etching of the coating (~12 min), chromium and zinc within the trivalent CCC are detected. The zinc concentration rises with etch time to the substrate. As for chromium there is a marginal increase and decline upon etch time, with a maximum of approximately 10% concentration. At about 27 min etch time the transition between zinc oxide/hydroxide to metallic zinc is reached indicating the zinc electrodeposit.

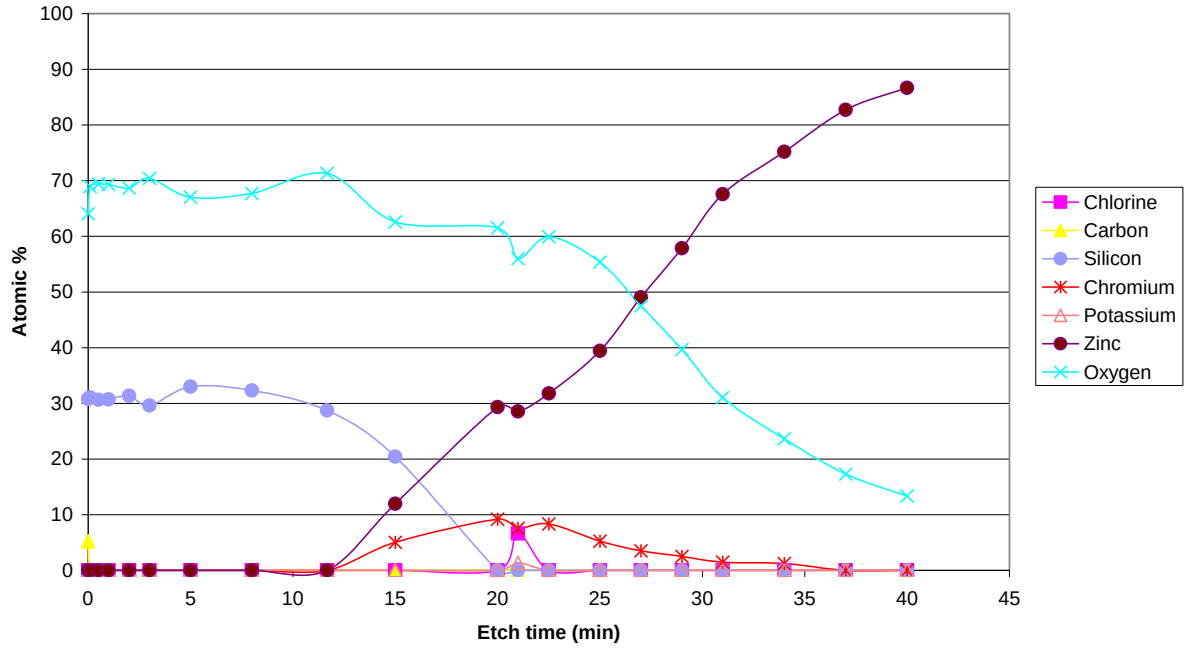

Figure 4.98 AES depth profiles for an organic topcoat (prepared from a 12 nm silica particle size treatment solution) on a trivalent CCC on acid zinc electrodeposited steel.

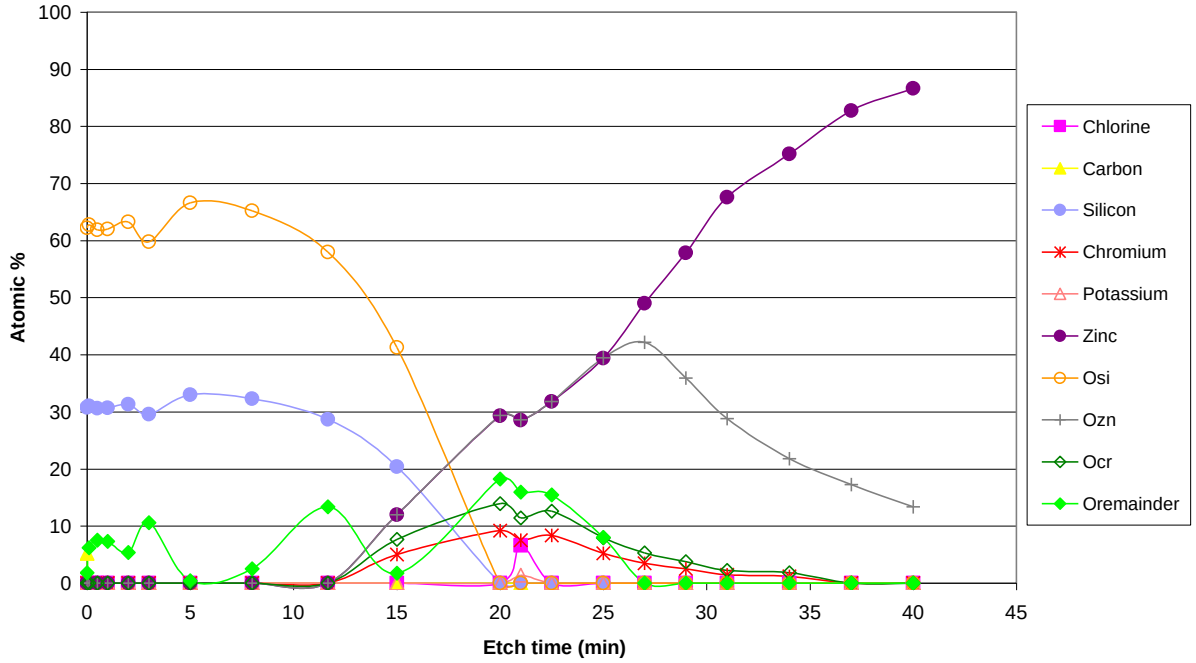

Figure 4.99 AES depth profiles for an organic topcoat (prepared from a 12 nm silica particle size treatment solution) on a trivalent CCC on acid zinc electrodeposited steel including proportionate associations of oxygen to silicon, chromium and zinc. Note: O_{Si}, O_{Zn}, O_{Cr} and $O_{Remainder}$ listed in the legend are short for oxygen association with silicon, zinc, chromium and unassociated oxygen.

Within the conversion coating region there is no clear evidence of cobalt hidden under a minor zinc Auger peak; see Table 4.24. There are, however, some traces of chlorine and potassium detected within the conversion coating region, which are likely to be contaminants.

Table 4.24 AES spectrum data for an organic topcoat (prepared from a 12 nm silica particle size treatment solution) on a trivalent CCC on acid zinc electrodeposited steel including potential overlapping cobalt Auger peak contribution.

Etch time (min)	Zn – 994eV (mm)	Zn - 773eV (mm)	Potential overlapping cobalt Auger peak at 775 eV (mm)
0			
0.1			
0.5			
1			
2			
3			
5			
8			
11.67			
15	17		
20	27		
21	34.5		
22.5	36		
25	49		
27	73		
29	68		
31	91	4	0.09
34	101	4.5	0.16
37	88.5		
40	96		

Table 4.25 AES spectrum data for an organic topcoat (prepared from a 22 nm silica particle size treatment solution) on a trivalent CCC on acid zinc electrodeposited steel including potential overlapping cobalt Auger peak contribution.

Etch time (min)	Zn – 994eV (mm)	Zn – 773eV (mm)	Potential overlapping cobalt Auger peak at 775 eV (mm)
0			
0.33			
1			
2			
4			
8			
12			
14			
16			
18			
21			
24			
28	19.5		
30	26.5		
34	49		
38	89	3	
42	107	4	
46	121	5.5	0.3
50	105	5.5	1.0
60	105	4	

Figures 4.100 and 4.101 provide AES depth profiles of an organic topcoat (based on 22 nm Silica particle size) on trivalent CCC (Tripass LT1500) on acid zinc electrodeposited steel substrate. The elemental profiles are very similar to that observed for the topcoat based on a 12 nm silica particle size. The only major difference is the increased etch time required for the depletion of silica (12 to 22 min). This indicates a thicker topcoat region. The presence of any contaminants such as potassium or chlorine is absent. Also there is no evidence to suggest any traces of cobalt within the conversion coating; Table 4.25. Like that of the topcoat based on 12 nm silica particle size, carbon is detected at the surface of the topcoat and indicative of atmospheric contamination.

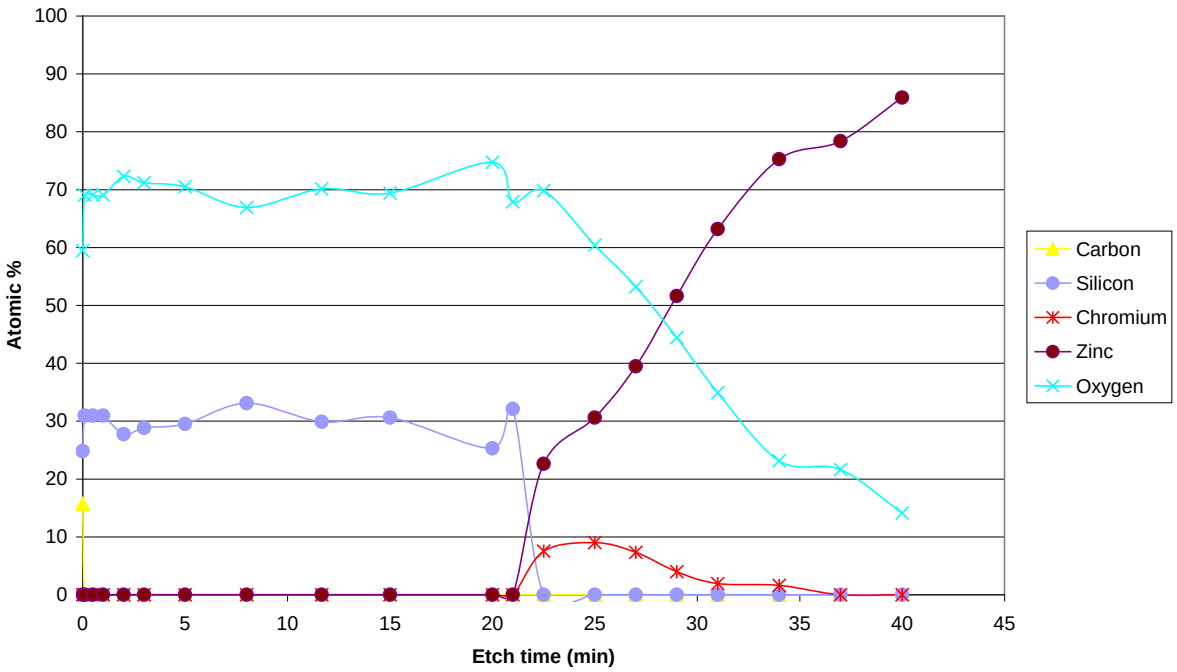

Figure 4.100 AES depth profiles for an organic topcoat (prepared from a 22 nm silica particle size treatment solution) on a trivalent CCC on acid zinc electrodeposited steel.

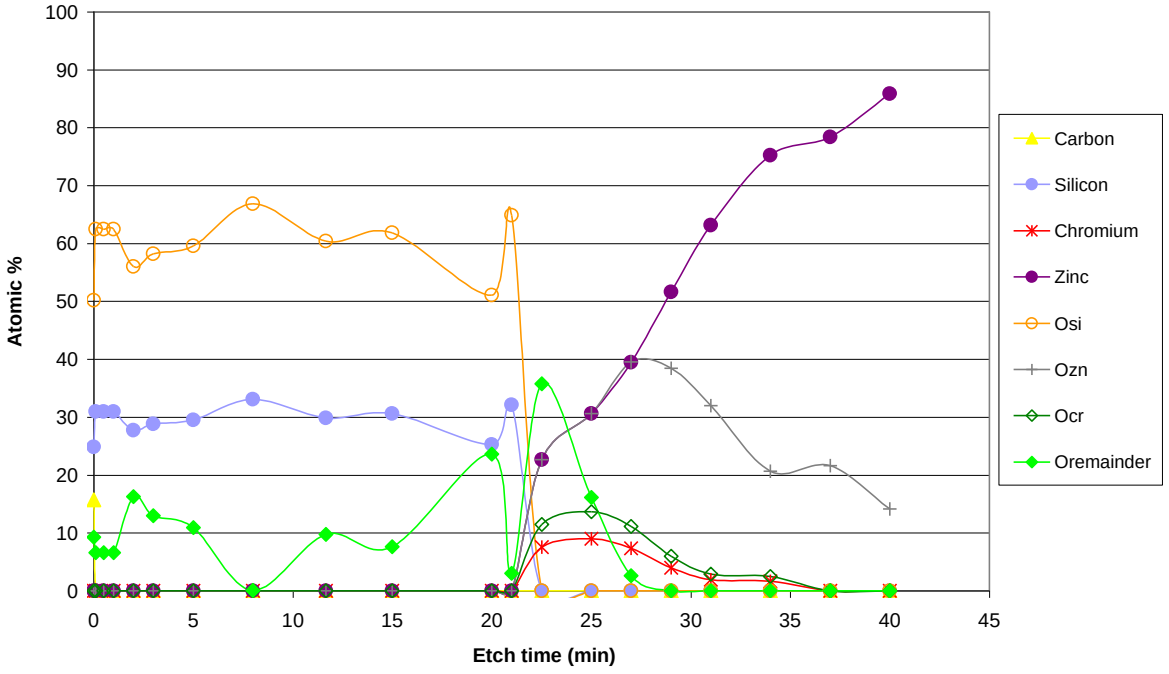

Figure 4.101 AES depth profiles for an organic topcoat (prepared from a 22 nm silica particle size treatment solution) on a trivalent CCC on acid zinc electrodeposited steel including proportionate associations of oxygen to silicon, chromium and zinc. Note: O_{Si}, O_{Zn}, O_{Cr} and $O_{Remainder}$ listed in the legend are short for oxygen association with silicon, zinc, chromium and unassociated oxygen.

4.2.3 Infra-red (IR) spectroscopy

Infra-red spectroscopy investigations were carried out to complement XPS and AES chemical analysis of hexavalent and trivalent CCCs on acid zinc electrodeposited steel. The specific samples included hexavalent CCC (chromate A – 40 s) and trivalent CCC (Tripass LT1500 – 90 s). To aid interpretation of the respective infra-red spectra, a number of reference standards were also investigated. These included oxalic acid ($H_2C_2O_4$), malonic acid ($H_4C_3O_4$), zinc oxide (ZnO), chromium oxide (Cr_2O_3), chromium trioxide (CrO_3) and chromium hydroxide ($Cr(OH)_3$).

4.2.3.1 Reference standards

4.2.3.1.1 Oxalic acid ($H_2C_2O_4$)

A oxalic acid FTIR spectrum is provided in Figure 4.102. Oxalic acid is an organic acid based on two branched carboxylic acid groups (COOH) from the central carbon-carbon single bond (HOOC-COOH). The respective absorption peaks for the functional groups O-H and C=O illustrative of carboxylic acid are evident on the spectrum. A broad / strong absorption peak is observed between 3800 to 2700 cm^{-1} which is representative of O-H stretching band, whilst that of C=O stretch absorption peak is observed at approximately 1692 cm^{-1} [147]. There is also an indication of a sharp C-O stretch carboxylic acid absorption peak (1275 cm^{-1}), however, is different to value stated in the literature of 1240 cm^{-1} [147]. It is important to note that the oxalic acid compound used was of a hydrated form and therefore some contribution within the broad / strong absorption peak observed between 3800 to 2700 cm^{-1} may have been associated to water too.

There is also a complex pattern of peaks below 1000 cm^{-1}. Some of the more pronounced peak absorption bands are located at 727, 577 and 482 cm^{-1}. These may be related to unaccounted C-H vibrations or minor vibrations associated with the carboxylic group.

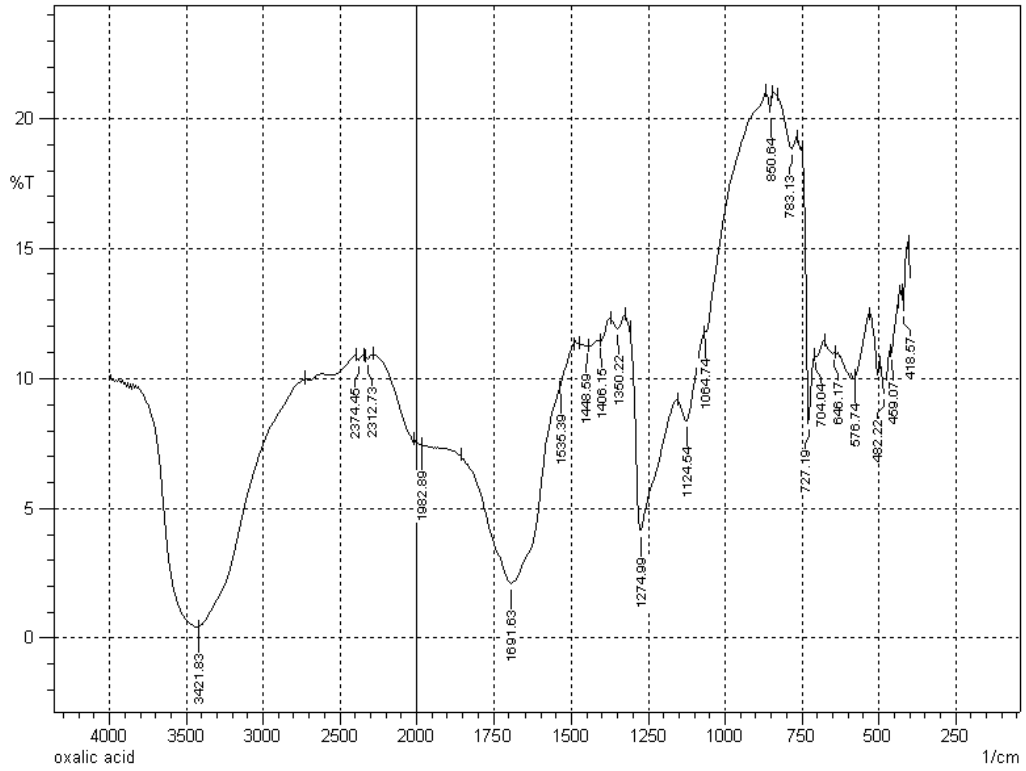

Figure 4.102 FTIR spectrum of oxalic acid reference standard obtained by transmission through pressed KBr pellets.

4.2.3.1.2 Malonic acid ($H_4C_3O_4$)

A malonic acid FTIR spectrum is provided in Figure 4.103. Like that of oxalic acid, it is also based on two side branched carboxylic acid groups (COOH), but with the addition of a carbon group (CH_2) within its main carbon chain ($HOOCCH_2COOH$). Carboxylic acid broad O-H stretch peak between 2400-3700 cm^{-1} and a C=O stretch peak at 1711 cm^{-1} are observed. It is difficult to attribute on the spectrum a C-O stretch which may be due to the carboxylic acid absorption peak ~1240 cm^{-1} [147]. However, carboxylic acid in-plane and out-of-plane C-O-H bending bands at approximately 1430 and 930 cm^{-1} do appear to be observed in the spectrum [147].

In addition, there are unaccounted peaks located between 1312 and 1177 cm^{-1} as well as peaks located at 769, 656, 542-692 and 428-453 cm^{-1}. These may be related to unaccounted C-H vibrations or minor vibrations associated the with the carboxylic group.

It is important to note that this spectrum's absorption peaks suffer from a strong malonic acid to KBr concentration ratio.

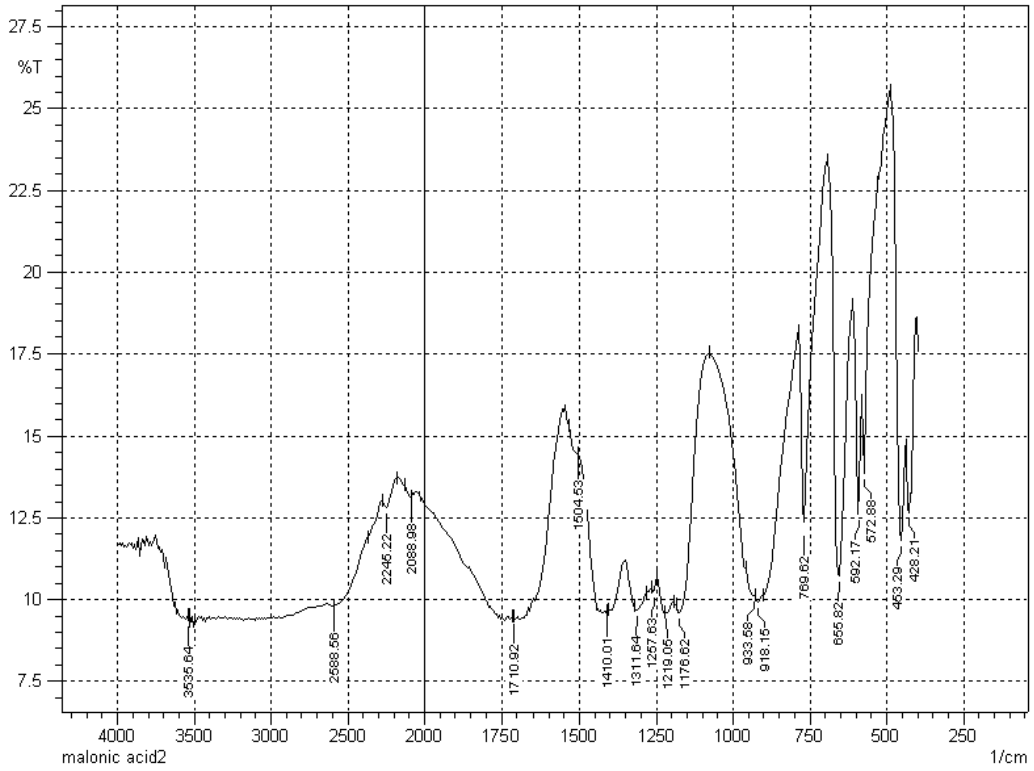

Figure 4.103 FTIR spectrum of malonic acid reference standard obtained by transmission through pressed KBr pellets.

4.2.3.1.3 Zinc oxide (ZnO)

A zinc oxide FTIR spectrum is provided in Figure 4.104. Three major peaks are observed at approximately 3474, 1641 and 444-478 cm^{-1}. It is surprising that a strong absorption band is observed between 3000 and 3700 cm^{-1}. This could be related to anti-symmetric and symmetric O-H stretch vibrations as a result of absorbed water possibly from the atmosphere. This is often referred to as water of crystallisation by a number of researchers [51,96,100]. It is also possible that the peak exhibited at 1641 cm^{-1} is a result of the corresponding O-H bend vibration [51,96,100,148-150]. Also in this spectrum carbon dioxide has been detected, possibly via atmospheric contamination. A sharp peak at 2359 cm^{-1} is representative of an asymmetric C=O stretch peak. However, the corresponding C=O bend peak at approximately 666 cm^{-1} is not observed.

Therefore, overall, the absorption peaks that appear to be representative of vibrations associated with ZnO species with some degree of confidence appear between 444-478 cm^{-1}.

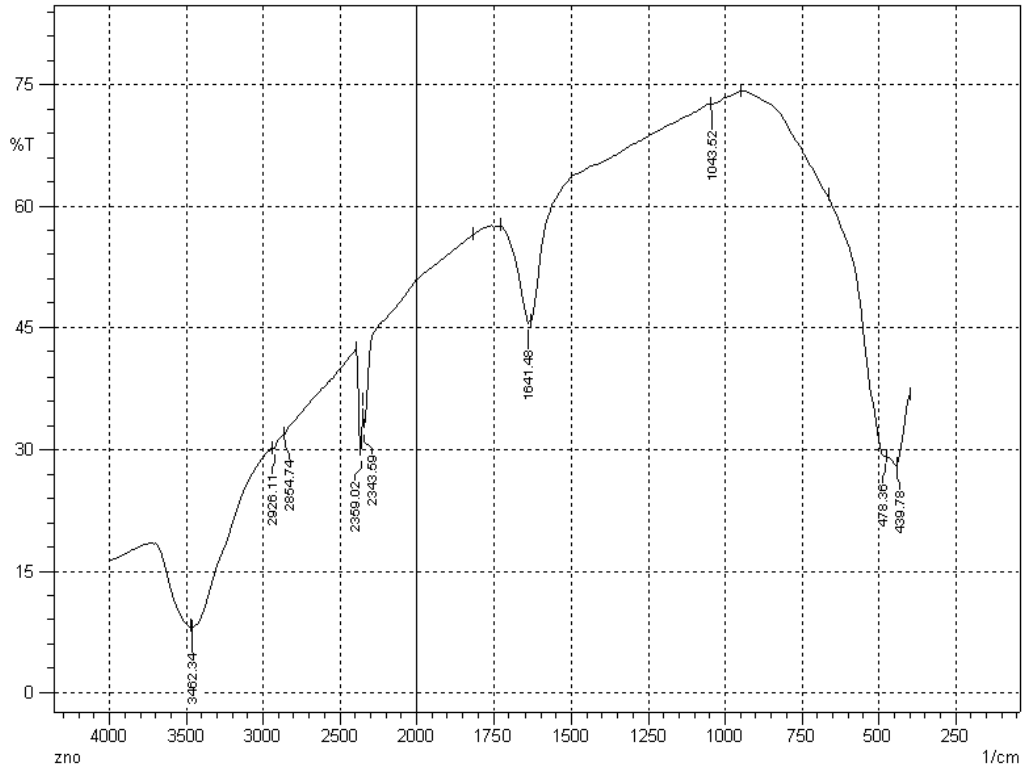

Figure 4.104 FTIR spectrum of zinc oxide (ZnO) reference standard obtained by transmission through pressed KBr pellets.

4.2.3.1.4 Chromium oxide (Cr_2O_3)

A chromium oxide FTIR spectrum is provided in Figure 4.105. Four major peaks are observed at approximately 3449, 1630, 617 and 556 cm^{-1}. There are also minor peaks observed at approximately 444 and 413 cm^{-1}. It is again surprising that absorption bands are observed between 3000 and 3700 cm^{-1}, as well as 1630 cm^{-1}. This could be related to O-H stretch and bend vibrations as a result of possible absorbed water from the atmosphere.

In this spectrum the presence of carbon dioxide has also been detected, possibly via atmospheric contamination. Sharp peaks at 2361 and 667 cm^{-1}, representative of asymmetric C=O stretch and corresponding C=O bend peaks, have been observed.

Therefore, overall, the absorption peaks that appear to be representative of vibrations associated with Cr_2O_3 species with some degree of confidence appear between 556-617 and 413-444 cm^{-1}.

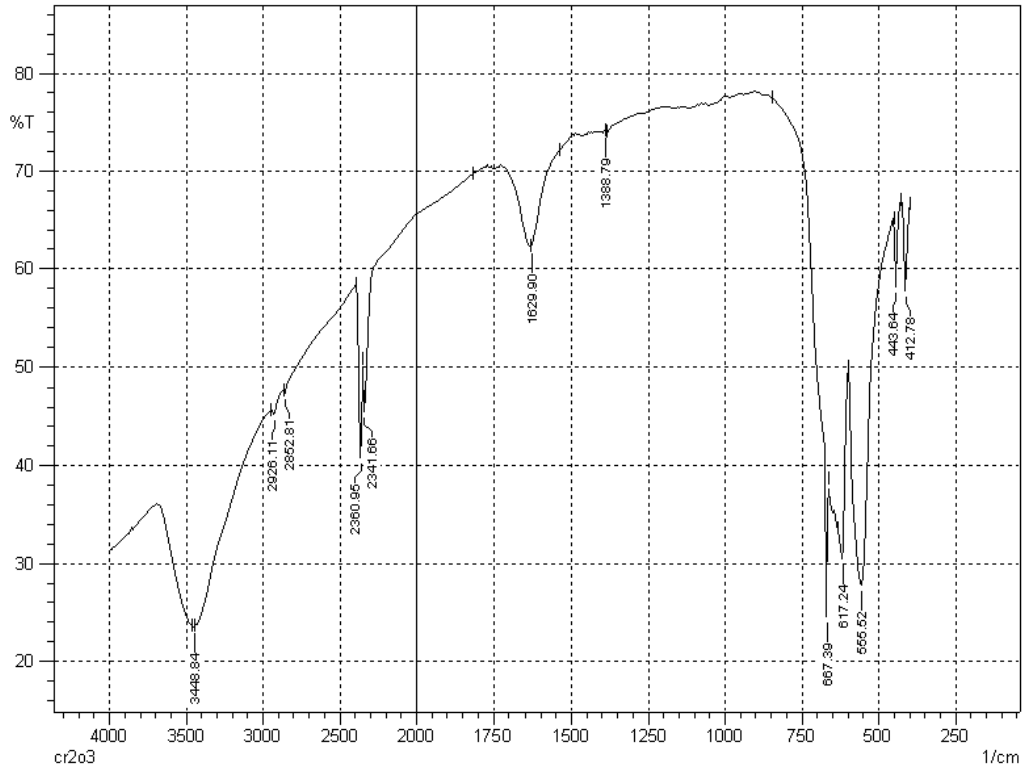

Figure 4.105 FTIR spectrum of chromium oxide (Cr_2O_3) reference standard obtained by transmission through pressed KBr pellets.

4.2.3.1.5 Chromium trioxide (CrO_3)

A chromium trioxide FTIR spectrum is provided in Figure 4.106. Moving from left to right, major peaks are observed at 781, 961, 1629, 3445 cm^{-1}. Sharp peaks are observed at 885 and 908 cm^{-1}, with minor peaks also observed at 565, 1316 and 1850 cm^{-1}. In addition, atmospheric carbon dioxide has also been detected, with a sharp peak at 2359 cm^{-1} observed (asymmetric C=O stretch peak).

In comparison to a $K_2Cr_2O_7$ reference standard FTIR spectrum studied by Xia et al. [100], a similar peak envelope between 565 and 949 cm^{-1} was observed, with some of the peaks in similar positions (565, 762, 884, 948 cm^{-1}). There are, however, no additional major peaks between 3000 to 3700 and 1629 cm^{-1} as exhibited in the CrO_3 spectrum, which further supports the view that these peaks are a contribution from adsorbed atmospheric water. Therefore, the peak envelope between 781 to 961 cm^{-1} is very much representative of vibrations as a result of Cr(VI) species.

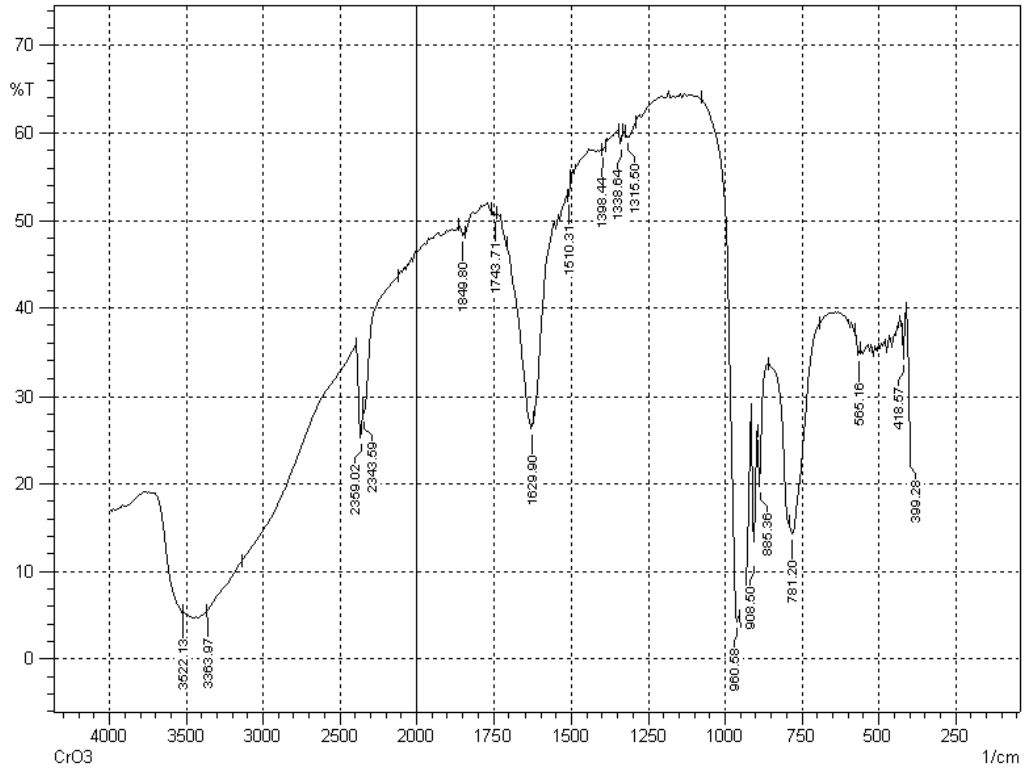

Figure 4.106 FTIR spectrum of chromium trioxide (CrO_3) reference standard obtained by transmission through pressed KBr pellets.

4.2.3.1.6 Chromium hydroxide ($Cr(OH)_3$)

A chromium hydroxide FTIR spectrum is provided in Figure 4.107. Five pronounced peaks are observed at approximately 3416, 1626, 1391, 1483 and 503 cm^{-1}. There are also peaks evident at approximately 1572 (shoulder) and 839 cm^{-1}.

In comparison to a $Cr(OH)_3$ reference standard FTIR spectrum by Xia et al. [100], a similar peak envelope between 1619 and 1386 cm^{-1} is observed, with peaks exhibiting comparable maximum peak positions (1386, 1494 and 1619 cm^{-1}). Similarity is also observed with a broad peak between 3000-3600 cm^{-1} and peaks at approximately 518 and 850 cm^{-1}. Peaks exhibited between 3000-3600 cm^{-1} could indicate that $Cr(OH)_3$ is associated with water possibly as ligands.

Therefore peaks which are representative of vibrations as a result of $Cr(OH)_3$ species include approximately three peaks between 1626 and 1391 cm^{-1}, two large peaks either side of the spectrum (3000-3600 and 503 cm^{-1}) and a small minor peak at 839 cm^{-1}.

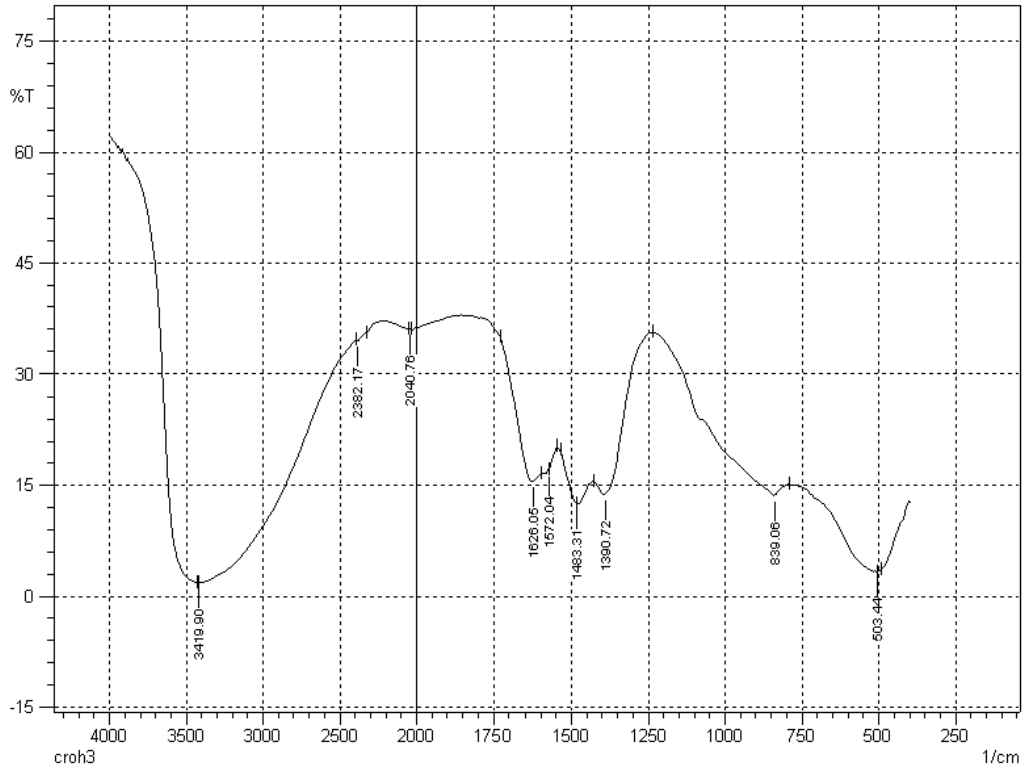

Figure 4.107 FTIR spectrum of chromium hydroxide ($Cr(OH)_3$) reference standard obtained by transmission through pressed KBr pellets.

4.2.3.2 Trivalent CCC

A trivalent CCC (Tripass LT1500 -90 s) FTIR spectrum is provided in Figure 4.108. The sample was obtained by abrading the conversion coating surface and pressing it into KBr pellets for analysis. To complement this study, reflectance absorption infra-red spectra of the sample in its untreated state were also acquired; Figure 4.109. In general, both FTIR and reflectance absorption infra-red spectra exhibited similar peak absorption envelopes, with the former exhibiting an improved resolution whilst the latter excelled in picking up absorption vibrations in the fingerprint region. Overall, this indicates that the abrasion removal method is in line with the non-destructive reflectance absorption infra-red method and does not appear to alter the conversion coating chemistry significantly. It is also important to note that the reflectance absorption infra-red spectrum does not include readings between 400 to 650 cm^{-1} unlike the FTIR spectrum.

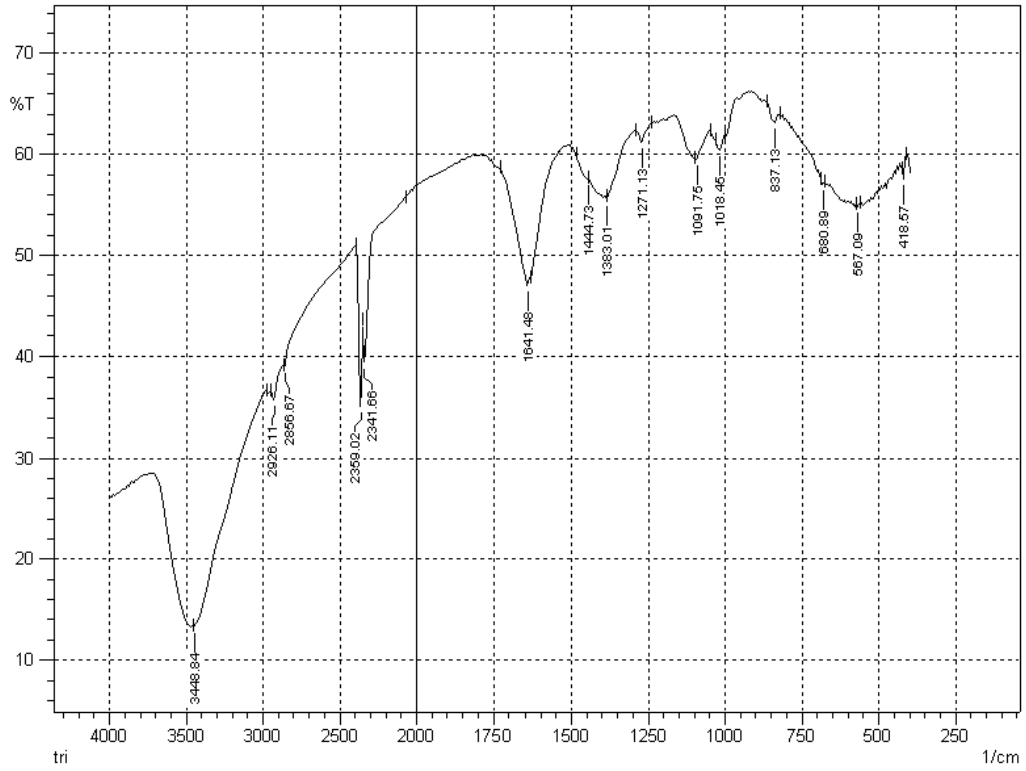

Figure 4.108 FTIR spectrum of trivalent CCC obtained by transmission through pressed KBr pellets.

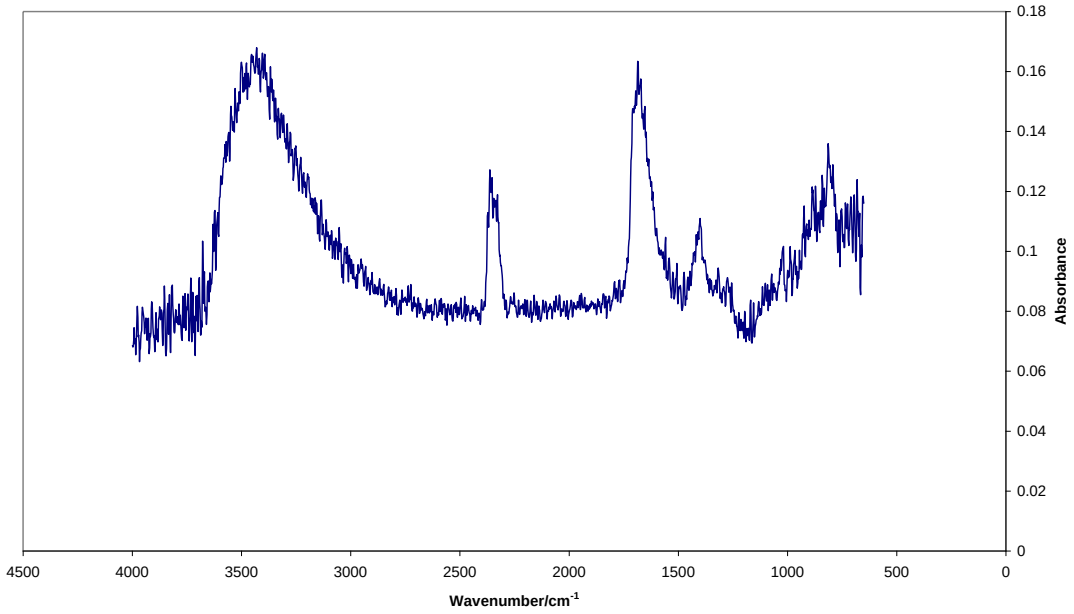

Figure 4.109 Infra-red spectrum of trivalent CCC obtained by reflectance absorption IR in its untreated state.

Observation of the FTIR and reflective absorption infra-red spectra from left to right highlights a broad absorption peak between 3000-3700 cm^{-1}. This could be either reflective of O-H stretch water or a carboxylic acid functional group. The next major absorption peak is that at 2359 cm^{-1}, which is representative of atmospheric carbon dioxide contamination (C=O stretch).

The next major absorption is that at 1641 cm^{-1}; Figure 4.108, which could be related to either water (O-H bend) or associated with chromium hydroxide which has a similar peak in this region (1626 cm^{-1}). The absorption value indicates that it is unlikely to be associated with carboxylic acid (C=O stretch ~ 1692 cm^{-1}). However, it must be noted that the reflectance absorption infra-red spectrum does exhibit a peak maximum between 1670 to 1760 cm^{-1} indicative of carboxylic acid (C=O stretch).

A major peak is evident at 1383 cm^{-1} with a slight shoulder exhibited at approximately 1445 cm^{-1}; Figure 4.108. The peak maximum absorption position is similar to that of a peak exhibited in the chromium hydroxide reference standard (1391 cm^{-1}). It is important to note that the reflectance absorption infra-red spectrum also exhibited a peak envelope in this region (1360-1460 cm^{-1}), with a peak maximum at approximately 1400 cm^{-1}.

The next absorption peak to be observed is a diminutive peak at 1271 cm^{-1}; Figure 4.108. Its position could be related to a C-O stretch carboxylic acid peak located at 1275 cm^{-1}. Other absorption peaks are located at 1092 and 1018 cm^{-1}; Figure 4.108. These absorption peaks do not appear on any of the reference standard spectra, thus possibly indicating another chemical species.

The next absorption peak at 837 cm^{-1}, which is also diminutive; see Figure 4.108, falls in a similar position to that of a small peak exhibited in the chromium hydroxide reference standard (839 cm^{-1}). The reflectance absorption infra-red spectrum exhibits a pronounced peak at approximately 815 cm^{-1}; Figure 4.109. The peak maximum position does not fall in the same peak absorption positions as exhibited by reference standards thus indicating an unknown chemical species.

The remaining peak absorption envelope between 400-750 cm^{-1}; Figure 4.108, is difficult to resolve. Its maximum peak position at approximately 567 cm^{-1} may be reflective of peak

absorptions found for the Cr_2O_3 reference standard (556 cm^{-1}), but this is not conclusive. It is also surprising that no absorption peak is exhibited at 444-478 cm^{-1} to reflect the presence of ZnO. This may be due to weak changes in dipoles for their respective vibrations to be accountable.

4.2.3.3 Hexavalent CCC

A hexavalent CCC (chromate A 40 s) FTIR spectrum is shown in Figure 4.110. Its reflectance absorption infra-red spectrum is provided in Figure 4.111. FTIR and reflectance absorption infra-red spectra both appear to exhibit similar peak absorptions between 1500 and 4000 cm^{-1}. However, below this region the ability to detect absorption peaks for the former is limited, and therefore only the latter will be used in the analysis of that region.

Moving from left to right in both spectra absorption peaks are observed at 3000-3700, 2359 and 1640 cm^{-1}. The broad absorption band between 3000 to 3700 cm^{-1} as mentioned for trivalent CCC is possibly either related to O-H stretch water (possibly associated with $Cr(OH)_3$ [51,96,100,151] or a carboxylic acid functional group. This absorption peak has also been observed for a hexavalent CCC applied onto a zinc substrate by Zhang et al. [45]. This absorption peak was also shown to reduce when hexavalent CCC samples were dried at higher temperatures (110 to 210°C for 30 min) indicating dehydration of the conversion coating. The absorption peak at 2359 cm^{-1} is related to atmospheric carbon dioxide contamination (C=O stretch). The absorption peak at 1640 cm^{-1} is related to either water (O-H bend) [51,96,100,148-150], associated to chromium hydroxide (1626 cm^{-1}) or indicative of carboxylic acid (C=O stretch) which has an absorption peak at approximately 1692 cm^{-1}.

Further absorption peaks were observed at 1130, 1080, 820-980 and 937 cm^{-1}. The absorption peak found at 1130 cm^{-1} could be attributed to SO_4^{2-}, given that sulphuric acid was used in part of the conversion coating treatment formulation. SO_4^{2-} has been attributed to 1126 cm^{-1} by Kasperek et al. [152]. The absorption peak found at 1080 cm^{-1} is difficult to attribute given that no reference standard spectra exhibited a similar absorption peak in this region. It is important to note that some researchers have noted at 1060 cm^{-1} the bending vibration of water coordinated to the $Cr_2O_3.2H_2O$, which could be related to this unassigned absorption peak [45,85,153]. The peak absorption band between 820-980 very much falls in line with the absorption band 781-961 cm^{-1} exhibited for the CrO_3 reference standard. Again, like the trivalent CCC infra-red spectrum; Figure 4.108, it is difficult to attribute absorption peaks

between 400-750 cm^{-1} for the hexavalent CCC FTIR spectrum; Figure 4.110. This makes the identification of potential ZnO, Cr_2O_3 and $Cr(OH)_3$ absorption peaks difficult.

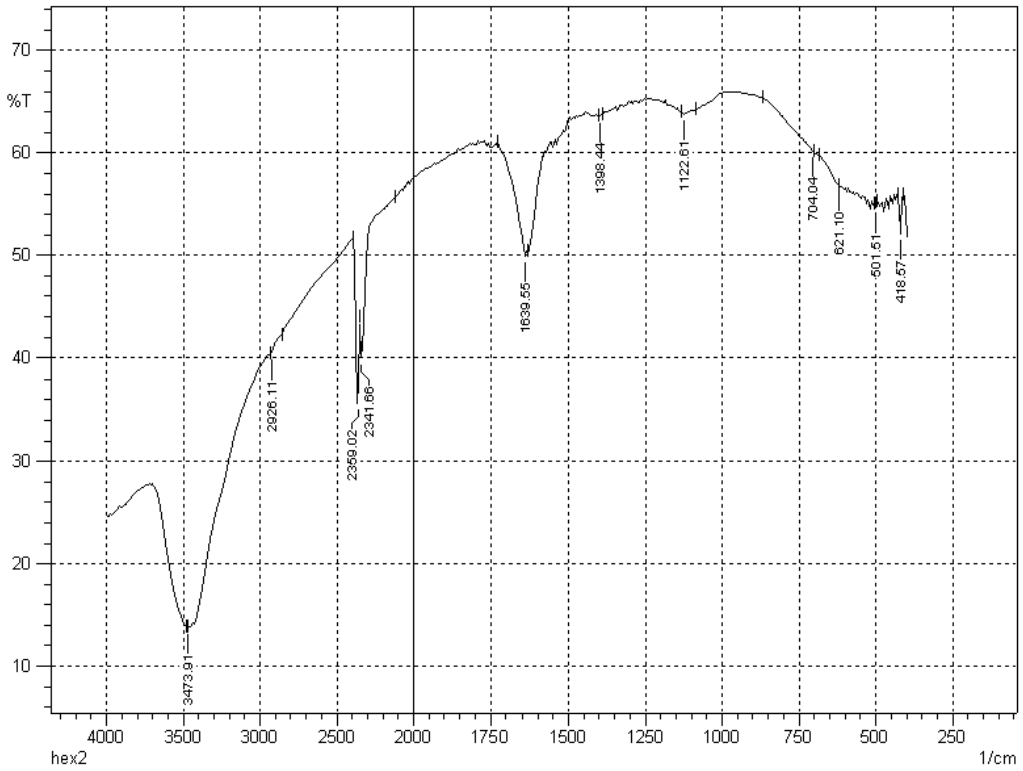

Figure 4.110 FTIR spectrum of hexavalent CCC obtained by transmission through pressed KBr pellets.

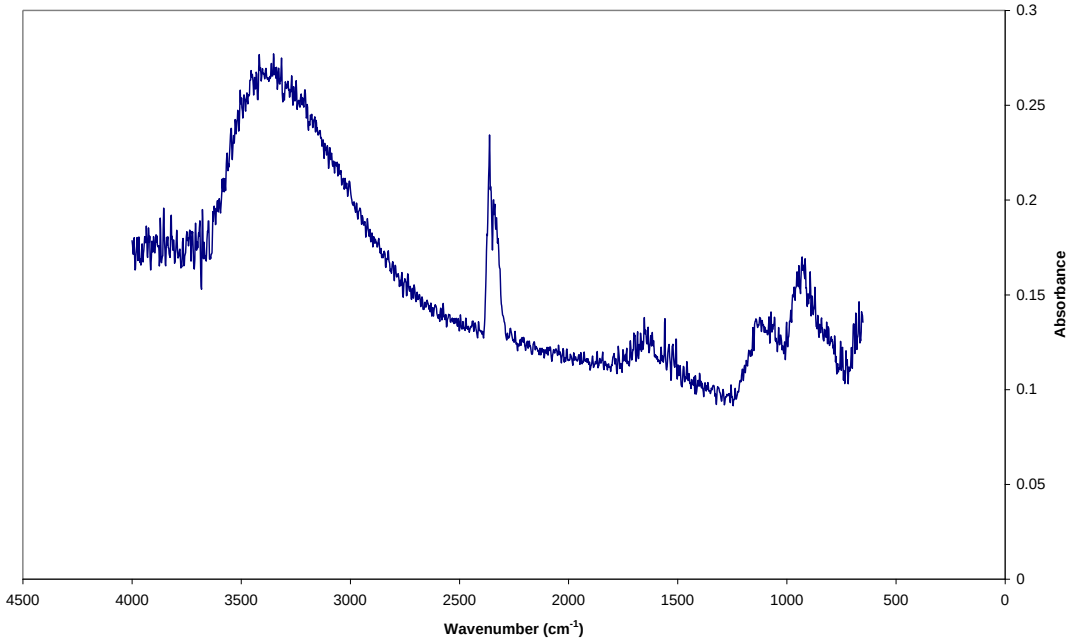

Figure 4.111 Infra-red spectrum of hexavalent CCC obtained by reflectance absorption IR in its untreated state.

4.2.3.4 Summary

Infra-red spectroscopy investigations of hexavalent CCC (chromate A) and trivalent CCC (Tripass LT1500) on acid zinc electrodeposited steel were carried out using chromium, zinc and organic acid reference standards. In general, results obtained were difficult to interpret. Analysis of the results indicated the presence of $Cr(OH)_3$, CrO_3 and H_2O within the hexavalent CCC. Analysis of trivalent CCC indicated the presence of a carboxylic species, H_2O either absorbed or associated with chromium, and $Cr(OH)_3$. The presence of carboxylic acids could account for the previously mentioned carbon in XPS studies.

4.3 Electrochemical corrosion characterisation

An electrochemical study, using polarisation curves and LPR measurements, was carried out to investigate the corrosion protection of hexavalent and trivalent CCCs. Also progressive LPR measurements were taken with increasing exposure time in 5% NaCl solution.

4.3.1 Electrochemical polarisation curves

Polarisation curves were carried out for an untreated acid zinc electrodeposited steel, hexavalent CCC (chromate A - 40 s) and trivalent CCC (Tripass LT1500 – 90 s); Figure 4.112. Note that two samples were used for the individual cathodic and anodic potential plots to prevent any physical or chemical changes in the conversion coating and untreated zinc coating state.

Evaluation of the open circuit values for zinc electrodeposited steel and hexavalent CCC appear to be similar, whilst that of trivalent CCC appears to be slightly more positive i.e. more noble.

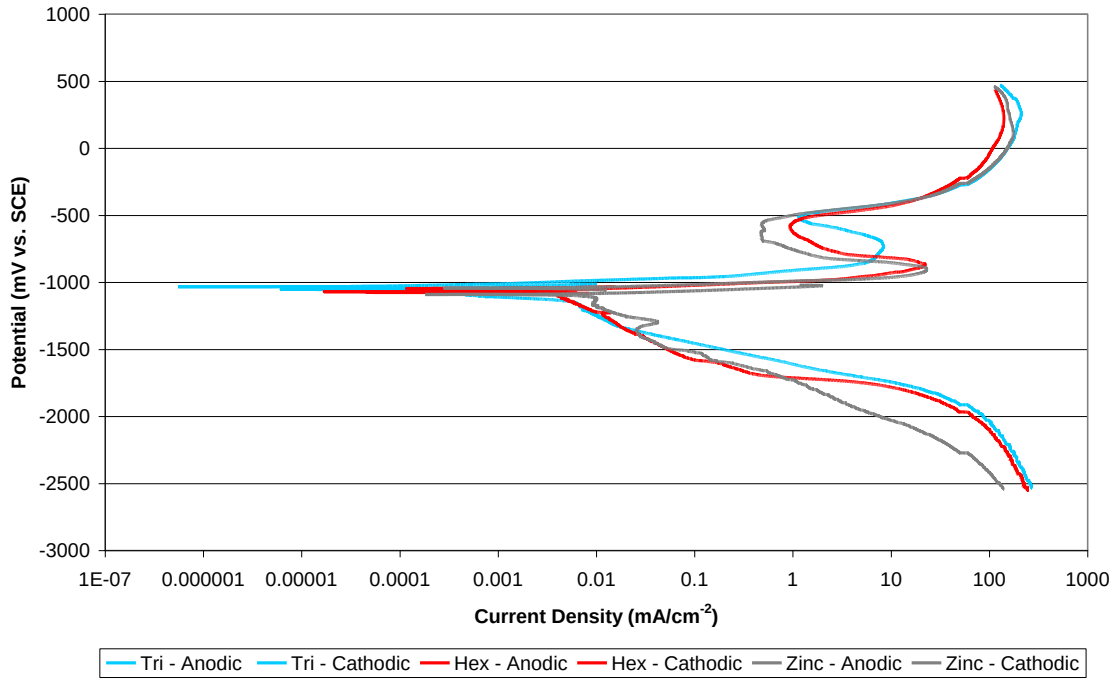

Figure 4.112 Anodic and cathodic polarisation curves for untreated acid zinc electrodeposited steel, hexavalent CCC (chromate A - 40 s) and trivalent CCC (Tripass LT1500 - 90 s) treated acid zinc electrodeposited steel recorded in 5% NaCl solution.

The anodic curves for the hexavalent CCC and zinc electrodeposited steel became active more quickly than the trivalent CCC as indicated by a sharp increase in current density. The initiation of an increased current from the open circuit current value indicates the start of the zinc/conversion coating dissolution. This continues until the largest current density value, which indicates the point at which corrosion products begin to form on the surface of the zinc electrodeposit and / or conversion coating following interactions with oxidising species within the electrolyte. For the trivalent CCC there appears to be a more gradual increase in current density as opposed to a sharp increase exhibited by the hexavalent CCC and zinc electrodeposited steel. This indicates a reduced rate of corrosion. Also, following the maximum current density value on the anodic branch, a decrease in current density for all coatings is observed with trivalent CCC undergoing a slower response. A slower decrease in current density is possibly due to the formation of corrosion products in localised regions only, as opposed to complete coverage of the surface as in the case of the hexavalent CCC and zinc electrodeposited steel. The 5% NaCl solution with normal levels of oxygen could have provided sufficient oxygen for passivation in active sites. Note no measurements were taken of the NaCl solution oxygen concentration before and after purging. The corrosion products are likely to be zinc oxide/hydroxide or possibly even associated with chloride. A slower response for the trivalent CCC may suggest reduced regions of physical defects e.g. the absence of micro-cracks exhibited in FEGSEM studies; Figure 4.22a-f, lower conductivity or good insoluble barrier protection thus helping to improve its corrosion resistance properties. In the case of the hexavalent CCC, a similar curve pattern to the zinc electrodeposited steel suggests less corrosion resistance than the trivalent CCC. This may suggest that self-repair protection properties are lacking and that corrosion performance may in fact be only based on barrier protection, with any imperfections such as micro-cracks and poor adhesion to the zinc substrate reducing its performance.

For all coatings, a minimum current density value is reached on the anodic curve following the maximum current density value. This possibly reflects maximum accumulation of zinc and/or conversion coating corrosion products on the steel substrate. Following this point a further increase in current density is observed before a near limiting current is reached. The further increase in current density may indicate removal of corrosion products as well as dissolution of the steel substrate. Visual observation of the substrate, revealed a black colouration observed on all samples.

To observe the electrochemical polarisation curves for the hexavalent CCC, the trivalent CCC and the zinc electrodeposited steel samples under reduced oxygen concentration the 5% NaCl solution was purged with nitrogen gas for 1 h prior to testing. Corresponding anodic and cathodic polarisation curves are provided in Figure 4.113. In comparison to polarisation anodic curves from an oxygen containing solution the only minor differences are with the hexavalent CCC curve. In comparison to the zinc electrodeposited steel curve, and similar to that of trivalent CCC, there is a gradual rise in current density as well as a reduced point at which corrosion products begin to form indicating a reduced rate of corrosion like that of trivalent CCC. These minor improvements in hexavalent CCC corrosion protection behaviour could be related to a reduced number of physical imperfections. It is important to note that under a reduced oxygen containing 5% NaCl solution environment there is less opportunity for self-repair properties.

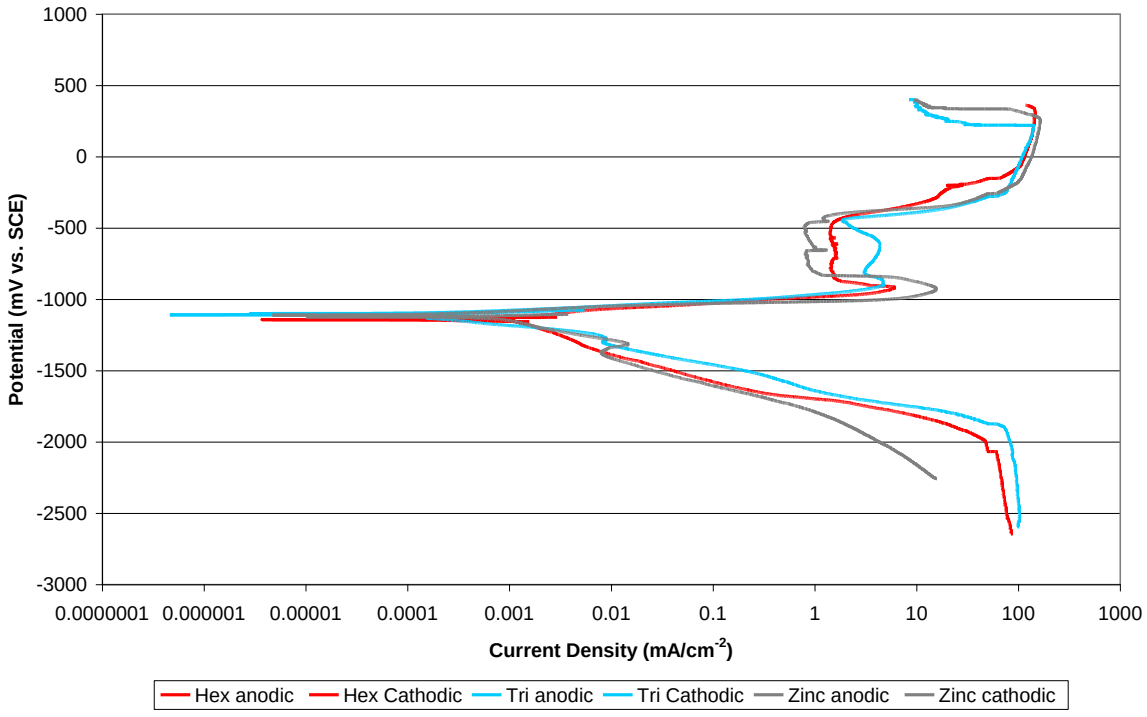

Figure 4.113 Anodic and cathodic polarisation curves for untreated acid zinc electrodeposited steel, hexavalent CCC (chromate A - 40 s) and trivalent CCC (Tripass LT1500 - 90 s) treated acid zinc electrodeposited steel recorded under reduced oxygen containing 5% NaCl solution.

Polarisation cathodic curves for hexavalent CCC, trivalent CCC and zinc electrodeposited steel recorded under normal and deficient levels of oxygen in the 5% NaCl solution are shown in Figures 4.112 and 4.113. In both conditions, and the former to a greater extent, the zinc electrodeposited steel exhibits a sharp increase in current density from the open circuit current

value (i.e. zero). This is possibly indicative of the conductive nature of the zinc electrodeposited steel. The reactions taking place at the inert platinum electrode would not be metal dissolution but would encourage oxygen (under oxygen containing conditions) and chlorine gas generation; see Equations 2.22 and 4.1 [154]. The reactions alternatively taking place at the zinc electrodeposited steel surface would most likely be hydrogen evolution and the reduction of oxygen (under oxygen containing conditions) if the conditions are acidic at the sample / electrolyte interface; see Equations 2.2 and 2.21. If neutral or alkaline conditions are present, hydroxide ions may be generated under oxygen containing conditions; see Equation 2.3, particularly if sufficient hydrogen evolution increases the pH locally at the interface.

$$2Cl^- \rightarrow Cl_2 + 2e^- \qquad \textbf{Equation 4.1}$$

$$Cr^{6+} + 3e^- \rightarrow Cr^{3+} \qquad \textbf{Equation 4.2}$$

In the case of the hexavalent and the trivalent CCCs their semi-conductive nature results in a gradual rise in current density, particularly under normal oxygen containing levels in the 5% NaCl solution. Possibly indicating a suppression of the chemical reactions mentioned above. The curves thereafter appear to differ for the trivalent CCC in comparison to the hexavalent CCC and the zinc electrodeposited steel. The curves for the latter appear to show slight current increases with potential, indicating increased cathodic reactions such as hydrogen evolution and oxygen reduction reactions. It is also interesting to note that under a reducing environment soluble Cr(VI) species could even be reduced to Cr(III) within hexavalent CCCs; Equation 4.2, however, evidence for this is somewhat difficult to prove.

Finally, the limiting current density value, shown by the largest current value appears to show that the trivalent CCC exhibits the largest value, with that of the zinc electrodeposited steel the smallest unexpectedly given the conductive nature of the zinc electrodeposited steel.

4.3.2 LPR measurements

4.3.2.1 Hexavalent and Trivalent CCC

Average LPR values for the trivalent CCC (Tripass LT1500 - 90 s) sample in comparison to the hexavalent CCC (chromate A 40 s) are significantly greater for all coating immersion times; see Table 4.26. The enhanced performance could be related to the morphology or

chemical composition of the trivalent CCC. FEGSEM studies of the trivalent film exhibited a surface morphology free of any micro-cracks or the presence of any other physical defects for the trivalent CCC; Figure 4.22a-f. An effective insoluble barrier corrosion protection mechanism may also have helped prevent the penetration of aggressive chloride ions present within the 5% NaCl solution used for the LPR testing.

Average LPR values for the hexavalent CCCs appear to show a decline in performance on increasing coating immersion time. It is important to note that micro-cracking, blistering and adhesion problems were noted from SEM studies for 40 and 80 s immersion time; Figures 4.8a-b and 4.9b-d. Also the physical appearance of the hexavalent CCC 80 s samples when exposed for 18 h in 5% NaCl solution exhibited loss of the conversion coating from the zinc substrate in some cases; Figure 4.33b. These observations are clearly detrimental to the hexavalent CCC corrosion resistance performance, particularly for increased coating immersion times which are reflective of an increased coating thickness; Table 4.1.

Alternatively, average LPR values for increased coating immersion times for trivalent CCCs appears to show no performance enhancement or decline. This could be related to the lack of physical defects such as micro-cracking or blistering on increasing immersion time; Figure 4.22a-f. The increased coating immersion time which is also reflective of increased coating thickness; Table 4.1, is possibly less influential in short term tests such as LPR as opposed to neutral salt spray which measures the coating's performance over a longer period of time.

Table 4.26 LPR measurements for hexavalent (chromate A) and trivalent (Tripass LT1500) CCCs on acid zinc electrodeposited steel formed at different immersion times. Recorded after 40 min exposure in quiescent 5 wt.% (pH 6) NaCl solution at room temperature.

Treatment solution	LPR measurement						
	Number of readings						Average Value (Ω cm^2)
	1	2	3	4	5	6	
Hexavalent CCC 20 s	12500	4688	6667	10000	7750	11250	8809
Hexavalent CCC 40 s	850	1650	2800	8350	6650	8036	4723
Hexavalent CCC 80 s	5250	1100	625	1330	1500	1500	1884
Trivalent CCC 45 s	85000	66667	35714	52000	33300	57667	55058
Trivalent CCC 90 s	34000	41500	70800	50000	68000	43750	51342
Trivalent CCC 180 s	60000	46000	46000	74000	57350	45600	54825

4.3.2.2 Effect of Tripass LT1500 additives on LPR measurements

4.3.2.2.1 Tripass LT1500 – control

Generally, similar high average polarisation resistance values (64620 to 51342 Ω cm^2) were observed for the Tripass LT1500 control specimens prepared in-house to those of Tripass LT1500 samples prepared from a proprietary concentrate, distributed from MacDermid plc; see Tables 4.26 and 4.27. These values concur with surface morphology FEGSEM images of the two samples, which exhibited surfaces free from physical defects; Figure 4.43a-c and 4.22a-f. A slight improvement in the average polarisation resistance value for the in-house sample to that prepared from a proprietary concentrate (~10000 Ω cm^2) could be because of differences between a treatment solution prepared in a laboratory to that within a factory e.g. additive concentration tolerances, contamination and processing variables.

Table 4.27 LPR measurements for trivalent CCC on acid zinc electrodeposited steel samples produced from Tripass LT1500 with different solution variables; see Table 3.7. Treatment operating conditions 90 s immersion time / pH 1.8 / 21°C. Note: * treatment solution allowed to age with additional heating before sample preparation.

	LPR measurement						
	Number of readings						
Sample	1	2	3	4	5	6	Average (Ω cm^2)
Tripass LT1500 - control	60000	60800	67679	70000			64620
No sodium molybdate	71428	87500	85000	50000	66667	22143	63790
0.4 g/l sodium molybdate	24400	37500	37308	20000	19200	41667	30013
No cobalt nitrate	32400	26400	29200	37500	35536	42000	33839
14.6 g/l cobalt nitrate	60000	70000	74285	60000	66607	81000	68649
No malonic acid	41250	37142	42857	56606	50833		45738
13 g/l malonic acid	3917	5833	6292				5347
13 g/l malonic acid*	55000	70000	64200	57917	72083		63840
No chromium nitrate	740	1036	800				859
212 g/l chromium nitrate	3890	4640	4800	5000	4692	4800	4637
No oxalic acid	34583	35000	36000	25429	26429	28000	30907
52 g/l oxalic acid	857	1200	1221	800	860	780	953

4.3.2.2.2 Effect of sodium molybdate

The average polarisation resistance measurement for the samples produced from Tripass LT1500 modified with a further addition of sodium molybdate (0.4 g/l) in comparison to the Tripass LT1500 control results in a decrease in value (64620 to 30013 Ω cm^2); see Table 4.27. Corresponding FEGSEM surface morphology images did not reveal any physical defects to

support a decline in corrosion resistance; Figure 4.44c-d. FEGSEM thickness measurements, however, did show a reduced coating thickness in comparison to the Tripass LT1500 control; Table 4.9. Whether this has a significant effect upon LPR reading is debatable given that earlier investigations into coating immersion time for Tripass LT1500 (based on a factory concentrate) did not show any increase in average LPR measurement; Table 4.26.

The average polarisation resistance measurements for the samples produced from Tripass LT1500 modified with the exclusion of sodium molybdate shows similar values to that of Tripass LT1500 control; see Table 4.27. FEGSEM surface morphology images and coating thicknesses were also found to be similar; Figure 4.44a-b and Table 4.9. It is important to note that molybdenum was only detected in the XPS survey scan studies of the sodium molybdate (0.4 g/l) variable. This possibly highlights the limited role of sodium molybdate in terms of corrosion resistance.

4.3.2.2.3 Effect of cobalt nitrate

The average LPR value of the samples produced from Tripass LT1500 modified with the exclusion of cobalt nitrate shows a reduction in value to that of the Tripass LT1500 control sample (33839 to 64620 Ω cm^2); see Table 4.27. Tripass LT1500 modified with the inclusion of further cobalt nitrate (14.6 g/l) appears to produce a surface with a slightly increased average LPR measurement; see Table 4.27. In both cases their respective surface morphologies were free of micro-cracks or other physical defects; Figure 4.45. Therefore, the addition of cobalt nitrate to a certain extent influences corrosion resistance. However, the role of cobalt as an inhibitor within the conversion coating is debatable given the trace amounts detected using XPS; Figure 4.76. Therefore the role of cobalt may only be as a catalyst during the conversion coating film formation stage.

4.3.2.2.4 Effect of malonic acid

The average LPR value of the samples produced from Tripass LT1500 modified with a further addition of malonic acid (13 g/l) shows a very significant reduction in value to that of the Tripass LT1500 control sample (5347 to 64620 Ω cm^2); see Table 4.27. However, when the same treatment solution was allowed to age with additional heating before sample preparation, an increase in average polarisation resistance was observed to 63840 Ω cm^2; see Table 4.27. FEGSEM surface morphology images also correspond to this change in value as

no micro-cracks or any other physical imperfections observed for samples prepared from the solution allowed to age with additional heating; Figure 4.46e-f.

The exclusion of malonic acid from the Tripass LT1500 formulation produced a surface which exhibited a slightly lower average LPR value of 45738 Ω cm^2; see Table 4.27. This sample also did not reveal micro-cracks or any other physical imperfections when observed using a FEGSEM; Figure 4.46a-b.

4.3.2.2.5 Effect of chromium nitrate

The average LPR value for samples produced from Tripass LT1500 modified with the exclusion of chromium nitrate shows a significant reduction in value to that of the Tripass LT1500 control (859 to 64620 Ω cm^2); see Table 4.27. This agrees well with XPS chemical compositional analysis; Figure 4.82, which exhibited the absence of chromium within the conversion coating, and as a result zinc and oxygen containing compounds were present across the surface with the underlying zinc substrate altered; Figure 4.49a-e. No effective barrier or corrosion inhibiting chemistry is available for effective corrosion resistance.

The average LPR value for samples produced from Tripass LT1500 modified with the inclusion of additional chromium nitrate (212 g/l) shows a significant reduction in value to that of the Tripass LT1500 control (4637 to 64620 Ω cm^2); see Table 4.27. The severely reduced performance could be attributed to circular micro-cracks observed in FEGSEM studies of the surface morphology; Figure 4.50 a-c. It is also important to note that even with an increased coating thickness in comparison to the Tripass LT1500 control (260 to 175 nm) the corrosion performance was still inferior.

4.3.2.2.6 Effect of oxalic acid

The average LPR value for samples produced from Tripass LT1500 modified with a further addition of oxalic acid (52 g/l) showed a significant reduction in value to that of the Tripass LT1500 control sample (953 to 64620 Ω cm^2); see Table 4.27. This corresponds to FEGSEM surface morphology images in which an extensive network of micro-cracks were observed as well as cross-sectional images revealing a less than compact coating; Figure 4.48c-d and f.

The average LPR value of samples produced from Tripass LT1500 modified with the exclusion of oxalic acid shows a reduction in value to that of the Tripass LT1500 control

(30907 to 64620 Ω cm^2); see Table 4.27. The reduction in corrosion resistance could be attributed to tiny micro-cracks observed in FEGSEM studies of the surface morphology; Figure 4.48a-b.

4.3.2.3 Black trivalent CCC

The average LPR values of a black trivalent CCC on an acid zinc electrodeposited steel substrate and that for an alkaline zinc electrodeposited steel substrate; Table 4.28, exhibit values inferior to that of a trivalent CCC treated surface (Tripass LT1500); see Tables 4.26 and 4.27. The inferior performance could be related to physical defects observed from FEGSEM studies such as micro-cracks; Figures 4.51a-c and 4.52a-c. In the case of black trivalent CCC formed on alkaline zinc electrodeposited steel, the micro-crack width was found to be larger than that formed on acid zinc electrodeposited steel. An increase in crack width increases the passage for corrosion media thus reducing the corrosion resistance of the coating. It is also important to note that the conversion coatings in both cases do not appear as distinct separate conversion coating entities which adhere to the underlying zinc substrate, but as part of the zinc substrate; Figures 4.51a-c and 4.52a-c. Therefore access of corrosive ions such as chlorides would have no problem penetrating surface cracks to the more localised zinc concentrated regions.

Table 4.28 LPR measurements for black trivalent CCCs and organic topcoats.

Sample	LPR measurement			
	Number of readings			
	1	2	3	Average (Ω cm^2)
Black trivalent CCC on acid zinc electrodeposited steel	5040	5060	5020	5040
Black trivalent CCC on alkaline zinc electrodeposited steel	2000	6429	4216	4215
Trivalent CCC with an organic topcoat (12 nm silica particles) on acid zinc electrodeposited steel	71429	89286	80359	80358
Trivalent CCC with an organic topcoat (22 nm silica particles) on alkaline zinc electrodeposited steel	71429	70833	71131	71131

4.3.2.4 Organic topcoat

The average LPR values of a trivalent CCC (Tripass LT1500) is greatly improved with the introduction of a nano silica based organic topcoat with both 12 and 22 nm particle size; see

Table 4.28. Corresponding FEGSEM studies of these topcoats exhibited in both cases a compact structure which was free from micro-cracks; Figure 4.53a-c and 4.54a-c. In the case of the organic topcoat based on 22 nm silica particles, there was some agglomeration of silica nano-particles which may account for the slight reduction in corrosion resistance performance.

4.3.2.5 Hexavalent and trivalent CCC time-dependent measurements

LPR measurements were conducted on increasing exposure time within 5% NaCl solution for a hexavalent CCC (chromate A- 40 s) and trivalent CCC (Tripass LT1500 - 90 s) specimens.

LPR measurement for hexavalent CCC at 24 h exposure; Figure 4.114, is approximately half the value in comparison to the average value exhibited for 1 h exposure; Table 4.26, for a similar sample. FEGSEM surface morphology images of a similar sample imaged following 18 h 5% NaCl solution exposure indicated regions of peeling and blistering which could account for the reduced corrosion resistance performance i.e. loss in barrier protection; Figure 4.31a-d.

LPR measurements appear to show that on increasing exposure time a larger value is observed for the hexavalent CCC, comparing values at 24 to 150 h; Figure 4.114. An increase in value may be related to the formation of temporary insoluble zinc corrosion products within defects of the conversion coating such as cracks exhibited in FEGSEM studies; Figure 4.31a-d. Alternatively, soluble Cr(VI) species may have reduced to insoluble Cr(III) products thus increasing the corrosion resistance, provided that the corresponding oxidising reactions occurred.

The initial LPR values for trivalent CCCs at 24 and 50 h NaCl solution exposure indicate a reduction in corrosion resistance in comparison to a similar sample exposed for less than 1 h; Figure 4.115 and Tables 4.26-4.27. This indicates that the sample underwent some form of deterioration to produce the reduced corrosion resistance before stabilising and increasing its corrosion resistance values beyond this point up until ~125 h. FEGSEM studies of a trivalent CCC following exposure to 18 h 5% NaCl solution, revealed a conversion coating surface morphology free of any major physical defects; Figure 4.35a-d, however, cross-sectional images did indicate changes in the morphology of the underlying zinc substrate; Figure 4.36a-c.

The increase in corrosion resistance from 24 to approximately 125 h possibly indicates the sparse formation of temporary zinc corrosion products in regions of damage whether physical or chemical. Beyond this exposure time a reduction in corrosion resistance performance is observed, possibly indicating increased regions of physical and chemical damage.

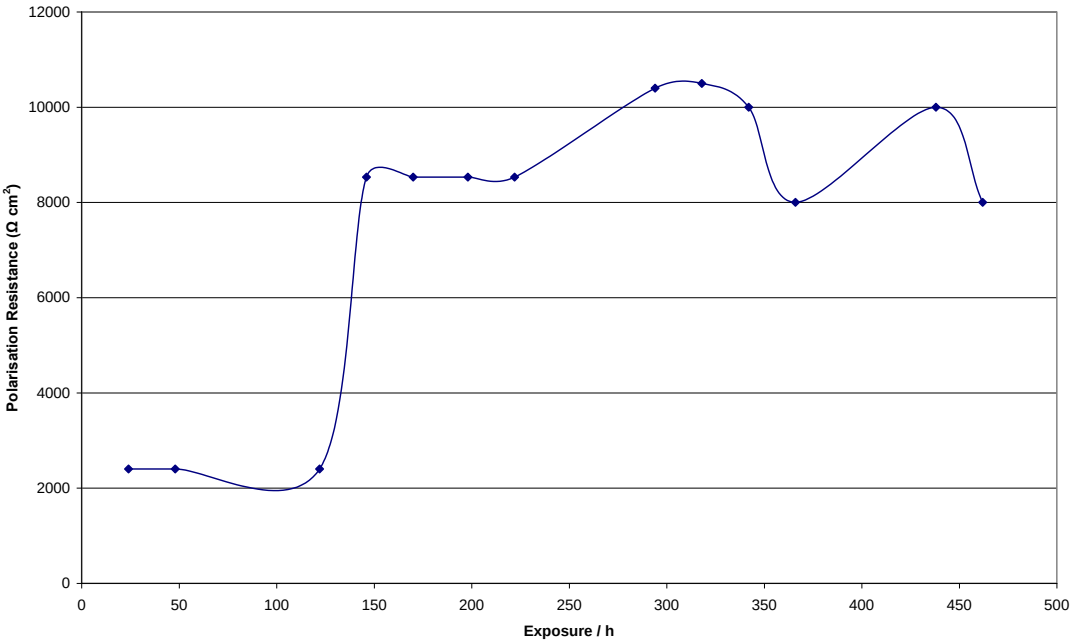

Figure 4.114 LPR vs. exposure time in 5% NaCl solution for hexavalent CCC (chromate A - 40 s) on acid zinc electrodeposited steel.

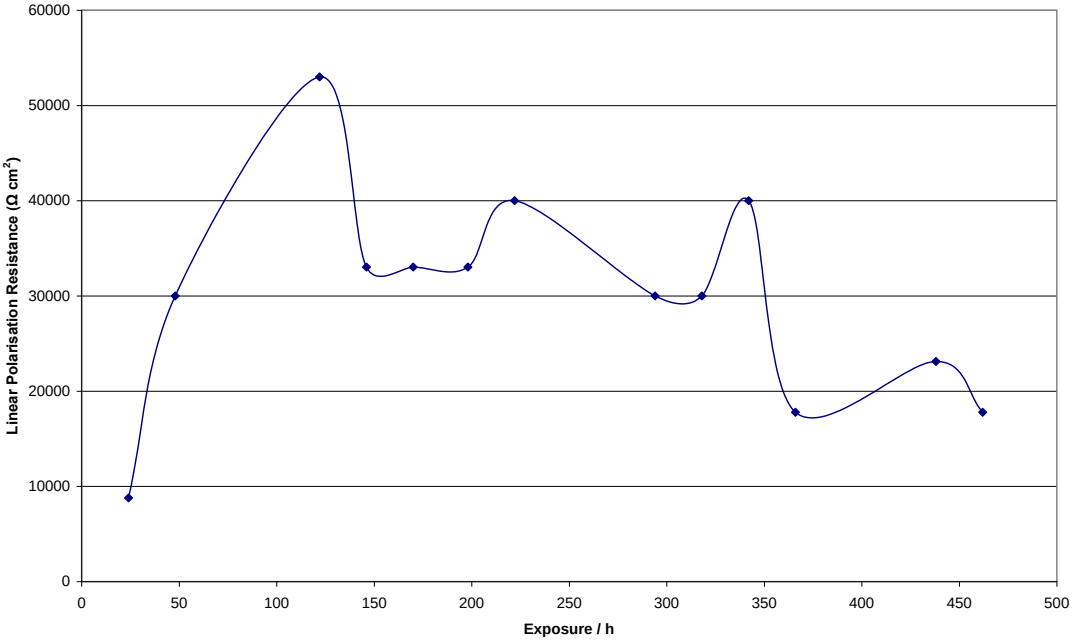

Figure 4.115 LPR vs. exposure time in 5% NaCl solution for trivalent CCC (Tripass LT1500 – 90 s) on acid zinc electrodeposited steel.

5 Discussion

5.1 Hexavalent CCC film formation

In order to elucidate the film formation process for hexavalent CCC it is important to identify the role of additives during the solution preparation and coating formation stage. During the latter, in which the zinc electrodeposited steel is immersed into the treatment solution, a series of anodic/cathodic reactions are likely to take place. Initially, the acidic nature of the solution initiates zinc dissolution and as a consequence certain additives are likely to be reduced forming insoluble compounds which form part of the coating [79]. These reactions are listed in Table 5.1. A favourable condition for the deposition of insoluble compounds is thought to be the rise in pH at the zinc interface following H_2 evolution; Table 5.1. Some of these reactions (e.g. the formation of $Cr(OH)_3$) are more favourable than others, which was identified by reference to the curve fitted hexavalent CCC Cr 2p data; see Table 4.17. However, for this electrochemical reaction to be sustained the film formation would, in theory, have to be linked to zinc oxidation to complement dichromate (or chromate) reduction. Zinc oxidation provides the necessary electrons for these reactions to take place.

Table 5.1 Potential redox reactions between substrate and conversion coating treatment solution, after Gigandet et al. [79]**.**

	Equations
Oxidation reactions	$Zn \leftrightarrow Zn^{2+} + 2e^-$
Reduction reactions	$2H^+ + 2e^- \leftrightarrow H_2$ $O_2 + 4H^+ + 4e^- \leftrightarrow 2H_2O$
Secondary reactions (formation of insoluble / soluble products	$Cr_2O_7^{2-} + 2H^+ \leftrightarrow 2CrO_3 + H_2O$ $CrO_4^{2-} + Zn^{2+} \leftrightarrow ZnCrO_4$ $Cr_2O_7^{2-} + Zn^{2+} \leftrightarrow ZnCr_2O_7(s)$ $Cr_2O_7^{2-} + 8H^+ + 6e^- \leftrightarrow Cr_2O_3 + 4H_2O$ $2HCrO_4^- + 8H^+ + 6e^- \leftrightarrow 2Cr(OH)_3 + 2H_2O$ $Zn + 2H_2O \leftrightarrow Zn(OH)_2 + H_2$ $Zn + H_2O \leftrightarrow ZnO + H_2$
Complex reactions & deposition	$Cr_2O_7^{2-} + 14H^+ + 6e^- \leftrightarrow 2Cr^{3+} + 7H_2O$ $Cr^{3+} + 6H_2O \leftrightarrow [Cr(H_2O)_6]^{3+}$ $[Cr(H_2O)_6]^{3+} + C_3O_4H_2^{2-} \leftrightarrow [CrC_3O_4H_2(H_2O)_4]^+ + 2H_2O$ $[Cr(H_2O)_6]^{3+} + C_2O_4^{2-} \leftrightarrow [CrC_2O_4(H_2O)_4]^+ + 2H_2O$ $[CrC_2O_4(H_2O)_4]^+ + 2C_2O_4^{2-} \leftrightarrow [Cr(C_2O_4)_3]^{3-} + 4H_2O$ $[CrC_2O_4(H_2O)_4]^+ \leftrightarrow Cr(OH)_3 + C_2O_4^{2-} + 3H^+ + H_2O$

XPS survey scan results; Figure 4.62, have shown the incorporated zinc content at the conversion coating surface to be minimal. AES depth profiling has also indicated a low

surface/sub-surface content of zinc, with levels only increasing at the zinc electrodeposit interface or if the conversion coating is very thin; see Table 4.19 and Figures 4.84-4.87. Such a situation whereby zinc levels are low throughout the coating indicates that the conversion coating growth mechanism may not be entirely a simultaneous electrochemical dissolution / precipitation process as suggested by previous researchers [82,86,87,89]. FEGSEM images reveal a smooth and flat surface morphology with the absence of significant porosity for the passage of chromating solution to promote the continued oxidation of zinc and outward growth of the conversion coating; see Figures 4.7a-c, 4.8a-c, 4.11a and d. Therefore, the passage of ions and electrons for redox reactions could only have been achieved via hydrated and semi-conductive regions of the already formed conversion coating. For such a theory the conversion coating thickness would not be dependent upon physical pathways, but the point at which zinc chemical reactions cease. These could include, for instance, the full conversion of the underlying zinc substrate, a threshold being met for ion/electron transport from the treatment solution to the underlying zinc substrate through a growing conversion coating e.g. a lack of hydrated and semi-conductive regions for ion and electron transport, saturation, or a dependency upon a required pH (e.g. 2) for zinc dissolution / chromium-zinc precipitation. The majority of these could have been identified, to a certain degree, using AES depth profiling by observing any fluctuations in zinc levels at certain depths across the sample.

An alternative film formation mechanism which leads on from the proposed mechanism described above could be based on a electrochemical / sol-gel deposition following sufficient zinc dissolution [88]. This is partially supported by a high concentration of $Cr(OH)_3$ at the conversion coating surface, detected using XPS and curve fitting; see Table 4.17. As well as a spherical-like particulate surface morphology, observed using FEGSEM and AFM. High magnification FEGSEM images of the hexavalent CCCs in Figure 4.11a and d revealed a spherical-like deposited conversion coating structure (~ 20-70 nm size) which appeared interlocked and fused together. Within the latter the appearance of tiny pores (> ~10 nm) was observed in some regions, but this was certainly not representative of an overall porous coating structure. AFM images also revealed a fused spherical-like particulate surface morphology; Figure 4.12a-c. The science supporting a sol-gel deposition is thought to be via a two stage process [89-92]. Firstly, a number of Cr(III) ions following Cr(VI) reduction hydrolyse to colloidal particles of $Cr(OH)_3$ based complexes, which upon a critical size coagulate and form a gel in close proximity to the zinc surface. The coating growth is sustained via high water retention and an open structure which is permeable and conductive

for the required electrochemical redox reactions. The second stage, would involve drying of the gel following removal from the treatment solution. Upon drying the gel would undergo water loss and shrinkage via capillary forces, leading to, in general, a layered particulate structure with some micro-pores.

Another film formation mechanism which has been proposed to be a factor in trivalent chromium electrodeposition [155-158] and could be related to both hexavalent and trivalent CCC formation is the tendency for stable trivalent chromium III complex species such as $[Cr(H_2O)_6]^{3+}$, to undergo polymeric olation and become 'inactive'. These species could possibly be absorbed, however, their ability to form a functional coating is unclear.

It is important to note that not all of the chromium content relies upon the dissolution of zinc in order to form part of the coating. CrO_3 (~At. 29%) has been established from curve fitted hexavalent CCC data with its percentage value increasing marginally when conducting lower XPS TOA measurements; see Table 4.17. Other similar oxidation state species may also be incorporated in small quantities such as soluble $Cr_2O_7^{2-}$ or CrO_4^{2-} ions or associated zinc compounds ($ZnCrO_4$, $ZnCr_2O_7$). The presence of the latter, however, would be difficult to support given the lack of incorporated zinc within the conversion coating, particularly at surface/sub-surface; see Tables 4.17 and 4.19 and Figure 4.87. In terms of film formation these Cr(VI) oxidation state species are more or less adsorbed from the treatment solution either as complex compounds associated with Cr(III) species [105] or with absorbed water molecules. Their presence at depth within the conversion coating would most likely be minimal. It is important to note, however, that no such data presented in this work supports contributions of Cr(VI) and Cr(III) oxidation state compounds at depth. Also the determination of Cr(VI) products or Cr(III) products at sub-surface is particularly difficult to evaluate using XPS due to the potential mixing of atoms and compounds as well as the increased opportunity for Cr(VI) to be reduced to Cr(III) under increased acquisition time and beam exposure.

As part of the hexavalent CCC treatment solution formulation, sulphuric and nitric acid were present. The role of these acids are thought to provide H^+ ions following dissociation and initiate zinc dissolution at the zinc substrate interface. The incorporation of sulphur within the hexavalent CCC exhibited by AES surface and depth profile data; see Table 4.19 and Figure 4.87, potentially supports this theory. AES depth profile data for the sulphur content in

general was found to initially decrease from the level exhibited at the surface/subsurface region and at depth its content stabilised before declining at the conversion coating / zinc electrodeposit interface. Sulphur detected could be as an absorbed sulphate residue e.g. SO_4^{2-} or HSO_4^-, following H^+ ion dissociation or alternatively, sulphur may provide an even greater role during the film formation process as suggested by Gigandet et al. [79], in which basic chromium sulphates are thought to form at the surface of the conversion film following initial anion reaction. Data presented in the present investigation does not support the presence of such chromium compounds. The absence of nitrogen in the AES data may indicate that the nitric acid concentration within the treatment solution is too weak, or that it only operates as a catalyst e.g. oxidising agent in the form of nitrate.

5.2 Hexavalent CCC micro-cracking and blistering

5.2.1 Instrumental effect on micro-cracking

FEGSEM images; Figures 4.7a-c and 4.8a-b, and thickness measurements; Table 4.1, showed that in this investigation as the chromate A conversion coating thickness increased above ~122 nm the appearance of micro-cracks resulted. Both low vacuum and InLens modes displayed this, as well as samples prepared with a gold sputter coating. In the case of the latter, additional blistering of the conversion coating was exhibited, possibly related to the vacuum environment used; Figures 4.9 a-d. When the chromate A, as well as chromate B conversion coatings which also exhibited micro-cracking and blistering; Figures 4.15a-c and 4.16a-c, were analysed using AFM, the presence of micro-cracks/blistering was not observed; Figures 4.12a-c and 4.17a-c. This indicates that the electron beam and/or the vacuum environment of the FEGSEM induces micro-cracks at a given coating thickness as with the case of chromate A conversion coatings. Further confirmation of this may also be found via Cryo stage-SEM analysis carried out on chromate B conversion coatings imaged at -180°C stage temperature and following stabilisation of stage to room temperature (21°C); Figures 4.18a-c and 4.19a-c. It was shown that as the temperature stabilised to room temperature the appearance of micro-cracks and blistering was exhibited. It appears that at -180°C the samples are in a frozen hydrated state and not influenced by heating from the electron beam or vacuum environment during imaging. Conversely, this technique should be treated with caution as water in the form of ice expands and could actually form cracks within the conversion coating given that water has been detected in IR studies; see Figure 4.110 and 4.111. In general, however, this instrument along with the AFM clearly show that exposing a hexavalent CCC

to a vacuum environment, coupled with exposure to an electron beam, will induce micro-cracking. The primary factor for micro-cracking, however, does appear to be coating thickness as observed for chromate A conversion coatings. An increased coating thickness is thought to increase tensile stress within the coating, which upon a given stress initiates crack propagation at a defect [99].

Internal stresses within chromate conversion coatings have previously been investigated using the bent cathode deflection method [99]. An alternative method of measuring internal stress could be via X-ray diffraction, however, given that conversion coatings have a mixed metal oxide composition determination of internal stress using this technique may prove to be difficult. It is important to note that thermal treatment could relieve residual stress in a conversion coating, however, given the presence of water in the conversion coating this could be compromised; see Section 5.2.3.

5.2.2 Treatment solution chemistry and substrate effect on micro-cracking

FEGSEM images of chromate A conversion coating surface morphology on acid zinc electrodeposited steel exhibited parallel micro-crack patterns, aligning predominately in one direction; Figures 4.7b-c and 4.8a-b. The crack pattern possibly indicates the direction in which stress is most relieved. FEGSEM images of chromate A conversion coating surface morphology on alkaline zinc electrodeposited steel also exhibited an aligned micro-crack pattern; Figures 4.13a-c and 4.14a-d. However, in comparison, the cracks appeared to initiate and end from pores within the coating thus also resulting in crack intersections between the aligning crack pattern. FEGSEM images of chromate B conversion coatings on acid and alkaline zinc electrodeposited steel; Figures 4.15a-c and 4.16a-c, also exhibited a similar aligned micro-crack morphology to that of chromate A conversion coatings on acid zinc electrodeposited steel. In all these cases the flat and smooth underlying zinc surface morphology does not appear to influence the crack pattern; Figures 4.1a-c and 4.3 a and b. Alternatively, the rolling direction of the underlying polished steel sheet could have influenced the crack pattern.

FEGSEM imaging of a chromate B conversion coating on zinc foil exhibited a surface morphology with a dense crack network similar in appearance to ‘dried cracked river bed’; Figure 4.20a-c, which is almost certainly a contribution from the underlying zinc foil surface defects as illustrated in Figures 4.5a and b. Variation in thickness and surface defects on the

zinc substrate could well have acted as localised stress regions which resulted in the formation of a crack network.

Therefore in summary, chromate A and B conversion coating treatment solutions on a flat and smooth substrate; zinc electrodeposited steel, will result in a crack pattern which predominately aligns in one direction, however, on a rough substrate; zinc foil, a dense crack network will result. Any variations in the conversion coating film formation process resulting in pores and uneven regions may also be a factor in the resulting crack pattern.

5.2.3 Water loss effect on micro-cracking

Another theory for the creation of micro-cracks is the loss of water from within the conversion coating upon heating. This could also be related to the instrumental effect on micro-cracking mentioned earlier. Infra-red analysis has indicated the presence of H_2O within chromate A conversion coated acid zinc electrodeposited steel; Figure 4.110 and 4.111. Water may be associated with chromium or zinc compounds such as hydrated oxides or as water of crystallisation in addition to its natural state possibly as absorbed moisture from the atmosphere. Water has also potentially been detected following curve fitting of the high resolution XPS O 1s peak envelope; see Figures 4.67a and 4.69, a similar envelope and prognosis was also established by other researchers [45]. In addition to this, thermogravimetric data carried out by Smith et al. on similar samples [159], showed a greater weight loss for a non-preheated chromate A acid zinc electrodeposited steel sample to preheated samples (24 h at 60 and 100°C) thus indicating the potential loss of water within the conversion coating upon heating; see Figure 5.1.

In this investigation only the presence of water has been investigated, no attempt has been made to estabilish the exact quantity of water in the conversion coating.

Data presented in this investigation has established the presence of water within chromate A conversion coatings and indicates that it is possibly removed from the bulk coating under thermal exposure. Therefore, in theory, the loss of water could initiate contraction via internal compressive forces, and that if the contracting forces within the coating, coupled with reduced adhesive forces between the coating and the substrate, increase stress beyond the local tensile strength, the coating will fracture to relieve the stress. The crack tip will propagate until the stress there is reduced to less than the local strength of the coating material [101,102]. An

increased coating thickness would potentially have increased water content and have a raised stress level for micro-cracking following water loss.

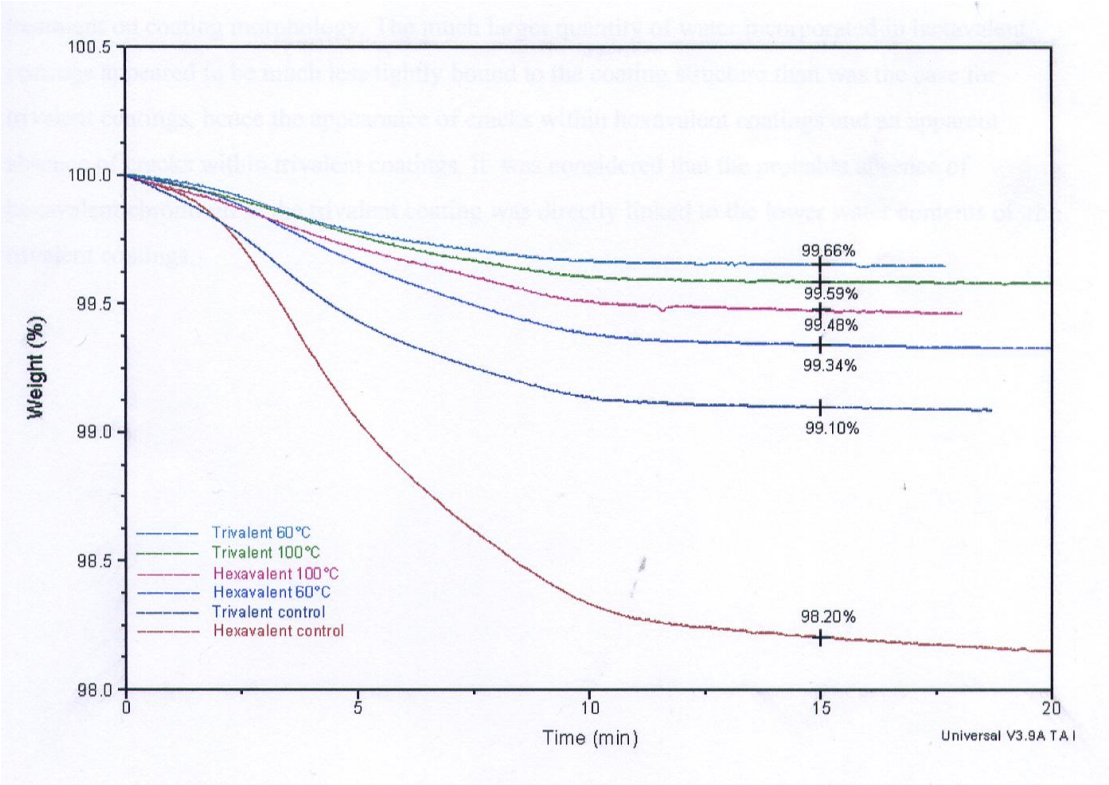

Figure 5.1 Thermogravimetric plot of hexavalent (chromate A) and trivalent (Tripass LT1500) CCC on acid zinc electrodeposited steel and following prior heat treatment for 24 h at 60 and 100°C [159]**.**

5.2.4 Blistering

FEGSEM studies of chromate A and B conversion coatings following gold sputter coating exhibited blistering; Figures 4.9c-d, 4.15b-c and 4.16b-c. The blistering appeared to be primarily a function of increasing coating thickness as coatings formed at shorter immersion times did not exhibit blistering.

Chromate A conversion coating AES depth profile studies have shown that zinc concentrations are highest within the coating for shorter immersion treatments; see Figures 4.84-4.87. It may be that sufficient zinc content within the conversion coating is necessary in order to meet adhesion requirements. Otherwise in a scenario where the conversion coating is contracting e.g. following loss of water adhesion forces to the substrate will be tested.

Surface characterisation of hexavalent CCC following scratching with a carbide tip followed by 18 h exposure to 5% NaCl solution, exhibited additional blistering and cracking in scratched regions indicative of a brittle coating; see Figures 4.37a, 4.38a and 4.39a-c.

Trivalent CCC exhibited significantly less blistering and cracking thus possibly indicative of a more ductile coating; see Figures 4.40a and 4.41a. These properties were also evident following cryo-freeze fracture preparation of untreated samples thus highlighting a well adhered conversion coating/zinc electrodeposited interface; see Figures 4.11a-g and 4.23b, d and f.

Blistering is likely to take place when the internal forces within a conversion coating are greater than the conversion coating/zinc substrate adhesive forces. The additional coiling and bending of blistered coating strips exhibited in Figures 4.15b-c and 4.16b-c, could be the result of compressive stresses found in the upper surface regions of the coating structure. It is important to note, in a wider context, that adhesive forces between the conversion coating and zinc substrate provide not only important corrosion protection but also integral adhesion for possible subsequent primer or lacquer finishes.

Sufficient zinc content within the conversion coating may also be necessary to prevent stripping of a conversion coating when treated in 5% NaCl solution. Stripping was observed for an increased chromate A conversion coating thickness when treated in 5% NaCl solution for 18 h exposure; Figure 4.33a-b. Stripping may have occurred due to a loss of adhesion between the conversion coating and zinc substrate as a result of zinc corrosion or swelling of the conversion coating; see Table 4.1 and 4.8.

5.3 Effect of heat treatment exposure

5.3.1 Zinc electrodeposited steel

FEGSEM micrographs of a bright acid zinc electrodeposited steel surface following heat treatment at 150°C for 1 h in a circulating oven and subsequent air cooling to room temperature (21°C); Figures 4.25a and b, displayed a surface covered with filamentous growths known as ‘whiskers’ [143], approximately 2-8 µm in lateral size. These were not evident in samples which did not undergo the heat treatment; see Figure 4.1a-d. From such findings it may be suggested that zinc whisker growth could be directly related to heat exposure, however, the cause of its initiation is somewhat unclear. A number of factors have been proposed by researchers, with some consensus based upon internal stress. Some studies have noted that internal compressive stresses are inherent from electroplating these have been

reported in the range 6.9 to 13.8 MPa [160], however, studies by Lahtinen et al. [140,141], have examined HDG specimens, thought to be at a lower stress level and these too have exhibited whisker growth, albeit after 20 years in service. [161]Sugiarto et al. [161], have suggested that zinc whisker growth initiation is linked to micro-stresses caused by brightener residues within electrodeposited coatings. Their studies of coatings produced without brighteners showed no whisker growth. In light of this, further investigations into the role of additives to zinc whisker growth are necessary.

Methods such as heat treatment provide energy for the refinement of lattice structure and thus reduction of localised stressed regions such as those associated with dislocations. The 1 h heat treatment at 150°C and associated cooling may not have met the required level of energy for stress relaxation. Lahtinen et al. [142] suggested a large difference in the coefficient of thermal expansion (CTE) values between the 'c' and 'a' axes of zinc and this could create the circumstances for localised stress to promote whisker growth in hot dipped galvanised coatings. In comparison, magnesium, which also has a hexagonal close packed crystal structure, but has similar CTE axis values, is not known to form whiskers [61]. Table 5.2 illustrates data for coefficients of thermal expansion for some metals.

Table 5.2 Coefficient of thermal expansion data for some hexagonal close packed (HCP) and body centred tetragonal (BCT) metals. After Honeycombe [162]**.**

Metal	**Crystal Structure**	**Coefficient of Thermal Expansion at 293 K, x 10^{-6} K^{-1}**	
		c – axis	**a – axis**
Cadmium	HCP	52.6	21.4
Zinc	HCP	63.9	14.1
Magnesium	HCP	27.0	25.4
Zirconium	HCP	6.96	5.65
Tin	BCT	30.5	15.5

In addition to stresses produced from anisotropic expansion, others could result from elevated temperature excursions, particularly from differences in thermal expansion between coating and substrate. For example values for thermal expansivity for monolithic iron, tin and zinc are 11.7, 21.2 and 29.7 x 10^{-6} K^{-1} [163], respectively.

As well as SEM studies, experimental EDX was also carried out on and around a typical zinc whisker to identify whether there were any significant differences in elemental composition. In both cases Zn and Fe were identified at similar levels; see Table 4.3. Zinc whisker studies by Lahtinen et al. [141], on long term growth (20 years) in an active environment, have observed changes in elemental composition with Cl and S on and near a HDG whisker root as well as the detection of K at the root of a long whisker. These impurities were associated with airborne pollutants. Clearly the experimental conditions in the present work would preclude a similar situation, however, it was thought that localised differences might occur due to absorbed electroplating additives. This possible anomaly was not detected.

In addition to SEM studies, FIB cross-sectional examination was also carried out on heat treated samples; Figures 4.26a-c and 4.27a-c, to observe whether or not grain structure has any influence upon zinc whisker growth or initiation. Overall it was difficult to establish grain patterns in and around the whisker root. A columnar structure was identified, however, this may also be an artefact of the ion milling and cleaning process created during sectioning. Reynolds et al. [61], also found it difficult to observe grain patterns using FIBSEM and TEM of whiskers growing from zinc electroplated specimens. Their corresponding XRD analysis approximated particle size to be 32 nm. Particles were deemed to be very small grains of size < ~ 100 nm. With this in mind, it was suggested that mass transport and grain diffusion could be another mechanism for zinc whisker formation.

5.3.2 Hexavalent and trivalent CCC

FEGSEM micrographs of a chromate A (40 s) conversion coated on acid zinc electrodeposited steel surface following heat treatment exposure at 150°C for 1 h in a circulating oven and cooled naturally to room temperature (21°C); Figure 4.28a-d, displayed a micro-cracked surface morphology with zinc whiskers protruding from cracks, from which point their growth appeared both lateral and perpendicular. In the case of trivalent CCC (Tripass LT1500 - 90 s) no micro-cracks or protruding zinc whiskers were observed; Figure 4.28e-f. From the present investigation this may indicate that zinc whisker growth may actually require direct exposure via micro-cracks. However, further studies by Ebbage et al. [164], using similar samples and conditions but over a longer exposure time (150°C for 24 h) exhibited zinc whiskers protruding out of the trivalent CCC without the presence of initial micro-cracks; see Figure 5.2. Thus indicating that conversion coatings in general, probably only delay the formation of the whiskers and certainly do not preclude their growth. These

findings also agree with suggestions made by Sugiarto et al. [161]. These findings may also indicate that trivalent CCC is under less tensile stress in comparison to hexavalent CCC [98] and that it is well adhered to the substrate to withstand localised stresses created by the underlying whisker.

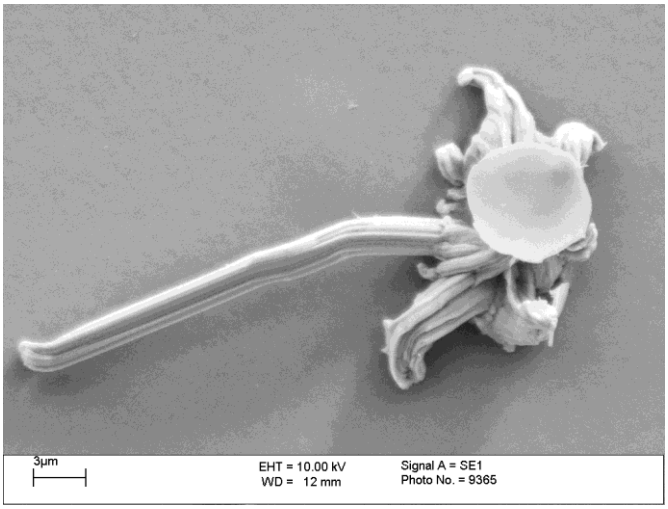

Figure 5.2 FEGSEM micrograph of a trivalent CCC (Tripass LT1500 - 90 s) on bright acid zinc electrodeposited steel surface following exposure at 150°C for 24 h in a circulating oven [164]**.**

5.4 Trivalent CCC film formation

The film formation process for trivalent CCC appears to be different to that of the mechanism by which a hexavalent CCC is formed. The addition of complexants, organic acids and other metal ions may have promoted this difference. As with the case for hexavalent CCC the acidic nature of the treatment solution (pH 1.8) initiates zinc dissolution, however, as AES chemical analysis of the surface and sub-surface has demonstrated there is a higher content of zinc within the conversion coating; see Table 4.19 and Figures 4.88-4.89. One possibility for this could be related to the weaker oxidising power of the nitrates used, as an alternative to Cr(VI) species within the treatment solution. The weaker oxidising power may have the effect of slowing down the film formation process and thus potentially resulting in the entrapment of higher concentrations of zinc throughout the coating.

The effect of weak organic acids such as malonic and oxalic acid could also have contributed to higher zinc levels within the conversion coating, however, conclusive evidence from the present investigations is not available. Investigations into the role of these additives were carried out using XPS; see Figure 4.77-4.79 and 4.80-4.81, but these did not include quantitative chemical composition data of zinc content. Dikinis et al. [129], found that the

inclusion of malonic acid within a basic chromium (III) nitrate treatment solution increased the zinc concentration within the conversion coating when the processing temperature was increased (20 to 60°C) or used in conjunction with a cobalt (II) salt.

As with the case of hexavalent CCC, hydrogen evolution is thought to occur to supplement zinc oxidation at the zinc/treatment solution interface. This consequently leads to a rise in pH which provides the operating pH window for Cr(III) deposition to occur. An XPS high resolution Cr 2p envelope has indicated that the chromium oxidation state is composed of Cr(III); see Figure 4.66b. Moreover, curve-fitting of the Cr $2p_{3/2}$ envelope indicates the presence of Cr_2O_3 and $Cr(OH)_3$; Table 4.17. This is also, to a certain extent, supported by IR investigations, in which $Cr(OH)_3$ was identified; Figure 4.108 and 4.109. IR analysis has also indicated the presence of carboxylic species which may indicate the method by which chromium is deposited.

In the absence of Cr(VI) species such as dichromate or chromate ions within the treatment solution, simple electrochemical reduction to $Cr(OH)_3$ is not possible; Table 5.1. Therefore the deposition could be via a number of alternative paths. These could include from a complex ion species or the reaction between Cr(III) metal ion and hydroxide ions. Deposition for the former could be either from a hexaquachromium (III) ion or a complex including organic acid based ligands. Both of which are thought to be deposited at the zinc / treatment solution interface following a rise in pH due to zinc dissolution and hydrogen evolution; see Table 5.1. The film formation could be sustained by an appropriate pH range which is linked to zinc oxidation, nitrate reduction and hydrogen evolution. The rate of deposition from a complex ion is thought to be influenced by its stability. In the case of a metal ion organic acid ligand complex, its stability is less than that of a hexaquachromium (III) ion and hence supports faster ligand exchange for deposition to occur [165]. An example of a chromium organic acid based complex ion within the Tripass LT1500 is $[CrC_2O_4(H_2O)_4]^+$ given that the chromium to oxalic acid molar ratio is approximately 1:1. The formation of the more stable trisoxalatochromium III complex ion $[Cr(C_2O_4)_3]^{3-}$, is less likely given the chromium to oxalic acid molar ratio is 1 to 3. The formation and deposition from chromium malonic acid based complex ions such as $[CrC_2O_4(H_2O)_4]^+$ is also possible [165]. The content of malonic acid is, however, lower than that of oxalic acid within the treatment solution and thus may have a lesser influence.

Cr_2O_3 is thought to form directly from $Cr(OH)_3$, possibly following thermal exposure; see Table 5.3. Cr_2O_3 can also be formed from reduction of Cr(VI) oxidation state species e.g. CrO_3, however, given that no Cr(VI) was detected in trivalent CCCs this particular reaction is highly unlikely; Table 5.3.

Table 5.3 Potential reaction paths for Cr_2O_3 formation.

Formation mechanism	Equations
Reduction reaction of CrO_3	$2CrO_3 + 3Zn \leftrightarrow Cr_2O_3 + 3ZnO$
Possible Cr hydroxide reactions	$2Cr(OH)_3 \leftrightarrow Cr_2O_3 + 3H_2O$ $2Cr(OH)_3.3H_2O \leftrightarrow Cr_2O_3 + 9H_2O$

FEGSEM images of the trivalent CCC illustrated a spherical-like particulate (below ~50 nm size) surface morphology; Figures 4.23 b, d, f, similar to that of hexavalent CCC; Figure 4.11 a, d. Therefore it is possible that trivalent CCC film formation could also have occurred via electrochemical / sol-gel reactions. The exception would be that the spherical shaped particulates were mainly either zinc oxide based with some chromium oxide within the matrix, or zinc entrapped within the spherical shaped particulates.

5.4.1 Effect of organic acids on film formation

During film formation the effect of weak organic acids such as malonic and oxalic is integral, as they provide the necessary H^+ ions to help initiate and maintain anodic zinc dissolution. The corresponding anion species could then provide ligands for association with metal ions in the treatment solution such as chromium, cobalt or even zinc, before deposition under the required conditions. To try to evaluate this malonic or oxalic acid were excluded from the trivalent CCC treatment solution formulations. It was found that for the former a similar surface morphology and coating thicknesses was observed to that of the control formulation (Tripass LT1500). LPR corrosion resistance values of this sample was found to be ~ 70% of that exhibited by the control formulation. In the case of excluding oxalic acid from the treatment solution formulation resulted in a surface morphology with tiny randomly orientated micro-cracks and some isolated blistering of the conversion coating. Consequently, only ~ 48% LPR corrosion resistance value was exhibited in comparison to the control formulation. On increasing the content of both these acids in the treatment solution (13 g/l malonic acid and 52 g/l oxalic acid) their respective surface morphologies and coating thickness changed significantly. With the inclusion of additional oxalic acid (52g/l), FEGSEM images revealed an extensive crack network and large spherical-like particulate

structures (~100 nm); Figure 4.48d,f. XPS surface studies indicated that these could well be ZnO or $Zn(OH)_2$ particulates, given that no chromium was detected. For the case of additional malonic acid (13 g/l), FEGSEM images exhibited a similar structure to that of the trivalent CCC control albeit with a network of randomly orientated micro-cracks; Figure 4.46 c-d. These micro-cracks were found to disappear after the treatment solution was allowed to age with additional heating (60°C); Figure 4.46e-f. This indicates that the treatment solution chemistry changes. Ageing and additional heating may encourage dissociation and complexing of unreacted malonic acid and hence help to stabilise the treatment solution pH. This may also help to explain why a white residue was found at the bottom of the treatment solution before ageing and heating. It is also important to note that the molar ratio between chromium and carboxylic acid would be different upon increased addition of malonic and oxalic acid to the control standard, hence possibly resulting in excess carboxylic species for alternative chromium complexes to form or insoluble products.

5.4.2 Effect of chromium nitrate on film formation

The exclusion of chromium nitrate from the trivalent CCC formulation resulted in the formation of a pink coloured residue at the bottom of the treatment solution. The pink precipitate formed instantly following addition of cobalt nitrate and settled. This possibly indicates a reaction between cobalt ions and carboxylic ligand species. It is possible that the reactions that took place may have resulted in insoluble products being formed as opposed to complex ion species and consequently were not held in suspension within the treatment solution. Further studies would be required to ascertain the structure of this product.

Without the presence of chromium, the treatment solution is effectively an etchant and this is exhibited in SEM studies which demonstrated a rough zinc morphology following treatment; Figure 4.49a-e. It is also worthy of note that the treatment solution became darker in appearance following the immersion process, possibly indicating the dissolution of zinc ions.

The further addition of chromium nitrate to the standard trivalent CCC formulation has been shown to increase the conversion coating thickness; Table 4.9. The increase in coating thickness is logical given a higher chromium content. However, poor corrosion resistance; Table 4.27, and a micro-cracked morphology; Figure 4.50a-d, undermines the use of a higher chromium level. It is possible that the change in molar ratio between chromium and carboxylic acid ligand species might have affected the deposition process. An excess of

chromium ions could be uncomplexed or chromium ions could be associated with aqueous ligands as opposed to carboxylic acid ligand species.

5.4.3 Effect of sodium molybdate on film formation

Within the trivalent CCC treatment solution formulation sodium molybdate was also added (0.08 g/l). Its role during film formation was probably limited given the small concentration used within the treatment solution. In theory, following dissociation from sodium, molybdate (MoO_4^{2-}) could have reduced in oxidation state and deposited following zinc oxidation. However, XPS survey scan and AES depth profile data has revealed a lack of molybdenum within the conversion coating; see Figure 4.72, 4.88, 4.89 and Table 4.19. Only when the concentration of sodium molybdate was increased to 0.4 g/l was molybdenum detected; see Figure 4.74. This also coincided with a decrease conversion coating thickness and corrosion resistance as exhibited by LPR measurements; see Table 4.27.

A problem with the use of sodium molybdate within trivalent CCC treatment solution could be the potential oxidation of trivalent chromium species to the hexavalent state following reduction of molybdate. In these present investigations no data supports this theory. Also most molybdate conversion coatings are known to exhibit a dense micro-cracked morphology [117], again in this present investigation this was not exhibited; Figure 4.44c-d.

Overall molybdate conversion coatings are not particularly known for their corrosion resistance [117]. The presence of sodium molybdate within trivalent CCC probably only improves the physical colour appearance of the conversion coating, however, no evidence from these investigations can conclude upon this.

5.4.4 Effect of cobalt nitrate on film formation

Cobalt nitrate 7.3 g/l (Co 0.9 g/l), was also added as part of the trivalent CCC treatment solution formulation. The presence of cobalt was not detected within the standard conversion coating using XPS, AES depth profiling or IR data; see Figure 4.72 , 4.88-4.89 and 4.108-4.109. Only when the concentration of cobalt nitrate added was increased to 14.6 g/l was cobalt detected; see Figure 4.76. The use of cobalt nitrate, though not a major constituent of the conversion coating, appears to improve corrosion resistance. The LPR corrosion resistance measurements from a sample prepared from a trivalent CCC treatment solution formulation without cobalt nitrate had a reduced value; see Table 4.27. It did, however,

exhibit a similar surface morphology; Figure 4.45a-f. The role of cobalt nitrate therefore during film formation is unclear. It could be as a catalyst of reactions supporting deposition such as undergoing a change in it's oxidation state e.g. Co(II) to Co(III), but in no way does it increase coating thickness as shown in Table 4.9. One possible reaction may be increasing the displacement of oxalate ($C_2O_4^{2-}$) from chromium oxalate complexes. However, the lack of cobalt by-products (e.g. CoC_2O_4) being detected as cobalt within the conversion coating, particularly for the control sample, somewhat negates this theory; see Equation 2.30.

5.5 Corrosion protection behaviour

5.5.1 Hexavalent CCC

A self-repair corrosion protection mechanism for hexavalent CCCs is widely proposed amongst researchers [43,46,47,49-52,86,100,105]. Such a theorem acknowledges that soluble Cr(VI) species reduce to insoluble Cr(III) species and consequently repairs defective regions on or within the conversion coating. Results from the present investigation indicate that such a protection mechanism is unlikely.

Electrochemical Linear Polarisation Resistance (LPR) measurements on increasing exposure time within 5% NaCl solution; see Figure 4.114, and polarisation curves; see Figure 4.112 and 4.113, show no indication of self-repair properties. In addition, hexavalent CCC did not appear to exhibit self-repair protection properties on the anodic or cathodic polarisation curves. On the other hand XPS high resolution data did show a reduction in size for a peak shoulder representing Cr(VI) species following NaCl solution exposure; see Figure 4.70a and Table 4.17, which complies with the theorem. However, whether or not these species are reduced and repair defects is unknown as they could easily have leached into the exposure environment.

Therefore in light of the data presented in this investigation, it is proposed that the corrosion protection behaviour of hexavalent CCC is based on a barrier mechanism. The integrity of this mechanism, however, is compromised by micro-cracking and delamination or blistering as observed in SEM studies for these conversion coatings; Figures 4.7b-c, 4.8a-b, 4.9b-d, 4.13a-c, 4.14a-d, 4.15a-c and 4.16a-c. This exposes the underlying zinc substrate to the corrosive medium and consequently reduces its corrosion resistance; see Table 4.26. AES

depth profile analysis following NaCl solution exposure also concurs with this observation, in which zinc levels increase following exposure; see Figures 4.90 and 4.91.

5.5.2 Trivalent CCC

Self-repair corrosion protection by trivalent CCC is unlikely. XPS high resolution studies did not indicate the presence of Cr(VI) species; see Figure 4.66b and Table 4.17, which is thought to be necessary for self-repair. Nor was there any indication of Cr(III) reducing to a lower oxidation state such as Cr (metal). Therefore the corrosion protection for trivalent CCC also based upon barrier properties. For a standard trivalent CCC without any change in the treatment solution formulation, SEM micrographs; Figures 4.22a-f and 4.43a-c, of its surface morphology were free of any defects such as micro-cracks and importantly this film exhibited good adhesion to the underlying zinc substrate. This is particularly important for an increased conversion coating thickness. Such properties confer improved corrosion resistance in comparison to hexavalent CCC as exhibited in LPR corrosion resistance values; see Table 4.26. In addition, trivalent CCC following 18 h 5% NaCl solution exposure resulted in only minimal surface deterioration in comparison to hexavlent CCC which exhibited a number of blistered regions on increasing conversion coating thicknesses; see Figures 4.30, 4.31, 4.34 and 4.35. However, it must be noted that the precipitate like structure of the trivalent and hexavalent CCCs does not retard total penetration and migration of corrosive ions. SEM cross-sectional images of the underlying zinc substrate show a change in morphology following exposure to a NaCl solution environment; see Figure 4.36a-c and 4.32a-c. AES depth profiles of hexavalent and trivalent CCCs following 18 and 48 h 5% NaCl exposure; see Figures 4.90-4.93, have indicated increasing levels of zinc incorporated within the conversion coating to that of an untreated sample for the former. In comparison, trivalent CCC, in general, reflected a similar elemental composition to that of an untreated sample. As in the case of hexavalent CCC, following 48 h solution exposure, chlorine was detected at the surface and sub-surface regions of the conversion coating. All in all this signifies that conversion coatings help to reduce penetration of corrosive ions, but by no means prevent their penetration.

Electrochemical polarisation curves of trivalent CCC, in comparison to hexavalent CCC on acid zinc electrodeposited steel, indicated a slightly more noble rest potential value, less active anodic polarisation curve; see Figure 4.112. Again illustrating good barrier properties.

Barrier properties could also be affected by the chemical composition of the conversion coating. XPS survey studies mainly indicate the presence of chromium, oxygen and zinc within a standard trivalent CCC treatment solution formulation; see Figure 4.63 and 4.72. AES depth profile studies have shown that zinc is at a higher concentration throughout the conversion coating in comparison to hexavalent CCC; see Figures 4.87-4.89. It is possible that zinc could be in a passive state, such as ZnO or $Zn(OH)_2$, which contribute additionally to the chemical inhibitor properties of chromium (e.g. $Cr(OH)_3$ or Cr_2O_3) for barrier protection. However, as shown with black trivalent CCCs, high levels of zinc, particularly with low concentrations of chromium; see Figure 4.94 and 4.96, and physical cracks; Figures 4.51a-c and 4.52a-c, lead to potential pure zinc regions, and the overall corrosion resistance is compromised; see Table 4.28.

In the present investigation it has also been shown that the introduction of additional sodium molybdate into the trivalent CCC treatment solution formulation as an corrosion inhibitor, actually reduces the conversion coating's corrosion resistance; see Table 4.27. Whether this is a reflection of the low corrosion inhibiting properties of molybdates, the use of sodium molybdate for improving corrosion resistance is debatable. The inclusion of cobalt nitrate as an corrosion inhibitor is also debatable, it has only been detected at trace levels for an increased addition using XPS; see Figure 4.76, and its role may only be during the conversion coating film formation stage. The exclusion of this additive has resulted in a decline in corrosion resistance; see Table 4.27.

5.6 Black trivalent CCC

Detailed discussion of the two black trivalent CCCs is difficult given the limited number of variables investigated as well as the lack of full disclosure of operating and formulation concentrations used for the preparation of samples by the sponsor. However, some remarks can be made and further work could be carried out.

Two different black trivalent CCC formulations were investigated for an acid and alkaline zinc electroplated substrate; Table 3.9. In each case the black trivalent CCCs exhibited micro-cracking and an unclear interface between the conversion coating and the underlying zinc substrate; Figures 4.51a-c and 4.52a-c. As a consequence poor corrosion resistance was exhibited; see Table 4.28.

Both black trivalent CCC treatment solution formulations utilised malonic acid as complexing agent. Depending upon its molar ratio with chromium a complexing reaction could have taken place or there might have been an excess of chromium. Also in both treatment solutions cobalt nitrate was used, with nickel nitrate used in addition for black trivalent CCCs on acid zinc electrodeposits. In both cases cobalt and nickel were at a trace level or undetectable; see Figures 4.94 and 4.96 and Tables 4.22 and 4.23. The effect of cobalt or nickel during film formation is unclear from the present investigation. It is possible that they have a catalytic effect given the concentration detected. The effect of cobalt or nickel oxides within the conversion coatings imparting a black appearance is debatable.

The addition of a sulphur compound (organosulphur) for a black trivalent CCC on alkaline zinc results in a considerable concentration of sulphur within the conversion coating, as shown in AES depth profile data; Figure 4.96. Sulphur might be helping to impart a black appearance, however, it may also contribute towards a micro-cracked morphology.

The use of colloidal silica for a black trivalent CCC acid zinc formulation does not appear to provide coverage of micro-cracks envinced from SEM studies; Figure 4.51a-c. Silicon in the form of silica has been detected using AES, particularly at the surface-subsurface region; see Figure 4.94. It is possible that the concentration used in the treatment solution formulation could have been increased or alternatively a silica based top coat could be used as a temporary method for imparting a low grade black appearance, as well as providing adequate corrosion resistance for low service corrosion applications.

5.7 Organic topcoat

Detailed discussion of the two silica based topcoats is difficult given the limited information provided by the sponsors concerning the preparation of samples.

FEGSEM studies showed that a nano-silica based topcoat (12 nm particle diameter) exhibited no micro-cracks or other major physical defects; Figure 4.53a-b. In the case of a 22 nm particle size based topcoat, some clusters of silica particles were displayed; Figure 4.54a-b. This could have been the result of coating formation or deposition from an agglomerated state within the colloidal silica treatment bath. Agglomeration of silica particles within the colloidal silica treatment bath could have occurred due to particle size, shape, ionic charge,

suspension, dispersion (wetting), concentration of particles, solution temperature, pH or treatment solution agitation [166].

Cross-sectional analysis showed that the topcoats were well adhered to the trivalent CCCs (Tripass LT1500); Figure 4.53c and 4.54c. A thicker coating observed for the 22 nm silica particle size topcoat in comparison to that based on a 12 nm (391 to 299 nm) is difficult to conclude upon as different process immersion times for the preparation of samples may have been used. Naturally the use of larger particles is likely to form a thicker coating.

AES analysis of the topcoats confirmed the deposition of silica (SiO_2); see Figures 4.99 and 4.101. Finally, LPR corrosion resistance values showed that a trivalent CCC supplemented with a topcoat is improved by up to ~ 19.6%.

6 Conclusions

In this investigation a third generation trivalent CCC (Tripass LT1500) has been compared to a hexavalent CCC. Listed below are conclusions regarding the physical, chemical and corrosion properties of the conversion coatings. Also included are conclusions regarding zinc whiskers, topcoats and black trivalent CCCs.

Physical properties of the conversion coatings and micro-cracking

- Surfaces morphologies for hexavalent and trivalent CCC were flat, smooth and spherical-like in structure.
- Micro-cracking was observed for hexavalent CCC using two different treatment solution formulations (chromate A and B). Microcracking was observed beyond a conversion coating thickness of ~ 122 nm in the case of chromate A.
- Micro-cracks in trivalent CCCs were only observed if the treatment solution was altered from the base formulation, such as changes in oxalic and malonic acid content.
- In the case of hexavalent CCC micro-cracks aligned predominately parallel to one another for flat underlying substrates such as acid or alkaline zinc electrodeposited steel. A dense crack network was found to result for a rough zinc foil substrate.
- SEM operating and specimen preparation conditions used for gold sputtering in which the hexavalent CCC is exposed to high vacuum and thermal conditions were found to induce micro-cracking and blistering of the conversion coating from the zinc substrate.

Mechanism of film formation and role of additives

- In both hexavalent and trivalent CCC film formation, the acidic nature of their treatment solutions initiate zinc dissolution.
- XPS and AES data analysis indicated higher proportions of zinc within the trivalent CCC at surface and sub-surface regions in comparison to hexavalent CCC. It is important to note that in this investigation high resolution XPS Cr $2p_{3/2}$ data from an Al X-ray source has been evaluated taking into consideration the overlapping Zn $L_3M_{23}M_{45}$ Auger peak.
- XPS data analysis has indicated that chromium is present in the Cr(III) oxidation state only in the case of trivalent CCC, moreover as $Cr(OH)_3$ and Cr_2O_3 compounds. Chromium oxide/hydroxide formation is via a complex mechanism. Important factors include: the chromium:complex molar ratio, higher content of oxalic to malonic acid in the treatment solution formulation and preparation of the treatment solution in which

ageing of the solution with additional heating prevents formation of micro-cracks and a reduction in corrosion peformance.

- AES data analysis of hexavalent CCC showed that the zinc content detected at the surface and at the sub-surface regions decreased for increased conversion coating thickness. This indicated that a simultaneous electrochemical zinc oxidation / Cr(VI) reduction leading to the formation of a chromium / zinc preciptate film mechanism is less likely. More favourable is an electrochemical / sol-gel mechanism, in which zinc dissolution, high water retention for continued electrochemical redox reactions and a $Cr(OH)_3$ particulate based structure are fundamental requirements for film formation. In further support of this mechanism is XPS and IR data analysis indicating the presence of H_2O and in particular the contribution of $Cr(OH)_3$ as opposed to Cr_2O_3 in the film.
- XPS data analysis of the hexavalent CCC surface revealed the presence of CrO_3. An increased content was observed for a lower TOA (10 and 30°) analysis. In comparison no Cr(VI) was detected for trivalent CCC, which is important with respect to EU legislation.
- The role of cobalt nitrate and sodium molybdate during trivalent CCC film formation is unclear as no cobalt or molydenum was detected using XPS and AES. Only upon increased addition within the treatment solution was detection possible.
- The role of sulphuric acid in hexavalent CCCs is important as sulphur was detected throughout the coating. The exact mechanism for the presence of sulphur and chemical state in the coating is still unclear from this investigation. Alternatively, the role of nitric acid in hexavalent CCCs appears to be limited given that no nitrogen was detected within the conversion coating.

Corrosion protection mechanism and role of additives

- Hexavalent and trivalent CCC corrosion protection behaviour is based on a barrier mechanism.
- Self-repair corrosion protection properties for hexavalent CCC appear to be lacking. Electrochemical linear polarisation resistance measurements on increasing exposure time within 5% NaCl solution and anodic and cathodic polarisation curves show no indication of such properties. XPS data analysis of samples following 18 h 5% NaCl solution exposure, however, did indicate possible self-repair properties.
- An improved corrosion performance was observed for trivalent CCCs in comparison to hexavalent CCCs. Higher LPR corrosion resistance values were exhibited across all conversion coating thicknesses. In addition, on increasing exposure to 5% NaCl solution

LPR measurements for trivalent CCCs were overall higher in comparison to hexavalent CCCs. A slightly more noble rest potential value and a less active anodic polarisation curve were also observed. AES data and SEM cross-section analysis of hexavalent and trivalent CCC following 18 and 48 h 5% NaCl solution exposure indicated penetration of corrosive ions such as chloride with, however, better retardation of this for trivalent CCCs.

- This investigation has shown, through LPR results, that an increased addition and an omission of cobalt nitrate slightly improves and significantly reduce (~52%) corrosion resistance respectively over the control formulation. This investigation has also shown, through LPR results, that sodium molybdate can be omitted from the formulation and that a decline in corrosion performance (~ 46%) is observed if the content is increased.

Zinc whiskers

- Zinc whiskers were observed for both acid and alkaline zinc electrodeposited steel following heat treatment at 150°C for 1 h. Elemental analysis and grain pattern investigations failed to help determine the cause of zinc whisker initiation.
- Zinc whiskers were seen to protrude out of hexavalent CCC micro-cracks. Whiskers emerged through trivalent CCC after a longer (24 h) heat treatment time.

Topcoats

- A trivalent CCC supplemented with nano silica based topcoats exhibited surfaces free of any major physical defects and an overall improvement in LPR corrosion resistance values.

Black Trivalent CCCs

- Randomly orientated microcracks as well as an undefined conversion coating / zinc electrodeposit interface cross-section was exhibited for black trivalent CCCs on acid and alkaline zinc electrodeposited steel. Inferior corrosion resistance values were found in comparison to the standard trivalent CCC (Tripass LT1500). Chemically, in addition to common elements carbon, chromium, oxygen and zinc, silicon in the form of silica was detected for black trivalent CCC on acid zinc electrodeposited steel. In the case of black trivalent CCCs on alkaline zinc, sulphur was additionally detected.

7 Further work

Listed below are subject areas in which further investigative work could be carried out.

Trivalent CCCs

- Tripass LT1500 treatment solution uses malonic and oxalic acids as complexants. These could be replaced with other complexants such as malic acid or glycine. These alternatives as well as investigations into the molar ratio between chromium and complexant (e.g. carboxylic acids) may increase or decrease the stability of the chromium complex for deposition. A less stable chromium complex in theory should encourage faster deposition.
- Even though the concentration of cobalt detected within the conversion coating was minimal (if not zero) using XPS and AES, there is a consensus for its removal from treatment solutions [131]. Further work should be to evaluate potential metal ion alternatives, which appear to have similar or improved film formation characteristics as those exhibited by cobalt in the present investigation.
- A comprehensive study should be carried out to determine the cause of white and pink precipitates formed during the investigation into the role of additives within Tripass LT1500. The precipitates could be filtered, dryed and analysed using XPS and IR.

Black trivalent CCC / Non chromium based alternatives / topcoat

- Further work should be carried out into the role of additives, effect of black pigment additives (inorganic and organic) used in black trivalent CCC treatment formulations and supplementary topcoat finishes for the sealing of cracks observed in SEM studies [167].
- To meet potential future environmental and / or legislative pressures, investigative work could be carried out for a non-chromium based conversion coating treatment solution. This could include work, on a combination of metal ions known to form conversion coatings (e.g. molybdenum, cerium, tungsten, rhodium).
- Further investigations should be carried out into preventing agglomeration of silica particles in silica based topcoat treatment solutions.

Conversion coating properties on zinc/zinc alloy substrates

- Chemical analysis using techniques such as AES and XPS has shown that zinc content within trivalent CCCs is greater than in hexavalent CCCs. Further work should explore conversion coating properties on alkaline zinc and zinc alloy (e.g. ZnNi, ZnFe, ZnCo and

ZnMn) substrates, particularly with the effects provided by alloying metals. Further work should also evaluate the tolerable levels of Zn and Fe / alloy build up within the treatment solution using techniques such as titrations, ion exchange [168] and the use of purifier resins. Purifier resins are selected in accordance to the contaminant element which drops to the base of the treatment solution leaving the desired elements intact.

Chemical characterisation

- Future XPS work carried out on chromium based conversion coatings on zinc substrates should utilise a monochromatic magnesium X-ray source for survey and Cr high resolution scans to eliminate potential overlapping of zinc Auger and chromium photoelectron peaks.
- Further work should be carried out to identify whether or not Cr(III) species within a trivalent CCC oxidise to Cr(VI) following exposure to elevated temperatures, particularly from those formed from treatment solutions with increased cobalt content [131].
- To further support AES elemental depth profile investigations for the identification of cobalt or nickel DSIMS should be performed.

Corrosion characterisation

- Further investigations on the self-repair properties for hexavalent CCCs could be carried out using Scanning Vibrating Electrode Technique (SVET) and possibly AES depth profiling following scratching of conversion coating and exposure to an corrosive environment such as 5% NaCl solution. An alternative scratch method should also be explored in comparison to ASTM D1654 [10], such as nano-scratch technology.
- Neutral salt spray ASTM B117-90 [73] should be carried out for future improved trivalent CCCs in support of electrochemical corrosion analysis.

Zinc whisker analysis

- Further investigations into zinc whisker formation could include brightener content in acid zinc electrolyte formulation, intentional introduction of areas of stress e.g. a hardness indentation, different heat treatment exposure times / temperatures and the use of different zinc coated substrates e.g. hot dip galvanised steel.
- Observe initiation and growth of a zinc whisker from a zinc electrodeposited steel sample using a SEM installed with a hot stage. This would also enable evaluation without circulating air, which was present in the oven used in this investigation.

References

[1] Amirudin A. and Thierry D., Corrosion mechanisms of phosphated zinc layers on steel as substrates for automotive coatings, *Progress in Organic Coatings*, (1996), **Vol. 28,** No.1, pp. 59-76.

[2] Jiang H.M., Chen X.P., Wu H., Li C.H., Forming characteristics and mechanical parameter sensitivity study on pre-phosphated electro-galvanized sheet steel, *Journal of Materials Processing Technology*, (2004), **Vol. 151,** No.1-3, pp. 248-254.

[3] Wilson R., The steel industry offers solutions for an auto industry bent on trimming cost and weight, *Automotive Industries AI*, (2003), **Vol. 183,** No.4, pp. 1-3.

[4] Derun E.M., Demirozu T., Piskin M.B., Piskin S., The analysis of corrosion performance of car bodies coated by no nickel and low nickel zinc phosphating processes, *Materials and Corrosion*, (2005), **Vol. 56,** No.6, pp. 412-416.

[5] Wyrostek M. and Wynn P., Driving away from hex chrome coatings. With compliance deadlines for new environmental regulations fast approaching, surface finishers are challenged to manage the transition to alternative materials, *Metal Finishing*, (2006), **Vol. 104,** No.4, pp. 22-29.

[6] Gardner A. and Scharf J., Trivalent passivation of plated zinc and zinc alloys - Alternatives to hexavalent based systems, *Transactions of the Institute of Metal Finishing*, (2003), **Vol. 81,** No.6, pp. 107-111.

[7] Wilcox G.D., Replacing chromates for the passivation of zinc surfaces, *Transactions of the Institute of Metal Finishing*, (2003), **Vol. 81,** No.1, pp. B13-B15.

[8] Wynn P.C. and Bishop C.V., Replacing hexavalent chromium, *Transactions of the Institute of Metal Finishing*, (2001), **Vol. 79,** No.2, pp. B27-B30.

[9] Rochester T. and Kennedy Z.W., Unexpected results from corrosion testing of trivalent passivates, *Plating & Surface finishing*, (2007), pp. 14-18.

[10] D1654 - 08, Standard test method for evaluation of painted or coated specimens subjected to corrosive environments, *Annual Book of ASTM Standards American Society for Testing and Materials*, (2008), **Vol. 6.01,** pp. 1-4.

[11] G59 - 97, Standard test method for conducting potentiodynamic polarization resistance measurements, *Annual Book of ASTM Standards American Society for Testing and Materials (ASTM)*, (2003), **Vol. 3.02,** pp. 1-4.

[12] Mobley R.K. (Editor). Plant engineer's handbook, Edition 5, (2001), p. 964, 978, Elsevier Butterworth-Heinemann.

[13] Smith E.H. (Editor). Mechanical engineers reference book, Edition 12, (1998), pp. 155-156, Elsevier Butterworth-Heinemann.

[14] Canning W., The Cannings handbook: surface finishing technology, integrated design, Edition 23, (1982), p. 271, 840, 841. Kluwer Academic Publishers.

[15] Metallic materials (MPP332) self study booklet, Materials for Industry (M.Sc.), (2005) pp. 6-20, Loughborough University, UK.

[16] Shreir L.L., Jarman R.A. and Burstein G.T. (Editors). Corrosion, Volume 1-2, Edition 3, (1994), p. 548, 693, Elsevier Butterworth-Heinemann.

[17] Vargel C., Corrosion of aluminium, Edition 1, (2004), pp. 102-105. Elsevier Science.

[18] Gabe D.R., Principles of metal surface treatment and protection, Edition 2, (1978), p. 5, 49, 130, 148. Pergamon Press.

[19] Gardner A., Decorative trivalent chromium plating. Emergence of alternative technology poses both direct and indirect repercussions across the supply chain, *Metal Finishing*, (2006), **Vol. 104,** No.11, pp. 41-45.

[20] Snyder D.L., Decorative chromium plating, *Metal Finishing*, (2007), **Vol. 105,** No.10, pp. 173-181.

[21] Schario M., Decorative trivalent chromium plating. Initially employed for its process advantages, trivalent chromium finishing now gives electroplaters more compelling reasons to make the switch from hex-chrome, *Metal Finishing*, (2008), **Vol. 106,** No.6, pp. 66-68.

[22] Lausmann G.A., Chromium plating, Edition 1, (2007), pp. 144-145. Schriftenreike Galvanotechnik.

[23] Tyler J.M., Automotive applications for chromium, *Metal Finishing*, (1995), **Vol. 93,** No.10, pp. 11-14.

[24] Fedrizzi L., Rossi S., Bellei F., Deflorian F., Wear-corrosion mechanism of hard chromium coatings, *Wear*, (2002), **Vol. 253,** No.11-12, pp. 1173-1181.

[25] Burstein G.T., Shreir L.L., Jarman R.A., Corrosion, Volume 2, (1994), p. 740. Elsevier Butterworth-Heinemann.

[26] Johnston C., An update on zinc plating, *Metal Finishing*, (1999), **Vol. 97,** No.8, pp. 40-41.

[27] Safranek W.H., Cadmium plating, *Plating and Surface Finishing*, (2004), **Vol. 91,** No.8, pp. 11-12.

[28] Zinc coatings, American Galvanisers Association, (2006), Online article, http://www.galvanizeit.org/images/uploads/publicationPDFs/Zinc_Coatings.pdf, accessed 20-05-09.

[29] Endres F.,Ionic liquids: Promising solvents for the electrodeposition of nanoscale metals and semiconductors, Presented at the Joint International Meeting - 206th Meeting of the Electrochemical Society, (2004), p. 2455. Electrochemical Society Inc,

[30] Kanami N., Electroplating, basic principles, processes and practice, Edition 1, (2004), p. 81, 106, 326. Elsevier Science.

[31] Boto K., Organic additives in zinc electroplating, *Electrodeposition and Surface Treatment,* (1975), **Vol. 3,** No.2, pp. 77-95.

[32] Mayanna S.M., Tharamani C.N., Venkatesha T.V., Development of new brightener for industrial zinc coating, *Transactions of the Institute of Metal Finishing*, (2002), **Vol. 80,** No.6, pp. 187-190.

[33] Kavitha B., Santhosh P., Renukadevi M., Kalpana A., Shakkthivel P., Vasudevan T., Role of organic additives on zinc plating, *Surface and Coatings Technology*, (2006), **Vol. 201,** No.6, pp. 3438-3442.

[34] Monev M., Mirkova L., Krastev I., Tsvetkova H., Rashkov S., Richtering W., Effect of brighteners on hydrogen evolution during zinc electroplating from zincate electrolytes, *Journal of Applied Electrochemistry,* (1998), **Vol. 28,** No.10, pp. 1107-1112.

[35] Lee J., Kim J., Lee M., Shin H., Kim H., Park S., Effects of organic additives on initial stages of zinc electroplating on iron, *Journal of the Electrochemical Society*, (2004), **Vol. 151,** No.1, pp. C25-C31.

[36] Wilcox G.D. and Gabe D.R., Electrodeposited zinc alloy coatings, *Corrosion Science,* (1993), **Vol. 35,** No.-8, pp. 1251-1258.

[37] Abou-Krisha, M.M., Assaf, F.H., El-Naby, S.A., Electrodeposition and characterization of zinc–nickel–iron alloy from sulfate bath: influence of plating bath temperature, *Journal of Solid State Electrochemistry,* (2009), **Vol. 13,** No.6, pp. 879-885.

[38] Smallman R.E. and Bishop R.J., Modern physical metallurgy and materials engineering, Edition 6, (1999), p. 384. Elsevier Butterworth-Heinemann.

[39] Biestek T. and Weber J. (Editors). Electrolytic and chemical conversion coatings, Edition 1, (1976), p. 4, 8, Portcullis Press Ltd.

[40] Preikschat P. and Jansen R.,Replacement of chromium (VI) in passivations on zinc and zinc alloys, presentation given at the Ulmer Gespraech conference, (2001), SurTec, Neu-Ulm, Germany.

[41] Almeida E., Diamantino T.C., Figueiredo M.O., Sa C., Oxidizing alternative species to chromium VI in zinc galvanized steel surface treatment. Part 1 - a morphological and chemical study, *Surface and Coatings Technology*, (1998), **Vol. 106,** No.1, pp. 8-17.

[42] Bustamante G., Fabri-Miranda F., Margarit I.C.P., Mattos O.R., Influence of prephosphating on painted electrogalvanized steel, *Progress in Organic Coatings*, (2003), **Vol. 46,** No.2, pp. 84-90.

[43] Zhang X., Van den Bos C., Sloof W.G., Hovestad A., Terryn H., De Wit J.H.W., Comparison of the morphology and corrosion performance of Cr(VI) and Cr(III) based conversion coatings on zinc, *Surface and Coatings Technology*, (2005), **Vol. 199,** No.1, pp. 92-104.

[44] Long Z.L., Zhou Y.C., Yang C.Q., Chromate conversion coating treatments for electrodeposited zinc-iron alloy coatings from an acidic sulphate bath, *Transactions of the Institute of Metal Finishing*, (2003), **Vol. 81,** No.5, pp. 148-153.

[45] Zhang X., Böhm S., Bosch A.J., Van Westing E.P.M., De Wit J.H.W., Influence of drying temperature on the corrosion performance of chromate coatings on galvanized steel, *Materials and Corrosion*, (2004), **Vol. 55,** No.7, pp. 501-510.

[46] Campestrini P., Terryn H., Vereecken J., De Wit J.H.W., Chromate conversion coating on aluminium alloys III. Corrosion protection, *Journal of the Electrochemical Society*, (2004), **Vol. 151,** No.6, pp. B370-B377.

[47] Treacy G.M. and Wilcox G.D., Surface analytical study of the corrosion behaviour of chromate passivated Al 2014 A T-6 during salt fog exposure, *Applied Surface Science*, (2000), **Vol. 157,** No.1, pp. 7-13.

[48] Zhang X., Sloof W.G., Hovestad A., van Westing E.P.M., Terryn H., de Wit J.H.W., Characterization of chromate conversion coatings on zinc using XPS and SKPFM, *Surface and Coatings Technology*, (2005), **Vol. 197,** No.2-3, pp. 168-176.

[49] Eppensteiner F.W. and Jennkind M.R., Chromate conversion coatings, *Metal Finishing*, (2007), **Vol. 105,** No.10, pp. 413-424.

[50] Gao Y., Ana U., Wilcox G.D., Corrosion inhibitor doped protein films for protection of metallic surfaces: Appraisal and extension of previous investigations by Brenner, Riddell and Seegmiller, *Transactions of the Institute of Metal Finishing*, (2006), **Vol. 84,** No.3, pp. 141-148.

[51] Chidambaram D., Vasquez M.J., Halada G.P., Clayton C.R., Studies on the repassivation behaviour of aluminium and aluminium alloy exposed to chromate solutions, *Surface and Interface Analysis*, (2003), **Vol. 35,** No.2, pp. 226-230.

[52] Zaki N., Trivalent chrome conversion coating for zinc and zinc alloys, *Metal Finishing*, (2007), **Vol. 105,** No.10, pp. 425-435.

[53] Directive 2000/53/EC of the European Parliament and of the Council of 18 September 2000 on End-of-Life Vehicles, *Official Journal of the European Communities*, (2000), **Vol. L269,** pp. 34-43.

[54] Directive 2002/96/EC of the European parliament and of the Council of 27 January 2003 on Waste Electrical and Electronic Equipment (WEEE), *Official Journal of the European Union*, (2003), **Vol. L37,** pp. 24-38.

[55] Tencer M., Electrical conductivity of chromate conversion coating on electrodeposited zinc, *Applied Surface Science*, (2006), **Vol. 252,** No.23, pp. 8229-8234.

[56] Vaughan D. (Editor). Energy dispersive X-ray microanalysis, An introduction, Edition 1, (1983), p. 8, Kevex Corporation.

[57] Postek M.T. and Vladár A.E., Variable pressure/environmental SEM a powerful tool for nanotechnology and nanomanufacturing, *Microscopy and Microanalysis*, (2005), **Vol. 11,** No.2, pp. 388-389.

[58] Hafner B. Scanning electron microscopy primer, University of Minnesota, (2007), Online article, http://www.charfac.umn.edu/sem_primer.pdf, accessed 12-03-09.

[59] Ohring M., The materials science of thin films, Edition 1, (1992), pp. 275-276. Academic Press.

[60] Critchlow G.W., Instrumental techniques for the surface analysis of materials, *Transactions of the Institute of Metal Finishing*, (1996), **Vol. 74,** pp. 108-114.

[61] Reynolds H.L. and Hilty R.,Investigations of zinc whiskers using FIB technology, Presented at the IPC/JEDEC Lead Free North America conference, (2004), pp. 1-7. Boston, USA.

[62] Watts J.F. and Wolstenholme J., An introduction to surface analysis by XPS and AES, Edition 1, (2003), p. 17, 22, 23, 33, 187, 192, 193. John Wiley & Sons.

[63] Briggs D. and Seah M.P. (Editors). Practical surface analysis by Auger and X-ray photoelectron spectroscopy, Edition 1, (1983), John Wiley & Sons.

[64] Chidambaram D., Halada G.P., Clayton C.R., Development of a technique to prevent radiation damage of chromate conversion coatings during X-ray photoelectron spectroscopic analysis, *Applied Surface Science*, (2001), **Vol. 181,** No.3-4, pp. 283-295.

[65] Kagwade S.V., Clayton C.R., Halada G.P., Causes and prevention of photochemical reduction of hexavalent chromium during X-ray photoelectron spectroscopy, *Surface and Interface Analysis*, (2001), **Vol. 31,** No.6, pp. 442-447.

[66] Biesinger M.C., Brown C., Mycroft J.R., Davidson R.D., McIntyre N.S., X-ray photoelectron spectroscopy studies of chromium compounds, *Surface and Interface Analysis*, (2004), **Vol. 36,** No.12, pp. 1550-1563.

[67] Unveren E., Kemnitz E., Hutton S., Lippitz A., Unger W.E.S., Analysis of highly resolved X-ray photoelectron Cr 2p spectra obtained with a Cr2O3 powder sample prepared with adhesive tape, *Surface and Interface Analysis*, (2004), **Vol. 36,** No.1, pp. 92-95.

[68] Beamson G., Haines S.R., Moslemzadeh N., Tsakiropoulos P., Weightnan P., Watts J.F., High-energy monochromated Cu K1 X-ray source for electron spectroscopy of materials: Initial results, *Surface and Interface Analysis,* (2004), **Vol. 36,** No.3, pp. 275-279.

[69] Beamson G., Haines S.R., Moslemzadeh N., Tsakiropoulos P., Watts J.F., Weightman P., Williams K., Performance and application of a high energy monochromated Cu K 1 X-ray source for the electron spectroscopy of materials, *Journal of Electron Spectroscopy and Related Phenomena,* (2005), **Vol. 142,** No.2, pp. 151-162.

[70] Critchlow G.W. Pretreatments for metal-metal bonding, Thesis (Ph.D), (1998), p. 9, Loughborough University, UK.

[71] Smith G.C., Quantitative surface analysis for materials science, Edition 1, (1991), pp. 9-14. Maney Materials Science.

[72] Lawrence D.E., Noel C.M., Paul W.P., Gerald E.R., Roland E.W., Handbook of Auger electron spectroscopy a reference book of standard data for identification and interpretation of Auger electron spectroscopy data, (1978), pp. 49-53. Physical Electronics Division, Perkin-Elmer Corporation.

[73] B117, Operating salt spray (fog) apparatus, *Annual Book of ASTM Standards American Society for Testing and Materials,* (1997), **Vol. 3.02,** pp. 1-10.

[74] Stern M. and Geary A.L., Electrochemical polarization, *Electrochemical Society -- Journal,* (1957), **Vol. 104,** No.1, pp. 56-63.

[75] Manickavasagam R., Jeya Karthik K., Paramasivam M., Venkatakrishna Iyer S., Poly(styrene sulphonic acid)-doped polyaniline as an inhibitor for the corrosion of mild steel in hydrochloric acid, *Anti-Corrosion Methods and Materials,* (2002), **Vol. 49,** No.1, pp. 19-26.

[76] Wilhelm E.J., Method of coating zinc or cadmium base metals, US patent 2035380, (1936).

[77] Johnson D.M., Zinc and cadmium passivating bath, US patent 2559878, (1951).

[78] Page B.J. and Loar G.W., Kirk-Othmer encyclopedia of chemical technology, chromium compounds, Edition 5, (2004), pp. 526-570. John Wiley & Sons,.

[79] Gigandet M.P., Faucheu J., Tachez M., Formation of black chromate conversion coatings on pure and zinc alloy electrolytic deposits: Role of the main constituents, *Surface & Coatings Technology,* (1997), **Vol. 89,** No.3, pp. 285-291.

[80] Perrin F.X., Gigandet M.P., Wery M., Pagetti J., Chromium phosphate conversion coatings on zinc electroplates: Cathodic formation and characterization, *Surface and Coatings Technology,* (1998), **Vol. 105,** No.1-2, pp. 135-140.

[81] Hulser P., Replacement of hexavalent chrome passivations on galvanised steel, Presented at the AESF Continuous Steel Strip Symposium, (2002), Cleveland, USA.

[82] Van de Leest R.E., Yellow chromate conversion coatings on zinc: chemical composition and kinetics, *Transactions of the Institute of Metal Finishing,* (1978), **Vol. 56,** pp. 51-54.

[83] Long Z.L., Zhou Y.C., Xiao L., Characterization of black chromate conversion coating on the electrodeposited zinc-iron alloy, *Applied Surface Science,* (2003), **Vol. 218,** No.1-4, pp. 123-136.

[84] Brown G.M., Shimizu K., Kobayashi K., Thompson G.E., Wood G.C., Growth of chromate conversion coatings on high purity aluminium, *Corrosion Science,* (1993), **Vol. 34,** No.7, p. 1045.

[85] Campestrini P., Van Westing E.P.M., Hovestad A., De Wit J.H.W., Investigation of the chromate conversion coating on Alclad 2024 aluminium alloy: Effect of the pH of the chromate bath, *Electrochimica Acta,* (2002), **Vol. 47,** No.7, pp. 1097-1113.

[86] Kendig M.W., Davenport A.J., Isaacs H.S., Mechanism of corrosion inhibition by chromate conversion coatings from X-ray absorption near edge spectroscopy (XANES), *Corrosion Science,* (1993), **Vol. 34,** No.1, pp. 41-49.

[87] Katzman H.A., Malouf G.M., Bauer R., Stupian G.W., Corrosion-protective chromate coatings on aluminium, *Applications of Surface Science,* (1979), **Vol. 2,** No.3, pp. 416-432.

[88] Osborne J.H., Observations on chromate conversion coatings from a sol-gel perspective, *Progress in Organic Coatings,* (2001), **Vol. 41,** No.4, pp. 280-286.

[89] Campestrini P., Goeminne G., Terryn H., Vereecken J., De Wit J.H.W., Chromate conversion coating on aluminium alloys I. Formation mechanism, *Journal of the Electrochemical Society,* (2004), **Vol. 151,** No.2, pp. B59-B70.

[90] Treverton J.A. and Amor M.P., High-resolution SEM studies of chromate conversion coatings, *Journal of Materials Science,* (1988), **Vol. 23,** No.10, pp. 3706-3710.

[91] Treverton J.A. and Amor M.P., Structures and surface composition of chromate conversion coatings; an XPS and SEM study, *Transactions of the Institute of Metal Finishing,* (1982), **Vol. 60,** pp. 92-96.

[92] Arrowsmith D.J., Dennis J.K., Sliwinski P.R., Chromate conversion coatings on aluminium; growth of layers of spherical particles, *Transactions of the Institute of Metal Finishing,* (1984), **Vol. 62,** pp. 117-120.

[93] Zhang W., Hurley B., Buchheit R.G., Characterization of chromate conversion coating formation and breakdown using electrode arrays, *Journal of the Electrochemical Society,* (2002), **Vol. 149,** No.8, pp. B357-B365.

[94] Ramanauskas R., Gudaviciute L., Diaz-Ballote L., Bartolo-Perez P., Quintana P., Corrosion behaviour of chromated Zn and Zn alloy electrodeposits, *Surface and Coatings Technology,* (May 30, 2001), **Vol. 140,** No.2, pp. 109-115.

[95] Campestrini P., Terryn H., Vereecken J., De Wit J.H.W., Chromate conversion coating on aluminium alloys II: Effect of the microstructure, *Journal of the Electrochemical Society,* (2004), **Vol. 151,** No.6, pp. B359-B369.

[96] Chidambaram D., Halada G.P., Clayton C.R., Synchrotron radiation based grazing angle infrared spectroscopy of chromate conversion coatings formed on aluminium alloys, *Journal of the Electrochemical Society,* (2004), **Vol. 151,** No.3, pp. B160-B164.

[97] Kulinich S.A., Akhtar A.S., Susac D., Wong P.C., Wong K.C., Mitchell K.A.R., On the growth of conversion chromate coatings on 2024-Al alloy, *Applied Surface Science,* (2007), **Vol. 253,** No.6, pp. 3144-3153.

[98] Martyak N.M., Surface structures of zinc chromate coatings, *Metal Finishing,* (1996), **Vol. 94,** No.1, pp. 20-20.

[99] Martyak N.M., Internal stresses in zinc-chromate coatings, *Surface and Coatings Technology,* (1997), **Vol. 88,** No.1-3, pp. 139-146.

[100] Xia L. and McCreery R.L., Chemistry of a chromate conversion coating on aluminum alloy AA2024-T3 probed by vibrational spectroscopy, *Journal of the Electrochemical Society,* (1998), **Vol. 145,** No.9, pp. 3083-3089.

[101] Freund L.B., Batchelor G.K., Freud L.B., Dynamic fracture mechanics, Edition 1, (1990), p. 1-2. Cambridge University Press.

[102] Shorlin K.A., De Bruyn J.R., Graham M., Morris S.W., Development and geometry of isotropic and directional shrinkage-crack patterns, *Physical Review E - Statistical Physics, Plasmas, Fluids, and Related Interdisciplinary Topics,* (2000), **Vol. 61,** No.6, pp. 6950-6957.

[103] Deflorian F., Rossi S., Fedrizzi L., Bonora P.L., EIS study of organic coating on zinc surface pretreated with environmentally friendly products, *Progress in Organic Coatings,* (2005), **Vol. 52,** No.4, pp. 271-279.

[104] Murase M. and Watts J.F., XPS study of coating delamination from non-rinse chromate treated steel, *Journal of Materials chemistry,* (1998), **Vol. 8,** No.4, pp. 1007-1018.

[105] Xia L., Akiyama E., Frankel G., McCreery R., Storage and release of soluble hexavalent chromium from chromate conversion coatings. Equilibrium aspects of CrVI concentration, *Journal of the Electrochemical Society,* (2000), **Vol. 147,** No.7, pp. 2556-2562.

[106] Raichevsky G., Ivanova V., Vitkova S., Nikolova M., Composition of passive chromate films on a Zn-Sn alloy, *Surface and Coatings Technology,* (1996), **Vol. 82,** No.3, pp. 239-246.

[107] Brenner A., Riddell G., Seegmiller R., Chromated protein films for protection of metals, *J.Electrochem.Soc.,* (1948), **Vol. 93,** No.3, pp. 55-62.

[108] Council Directive 88/379/EEC of 7 June 1988 on the approximation of the laws, regulations and administrative provisions of the Member States relating to the classification, packaging and labelling of dangerous preparations, *Official Journal of the European Communities,* (1988), **Vol. L187,** pp. 14–30.

[109] Morico J.L., Process for reduction of hexavalent chromium, US patent 5316684, (1994).

[110] Directive 2002/95/EC of the European parliament and of the council of 27 January 2003 on the restriction of the use of certain hazardous substances in electrical and electronic equipment, *Official Journal of the European Union,* (2003), **Vol. L37,** pp. 24-38.

[111] Tomachuk C.R., Rosa L., Monetta T. and Bellucci F.,Chromium free conversion treatments for the protection of electroplated zinc, Presented at the 15th International Corrosion Congress, (2002), pp. 273-273. Granada, Espanha.

[112] Wilcox G.D., Gabe D.R., Warwick M.E., Development of passivation coatings by cathodic reduction in sodium molybdate solutions, *Corrosion Science,* (1988), **Vol. 28,** No.6, pp. 577-587.

[113] Schweikher E.W., Electroplating, US patent 2351639, (1944).

[114] Wharton J.A., Wilcox G.D., Baldwin K.R., Electrochemical evaluation of possible non-chromate conversion coating treatments for electrodeposited zinc-nickel alloys, *Transactions of the Institute of Metal Finishing,* (1999), **Vol. 77,** No.4, pp. 152-158.

[115] Wharton J.A., Wilcox G.D., Baldwin K.R., Non-chromate conversion coating treatments for electrodeposited zinc-nickel alloys, *Transactions of the Institute of Metal Finishing,* (1996), **Vol. 74,** pp. 210-213.

[116] Treacy G.M., Wilcox G.D., Richardson M.O.W., Behaviour of molybdate-passivated zinc coated steel exposed to corrosive chloride environments, *Journal of Applied Electrochemistry,* (1999), **Vol. 29,** No.5, pp. 647-654.

[117] Walker D.E. and Wilcox G.D., Molybdate based conversion coatings for zinc and zinc alloy surfaces: A review, *Transactions of the Institute of Metal Finishing,* (2008), **Vol. 86,** No.5, pp. 251-259.

[118] Wilcox G.D. and Wharton J.A., Review of chromate-free passivation treatments for zinc and zinc alloys, *Transactions of the Institute of Metal Finishing,* (1997), **Vol. 75,** pp. B140-B142.

[119] Lewis O.D., Greenfield D., Akid R., Dahm R.H., Wilcox G.D., SVET investigation into use of simple molybdate passivation treatments on electrodeposited zinc coatings, *Transactions of the Institute of Metal Finishing,* (2006), **Vol. 84,** No.4, pp. 188-195.

[120] Almeida E., Fedrizzi L., Diamantinio T.C., Oxidizing alternative species to chromium VI in zinc-galvanized steel surface treatment. Part 2 - an electrochemical study, *Surface and Coatings Technology,* (1998), **Vol. 105,** No.1-2, pp. 97-101.

[121] Thiery L. and Pommier N. Hexavalent chromium-free passivation treatments in the automotive industry, (2004) pp. 1-8, Coventya, France.

[122] Wynn P., Managing the transition to hexavalent chromium free anti-corrosion coatings, *Transactions of the Institute of Metal Finishing*, (2006), **Vol. 84,** No.6, pp. 280-285.

[123] Crotty D.E., Stabilized trivalent chromium passivate composition and process, US patent 4359348, (1982).

[124] Huvar R.J., Trivalent chromium passivate solution and process, US patent 4349392, (1982).

[125] Da Fonte B., Trivalent chromium passivate solution and process, US patent 4359345, (1982).

[126] Leonard J., Diaddario L. and Marzano M., Trivalent chromate conversion coating, US patent 20030145909, (2003).

[127] Crotty D.E., Non-peroxide trivalent chromium passivate composition and process, US patent 4578122, (1986).

[128] Oshima K., Tanaka S., Inoue M. and Yamamoto T., Processing solution for forming hexavalent chromium free and corrosion resistant conversion film on zinc or zinc alloy plating layers, hexavalent chromium free and corrosion resistant conversion film, method for forming the same, US patent 20050103403, (2005).

[129] Dikinis V., Rezaite V., Demcenko I., Selskis A., Bernatavicius T., Šarmaitis R., Characteristics of zinc corrosion and formation of conversion films on the zinc surface in acidic solutions of Cr(III) compounds, *Transactions of the Institute of Metal Finishing*, (2004), **Vol. 82,** No.3-4, pp. 98-104.

[130] Preikschat P., Jansen R. and Hulser P., Chromate-free conversion layer and process for producing the same, US patent 6287704, (2001).

[131] Chromium (VI) study, Confidential report, Dipsol, (2007) pp. 1-15.

[132] Upton P., Effect of sealers on increasing the corrosion resistance of chromate free passivates on zinc and zinc alloys, *Transactions of the Institute of Metal Finishing*, (2000), **Vol. 78,** No.4, pp. B45-B48.

[133] Cho K., Shankar Rao V., Kwon H., Microstructure and electrochemical characterization of trivalent chromium based conversion coating on zinc, *Electrochimica Acta*, (2007), **Vol. 52,** No.13, pp. 4449-4456.

[134] Sarmaitis R., Bernatavieius T., Dikinis V., Rezaite V., Demeenko I., Influence of corrosion on microstructure of chromated zinc surfaces. Part 1. Microstructure changes of electrodeposited zinc in the process of chromating, *Transactions of the Institute of Metal Finishing*, (2002), **Vol. 80,** No.5, pp. 168-172.

[135] B201, Standard practice for testing chromate coatings on zinc and cadmium surfaces, *Annual Book of ASTM Standards American Society for Testing and Materials,* (2004), **Vol. 2.05,** pp. 1-3.

[136] Shirley D.A., High-Resolution X-Ray Photoemission Spectrum of the Valence Bands of Gold, *Physical Review B,* (1972), **Vol. 5,** No.12, pp. 4709-4714.

[137] XPS survey scan. ESCA300 DOS software, Scienta Instruments AB, Version 1.29.

[138] Kwok R.W.M. XPSPEAK - XPS peak fitting program, (2000), Version 4.1.

[139] G102 - 89, Standard practice for calculation of corrosion rates and related information from electrochemical measurements, *Annual Book of ASTM Standards American Society for Testing and Materials,* (2004), **Vol. 3.02,** pp. 1-7.

[140] Lahtinen R. and Gustafsson T., The driving force behind whisker growth - An investigation on what triggers this phenomenon in hot-dip galvanized zinc coating (Part 2), *Metal Finishing,* (2005), **Vol. 103,** No.12, pp. 33-36.

[141] Lahtinen R. and Gustafsson T., The driving force behind whisker growth - An investigation on what triggers this phenomenon in hot-dip galvanized zinc coating (Part 1), *Metal Finishing,* (2005), **Vol. 103,** No.11, pp. 25-29.

[142] Lahtinen R. and Gustafsson T.E., SEM investigation of zinc whiskers on hot-dip galvanized coatings and bright electroplated coatings, *Journal of Applied Surface Finishing.,* (2007), **Vol. 2,** pp. 15-19.

[143] NASA. NASA tin whisker (and other metal whisker) homepage, (2009), http://nepp.nasa.gov/whisker/, accessed 13-02-08.

[144] Ilton E.S., DeJong W.A., Bagus P.S., Intra-atomic many-body effects in *p*-shell photoelectron spectra of Cr^{3+} ions, *Physical Review B,* (2003), **Vol. 68,** No.12, pp. 125106.1-125106.8.

[145] Savitsky. A. and Golay. M., Smoothing and differentiation of data by simplified least squares procedures, *Analytical Chemistry,* (1964), **Vol. 36,** pp. 1627- 1639.

[146] Charles D., Wagner D.C., Naumkin A., et al. NIST X-ray photoelectron spectroscopy database, (2003), Online database, http://srdata.nist.gov/xps/, accessed 08-12-08.

[147] Barbara S., Infrared spectroscopy: fundamentals and applications, Edition 1, (2004), p. 242, John Wiley & Sons Ltd.

[148] Morterra C., Emanuel C., Cerrato G., Magnacca G., Infrared study of some surface properties of boehmite (γ-AlO_2H), *Journal of the Chemical Society Faraday Transactions,* (1992), **Vol. 88,** No.3, p. 339.

[149] Vlaev L., Damyanov D., Mohamed M.M., Infrared spectroscopy study of the nature and reactivity of a hydrate coverage on the surface of γ-Al_2O_3, *Colloids and Surfaces,* (1989), **Vol. 36,** No.4, pp. 427-437.

[150] Schram T. and Terryn H., The use of Infrared spectroscopic ellipsometry for the thickness determination and molecular characterization of thin films on aluminum, *Journal of the Electrochemical Society*, (2001), **Vol. 148,** No.2, pp. F12-F20.

[151] Socrates G., Infrared characteristic group frequencies, second edition. Tables and charts, *Journal of the American Chemical Society*, (1995), **Vol. 117,** No.5, pp. 1671-1671.

[152] Kasperek J. and Lenglet M., Identification of thin films on zinc substrates by FTIR and Raman spectroscopies, *Revue de métallurgie*, (1997), **Vol. 94,** No.5, pp. 713 - 720.

[153] Vandenberg J.T., Anderson D.G., Duffer J.K., Julian J.M., Scott R.W., Sutliff T.M., Vaickus M.J., An Infrared spectroscopy atlas for the coatings industry, Edition 1, (1980), Federation of Societies for Coatings Technology.

[154] Ahmad Z., Principles of corrosion engineering and corrosion control, Edition 1, (2006), pp.10-12, Butterworth-Heinemann.

[155] Watson A., Chisholm C.U., el-Sharif M., Role of chromium II and VI in the electrodeposition of chromium nickel alloys from trivalent chromium-amide electrolytes, *Transactions of the Institute of Metal Finishing*, (1986), **Vol. 64,** pp. 149-153.

[156] Watson A., Anderson A.M.H., el-Sharif M., Chisholm C.U., Role of chromium II catalysed olation reactions in the sustained deposition of chromium and its alloys from environmentally acceptable chromium III electrolytes, *Transactions of the Institute of Metal Finishing*, (1991), **Vol. 69,** pp. 26-32.

[157] Ibrahim S.K., Watson A., Gawne D.T., Role of formic acid and methanol on speciation rate and quality in the electrodeposition of chromium from trivalent electrolytes, *Transactions of the Institute of Metal Finishing*, (1997), **Vol. 75,** pp. 181-188.

[158] Handy S.L., Oduoza C.F., Pearson T., Theoretical aspects of electrodeposition of decorative chromium from trivalent electrolytes and corrosion rate study of different nickel/chromium coatings, *Transactions of the Institute of Metal Finishing*, (2006), **Vol. 84,** No.6, pp. 300-308.

[159] Smith R. Characterisation of hexavalent and trivalent chromium conversion coatings on zinc substrates electrodeposited from acid electrolytes, Materials for Industry project (M.Sc.), (2006), Loughborough University, UK.

[160] Dini J.W., Electrodeposition - The materials science of coatings and substrates, Edition 1, (1993), p. 292, Noyes Publications.

[161] Sugiarto H., Christie I.R., Richards B.P., Studies of zinc whiskers formation and growth from bright zinc electrodeposits, *Transactions of the Institute of Metal Finishing*, (Autumn, 1984), **Vol. 62,** No.3, pp. 92-97.

[162] Honeycombe R.W.K., The plastic deformation of metals, Edition 2, (1984), Edward Arnold.

[163] Harrison R.D. (Editor). Book of data, Edition 1, (1977), Nuffield Advanced Science (Longman).

[164] Ebbage A.J. Heat treatment effect on hexavalent and trivalent chromium conversion coatings, Final year project report (B.Sc.), (2007), Loughborough University, UK.

[165] Li B., Lin A., Gan F., Preparation and characterization of Cr-P coatings by electrodeposition from trivalent chromium electrolytes using malonic acid as complex, *Surface and Coatings Technology,* (2006), **Vol. 201,** No.6, pp. 2578-2586.

[166] Otterstedt J.E. and Brandreth D.A., Small particles technology, Edition 1, (1998), p. 8, 9, 80, 81, 272, 447, 458. Springer.

[167] Dingwerth B. and Bishop C.V., The black barrier: Characteristics of high-performance black passivates for zinc substrates, *Metal Finishing,* (2008), **Vol. 106,** No.10, pp. 37-44.

[168] Fernandez-Olmo I., Ortiz A., Urtiaga A., Ortiz I., Selective iron removal from spent passivation baths by ion exchange, *Journal of Chemical Technology and Biotechnology,* (2008), **Vol. 83,** No.12, pp. 1616-1622.

Appendix A

Calculations for electroplating treatment time

Current required for half a polished mild steel hull cell:

Total area of polished mild steel panel (i.e. half hull cell panel both sides):

Total area (mm^2) = Length (mm) x Width (mm) x both sides (2)
7500 = 50 x 75 x 2

Therefore current required:

Note: specified operating current density range as specified in Kenlevel, MacDermid, between 1.5 to 4 A/dm^2

Current Density (A/mm^2) x Total area plated (mm^2) = Current (A)

0.00015 x 7500 = 1.125 A
or 0.000275 x 7500 = 2.063 A
or 0.0004 x 7500 = 3 A

Required time for thickness of (8µm):

Required Volume:

Volume (mm^3) = length (mm) x width (mm) x height (mm)
= 50 x 75 x 0.008
= 30 mm^3
Therefore both sides = 60 mm^3

Required Mass:

Mass (g) = volume (mm^3) x density (g/mm^3)
= 60 x 0.00716
= 0.4296 g

Note: density of zinc taken as 7160 kg/m^3

Required Time for 0.000275 A/mm^2:

$$\text{Time (s)} = \frac{\text{Mass (g)} \times \text{no. of electrons} \times \text{faradays constant (C/mol}^{-1})}{\text{Mr (g/mol}^{-1}) \times \text{Current (A)}}$$

$$= \frac{0.4296 \times 2 \times 96500}{65 \times 2.063}$$

= 618.46 s (or 10.18 min)

1.125 A = 1133.9 s (or 18.54 min)
3 A = 425 s (or 7.05 min)

Appendix B

Table 4.17 $Cr2p_{3/2}$ curve fitted peak maximum BE, FWHM and area % values of chromium coating using Cr_2O_3, $Cr(OH)_3$ and CrO_3 as reference compounds as well as ZnO LMM. All energy values are charge corrected to C1s at 285 eV.

Sample	Peak 1	Area	FHWM	Peak 2	Area	FHWM	Zn (Area %)	Peak 3	Area	FHWM	$Cr(OH)_3$ (Area %)
Hexavalent CCC	573.49	216.91	0.71	576.72	366.58	0.58	2.06	577.79	19669.41	2.24	69.34
Trivalent CCC	573.49	11695.14	3.81	576.72	19764.79	3.08	43.15	577.79	17876.24	2.39	24.52
Hexavalent CCC 10° TOA	573.49	0.10	0.50	576.72	0.17	0.13	0.00	577.79	48918.19	2.14	69.46
Hexavalent CCC 30° TOA	573.49	1664.60	8.57	576.72	2813.18	6.94	2.13	577.79	135378.90	2.08	64.39
Hexavalent CCC + NaCl exposure	573.49	507.65	6.93	576.72	857.93	5.62	2.87	577.79	37673.37	2.18	79.20
Trivalent CCC + NaCl exposure	573.49	4559.36	1.62	576.72	7705.32	1.31	20.58	577.79	26450.34	2.07	44.39

Sample	Peak 4	Area	FHWM	Peak 5	FHWM	Area	Peak 6	FHWM	Area	Peak 7	FHWM	Area	Cr_2O_3 (Area %)
Hexavlent CCC	577	167.58	0.50	575.8	0.50	78.76	578.53	0.57	55.30	579.94	0.78	20.11	1.13
Trivalent CCC	577	12276.07	1.60	575.8	0.83	5769.75	578.53	1.80	4051.10	579.94	2.48	1473.13	32.33
Hexvalent CCC 10° TOA	577	0.10	12.18	575.8	6.29	0.05	578.53	13.68	0.03	579.94	18.86	0.01	0.00
Hexvalent CCC 30° TOA	577	0.10	5.38	575.8	2.78	0.05	578.53	6.60	0.03	579.94	8.33	0.01	0.00
Hexvalent CCC + NaCl exposure	577	2289.83	0.90	575.8	0.50	1076.22	578.53	1.01	755.65	579.94	1.40	273.86	9.24
Trivalent CCC + NaCl exposure	577	10871.84	3.82	575.8	1.97	5109.76	578.53	4.29	3587.71	579.94	5.91	1300.27	35.03

Sample	Peak 8	FHWM	Area	Peak 9	FHWM	Area	Peak 10	FHWM	Area	CrO_3 (Area %)
Hexavlent CCC	579.96	1.35	5411.07	581.06	1.29	1190.44	578.3	2.74	1190.44	27.47
Trivalent CCC	579.96	7.64	0.10	581.06	7.33	0.02	578.3	15.51	0.02	0.00
Hexvalent CCC 10° TOA	579.96	1.63	14978.91	581.06	1.57	3230.95	578.3	3.32	3295.36	30.54
Hexvalent CCC 30° TOA	579.96	1.75	49186.95	581.06	1.68	10609.62	578.3	3.56	10609.62	33.48
Hexvalent CCC + NaCl exposure	579.96	1.17	2868.89	581.06	1.13	631.16	578.3	2.38	631.16	8.69
Trivalent CCC + NaCl exposure	579.96	1.89	284.23	581.06	1.81	62.53	578.3	3.83	62.53	0.00